PhD Thesis

Towards Optimising Turbine Technology: Development and Analysis of Nonlinear Models for Monopile Lateral Loading

Jacques Tott-Buswell

Master of Engineering MEng (Hons)

University of Nottingham, UK

This thesis is submitted to the University of Nottingham for the degree of Doctor of Philosophy in the Department of Civil Engineering

November 2023

Head of Department:
Prof. Glenn McDowell

Supervisors:
Dr. Luke J. Prendergast
Dr. Charles Heron

Executive Summary

Monopiles support the majority of Offshore Wind Turbines (OWTs) in the North Sea due to their simplicity in design, installation, and fabrication. However, as demand outpaces research, modern practices have resorted to utilising offshore design methodologies from the oil and gas industry. This has lead to conservative designs, unnecessary costs, and uncertain structural longevity. To add, the industry is moving towards larger turbines, which are dynamically sensitive structures that are subject to millions of irregular loading cycles from wind and wave excitation. This can cause significant damage to the soil-pile system over time, which is often mis-represented in beam-spring models for monopiles with low slenderness ratios.

Many wind turbines are required in unique soil conditions for a given offshore wind array, therefore preliminary design estimates from in-situ ground investigations would be advantageous. Chapter 3 develops and analyses a simplified beam-spring element model that can be used to estimate the lateral response of a monopile using Cone Penetration Test (CPT) data, which is often available at the early stages of offshore projects. The multi-spring model is compared with site tests of scaled laterally loaded monopiles in sand, and captures pile head deflections within the anticipated operational range of a commissioned OWT.

Furthermore, many irregular load cycles can cause significant damage to the soil-pile system over time. As the industry moves towards larger turbines, the dynamic soil-structure interaction becomes increasingly more complex. The overall structural flexibility increases and resonance becomes likely, accelerating the rate of substructure damage accumulation. Chapter 4 details the development of a robust and efficient framework for a dynamic nonlinear beam-spring model that facilitates soil damping by means of discrete hysteretic springs. Particular attention is geared towards reviewing time marching algorithms for dynamic analysis and interrogating different definitions of hysteresis models. Such a model ensures that empirically derived degradation models can be applied to the soil spring elements with confidence, which would ultimately serve as a strong design tool when many simulations are of importance.

Finally, Chapter 5 investigates the suitability of the pseudostatic approach for the seismic analysis of piles in layered soils by means of experimental data from centrifuge tests at 60g. Various theoretical approaches are reviewed, including load characterisation, layering effects, and group efficiency modifiers. Bending moment profiles are compared with the experimental data, and the influence of the various parameters are discussed. The pseudostatic approach is found to be a suitable method for estimating the seismic response of group piles in layered soils, however, the damping ratio used to identify the idealised inertial load must be considered carefully.

Acknowledgements

I would like to express my sincerest gratitude my supervisor, Dr. Luke J Prendergast, for his support, guidance, and mentorship. His expertise, patience and commitment to my academic growth has been invaluable, and I am truly thankful for the opportunities I've had to learn.

I extend my heartfelt thanks to the University of Nottingham, which provided the academic environment in which I thrived. I am grateful for the resources and opportunities that enabled me to attend conferences and present my research to the wider academic community.

I owe an immense debt of gratitude to my better half, Charis, for her encouragement, understanding, and unwavering belief in my abilities. I am thankful for the sacrifices you've made to ensure my success. Your love and emotional support has been a bastion of strength and motivation.

Finally, I wish to extend this gratitude to my family and friends for being continuous source of positivity during this academic journey.

$\sim$ *Ut Tensio, Sic Vis* $\sim$

Contents

List of Figures

List of Tables

Chapter 1

Introduction

Fossil fuel energy has spearheaded technological advancements in transportation, agriculture and communication due to its high energy density and reliability. The lucrative markets and well-established harvesting infrastructure of oil, coal, and natural gas have been the economical backbone for developing countries in recent decades. However, the growing demand has led to a rapid depletion of resources, extreme environmental impacts, and geopolitical instability. Even as convenient sources are expiring, discovering new deposits will likely still be at the top of the political agenda, leading to less economically-viable harvesting practices in environmentally sensitive areas. Fuel prices are likely to surge, and the need for an alternative, greener means of producing energy will therefore always be inevitable.

The challenges imposed on sustainable energy solutions include competing with the financial viability of coal mining, oil drilling, and fracking. Achieving this will require innovative solutions across all disciplines, from cradle to grave, to catalyse investment and instil universal confidence. Wind power in Europe is emerging as a leader in the renewable energy sector due to the fruitful coasts of the North Sea and technological advancements in offshore wind infrastructure. However, the foundation design and maintenance processes have much room for improvement, and are crucial to the overall logistics of a wind farm project. This thesis will aim to address these issues by exploring numerical modelling practices for pile soil-structure interaction by significantly enhancing well-established methodologies.

1.1 Sustainable energy solutions

The environmental impacts of climate change are far-reaching and multifaceted, and will require a combined effort from governments, businesses and individuals around the world to reduce harmful emissions. International cooperation is often motivated by economical incentives to fulfil obligations, therefore many treaties and agreements have been held to ratify global regulations and promote ambitious commitments. As a product, domestic and transnational political processes play out in the interest of mitigating the impact of climate change, leading to large funding towards greener energy infrastructure. As an example, the Paris Agreement mobilised financial commitments towards both nuclear and offshore wind from the UK government to fulfil their nationally determined contribution targets, which include net zero emissions by 2050 (UNFCCC, 2015).

Because of their simple construction and energy harvesting methods, Offshore Wind Turbines (OWTs) provide quick energy returns. The consequence of their downtime is minimal, and they benefit from the success of their onshore counterpart. Nuclear fission, despite also being a strong contributor to sustainable energy, imposes extensive construction and planning processes that demand substantial investments. These financial commitments may present challenges to a nation's energy security. Additionally, nuclear power requires significant infrastructure and commissioning time that can take decades to complete. Although nuclear power plants have a lifespan of up to 60 years and OWTs have a lifespan of 20-30 years, both sources will play an important role in combating the climate crisis and lowering carbon emissions. It is clear that nuclear energy is a long-term investment, whereas offshore wind is a short-term solution to energy demand.

Hydrogen is abundant and emission-free at the point of use, making it a promising solution. However, due to the energy-intensive process of extracting hydrogen from hydrogen-rich sources, its widespread adoption is restricted. One potential solution is to leverage well-established sustainable energy sources, like offshore wind and nuclear, to offset the high energy demands of hydrogen production. This approach can enhance its viability, catalyse investment, and foster a more competitive market. While hydrogen may not address immediate economic concerns due to its relatively early stage of development, its long-term potential for clean and sustainable energy is evident. Beyond the scope of current climate action plans, hydrogen power could emerge as an effective and sustainable energy source. However, in the interim, the offshore wind sector may play a crucial role by offering a practical solution to the broader climate crisis. Its fast energy returns and scalability provide immediate benefits for combatting climate change, while also laying the foundation for more ambitious energy infrastructure, such as hydrogen generation, in the long term.

1.2 Wind energy in the UK and Europe

Onshore wind farms have successfully established themselves as a low-cost source of renewable energy, but outstanding issues of visual landscape pollution and limited space are ever-present. As turbine and wind farm sizes increase to meet demand, there are fewer suitable land areas for installation. For this reason, offshore wind farms are becoming more attractive, as they are less restricted by socially-imposed size restrictions on rotor diameter and array population.

The North Sea has significant potential for generating green energy from OWTs due to its low water depth average of 30 to 40 meters. Neighbouring countries are already exploiting these shallow coastal environments in recent decades. Figure 1.1 provides an overview of the total capacity and the number of new onshore and offshore installations in Europe as of 2021.

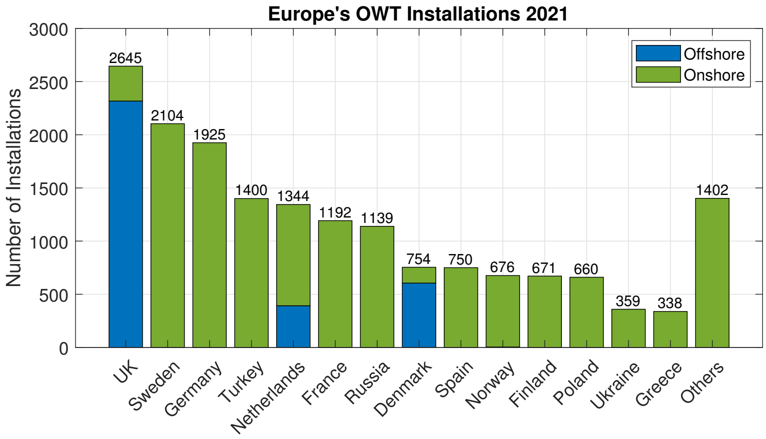

(a) Number of onshore and offshore installations per country as of 2021

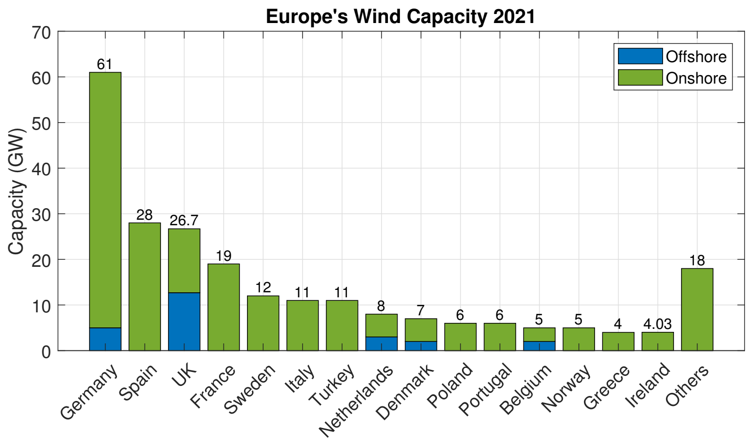

(b) Capacity (GW) of onshore and offshore wind turbine generators per country as of 2021

Figure 1.1: Onshore and offshore statistic for different countries. Data provided by Wind Europe (Wind Europe, 2021b)

Figure 1.1 shows the UK's shift from onshore to offshore wind farms, driven in part by significant investments made to meet Paris Agreement targets and limited onshore real estate. In 2022, offshore wind surpassed onshore wind in capacity, contributing 14% and 12% to the UK's total energy mix, respectively (Wind Europe, 2021a). The feasibility of offshore units was already well-established due to the success of their onshore counterparts. However, ambitious wind capacity targets naturally lead to significantly larger wind harvesting units that introduce unprecedented challenges of their own. Figure 1.2 demonstrates the scale of commissioned OWT hubs in 2021.

Figure 1.2: Image demonstrating the scale of the Nacelle for 2021's GE Haliade-X OWT (source: greentechmedia.com)

1.3 Offshore wind infrastructure

Offshore environments have permitted larger rotor diameters and more OWT units to be commissioned, overcoming the size constraints imposed by public concerns over visual pollution of onshore wind farms (see Figure 1.3). The increase in size is driven by demand, but the logistical challenges of offshore installations result in their units costing two to three times more than onshore wind turbines, depending on location (Wu et al., 2019).

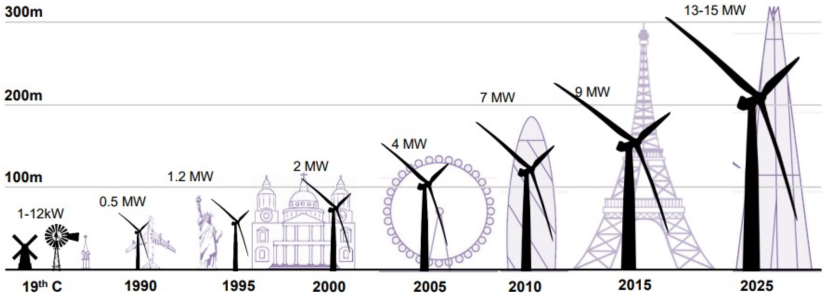

Figure 1.3: Evolution of OWT sizes and capacities over 30 years (source: robeco.com)

The North Sea has the potential to generate 120GW of energy, over twice the UK's demand, if one-third of its shallower regions are occupied by OWTs (MacKay, 2008). However, shallow sites are becoming increasingly more crowded and expedite the development of OWTs in deeper oceans. The harsh weather conditions impose horizontal loads that exceed what is expected in current design practices (API, 2014; DNV, 2021). The performance and longevity of OWTs under such conditions is therefore uncertain (Burd et al., 2017). Foundations can constitute up to 15% of the unit's cost in shallower waters and up to 35% in deeper waters (Kallehave et al., 2015). Therefore, the selection of foundation type is crucial for exploiting offshore wind. The water depth, soil stratum and turbine size have a significant influence on most type of substructures. Common foundations are illustrated in Figure 1.4, including both fixed and floating foundation types. A brief description of each type of foundation is given below.

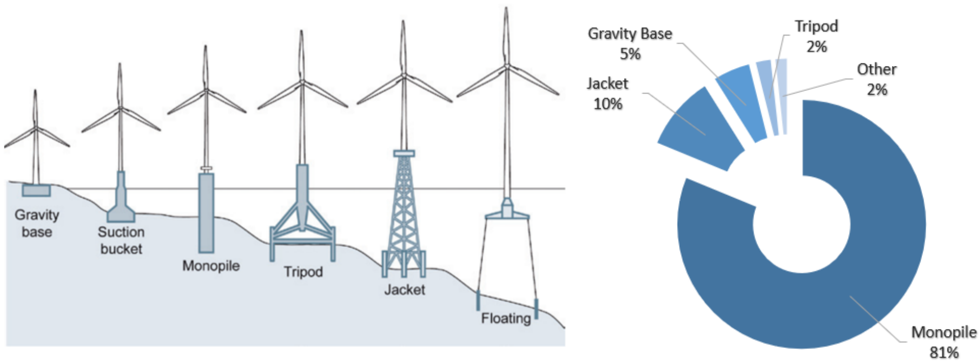

Figure 1.4: OWT foundation types and their percentage in Europe (Wind Europe, 2021a)

Gravity Base

Gravity-based foundations are reinforced concrete caissons that rely on the self-weight of the substructure to resist extreme overturning moments imposed by wind and wave loads applied to the OWT. Due to their simple design, shallow requirements, and well-understood physical behaviour, gravity-based foundations were adopted by early offshore wind farms, such as the 0.5MW turbines used in Vindeby, 1991 (Figure 1.3). Although commonly used in the onshore wind industry, their popularity in offshore wind farms quickly diminished once alternative methods were considered more industrially scalable for coastal conditions (Bhattacharya, 2019; Byrne & Houlsby, 2003). They are still widely used for onshore environments and are often combined with pile groups.

Suction Bucket

A suction bucket consists of a hollow open-bottom cylinder that self-embeds by generating a pressure differential within a cavity between the seabed and the bucket by pumping out seawater. This unique installation method results in an exceptionally cost-effective fixity, but its effectiveness is highly dependent on the type of soil, typically requiring soft clay, although it is not limited to such conditions (Ibsen et al., 2005; Remmers et al., 2019). The design and analysis process is similar to the monopile, where a suitable diameter and embedment depth are defined (Grecu et al., 2021; Ibsen et al., 2005). Suction buckets can also serve as an anchorage point for floating OWTs (Wu et al., 2019).

Monopile

Monopiles are steel tubular piles driven or vibrated into the seabed and are installed in water depths ranging between 20-40m. They are designed to have sufficient diameters and embedment lengths to ensure horizontal stability from lateral earth pressures. Monopiles can be geometrically quantified through a slenderness ratio (embedment depth over diameter) which is typically less than 10 (Doherty & Gavin, 2011). Recent advancements in infrastructure have led to slenderness ratios as low as 3 (Burd et al., 2020b; Byrne et al., 2015, 2020a). The manufacturing process of a steel tubular pile is simple and reproducible, and the on-site assembly is manageable on a large scale. As a consequence, it has become a popular choice for large offshore wind farms worldwide and supports 81% of OWTs in Europe as of 2020 (Figure 1.4).

Tripod/Jacket

A tripod foundation consists of a submarine-jacketed steel structure supported by three fixed points arranged in a triangular configuration (also known as a full jacket, see Figure 1.4). The upper tower loads transfer stresses to the foundation fixities, which can be either steel piles or suction buckets, each with their own installation challenges and site requirements (Sparrevik, 2019). The environmental loads are transferred through the jacketed structure to the piles/buckets, where resistance is generated through axial push-pull action. The tripod truss or space-frame jacket structure is prefabricated onshore and transported on-site, making it economical in terms of steel consumption. However; the storage, installation and logistical processes are expensive and heavily influence project costs.

Floating

The economic feasibility of bottom-fixed foundations becomes less practical in deeper environments due to the challenges associated with the required material and installation processes. Supporting OWTs on floating structures becomes more viable beyond 50 m depths, which presents complex problems in limiting pitch, roll, and heave motions of the superstructure during intense storm events (Castro-Santos & Diaz-Casas, 2016). The type of anchorage required varies depending on the soil and climate conditions, which can include pile anchors, suction buckets, and torpedo anchors (Wu et al., 2019). Although uncommon in the offshore industry to date (see Figure 1.4), floating wind turbines may become increasingly more important as shallow coastal capacities reduce and the industry expands to deeper oceans.

When considering the cost and construction differences between floating and bottom-fixed OWTs, it is advisable to use bottom-fixed foundations whenever possible (Byrne & Houlsby, 2003). With the increasing demand for renewable energy and the anticipation of more wind farms with larger wind turbines, specific infrastructure requirements becomes more important. Foundation design is therefore a crucial aspect to optimising the wind harvesting process, and is the reason why monopile foundations have a demonstrable presence in the European wind industry (Figure 1.4). Their simplicity in design, fabrication and installation should be exploited, yet do not come without their own design challenges. Demand has outpaced research, leading to a questionable re-appropriation of traditional pile design practices as a means to keep up (API, 2014; Doherty & Gavin, 2011; Murchinson & O'Neill, 1986; Reese et al., 1974). This has led to uncertain lifespans and over-conservative capacity designs in currently-commissioned OWTs. This can be optimised with an improved representation of the soil-structure interaction and other geotechnical challenges (Andersen, 2015; Byrne et al., 2017; Lehane & Suryasentana, 2014; Zhang et al., 2016). The design process must consider the environmental loads, wind turbine type, and soil-structure interaction for optimal design outputs, as these factors will also have an influence on the logistical and economical implications of the project accordingly (Arany et al., 2017; Bhattacharya, 2019; Lehane et al., 2020b; Randolph et al., 2009).

1.4 Monopile design challenges

Monopiles resist lateral wind and wave loads by mobilising horizontal earth pressures in competent near-surface soils. The diameter and embedment length of the monopile are sized to restrict ground line deflections to serviceable tolerances, while the wall thickness is selected to resist bending and material buckling without compromising efficient fabrication methods. Capacity checks are generally performed using a static analysis, where the nonlinearity of the soil-structure interaction is represented using semi-empirical methods to estimate the monopile's horizontal or vertical capacity. The applied load is designed to represent different combinations of harsh wind conditions and sea states (Arany et al., 2017).

Serviceability Limit State (SLS) design checks require that the foundation tilt remains within rotation limits at the ground line (0.25° with 0.25° allowable for installation error (DNV, 2021)), including a modal frequency analysis to determine the natural frequency of the OWT (Carswell et al., 2016; Darvishi-Alamouti et al., 2017; Prendergast et al., 2013). The designed natural frequency must avoid the frequencies expected from external loads in order to avoid resonance, otherwise excessive deflections occur and can result in an increased rate of accumulative damage to the soil-structure interaction (Andersen, 2015; Kaynia et al., 2015; Leblanc et al., 2010b).

Design procedures for OWTs must also factor in the longevity of the system to ensure a safe and functional operation throughout its lifespan. However, the design challenges for OWT durability and serviceability are compounded when considering the evolving properties of the soil-structure interaction over time. After many load cycles, monopiles may experience reduced lateral or horizontal capacity (Abadie et al., 2019; Damgaard et al., 2014; Lehane et al., 2020b), and the natural frequency of the turbine may shift towards external excitation frequencies (Darvishi-Alamouti et al., 2017; Kaynia et al., 2015). Additionally, the accumulated rotation may exceed turbine tilt limits specified by the manufacturer, affecting the wind harvesting efficiency. Thus, it is critical to consider substructure degradation at the design stage and monitor it throughout operation

Geotechnical phenomena, such as near-surface gaps and ratcheting, also pose common challenges for submerged piles in general, as this can affect the flexural rigidity of the system (Gerolymos & Gazetas, 2005c; Houlsby et al., 2017; Prendergast et al., 2013; Williams et al., 2021). Wind and wave load misalignment complicates these matters further (Mayoral et al., 2016; Pestana et al., 2000). Intense storm events can also lead to changes in pore pressure (Andersen, 2015). Large moments are expected due to longer turbine blades and deeper ocean environments, requiring stiffer pile cross-sections and lower embedment-diameter ratios (L/D). This, in turn, leads to alternative monopile failure mechanisms and additional mobilisation of soil resistances that must be considered in design models (Byrne et al., 2017; Fu et al., 2020; Murphy et al., 2018; Thieken et al., 2015; Van Impe & Wang, 2020; Zhang & Andersen, 2019).

1.5 Thesis objectives and content overview

This thesis explores the analysis of monopile foundations for OWTs, focusing on the response to lateral loads, dynamic loading conditions, and seismic events. Table 1.1 provides a summary of each chapter's focus and the specific contributions to the field of offshore wind and geotechnical engineering. Chapter 2 reviews the historical development of pile analysis and its influence on modern monopile design practices. Chapters 3 and 4 detail the development of advanced monopile beam-spring models for lateral static and lateral dynamic loading, respectively. Chapter 5 presents insights from centrifuge tests, shedding light on the seismic behaviour of pile foundations in layered soils. Finally, Chapter 6 summarises the findings from the preceding chapters, discussing their implications, limitations, and future directions. For each chapter, the work of collaborators is outlined, and the publication status is described.

This thesis is presented as a hybrid format of thesis and paper publications, whereby each chapter is either a standalone paper or derived from one.

Table 1.1: Thesis chapter summary and contributions

Chapter	**Contribution**
Chapter 2	This chapter provides an overview of monopile analysis and general pile modelling for lateral loads. The purpose of this chapter is to establish the evolution of design and modelling methodologies for laterally loaded piles and how it has influenced monopile design practices. The literature review will outline the course of research presented in subsequent chapters of this thesis.

Continued on next page

Table 1.1: Thesis chapter summary and contributions (Continued)

Chapter	Contribution
Chapter 3	This chapter details the development and analysis of a multi-spring monopile model for lateral monotonic loading informed with in-situ site investigation methods. The method modifies the traditional beam-spring model for piles to incorporate additional soil reactions expected from large-diameter monopiles, and the model is validated against pile pushover field test reports performed by Murphy et al. (2018) and McAdam et al. (2020). This work included a collaboration with Prof. Ken Gavin at Delft University of Technology, who provided insights to axial pile analysis and interpretation of cone penetration tests. The contributions to this chapter are currently under review for publication towards the Ocean Engineering Journal.
Chapter 4	The purpose of this chapter is to develop a robust and efficient dynamic modelling framework that facilitates irregular cyclic loading conditions for OWTs. This chapter will review different time marching algorithms and hysteresis models to facilitate the complexities associated with dynamic soil-structure interaction. Computational efficiency is important, as many time-domain simulations are required in design for many loading conditions expected in the offshore environment. An appropriate time marching algorithm and nonlinear spring model is identified and trialled by applying a realistic load history informed from wind and wave spectra typically used in the design process of OWTs. Features of the model's performance are discussed, and future work is outlined. The content of this chapter is pending submission towards the Journal of Sound and Vibration.

Continued on next page

Table 1.1: Thesis chapter summary and contributions (Continued)

Chapter	Contribution
Chapter 5	This chapter investigates the performance of the pseudostatic approach for seismic analysis of pile foundations in layered soils using centrifuge tests performed by Garala (2020) at Cambridge University. Single and group pile behaviour is examined in a layered soil profile of soft clay on top of dense sand, and are modelled using the American Petroleum Institute (API) reaction curves. Different modelling approaches for the soil-structure interaction are compared, including alternative approaches to idealising inertial loads and layered soil profiles. The results are discussed, and the implications for seismic design are outlined. This work included a collaboration with Dr Thejesh Garala and Prof. Gopal Madabhushi at Cambridge University, who supplied the centrifuge data. All other aspects of the research were conducted by the author, including model development, data analysis, and result discussion. This chapter is published in Soil Dynamics and Earthquake Engineering (Tott-Buswell et al., 2022).
Chapter 6	The findings of each chapter are summarised and discussed in the context of the broader research goals. The limitations of the research are outlined, and future work is proposed.

Chapter 2

Literature review

The rapid growth of the offshore wind industry has lead to a reappropriation of existing pile modelling methodologies that are well established in other industrial fields such as oil and gas (API, 2014; DNV, 2021). However, the unique characteristics of OWTs, such as the high horizontal to vertical load ratio configuration, have put these methodologies under heavy scrutiny. This chapter reviews the current modelling techniques available in literature and industrial design codes. A brief introduction to the design philosophy of monopile foundations is presented, highlighting general modelling techniques for the monotonic lateral response and reviewing the efficacy when applied to typical monopile geometries. Then, the cyclic and dynamic behaviour of OWTs will be reviewed and the various modelling techniques available in literature.

The Ultimate Limit State (ULS) design philosophy determines the maximum load required to cause structural collapse, and reviews both the structural and geotechnical capacity of the OWT system. The Serviceability Limit State (SLS) criteria limits the pile's ground line rotations such that wind harvesting routines are optimal (API, 2014; DNV, 2021). Calculating the natural frequency of the OWT and monopile structure is also necessary to avoid resonance from environmental and rotor excitations (Arany et al., 2017). However, soil can degrade over time due to numerous load cycles, resulting in permanent pile rotation and a change in soil properties (Andersen, 2015; Houlsby et al., 2017; Niemunis et al., 2005). Fatigue Limit State (FLS) design checks are therefore required. The natural frequency can change over its operational lifespan (Carswell et al., 2016; Kaynia et al., 2015; Prendergast et al., 2013), meaning the loading conditions for resonance may no longer align with initial design parameters. New resonance conditions may occur that are more common, further accelerating accumulated rotations and soil strength degradation. Ultimately, these factors may decrease the calculated capacity established during initial ULS design estimates (Lo Presti et al., 2000; Long & Vanneste, 1994; Rascol, 2009).

Designing for the capacity, serviceability, and longevity of OWTs is therefore an overlapping and multifaceted challenge, and each regard is summarised in the following sections, including discussions about their influence on one another.

2.1 Monotonic pile modelling

The ULS design philosophy against horizontal loading ensures that the maximum load capacity (i.e. the load that causes collapse) exceeds the maximum anticipated load during operation. This is determined by computing combinations of load cases that idealise complex load histories expected in the offshore environment via detailed environmental survey (Arany et al., 2017; Bhattacharya, 2019). According to design codes, the capacity of the foundation is determined as the minimum of either the load that causes (i) soil failure or (ii) pile failure via plastic hinge in the foundation (DNV, 2021). Typically, monopiles are designed to remain within the steel's elastic range of deformation to prevent permanent tilt due to the material yielding. The soil's bearing capacity is therefore considered as the principle design parameter under lateral loading.

2.1.1 Lateral bearing capacity of piles

The lateral bearing capacity of the mobilised soil is an important aspect of the design and analysis of piles. Piles under large monotonic horizontal loads develop a passive failure wedge that forms near the surface as shown in Figure 2.1. At a certain depth (the transition depth, z_r), the failure mode of the soil occurs by continued plastic flow around the pile (Figure 2.1c), which assumes only horizontal soil mobilisation (Broms, 1964a). The local capacity of a soil layer p_u therefore depends on the depth from the surface z, as the failure mode can vary.

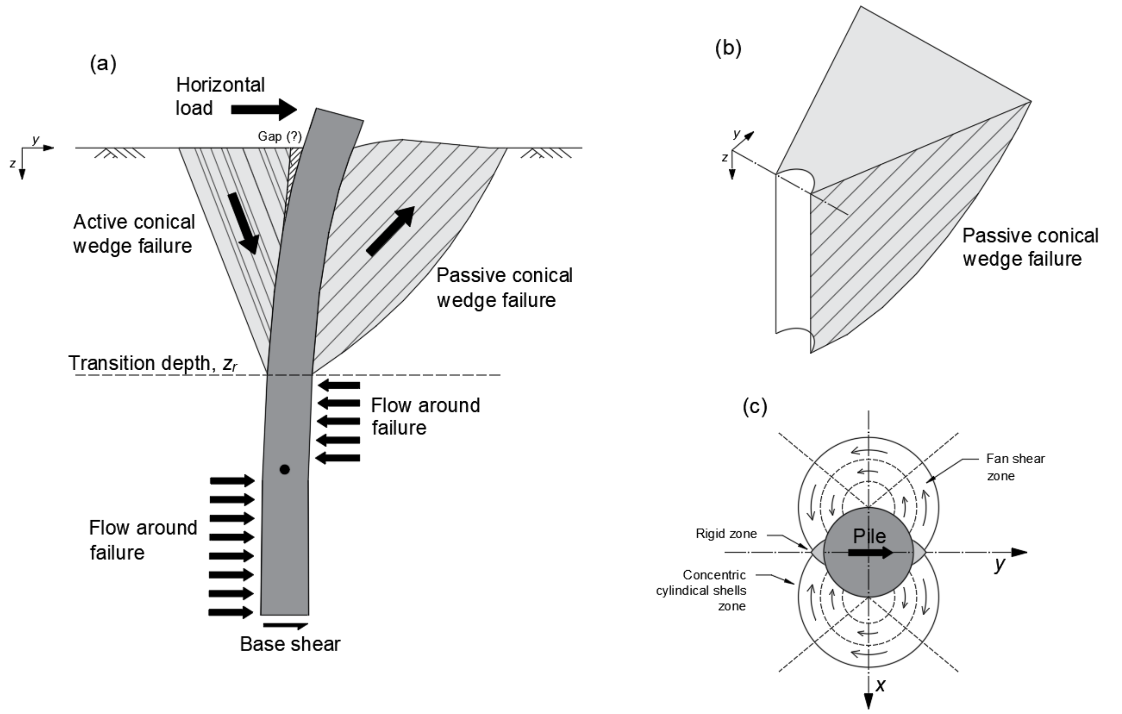

Figure 2.1: (a) Pile failure under horizontal load (b) 3D illustration of passive wedge failure mechanism (c) section view of flow-around failure mechanism

Broms (1964b) proposed that the lateral capacity of a circular pile P_u in sands can be determined using the simple expression described in Equation 2.1.

$$P_u = 3K_p\gamma' LD \tag{2.1}$$

where K_p is the passive earth pressure coefficient and γ' is the effective unit weight of the soil. Tests results indicate that this method underestimates the lateral capacities by approximately 30% (Poulos & Davis, 1980). This is likely due to Broms (1964b) assuming that the lateral pressure exerted by the soil acts only on the side opposite the the applied load, and applying a point load at the pile tip to ensure moment equilibrium. This is not representative of the true physical behaviour of a laterally loaded pile.

For circular piles in cohesive soils, Broms (1964a) assumed that the ultimate lateral resistance is $9c_uD$, which decreases based on the deformation modes of the pile. This value was derived from empirical analysis rather than theoretical justification, but was later confirmed by Randolph and Houlsby (1984) with theoretical analyses using plasticity-bound theorems for upper- and lower-bound solutions (shown in Figure 2.1c). Randolph and Houlsby (1984) suggested an average ultimate resistance of $10.5c_uD$ for cohesive soils, with the lower bound limit of $9.14c_uD$ (for a perfectly smooth pile) and an upper limit of $11.94c_uD$ (for a rough pile). A perfectly smooth pile is in close agreement with Broms (1964a), but assumes a full flow-around mechanism along the depth of the pile with no wedge-type mobilisation. This is only a valid approximation for laterally loaded piles with high L/D ratios (≥ 35). However, as L/D decreases, the flexural rigidity of the pile influences the mobilisation of the soil (Fan & Long, 2005; Murphy et al., 2018; Poulos & Hull, 1989). The soil profiles are also assumed to be homogenous.

Hansen (1961) proposed a method to discretise the stratum into layers and assume a lateral earth pressure on both sides of the pile, as opposed to Broms (1964b). Layering enabled independent control of different layer's failure mechanisms expected at certain depths z (Figure 2.1). The transition depth z_r was found by equating shallow and deep bearing capacities, which were defined using two different lateral soil pressure coefficients (Hansen, 1961). Assuming the pile is rigid and the rotation point is known, the maximum capacity was estimated and showed agreement to site tests.

A rigid pile is an appropriate assumption for low L/D piles (such as for modern monopiles, where $L/D \leq 4$) due to the limited pile bending expected when laterally loaded (Poulos, 1971). However, the bending stiffness and flexural rigidity of a pile has a marked effect on the pile-soil interaction (Ashford & Juirnarongrit, 2003; Poulos & Davis, 1980). This suggests that defining comprehensive analytical expressions for the lateral capacity of a pile becomes difficult when the geometry of a pile is neither very stocky nor exceedingly slender. Additionally, the lateral response prior to reaching capacity is an equally important parameter for monopiles supporting OWTs, as the maximum load is seldom reached during operation (Arany et al., 2015).

2.1.2 The p-y method

It is beneficial if the monopile modelling procedure is as simplified as possible to enable fast updates to the design process, offer quick tendering at the early design phase, and reduce computational spend (Arany et al., 2017; Kallehave et al., 2015). It is this reason why the most popular method for the analysis of laterally loaded piles in the offshore industry is the p-y method, which was adopted in modern design codes such as API (2014) and DNV (2021). The soil-structure interaction is idealised to one horizontal dimension, utilising elastic beam elements to model the pile and nonlinear springs as soil elements to encapsulate discrete layers in the stratum. The springs are characterised by modelling the lateral soil pressure, p, as a nonlinear function of the lateral displacement of the local pile section, y. The springs are positioned along the embedment of the pile to characterise the appropriate layer. This is similar to the methodology proposed by Hansen (1961) for computing the lateral bearing capacity, however the flexibility of the pile and lateral response is now considered due to the elastic beam elements. Figure 2.2 demonstrates a typical beam-spring configuration with a point load and moment applied at the pile head. Note that each p-y spring has a unique function.

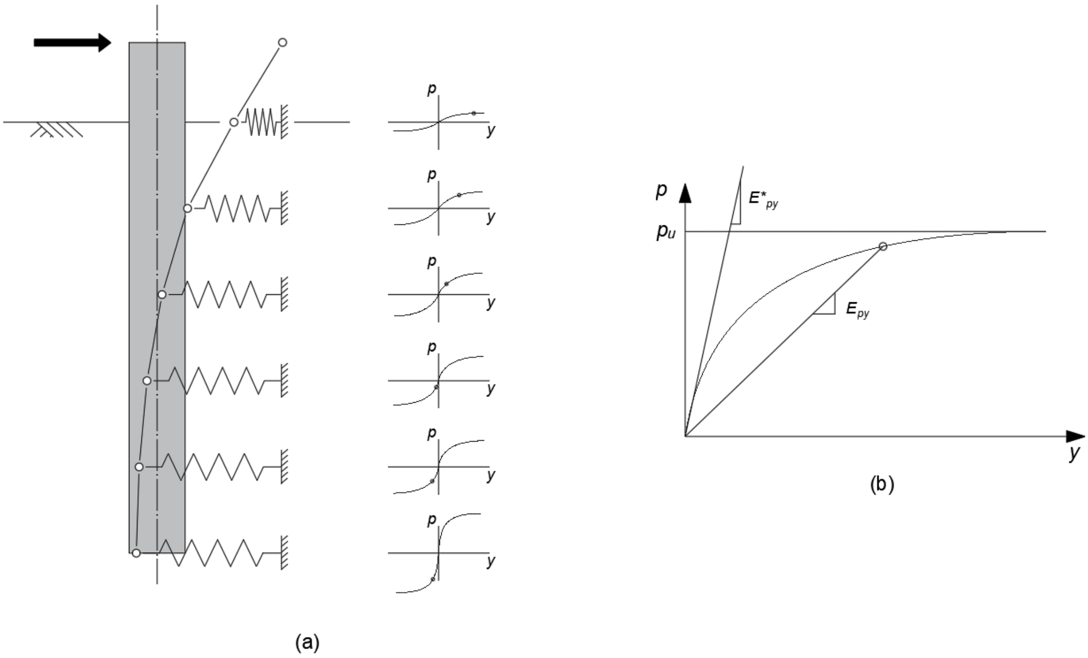

Figure 2.2: (a) p-y model under horizontal load at the pile head and (b) a typical p-y function and important parameters

This method is based on the Winkler approach, which states that the pressure exerted by the soil on a loaded beam at a given point is proportional to the deflection of the beam and is independent of the response of adjacent springs (Winkler, 1867). Hence, the pile-soil interaction is represented by beams supported by non-linear springs of bespoke material property values to encapsulate the soil layer, and adjacent springs are assumed uncoupled. The governing Winkler equation for a laterally loaded pile (using Euler-Bernoulli beam theory (Gupta & Basu, 2018)) is shown in Equation 2.2.

$$E_pI_p\left(\frac{d^4y}{dz^4}\right) + E_{py}(y)\cdot y = 0 \tag{2.2}$$

where E_pI_p is the bending stiffness of the pile (E_p is Young's modulus of pile and I_p is second moment of area of pile) and $E_{py}(y)$ is the stiffness of the spring as a function of y. For discrete systems, the continuous equation described in Equation 2.2 can be discretised using the Direct Stiffness Method. More details can be found in Appendix A. The modulus of subgrade reaction is calculated as $E_{py} = p/y$, and is illustrated in Figure 2.2b. The initial modulus of subgrade reaction $E_{py,0}$ is therefore the derivative of the soil reaction p evaluated at $y = 0$ (i.e $E_{py,0} = p'(0)$), but is not limited to this definition (Biot, 1937; Kallehave et al., 2012; Vesic, 1961). Table 2.1 summarises the parameters associated with subgrade reaction theory.

Table 2.1: Summary of subgrade reaction theory parameters

Description	**Symbol**	**Definition**	**Dim.**
Pile lateral deflection	y	–	L
Soil resistance per unit length	p	$p = f(y)$	F/L
Soil pressure	P	$P = p/D$	F/L^2
Modulus of subgrade reaction	E_{py}	$E_{py} = p/y$	F/L^2
Initial mod. of subgrade reaction	$E_{py,0}$	$E_{py,0} = f'(0)$	F/L^2
Coefficient of subgrade reaction	k_{sr}	$k_{sr} = P/y$, $k_{sr} = E_{py}/D$	F/L^3
Number of spring elements	N_s	–	–
Spring spacing	ΔL	$\Delta L = L/N_s + 1$	L
Spring force	F	$F = p\Delta L$	F
Soil spring stiffness	k	$k = F/y$, $k = E_{py}\Delta L$	F/L
Initial soil spring stiffness	k_0	$k_0 = E_{py,0}\Delta L$	F/L
Tangent spring stiffness	k_T	$k_T = f'(y)\Delta L$	F/L

Note the distinction between the dimensions of the modulus of subgrade reaction and the coefficient of subgrade reaction (E_{py} and k_{sr}, respectively). The former is a pressure, whereas the latter is the modulus divided by the pile diameter. E_{py} may also be considered as the secant stiffness of the p-y spring element (as shown in Figure 2.2).

p-y functions are derived from empirical or semi-empirical methods (Cox et al., 1974; Jeanjean et al., 2011; Li et al., 2014; Murchinson & O'Neill, 1986; Reese et al., 1974; Suryasentana & Lehane, 2016), and encapsulate both the lateral bearing capacity and initial lateral stiffness of the discrete layer as a function of depth, as shown in Figure 2.2b. As noted in Section 2.1.1, the failure mechanism of the pile-soil interaction varies along the depth, which must be included in models for pile ULS design. This imposes an important challenge for pile models of the Winkler-type, as the depth at which the failure mode transitions from a shallow wedge-type mechanism to a deep flow-around mechanism will influence the maximum value of the p-y function. Nevertheless, the shortcomings of the previous holistic lateral capacity modelling approaches such as those proposed by Broms (1964b), Hansen (1961), and Randolph (1981) are addressed with the p-y model, as non-homogenous soil strata and various L/D ratios can be considered within this model.

The following sections will provide a description of common *p-y* functions as well as modifications to facilitate certain soil-structure configurations.

API Sand

The *p-y* function proposed by Reese et al. (1974) for sands is defined by the hyperbolic tangent relationship described in Equation 2.3, and is illustrated in Figure 2.3.

$$p = Ap_u \tanh\left(\frac{k_{sr}z}{Ap_u}y\right) \tag{2.3}$$

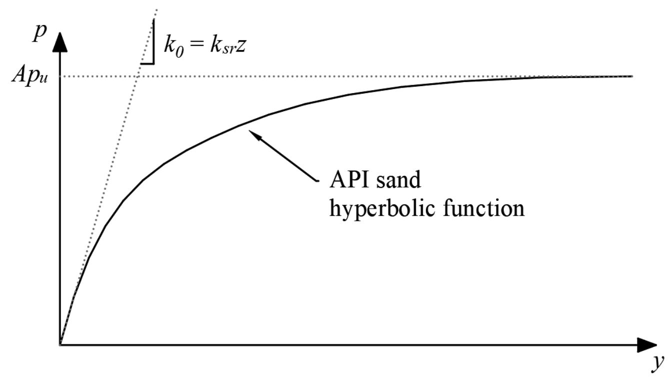

Figure 2.3: Hyperbolic *p-y* function for API sand

where A is an empirical correction factor and is described as $A = (3 - 0.8z/D) \geq 0.9$ (Reese et al., 1975). k_{sr} is the depth-independent coefficient of subgrade reaction (determined from Figure 2.4b or linear interpolation using Table 2.3), and z is the depth of soil elements in the sand layer. For cyclic loading conditions, a constant value of $A = 0.9$ (independent of depth) is recommended by API (2014).

p_u is the ultimate lateral resistance of the sand element and is described using the following expressions:

$$p_u = \min \begin{cases} (C_1 z + C_2 D)\sigma'_v & \text{Shallow failure, } p_{us} \\ C_3 D \sigma'_v & \text{Deep failure, } p_{ud} \end{cases} \tag{2.4}$$

where C_1, C_2 and C_3 are dimensionless constants which are functions of the angle of internal friction ϕ' of the sand, and can be derived using the equations in Table 2.2. σ'_v is the vertical effective stress in the sand and is taken as $\sigma'_v = \gamma' z$ for offshore conditions where the water table is above the ground line. σ'_v should be adjusted for soil profiles where the water table is below the ground line. C_1, C_2 and C_3 are plotted in Figure 2.4a.

Table 2.2: Summary of API sand parameters

Parameter	Equation
C_1	$K_0 \dfrac{\tan^2\beta\tan\alpha}{\tan(\beta-\phi')}\left(\dfrac{\tan\phi'\sin\beta}{\cos\alpha\tan(\beta-\phi')}+\tan\beta(\tan\phi'\sin\beta-\tan\beta)\right)$
C_2	$\dfrac{\tan\beta}{\tan(\beta-\phi')}-K_a$
C_3	$K_a(\tan^8\beta-1)+K_0\tan\phi'(\tan\beta)^4$
α	$\phi'/2$
β	$45+\phi'/2$
K_a	$K_a = 1-\sin(\phi')/1+\sin(\phi')$
K_0	0.4

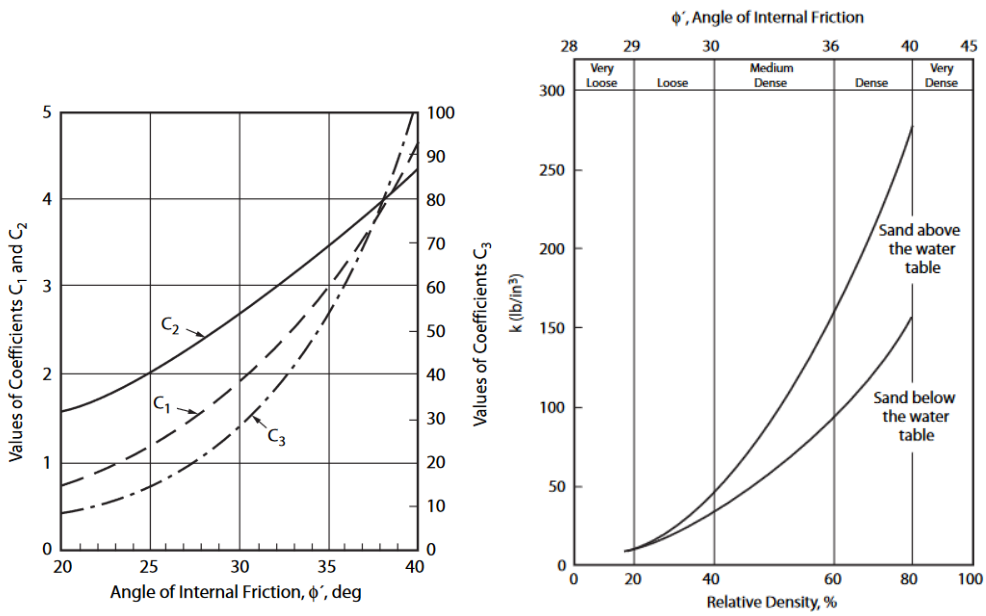

(a) C Coefficients for API sand (b) Coefficient of subgrade reaction, k_{sr}

Figure 2.4: API sand coefficient values (from API (2014))

Table 2.3: Tabulated values of k_{sr} for a given ϕ' below the water table, adapted from Figure 2.4b

Friction angle, ϕ'	k_{sr}	
	MN/m^3	lb/in^3
25°	5.4	20
30°	11	40
35°	22	80
40°	45	165

The tangent stiffness k_T of the API sand p-y function can be used to compute the initial stiffness k_0 of the spring using the first derivative of Equation 2.3 evaluated at $y = 0$.

$$k_T = \frac{d}{dy}\left[Ap_u \tanh\left(\frac{k_{sr}z}{Ap_u}y\right)\right] = k_{sr}z\,\mathrm{sech}^2\left(\frac{k_{sr}z}{Ap_u}y\right) \tag{2.5}$$

Therefore, the initial stiffness of the p-y function defined by the API sand model is:

$$k_0 = k_T|_{y=0} = k_{sr}z \tag{2.6}$$

Note that k_0 is independent of A, meaning the initial stiffness is independent of cyclic degradation effects. Cyclic degradation has a marked influence on small-strain stiffness (Carswell et al., 2016; Kaynia & Andersen, 2015), and this is not captured by the API sand model. This is covered in more detail in Section 2.2.

Equation 2.6 shows that the linear spring stiffness for sands can be determined using Figure 2.4b (or linearly interpolated from Table 2.3) for a given depth z. However, Kallehave et al. (2012) suggested improvements to the initial stiffness of the API sand model for piles of larger diameters (such as monopiles). This is important for calculating the natural frequency of OWTs, and is discussed in more detail in Section 2.3. Sørensen (2012) replaced k_{sr} with a parameter that is dependent on the spring depth, the soil's oedometric stiffness and pile diameter, which demonstrated a better performance for larger diameter piles.

API Clay

The API clay p-y function is a function of the ultimate lateral resistance p_u and the lateral pile displacement at one-half the ultimate lateral resistance y_c, calculated as $y_c = 2.5\epsilon_c D$ (Matlock, 1970). In the absence of experimental stress-strain curves, a representative value for ϵ_c can be adopted in terms of c_u using Table 2.4 (Sullivan et al., 1980).

Table 2.4: Representative values for ϵ_c for corresponding c_u (Sullivan et al., 1980)

Undrained strength, c_u	ϵ_c
0-25kPa	0.02
25-50kPa	0.01
50-100kPa	0.007
100-200kPa	0.005
200-400kPa	0.004

For soft clays with constant unit weight and shear strength in the upper zone of the pile, a transition depth (z_r) must be defined to describe the depth at which the ultimate capacities of the spring shift from a passive wedge-type failure mechanism at shallow depths to a flow-around failure mechanism at greater depths. The transition depth for the API clay model is defined in Equation 2.7.

$$z_r = \frac{6c_u D}{\gamma' D + J c_u} \tag{2.7}$$

where γ' is the effective unit weight of the clay and J is an experimentally derived dimensionless constant (Matlock, 1970). The shallow ultimate capacity p_{us} is defined as the ultimate capacity of the clay spring element for $z \leq z_r$, and the deep ultimate capacity p_{ud} is defined as the ultimate capacity of the clay spring element for $z > z_r$. Equation 2.8 and 2.9 define the ultimate capacity depending on the depth of the p-y spring.

$$p_{us} = \left(3 + \frac{\gamma_1'}{c_u} z + \frac{Jz}{D}\right) c_u D \tag{2.8}$$

$$p_{ud} = 9c_u D \tag{2.9}$$

Note that Equation 2.7 is obtained by equating Equation 2.8 and 2.9 and setting $z = z_r$. The corresponding p-y function for static loading conditions (monotonically increasing loads) is described in Equation 2.10, which is a piecewise relationship and illustrated as the solid line in Figure 2.5.

$$\frac{p}{p_u} = \begin{cases} 0.5\left(\dfrac{y}{y_c}\right)^{1/3} & \text{for } y \leq 8y_c \\ 1 & \text{for } y > 8y_c \end{cases} \tag{2.10}$$

For cyclic loading conditions, the p-y function is described using Equations 2.11 and 2.12 for shallow and deep failure modes, respectively. Figure 2.5 illustrates the various configurations of the cyclic p-y function as dashed lines. Note that Equations 2.11 and 2.12 are independent of the number of cycles N, which is known to have a marked effect on capacity (Hettler, 1981; Long & Vanneste, 1994; Pestana et al., 2000). Cyclic p-y functions are discussed in more detail in Section 2.2.

$$\frac{p}{p_{us}} = \begin{cases} 0.5\left(\dfrac{y}{y_c}\right)^{1/3} & \text{for } y \leq 3y_c \\ 0.72 & \text{for } y > 3y_c \end{cases} \tag{2.11}$$

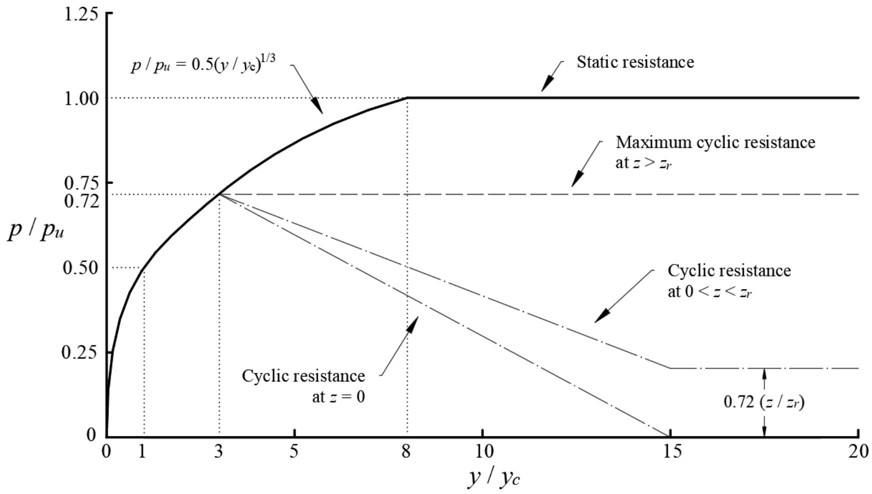

Figure 2.5: *p*-*y* function for API clay (modified from API (1993))

$$\frac{p}{p_{ud}} = \begin{cases} 0.5\left(\dfrac{y}{y_c}\right)^{1/3} & \text{for } y/y_c \leq 3 \\ 0.72\left(1-(1-\dfrac{z}{z_r})\left(\dfrac{y/y_c-3}{12}\right)\right) & \text{for } 3 < y/y_c \leq 15 \\ 0.72\left(\dfrac{z}{z_r}\right) & \text{for } y/y_c > 15 \end{cases} \tag{2.12}$$

To prevent an infinite initial stiffness with the current API clay *p*-*y* definition (i.e. $E_{py,0} = \infty$), the initial stiffness of the clay spring elements can be defined as $E_{py,0} = 0.5p_u/y_c$ (Taciroglu et al., 2006) and p_u is the appropriate ultimate soil resistance value defined by either Equation 2.8 and 2.9.

CPT-based functions

The Cone Penetration Test (CPT) is a method of geotechnical investigation that is used to determine the soil strength profile and soil properties. The CPT involves pushing a cone-tipped rod into the ground at a constant rate of penetration, and measuring the resistance of the soil. The resistance to penetration is measured by the tip resistance q_c and the sleeve friction f_s, and is widely used due to its simplicity, low cost, and non-destructive investigation process. The fast and reliable nature of the CPT has led to the development of many empirical correlations between CPT results and soil properties (Ariannia, 2017; Baldi et al., 1989; Jardine et al., 2005; Lunne & Christoffersen, 1983; Robertson & Cabal, 2014), which makes it an ideal tool for offshore foundation design.

CPTs are characterised by configurations that closely resemble those of piles, which has opened up many research opportunities to develop both lateral and axial CPT-based design methodologies for monopiles and piles in general (Byrne et al., 2018; Lehane et al., 2020b; Lehane et al., 2005; Lunne et al., 1997; Wang et al., 2022b). In particular, correlations from q_c to p-y relationships can be empirically derived from either three-dimensional Finite Element Analyses (FEA) or site experiments. Table 2.5 summarises some of the CPT-based p-y functions for sands derived in previous studies. It should be noted that CPT-based p-y functions are not limited to cohesionless soils (Kim et al., 2016).

Table 2.5: Various CPT-based p-y functions derived in previous studies

Reference	p-y Equation	
Novello (1999)	$2D(\sigma'_v)^{0.33}(q_c)^{0.67}\left(\frac{y}{D}\right)^{0.5}$	(2.13)
Dyson and Randolph (2001)	$1.35\gamma D^2\left(\frac{q_c}{\sigma'_v}\right)^{0.72}\left(\frac{y}{D}\right)^{0.58}$	(2.14)
Li et al. (2014)	$3.6D(\gamma' D)\left(\frac{q_c}{\gamma' D}\right)^{0.72}\left(\frac{y}{D}\right)^{0.66}$	(2.15)
Suryasentana and Lehane (2014)	$2.4\gamma z D\left(\frac{q_c}{\gamma z}\right)^{0.67}\left(\frac{z}{D}\right)^{0.75} \times \left(1-\exp\left[-6.2\left(\frac{z}{D}\right)^{-1.2}\left(\frac{y}{D}\right)^{0.89}\right]\right)$	(2.16)

Note that Equations 2.13, 2.14, and 2.15 are p-y functions described by a power law relationship, whereas Equation 2.16 is of the exponential type. Power law relationships are incapable of representing the initial spring stiffness $E_{py,0}$ or ultimate soil resistance p_u analytically, which are important parameters for small-strain dynamic and ultimate capacity analyses, respectively. Suryasentana and Lehane (2016) suggested a piecewise linearisation for small-strain mobilisation in the p-y functions. Equation 2.17 relates the shear modulus of the soil G_0 to the small-strain stiffness of the spring k_0.

$$k_0 = \left(\frac{dp}{dy}\right)_{y=0} = 4G_0(1-\mu_s) \tag{2.17}$$

$$p = \begin{cases} k_0 y & \text{for } y/D \leq 0.0001 \\ f(y) & \text{for } y/D > 0.01 \end{cases} \tag{2.18}$$

where $f(y)$ is a CPT-based *p*-*y* function described in Table 2.5. Note that interpolation is required if $0.0001 < y/D \leq 0.01$. G_0 can be correlated directly from end resistance q_c values using correlations derived by Baldi et al. (1989), and is recommended by the ICP design standards if site data is not available (Jardine et al., 2005). The equation for G_0 is shown in Equation 2.19.

$$G_0 = \frac{q_c}{A + B\eta + C\eta^2} \tag{2.19}$$

where A, B, and C are empirically derived and are 0.0203, 0.00125, and 1.216×10^{-6}, respectively (Baldi et al., 1989; Jardine et al., 2005). η is equal to $q_c/\sqrt{P_a\sigma_v'}$ and P_a is the atmospheric pressure, taken as 100 kPa.

CPT-based *p*-*y* functions can offer fast estimates to soil strength profiles in offshore environments and enable preliminary design approximations for offshore foundations until more detailed site investigations can be carried out. This is ideal for the tendering phase of a project where the foundation design is not yet finalised. Naval units equipped with CPT apparatuses can be quickly deployed to survey a site, and locations between investigation points can be interpolated using geostatistical methods (Liu et al., 2021).

Layering effects

CPT-based *p*-*y* functions are informed directly from strength profiles measured from variations in q_c with depth. It is therefore possible to correlate variations in the soil strength profile to appropriate *p*-*y* spring elements. However, all *p*-*y* functions discussed thus far are derived from homogenous soil states, which may not be applicable for piles in layered soils of different types.

Homogenous *p*-*y* functions assume the same soil type at all depths. However, layers of different soil types will change the overburden pressure expected at certain depths z (Georgiadis, 1983). This can have a marked effect on the lateral capacity p_u of the discrete layers. Georgiadis (1983) proposed a methodology to modify the ultimate capacity of underlying soil layers to account for the change in overburden pressure due to upper soil layers. Figure 2.6 illustrates an example of a single pile embedded in dense sand beneath soft clay, and the p_u values along the depth for each layer derived from the API sand and API clay capacity models.

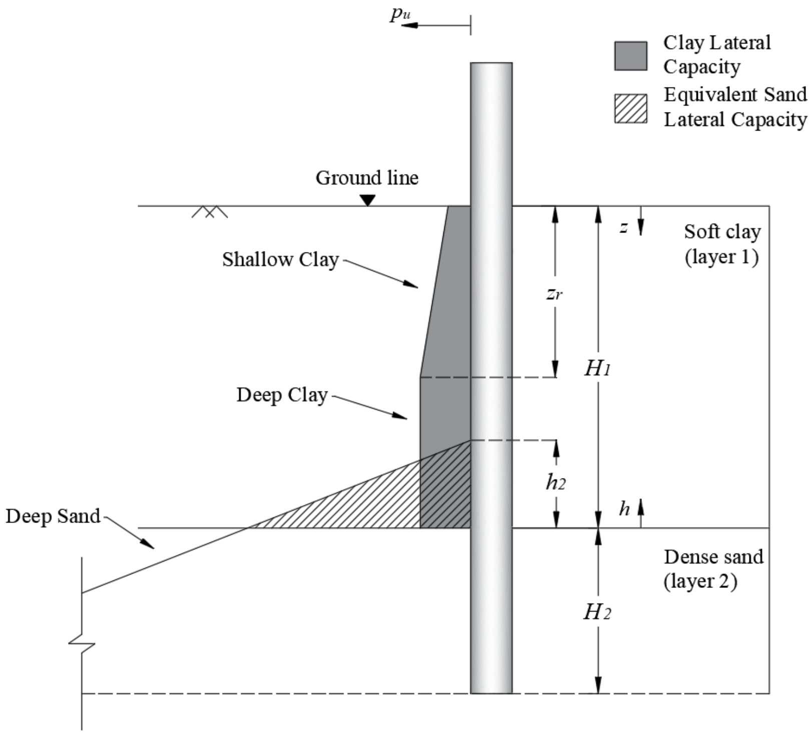

Figure 2.6: Adjusting ultimate lateral capacity of soils in layered strata using the API sand and API clay p-y model (Georgiadis, 1983)

As soft clay is typically lighter than dense sand, it is inappropriate to compute the ultimate capacity of the sand layer using Equation 2.4 from $z = 0$. Otherwise, this would consider a full stratum of sand and therefore a large lateral capacity for the sand elements. Instead, Georgiadis (1983) proposed that an equivalent ground line needs to be determined, which is the depth at which the capacity of the sand layer's lateral force capacity is equal to the lateral force capacity of the clay layer. i.e. $z = H_1 - h_2$ would be more appropriate for determining the p-y functions of sand, as illustrated in Figure 2.6. Graphically, this is the same as calculating when h_2 provides an equal hatched area in Figure 2.6.

This methodology is implemented in detail and reviewed in Chapter 5, and includes the calculations necessary for this pile-soil configuration (Tott-Buswell et al., 2022).

Pile groups

So far, only single piles have been discussed. In pile groups, the performance of neighbouring piles is influenced by the presence of piles, as the behaviour of soil surrounding one pile is impacted by the mobilised soil in the vicinity of another pile. As a consequence, pile groups under lateral loads will generally exhibit less lateral capacity than the sum of the lateral capacities of the individual piles, therefore p-y functions are not directly applicable. This is due to the so-called 'shadowing' effect, referring to the interference of the failure planes of the piles in trailing rows with the failure planes of the piles in front of them. This effect is illustrated in Figure 2.7. For this reason, the piles in the trailing rows exhibit less lateral resistance (Rollins et al., 2005). The group efficiency of laterally loaded pile groups increases with the ratio of pile spacing s over pile diameter D. Rollins et al. (2005) recommends that pile group effects under lateral loading may be considered negligible for a pile spacing of the order of $6D$-$8D$.

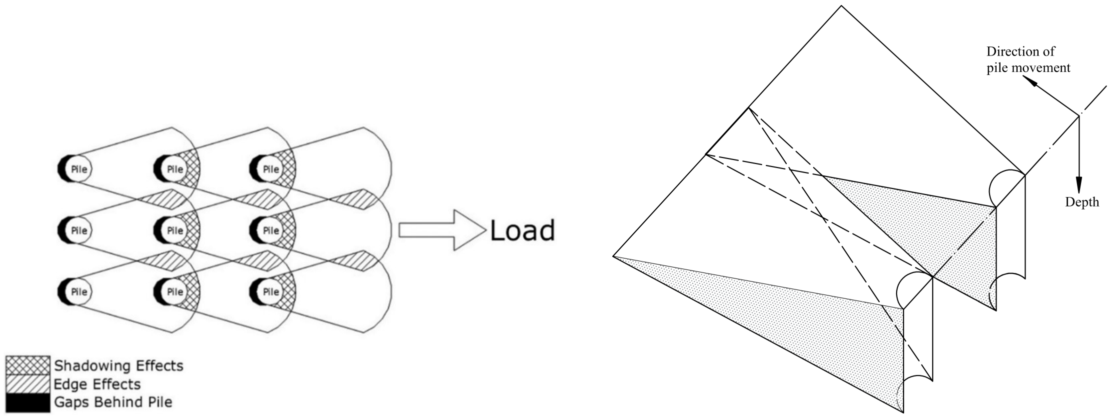

Figure 2.7: The failure mechanisms of pile groups (a) Shadowing effect of pile groups (Rollins et al., 2003), (b) Illustration of wedge failure mechanisms in pile groups (Brown et al., 1988)

For lower values of piles spacing, the shadowing effect is usually treated by employing an efficiency factor, commonly referred to as p-multipliers within the p-y curve concept. This relates the force driving the pile group to the force required to displace a single pile an equal distance (Brown et al., 1988). The p-y curves for the piles in a group are modified using p-multipliers, which reduce both the stiffness and the ultimate lateral capacity of the piles in a group with respect to the single pile case, as shown in Figure 2.8. This enables the use of traditional p-y models to model pile groups, as the p-y relationship is scaled to encapsulate the grouping effects.

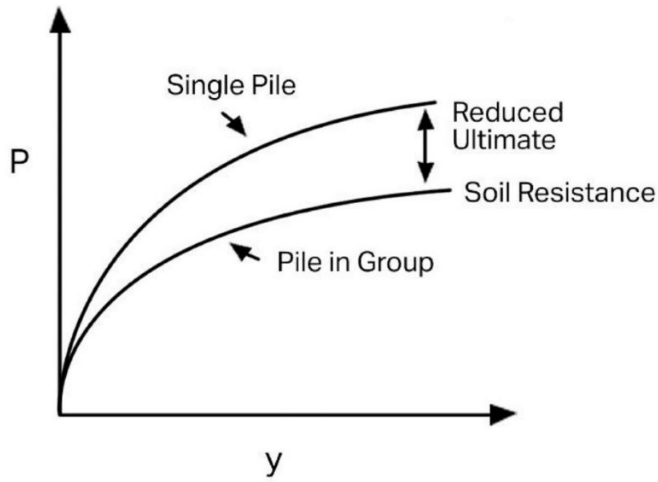

Figure 2.8: Illustration of the capacity reduction in p-y curves for group effects

Table 2.6 provides a summary of pile group p-multipliers proposed by various researchers based on physical models and field tests in clays and sands for pile groups subjected to monotonic and cyclic lateral loads at the pile head.

Table 2.6: Group interaction factors under lateral loads from previous studies.

Reference	**Soil type**	**Pile spacing**	**Group efficiency factor**	***p*-multipliers**			
				R1	**R2**	**R3**	**R4**
Brown et al. (1987)	Clay	$3D$	0.68-0.80	0.70	0.60	0.50	-
Rollins et al. (1998)	Clay	$2.83D$	0.59-0.80	0.60	0.38	0.43	-
Snyder (2004)	Clay	$3.92D$	0.85-0.90	1.00	0.81	0.59	0.71
	Clay	$3.3D$	0.45-0.67	0.90	0.61	0.45	0.45
Rollins et al. (2003)	Clay	$4.4D$	0.75-1.00	0.90	0.80	0.69	0.73
	Clay	$5.65D$	0.87-0.90	0.94	0.88	0.77	-
Brown et al. (1988)	Sand	$3D$	0.63-0.70	0.80	0.40	0.30	-
Ruesta et al. (1997)	Sand	$3D$	0.60-0.91	0.80	0.70	0.30	0.30
Rollins et al. (2005)	Sand	$3.3D$	0.72-0.94	0.80	0.40	0.40	-

R1: Leading row, **R2:** Second row, **R3:** Third row, **R4:** Fourth row

Table 2.6 shows that p-multipliers for the leading-row piles are significantly higher than those for the trailing-row piles. It is important to ensure that the head fixity condition of a single pile and pile groups is similar before implementing any efficiency factors, as the pattern of flexural deformation will be fundamentally different between the two. Literature related to p-multipliers under time-varying dynamic loading conditions is limited (Mostafa & Naggar, 2002), but is extensively used in modified Winkler-type p-y models (Fayyazi et al., 2014; Reese & Van Impe, 2010).

2.1.3 Modulus of subgrade reaction

The elastic beam elements in the *p*-*y* model encapsulate the flexural rigidity for a range of L/D ratios if an appropriate beam theory is applied (Gupta & Basu, 2018). However, as *p*-*y* functions are empirically or semi-empirically derived, their application is bound to the geometric calibration space for which they were initially derived (Lehane & Suryasentana, 2014; Li et al., 2014; Murphy et al., 2018). This includes the influence of diameter size on the modulus of subgrade reaction ($E_{py} = p/y$). Terzaghi (1955) used the idea of a stress bulb to demonstrate the influence of the pile diameter on subgrade reaction, and evaluated a large diameter stress influence compared to a smaller diameter. A larger pile diameter experiences greater displacement with the same pressure applied, generating a lower E_{py} value. Terzaghi (1955) concluded that the *coefficient* of subgrade reaction ($k_{sr} = E_{py}/D$) is inversely proportional to the diameter of the pile. In other words $E_{py}/D \propto 1/D$, therefore the *modulus* of subgrade reaction (E_{py}) is independent of diameter. The reader is referred to Table 2.1 for parameter definitions.

Vesic (1961) proposed an equation for the initial modulus of subgrade reaction, $E_{py,0}$, which can be used to define elastic Winkler models, and is defined in Equation 2.20.

$$E_{py,0} = \frac{0.65E_s}{1-\mu_s^2}\left[\frac{E_s D^4}{E_p I_p}\right]^{1/12} \tag{2.20}$$

where E_s is the elastic modulus of the soil and μ_s is the Poisson ratio of the soil. Considering that the second moment of area of a pile's annulus is $I_p = \frac{\pi}{64}(D_{out}^4 - D_{in}^4)$ (where D_{out} and D_{in} are the outer and inner diameters of the pile, respectively), it can be shown that Equation 2.20 implicitly demonstrates that E_{py} is independent of the diameter, as the D^4 terms cancel. This is further supported by full-scale pile tests on sand and clay in Reese et al. (1974) and Reese et al. (1975), respectively. Additionally, Ashford and Juirnarongrit (2003) performed 3D finite element analyses comparing two models; one with independent E_{py} and diameter, and the other with E_{py} linearly dependent on diameter. The independent model was found to be more accurate.

Other properties of the *p*-*y* relationship, such as the ultimate soil resistance p_u, has been noted to depend on the geometry of the pile (Fan & Long, 2005). To add, a large diameter relative to embedment depth can introduce additional soil resistance mechanisms outside of the modelling capability of lateral springs (see Section 2.1.4). Considering the anticipated rigidity of low L/D ratios of prospective monopile geometries used to support the size of modern OWTs, the efficacy of the traditional p-y model therefore comes into question.

2.1.4 Diameter effects

As the diameter of a pile becomes large relative to its embedment, the overall deflection mode shifts from a slender, bending type, to a rigid, rotating type. This is illustrated in Figure 2.9. The increased rigidity of the pile introduces additional resistance mechanisms that are outside of the modelling capabilities of the lateral spring (Byrne et al., 2015). Vertical interface frictional resistances will become increasingly more present due to the rotation as the diameter increases (Fu et al., 2020; Lam, 2013), and the influence of the large area of the pile tip can no longer be ignored (Van Impe & Wang, 2020; Zhang & Andersen, 2019).

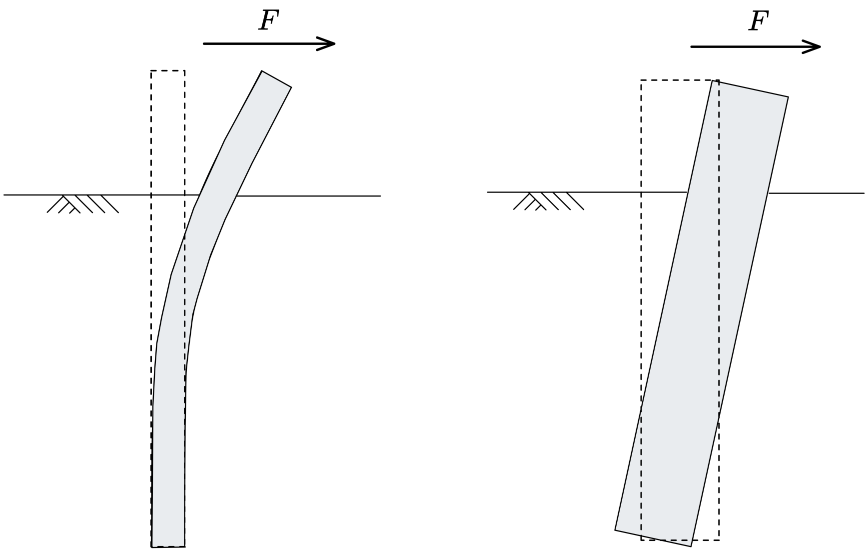

(a) Slender pile bending (b) Rigid pile rotation

Figure 2.9: Deflection modes of slender and rigid piles

When slender piles are laterally loaded, rotation attenuates along its depth and leads to minimal mobilisation near the tip of the pile. However, rigid piles transfer more of the applied horizontal load to the base (Van Impe & Wang, 2020; Zhang & Andersen, 2019). This is not encapsulated in traditional p-y functions due to their derived geometrical calibration space (Doherty & Gavin, 2011; O'Neill & Murchison, 1983; Reese et al., 1974). Furthermore, plugging effects, where soil enters the annulus of the pile during the installation process, will also become more prevalent in lateral and axial resistance as the diameter increases (Amar Bouzid, 2018; Byrne et al., 2018; Lehane et al., 2020a; Prendergast et al., 2020). This is particularly relevant for laterally loaded rigid monopiles, as the annular cross-section can lead to direct shearing resistance across the base of the pile (Byrne et al., 2020b; McAdam et al., 2020; Murphy et al., 2018; Zhang & Andersen, 2019). The large diameter at the tip also introduces a restoring moment due to the mobilised bearing stresses when rotated (Byrne et al., 2017; Van Impe & Wang, 2020). In all, the total contribution towards lateral capacity from these additional resistance mechanisms is as much as 20% for piles of $L/D = 3$ (Murphy et al., 2018).

The additional resistance mechanisms deriving from low L/D ratio monopiles can be encapsulated by appropriately calibrated p-y functions that are bespoke to particular pile-soil configurations modelled in three-dimensional FEA. However, the application of the traditional p-y model, comprising of lateral springs only, to piles with stocky configurations is questionable. Adding new spring types to the Winkler model may be more appropriate if their reaction curves can appropriately isolate the soil-structure interaction (Lam, 2013; Zhang & Andersen, 2019).

2.1.5 PISA design method

A joint industry project was initiated in 2015 to develop a new design method for OWT monopiles, accounting for the shortcomings of the traditional p-y method originally developed for slender piles in the oil and gas industry (API, 2014; DNV, 2021). The Pile Soil Analysis (PISA) project was a collaboration between 13 industry partners and 5 research institutes, including the University of Oxford, Imperial College London, and University College Dublin. The PISA model is illustrated in Figure 2.10, including a diagram of the expected additional resistances for laterally loaded low L/D monopiles.

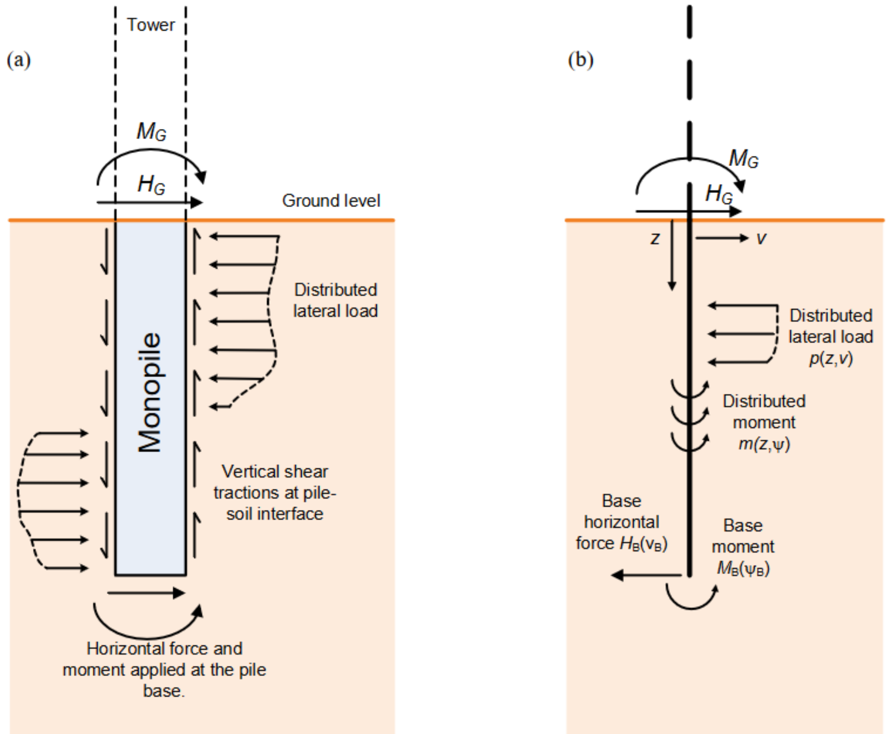

Figure 2.10: Illustration of the PISA model (a) additional resistance mechanisms expected in monopiles and (b) PISA's modified *p*-*y* model (Figure from Burd et al. (2017))

The PISA model is an extension to the traditional *p*-*y* model, using both lateral and rotational springs to represent the stiffness of the soil and resistance mechanisms, as described in Section 2.1.4. The spring reaction functions are informed using a conic function described in Equation 2.21, which is normalised for generality and illustrated in Figure 2.11. The normalised parameters are calibrated using three-dimensional FEA results for a particular pile-soil configuration and slenderness ratio (Taborda et al., 2020; Zdravković et al., 2020b).

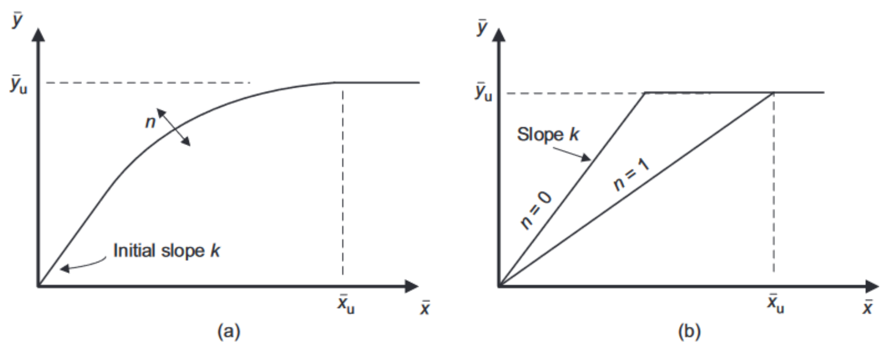

Figure 2.11: Illustration of the conic function used to describe the spring reaction curves in the PISA model: (a) conic form; (b) bilinear form (Figure from Burd et al. (2020b))

$$\bar{y} = \begin{cases} \bar{y}_u \dfrac{2c}{-b + \sqrt{b^2 - 4ac}} & \text{for } \bar{x} \leq \bar{x}_u \\ \bar{y}_u & \text{for } \bar{x} > \bar{x}_u \end{cases} \tag{2.21}$$

where

$$\begin{aligned} a =& 1 - 2n \\ b =& 2n \frac{\bar{x}}{\bar{x}_u} k - (1 - n) \left(1 + \frac{\bar{x}}{\bar{y}_u} k \right) \\ c =& (1 - n) \frac{\bar{x}}{\bar{y}_u} k - n \frac{\bar{x}^2}{\bar{x}_u^2} \end{aligned}$$

k is the initial slope of the function, n determines the bilinearity of the curve and varies between 0 and 1 ($n = 0$ for bilinear, $n = 1$ for conic), $\bar{x}_u$ is the normalised displacement at the ultimate resistance, and $\bar{y}_u$ is the normalised ultimate resistance (Burd et al., 2020b).

Lateral monopile push-over tests were performed at two different sites, Dunkirk and Cowden, each having geological properties similar to sand and clay in offshore conditions, respectively (Byrne et al., 2020b; McAdam et al., 2020; Zdravković et al., 2020a). Each site investigation included 12 laterally loaded monopile push-over tests of various geometries and scales. These site tests directly informed three-dimensional finite element models, which in turn were used to calibrate the parameters for the conic function described in Equation 2.21 (Taborda et al., 2020; Zdravković et al., 2020b). Burd et al. (2020b) and Byrne et al. (2020b) described the calibration process in detail for monopiles in sand and clay, respectively; including preliminary design tables for reaction curve parameters within a certain calibration space.

The PISA model therefore has two design methodologies; (i) using look-up tables for the reaction curves, and (ii) using the reaction curves calibrated directly from bespoke three-dimensional finite element models. The former is more general and can be used for piles within specific geometrical limits ($2 \leq L/D \leq 6$, $5 \leq h/D \leq 15$, $40\% \leq D_r \leq 90\%$), whereas the latter is more bespoke to the particular pile-soil configuration and requires extensive geotechnical investigation and three-dimensional finite element modelling to extract the necessary reaction curves for the modified *p*-*y* model. Whilst effective, this undermines the simplicity of the traditional *p*-*y* method, as three-dimensional finite element models are still required for optimal design outputs.

2.1.6 Summary

The p-y model is an effective and versatile design methodology for efficiently modelling the lateral response of laterally loaded piles. However, it is limited in its ability to model the additional resistance mechanisms that are present in low L/D monopiles. The simplified representation of the soil-structure interaction enables a computationally inexpensive simulation where the lateral deflection and bending moments of the pile can be estimated. Complex pile configurations can also be encapsulated with appropriate modifications, such as pile grouping and layering effects, without compromising computational spend.

The PISA model extends the p-y method by accounting for additional mechanisms due to diameter effects. However, it requires bespoke three-dimensional finite element models to calibrate the reaction curves effectively. This compromises the simplicity of the p-y method, as three-dimensional finite element models are still required for optimal design outputs. In this light, it would be beneficial to inform the additional mechanical analogies in a multi-spring model with more accessible data in offshore environments, such as CPT data. Such a model would serve as a valuable tool for the design of OWTs, at least preliminarily, as low L/D monopiles are common. CPT profiles are often the first indication of the seabed's strength during offshore site investigations. Therefore, appropriate CPT-based formulations for all spring types in a preliminary OWT monopile design tool is desirable. This type of model is investigated in Chapter 3, where a CPT-based multi-spring model is developed and appraised.

The discussion thus far has been limited to monotonic loading. However, it is important to consider the cyclic response of laterally loaded piles, as OWTs will be subjected to millions of load cycles of various frequencies and amplitudes throughout their operational lifetime. The design methodologies against cyclic fatigue and degradation in industrial practice and literature are detailed in the following section.

2.2 Cyclic pile modelling

OWTs supported by monopiles are exposed to many years of cyclic wind and wave loads that can lead to structural failure if not appropriately accounted for in design models. According to DNV (2021), a typical OWT is designed for a fatigue load with up to 10^7 cycles for FLS compliance. It is expected that, due to the cyclic nature of wind and wave loads, the pile-soil interaction degrades overtime, leading to both a reduced lateral capacity and a change in lateral stiffness (Andersen, 2009; Houlsby et al., 2017; Leblanc et al., 2010b; Long & Vanneste, 1994). A continuous reconfiguration of stress states and particle arrangement in the soil adjacent to the pile leads to permanent changes in soil properties. It is therefore important that soil degradation is appropriately accounted for in the modelling processes to fulfil a safe and serviceable operation.

2.2.1 Reduced capacity in *p*-*y* functions

For monopiles in sand, the API design codes recommend that the empirical scaling factor in Equation 2.3 is taken as $A = 0.9$ for all spring depths (API, 2014; Reese et al., 1974). This is based on field tests performed by Cox et al. (1974), and encapsulates the effects due to cyclic loading after 100 cycles. The limited cyclic loading data used to calibrate the p-y model is another significant limitation for its application to OWT monopiles. The original cyclic loading modifications used in the API clay's p-y function are not as straight forward as the sand model (see Figure 2.5), but also shares similar limitations (Reese et al., 1975).

Equation 2.3 shows that, since A affects the argument of the hyperbolic tangent function, A scales both the p and y coordinate. Consequentially, the initial modulus of subgrade reaction $E_{py,0}$ does not scale to reflect cyclic degradation in the initial response of a pile (implicit in Equation 2.5 at $y = 0$). This is an important consideration for small-strain dynamic analysis in OWT monopiles where the initial response is of interest (Carswell et al., 2016; Darvishi-Alamouti et al., 2017; Prendergast et al., 2013) (see Section 2.3.1). Dührkop et al. (2009) modified the API sand model such that A is a function of N and appropriately influences the initial stiffness of the p-y function. The modified p-y model for sand that accounts for cyclic degradation is described in Equation 2.22 (Dührkop et al., 2009).

$$p = \hat{A} p_u \tanh\left(\frac{k_{sr}}{0.9 p_u} y\right) \tag{2.22}$$

where $\hat{A} = r_A(3 - 1.143z/D + 0.343z/D)$. r_A is dependent on the number of cycles and $r_A = 0.3$ is for 100 cycles. $r_A = 1$ gives the original API sand monotonic p-y function described in Equation 2.3. Note that $\hat{A}$ is omitted from the denominator of the hyperbolic tangent argument and is fixed to 0.9, resulting in a p-multiplier effect that reduces the spring stiffness and capacity. Whilst this method demonstrates an improvement to the original API sand p-y function for near-rigid monopiles under cyclic loading conditions, further model tests and numerical investigations are necessary for systems with alternative pile-soil arrangements and cyclic loading configurations, such as one-way or two-way loading (Dührkop et al., 2009). However, it was shown that scaling p or y is an appropriate method to encapsulate the effects of cyclic degradation on pile capacity, if appropriately informed.

2.2.2 Computing accumulated displacement

For monopiles under cyclic loading, the amount of accumulated displacement (or rotation) after N load cycles is the primary design consideration, as it will directly impact the efficiency of the wind turbine (Andersen et al., 2013; Leblanc et al., 2010b; Song & Achmus, 2021). Equation 2.23 describes a general expression for estimating pile head deflection after N number of cycles.

$$y_{h,N} = y_{h,1} \cdot f(N) \tag{2.23}$$

where $y_{h,N}$ is the pile head deflection after N cycles, $y_{h,1}$ is the head deflection after 1 cycle (i.e. monotonic response), and $f(N)$ is a function that describes how the head deflection varies with the number of cycles. The change in displacement derives from a change in the modulus of subgrade reaction, E_{py}. Recall from Table 2.1 that E_{py} can be considered as the secant stiffness of the p-y reaction curves ($E_{py} = p/y$), then the cyclic degradation function $f(N)$ can be directly applied to local p-y functions to encapsulate the global response from the head displacement, effectively serving as p- or y-multipliers.

Little and Briaud (1988) proposed an exponential function $f(N) = N^{\alpha}$, where α is an empirical factor derived from seven experimental pile tests. Tests were performed with 50 one-way load cycles on slender piles ($L/D = 39$), but a generalised interpretation of the results was limiting. Long and Vanneste (1994) compiled many cyclic pile experimental studies, including Hettler (1981), Little and Briaud (1988), O'Neill and Murchison (1983), and Reese et al. (1974), and further generalised Little and Briaud (1988)'s conclusion. Long and Vanneste (1994) built upon the exponential form proposed by Little and Briaud (1988) and showed that α is a function of the cyclic load configuration, soil density and installation method. One-way loading was deemed more onerous for laterally loaded piles, and suggested scaling factors to p-y functions for both p and y. However, many of the tests within this calibration space were below 100 load cycles under sinusoidal loading, therefore extrapolation to many irregular cyclic loads is uncertain. The application to low L/D monopiles is also questionable.

Lin and Liao (1999) proposed an extension to predictive accumulated displacement models for variable cyclic loads. Using a strain superposition approach, the cumulative strains due to the mixing of different amplitude loads can be estimated. This is an extension of Stewart (1986), who explored this concept with triaxial tests on ballast. The approach is illustrated in Figure 2.12, and utilises the accumulation expression described in Equation 2.24.

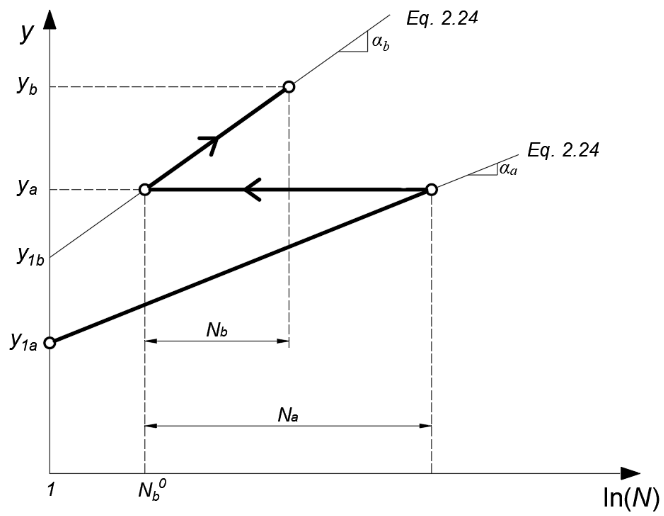

Figure 2.12: Example method for strain superposition of various load packages applied to piles (Lin & Liao, 1999; Stewart, 1986)

$$y_{1,i}f(N) = y_{1,i}(1 + \alpha_i \ln(N_i)) \tag{2.24}$$

where i denotes the load parcel. This is an adaptation to Miner's law (Miner, 1945), where the damage from one load parcel after N_a number of cycles is assumed equivalent to another for N_b cycles.

Leblanc et al. (2010b) contextualised the above studies for OWT monopiles and investigated many number of cycles ($N = 10^4$) using scaled 1g model experiments. It was assumed that the pile was rigid and defined the loading configuration with two parameters, ζ_b and ζ_c. ζ_b can be interpreted as a metric that determines how close the peak cyclic load is towards the maximum capacity of the pile, and follows that $0 \leq \zeta_b \leq 1$. ζ_c defines the characteristics of the cyclic loading, where one-way loading is $\zeta_c = 0$, two-way loading is $\zeta_c = -1$, and monotonic loading is $\zeta_c = 1$.

The two parameters are defined in Equation 2.25 and Illustrated in Figure 2.13.

$$\zeta_b = \frac{M_{\text{max}}}{M_{\text{R}}} \qquad \zeta_c = \frac{M_{\text{max}}}{M_{\text{min}}} \tag{2.25}$$

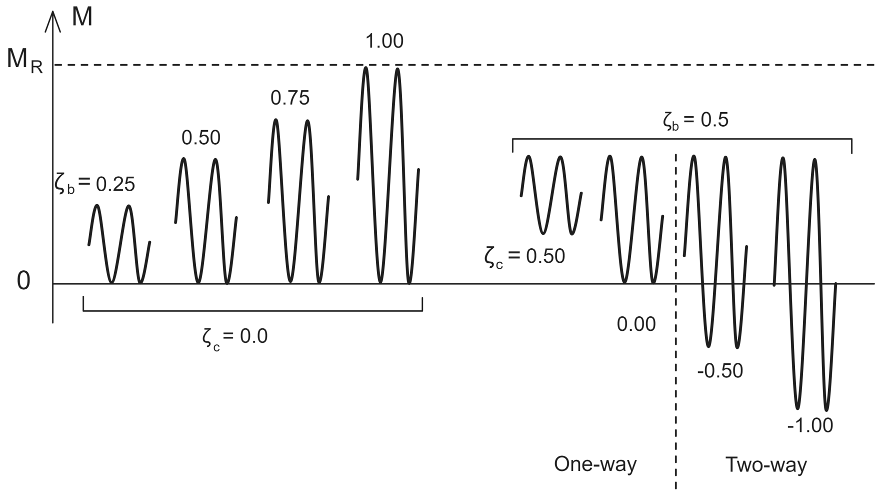

Figure 2.13: Illustration of cyclic loading configurations (Leblanc et al., 2010b)

Using the same logarithmic model as Lin and Liao (1999), Leblanc et al. (2010b) found that the most onerous cyclic loading configuration for rigid OWTs exist when $\zeta_c = -0.5$, as accumulated displacements were four times greater than that of one-way loading ($\zeta_c = 0$). This has profound implications on OWT design, and contradicts previous research outputs (such as Little and Briaud (1988) and Long and Vanneste (1994)). However, it is unclear if this is a consequence of the pile's low L/D ratio. It could be postulated that soil near the tip is more likely to be cyclically mobilised due to less attenuated rotation along embedment in low L/D monopiles due to low flexural rigidity, hence more soil-structure degradation along the pile (Lesny et al., 2007). The various pile tests show that the stiffness also significantly increased after 10^4 load cycles for all cases, and was estimated to reach a 60% increase after 10^7 cycles (expected number of cycles during operational lifetime of OWT) (Leblanc et al., 2010b). This may be an overestimation due to scaling effects inherent in the small-scale 1g modelling approach (Chang & Whitman, 1988).

Lesny and Hinz (2007) underlines the importance of integrating cyclic sample tests with cyclic monopile design, as the complex behaviour of bespoke site samples should be reflected in competent three dimensional FEA models. Ronold (1993) proposed the use of Cyclic Contour Diagrams (CCD) to encapsulate the response of numerous sample tests, either Direct Simple Shear (DSS) or Triaxial (TX), of various cyclic stress configurations, which was later generalised by Andersen et al.

(2013). Figure 2.14a illustrates the cyclic and average stress/strain notation for sample tests, and Figure 2.14b demonstrates how sample test data is represented in three-dimensional space using the CCDs.

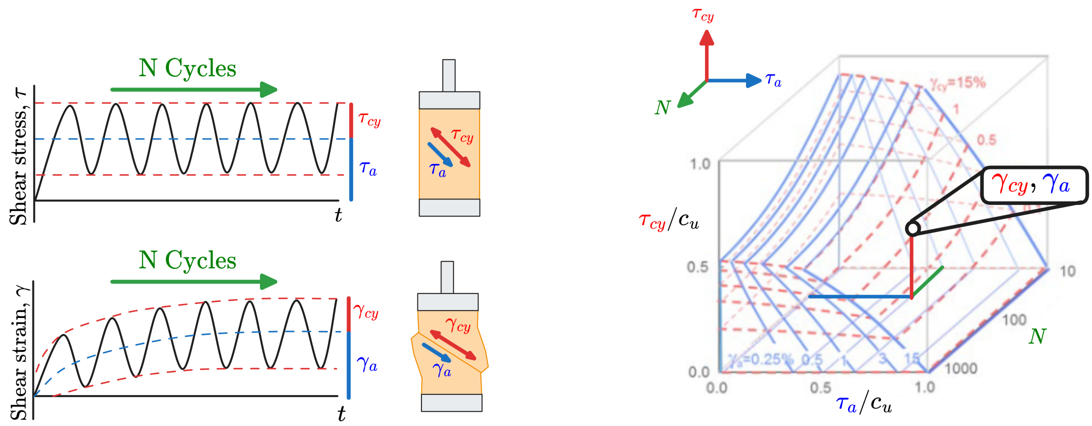

(a) Applied stresses and recorded strains of a TX test

(b) Typical CCD for Drammen clay (Andersen, 2015)

Figure 2.14: Typical cyclic triaxial test and stress/strain response

Figure 2.14b demonstrates that the three-dimensional coordinates indicate the loading configuration described in Figure 2.14a (typically normalised by c_u or σ'_v for clay or sands, respectively). After N cycles for a given τ_a and τ_{cy} test configuration, the associated strains γ_a and γ_{cy} are encapsulated as scalar values at the respective coordinate point. Many cyclic tests therefore begin to form a three-dimensional scalar field for interpolating average and cyclic strains for any test configuration. Furthermore, two-dimensional planes can be extracted from the three-dimensional CCD to produce convenient design charts, as shown in Figure 2.15.

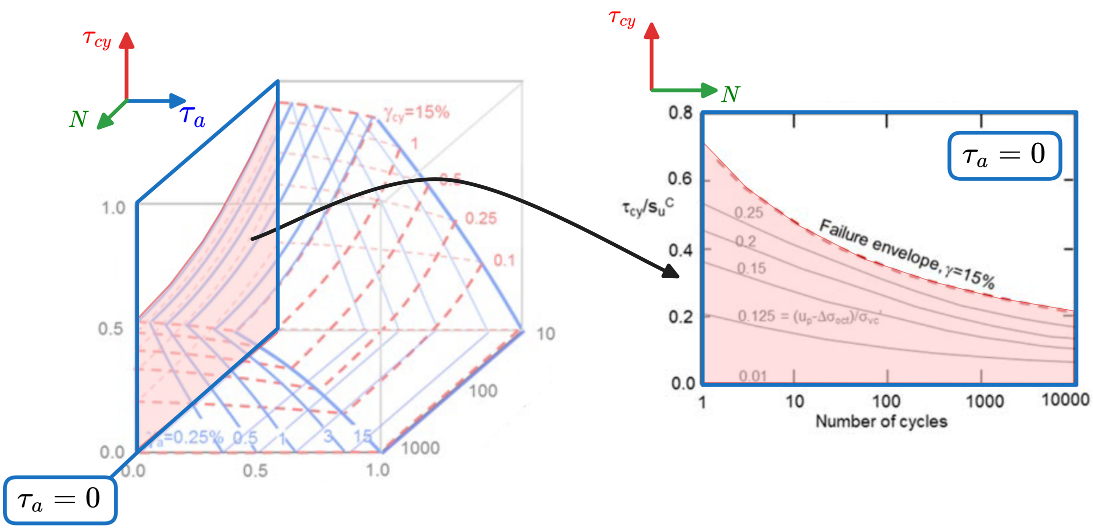

Figure 2.15: Example CCD plane extract for $\tau_a = 0$ and the associated contour plot (Andersen, 2015)

Originally developed for offshore gravity based systems, this method can estimate the soil response to highly irregular load histories expected in the offshore environment (Andersen et al., 2013). Cycle counting methods, such as the rain flow counting algorithm (Anthes, 1997; Downing & Socie, 1982), can process load signals of various cyclic averages and amplitudes and define load intervals known as Load Parcels (LP), as shown in Figure 2.16a. Each LP therefore has an associated N, τ_{cy} and τ_a, which can be directly applied to the contour diagrams under appropriate assumptions (Jostad et al., 2014). An equivalent number of cycles N_{eq} is then determined, which is a value representative of the original force time series (Andersen, 2015). This methodology is illustrated in Figure 2.16b. Figure 2.16 demonstrates the navigation process for finding equivalent strains for an irregular stress history. This is similar to the strain superposition process described by Lin and Liao (1999) and Stewart (1986) (Figure 2.12), but sums the strains generated after a load parcel is complete instead of determining a strain equivalency. Full details on the calculating the accumulated strain can be found in Andersen (2015).

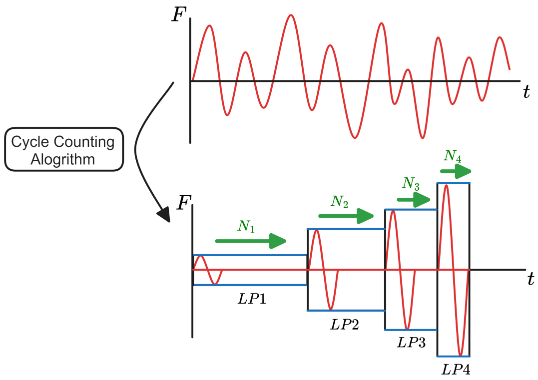

(a) Load parcels from force-time history

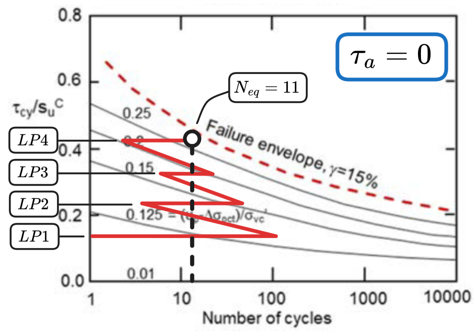

(b) Load parcels applied to CCD slice

Figure 2.16: Example illustration of applying irregular force-time signals to CCDs (Andersen, 2015)

For OWT cyclic design, force-time signals from intense storm events can be processed and directly applied to CCDs to estimate the foundation response, however conservative assumptions are necessary (Andersen, 2015). After cycle-counting, the signal is rearranged as load parcels in ascending order (shown in Figure 2.16a). If the LP with the largest cyclic load is applied at the end, the majority of cyclic degradation is expected to have occurred prior to this LP. Therefore, sequencing the maximum load at the end enables a conservative estimate for the equivalent strains, and is inline with post-storm capacity check methodologies (DNV, 2021; Jostad et al., 2014).

Note that Figure 2.16a shows a force-time signal that has an irregular two-way configuration. As such, the average stress in the load parcels is 0. This enables direct application to the $\tau_a = 0$ plane of the CCD to find N_{eq}, as shown in Figure 2.15. This methodology may be appropriate for capacity checks for gravity based structures such as oil and gas platforms, as two-way loading ($\tau_a = 0$, $\tau_{cy} > 0$) is more critical (Kaynia et al., 2015). However, it is demonstrated by Leblanc et al. (2010b), Lin and Liao (1999), and Long and Vanneste (1994) that one-way loading ($\tau_a > 0$, or $\zeta_c < 0$) can be more critical for OWTs supported by monopiles. This is especially true when accumulated strains are of concern, and would require more advanced navigation methodologies that utilise the full three-dimensional CCD, such as the method proposed by Page et al. (2021).

Applying CCDs to monopiles requires further considerations for capacity or fatigue design checks (Zhang et al., 2016). Cycle counting methods combined with strain superposition techniques have been proven to work well for estimating pile head accumulation (Leblanc et al., 2010a; Lin & Liao, 1999). However, additional modifications are required to modify p-y functions. Springs at different depths experience different cyclic mobilisation magnitudes compared to the force-time history applied to the pile head (Lesny & Hinz, 2007; Zhang et al., 2020). This requires deriving unique stress histories local to the spring such that a bespoke N_{eq} can be found from CCDs and used to scale the *p*-*y* function appropriately (Zhang et al., 2017; Zhang et al., 2016). The soil sample test used to inform CCDs (either DSS or TX) is also important, as soil loading must be representative of the failure mode expected at a given depth along the pile (Andersen, 2015). Zhang and Andersen (2017) suggested a method for scaling stress-strain to *p*-*y* for clays using DSS tests, but this is limited to slender piles due to physical similarities associated with DSS tests and the flow-around mobilisation inherent with slender piles (Figure 2.1c). Pore pressure accumulation and soil densification can also be represented in CCDs (Andersen, 2015; Long & Vanneste, 1994), however direct application to monopiles is uncertain (Leblanc, 2009).

An ascending arrangement for load parcels provides a conservative estimate for N_{eq} when estimating a monopile's degraded ultimate capacity. However, Luo et al. (2020) demonstrated that the estimate N_{eq} is highly dependent on the load parcel order. Additionally, Norén-Cosgriff et al. (2015) suggested that the cycle counting method has a large influence on the load parcels generated, and proposed a user-dependent frequency-filtering algorithm that may be more appropriate. However, the influence of LP order configuration and cycle counting method on N_{eq} is still not well understood, and requires further investigation. In some dynamical systems, the nonlinear behaviour between cycles may be of importance, especially when energy dissipation and resonance design is of concern.

2.2.3 Summary

For lateral capacity design, it is already well established that the API *p*-*y* methodology for OWT monopiles is not adequate due to its empirical derivation from slender pile tests (Reese et al., 1974). This is further exacerbated when considering cyclic effects, as the test data used to calibrate the *p*-*y* model is limited to 100 cycles with no consideration on the effects of cyclic amplitude or configuration type (Cox et al., 1974).

The *p*-*y* method facilitates cyclic degradation by encapsulating cyclic loading effects with scaling adjustments to the *p*-*y* functions, leading to a modified subgrade reaction modulus E_{py}. These models have demonstrated that this methodology can be extended to embody irregular cyclic loading, including one-way or two-way cyclic configurations. Additionally, CCDs are an effective way of simplifying the irregularity of wind and wave loads imposed on offshore infrastructure, but requires underlying assumptions that are heavily dependent on cycle counting and LP arrangement methods (Luo et al., 2020; Norén-Cosgriff et al., 2015). Additional assumptions become necessary when applying the theory to monopiles (Zhang, 2016; Zhang, 2017a), which may compromise the initial goal of accurately representing the wind and wave load history. Furthermore, none of the above methods account for the nonlinear cycle-by-cycle behaviour, which can lead to excessive nonlinear mobilisation and further accelerate degradation effects (Houlsby et al., 2017; Matasović & Vucetic, 1993; Ting, 1987; Vucetic & Dobry, 1988).

2.3 Dynamic pile modelling

OWTs supported by monopiles are dynamically sensitive structures exposed to many excitations of varying amplitudes and frequencies. These excitations include environmental loads deriving from wind and waves, as well as rotor forces generated by the passing turbine blades. The available design bandwidth for the natural frequency of the system is therefore limited, making resonance likely to occur. As a result, OWTs are prone to large displacements that can accelerate soil degradation and accumulate displacements over time (Andersen et al., 2013; Carswell et al., 2016; Houlsby et al., 2017).

The standard approach for determining the natural frequency of a structural system involves defining stiffness and mass matrices and conducting an eigenanalysis, which is detailed in Section 2.3.2. However, due to the variability of environmental loads, it's customary to employ a time-domain analysis for integrated OWT-monopile systems to gauge the structure's dynamic response (Arany et al., 2017; Bhattacharya, 2019; IEC, 2009). This process involves generating numerous force histories based on wind and wave frequency spectra for different sea states and wind speeds, which are then applied to the model as loads to assess its dynamic response (Arany et al., 2015; Branlard, 2010; Corciulo, 2015).

Given the multitude of load cases in design, computational efficiency is paramount. Consequently, dynamic one-dimensional beam-spring models with linear spring elements are commonly employed to represent soil-structure interaction, as nonlinear models can incur substantial computational costs if not implemented judiciously (Bathe, 2006; Chopra, 2013; Kontoe et al., 2008). However, in light of concerns regarding dynamic amplification in such analyses, it is crucial to account for the energy dissipation mechanisms of the soil to mitigate the risk of large oscillation amplitudes and potential resonance (Andersen, 2010; Anoyatis & Lemnitzer, 2017b; Carswell et al., 2015; Krathe & Kaynia, 2016; Novak, 1974; Tarp-Johansen et al., 2009).

This section will review the literature concerning dynamic pile modelling, encompassing small-strain dynamics, energy dissipation, and the utilisation of nonlinear hysteresis models to incorporate material damping effects within beam-spring models.

2.3.1 Natural frequencies

As part of SLS design requirements, it is necessary to estimate the initial natural frequency of the OWT structure such that resonance is appropriately avoided

(Arany et al., 2017; Bhattacharya, 2019; DNV, 2021). Resonance occurs when a system vibrates at its natural frequency in response to an external force, resulting in increased amplitude and energy transfer. Figure 2.17 illustrates the anticipated excitation frequencies imposed on a typical OWT-monopile structure, and the permissible design bandwidths as defined by design codes (DNV, 2021).

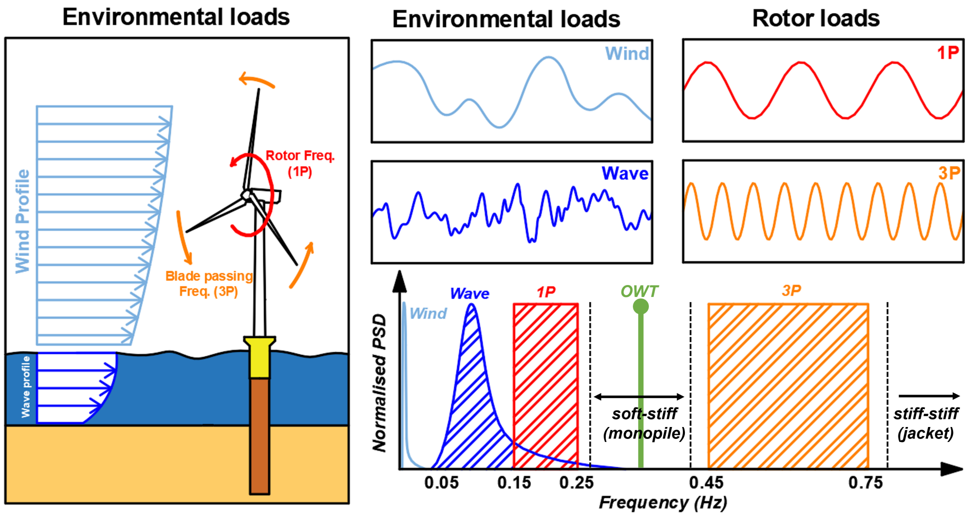

Figure 2.17: Illustration of the different OWT excitation loads and the normalised spectral density of the external and internal frequencies

1P and 3P denote the 1-Pass and 3-Pass frequencies of the rotor and blades, respectively, where 1P is a full blade rotation and 3P is each blade passing (for three-blade turbines). According to the normalised power spectral density in Figure 2.17, the natural frequency of an OWT supported by monopiles are designed to exist within the 'soft-stiff' bandwidth, which is between the 1P and 3P regions (DNV, 2021). Design frequencies are far enough from both the environmental and rotor excitations to avoid resonance, yet not too high to make the foundations overly rigid and costly to fabricate. The soft-stiff region presents a distinct design challenge due to an upper and lower limit, making it unclear whether design outputs are over- or under-conservative. Accurately computing the system's natural frequency is therefore crucial.

Turbine sizes are increasing due to the demand for renewable energy, meaning the rotor speeds (and therefore blade-passing frequencies) are likely to decrease. Consequently, this reduces the permissible design frequency bandwidth (as $3f_{1\mathrm{P}} = f_{3\mathrm{P}}$, see Figure 2.17) and shifts the permissible region towards the environmental excitation frequencies expected from wind and waves. Resonance therefore becomes an increasing concern as the size of OWTs grow and appropriate energy dissipation must be considered in models.

2.3.2 Small-strain dynamics

The natural frequency of a monopile is dependent on the soil stiffness, pile geometry, and the mass of the structure, which can be estimated using numerical methods such as linear (elastic) time-domain analyses or frequency domain analyses (Chopra, 2013; Tedesco, 1999). Frequency domain offers quicker analysis for linear systems, and the vibration and frequency modes are computed by solving the eigenvalue problem of the system. The constitutive small-strain model is a derivative of the traditional *p-y* model shown in Figure 2.2, where spring stiffnesses are elastic and an appropriate mass matrix is defined (see Appendix A). The characteristic eigenproblem of the system is given in Equation 2.26.

$$([K] - [\Lambda][M])\,[\Phi] = \{0\} \tag{2.26}$$

where $[K]$ and $[M]$ are the global stiffness and mass matrices of the system, respectively, $[\Lambda]$ stores the eigenvalues along the leading diagonal, $[\Phi]$ contains the eigenvectors, and $\{0\}$ is the zero vector. n corresponds to the vibrational mode. Each vibrational mode is stored in the eigenvector $[\Phi]$ as a column vector ϕ_n, and the corresponding modal frequencies are stored in $[\Lambda]$ as the eigenvalues ω_n^2.

The spring coefficients for the small-strain model can be defined using the initial spring stiffness $k_0 = E_{py,0}\Delta L$, where $E_{py,0}$ can be determined from *p-y* relationships. Dührkop et al. (2009) and Kallehave et al. (2012) suggested updated formulations for small-strain API sand, and Prendergast and Gavin (2016) investigated the efficacy of different formulations of k_0 derived from alternative theories. However, the mass matrix of pile-soil systems are not as well defined in the literature, as it is difficult to determine the contributing soil mass to the modal vibrations. It is therefore often misrepresented in analyses (Fitzgerald et al., 2019).

It is possible to derive appropriate mass and stiffness matrices by comparing the frequency response of a numerical model to empirical data using a model updating approach (Dezi et al., 2012; Prendergast et al., 2019; Wu et al., 2018). Such methods are used in SHM practices to detect damage in structures by comparing the frequency response of a structure to its baseline response (Domaneschi et al., 2013; OBrien & Malekjafarian, 2016). This methodology can be applied to pile-soil systems to detect geotechnical phenomena such as scour and gapping (Fitzgerald et al., 2019; Giordano et al., 2020) which can have a marked effect on the natural frequency (Prendergast et al., 2015, 2018).

The system's design frequency is likely to evolve over time towards excitation bandwidths (Darvishi-Alamouti et al., 2017; Ziegler et al., 2015), which means that resonance may occur at some point during the operational lifetime of an OWT and accelerate degradation due to large oscillation amplitudes. It is therefore essential for modelling techniques to incorporate stiffness degradation following cyclic events to prevent frequency shifts towards potentially onerous environmental excitations (Kallehave et al., 2012; Kaynia et al., 2015). Furthermore, models should include the principles of energy dissipation to mitigate large dynamic amplification factors expected in linear systems (Andersen, 2010; Anoyatis & Lemnitzer, 2017b; Carswell et al., 2015; Krathe & Kaynia, 2016; Novak, 1974; Tarp-Johansen et al., 2009). This is not possible in linear small-strain models evaluated using frequency domain methods, as the energy dissipation mechanisms are not accounted for in the eigenanalysis described in Equation 2.26.

2.3.3 Energy dissipation

Energy dissipation in OWT systems can originate from both the super- and substructure. Soil damping contributes the most to the first vibrational mode ϕ_1 (Tarp-Johansen et al., 2009), and stems primarily from hysteretic (material) damping when large strains are expected (Ishihara, 1997). In oscillating systems, the inclusion of energy dissipation is commonly represented in the equation of motion through an opposing force term that is proportional to velocity $\dot{y}$. Known as viscous damping, the damping coefficient c generalises the energy loss, and is demonstrated in Equation 2.27.

$$m\ddot{y} + c\dot{y} + ky = F(t) \tag{2.27}$$

where m is the mass of the object and $F(t)$ is the applied force as a function of time. $\ddot{y}$, $\dot{y}$ and y is the acceleration, velocity and displacement of the object, respectively. Figure 2.18 illustrates the total response of a viscously damped system using a linear spring in parallel configuration with a dashpot, which is the mechanical analogy of a viscous damper.

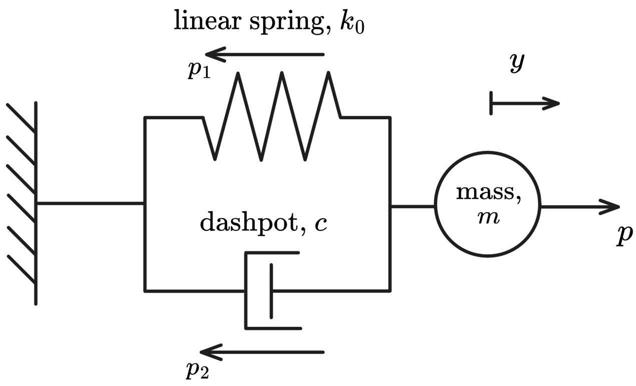

(a) Spring and dashpot in parallel

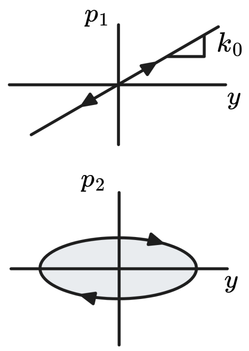

(b) Spring and dashpot response

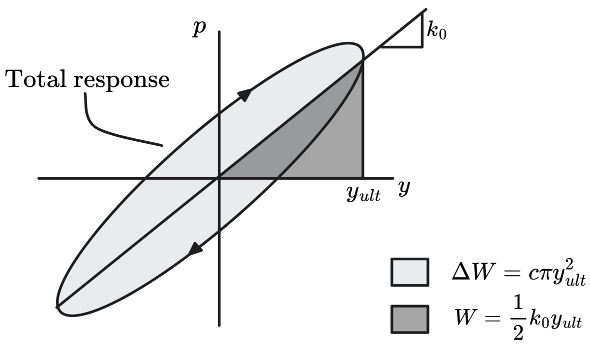

(c) Total response of the kinematic elements

Figure 2.18: Response of a linear spring in parallel with a dashpot

Note that the dashpot exhibits an ellipse-type hysteresis in the p-y domain as shown in Figure 2.18b. This corresponds to a linear behaviour in the p-$\dot{y}$ domain where the gradient is c, hence the viscous damping force is $p_2 = c\dot{y}$. The area of the Ellipses in Figures 2.18b and 2.18c are the same.

ΔW is the energy dissipated per cycle due to the dashpot, and W is the elastic potential energy stored in the linear spring. Hence, the damping ratio ζ is defined as the ratio of the energy dissipated per cycle to the energy stored in the spring, or $\zeta = \frac{\Delta W}{4\pi W}$. The model illustrated in Figure 2.18 is known as the visco-elastic model, and is the simplest form of damping that can be applied to an oscillating system. It has been successfully used in the dynamic analysis of Winkler-type piles (Anoyatis & Lemnitzer, 2017b; Badoni & Makris, 1996; Gazetas & Dobry, 1984b; Ishihara & Wang, 2019; Shadlou & Bhattacharya, 2016). However, as will be discussed in the following sections, this model alone is not sufficient to facilitate the complexities associated with the soil's nonlinearity and hysteretic behaviour for large-strain models subject to irregular loading (Ishihara, 1997; Pyke, 1979; Vucetic & Dobry, 1988).

Radiation damping

Radiation damping occurs due to the propagation of radial vibration waves through the soil medium induced by fast oscillations (Hardin & Drnevich, 1972a). The soil does not respond instantaneously due to its inertial and compressive properties, therefore the oscillatory response is out of phase from the applied stresses by a time lag δ. The stress-strain response is therefore hysteretic in shape. This is demonstrated in Figure 2.19.

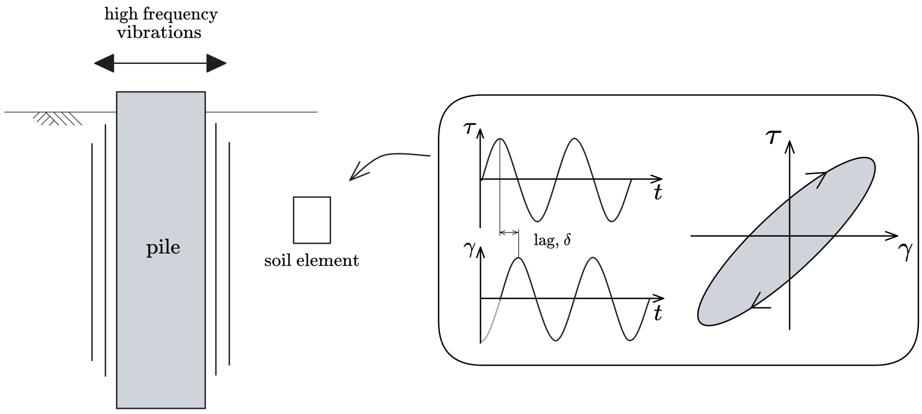

Figure 2.19: Illustration of a pile subject to high frequency vibrations, and the response of a distant soil element

The time lag δ is dependent on the frequency and distance from the vibrating pile. Figure 2.19 shows that the stress-strain response resembles the visco-elastic model described in Figure 2.18, therefore viscous dashpots can be used to model this behaviour. Gazetas and Dobry (1984b) developed a simple model to capture the radiation damping in piles by capturing the visco-elastic properties of soil layers with dashpots in parallel with linear springs. The equation for the damping coefficient due to radiation damping c_r is given by Equation 2.28.

$$\frac{c_r}{2D\rho_s V_s} = \left\{1 + \left[\frac{3.4}{\pi(1-\nu)}\right]^{5/4}\right\} \left(\frac{\pi}{4}\right)^{3/4} a_0^{-1/4} \tag{2.28}$$

where V_s is the shear wave velocity of the soil, ρ_s is the density of the soil, $a_0 = 2\pi f D/V_s$ is the dimensionless frequency. f is the frequency of the applied load. Frequency dependent dashpots have demonstrated to be effective in capturing the radiation damping pile-soil systems subject to high frequency loads (Badoni & Makris, 1996; Ishihara, 1997; Makris & Gazetas, 1992). However, piles subject to large-strain loading conditions, such as storm events or seismic activity, require additional dissipative methods due to large-strain irregular loading (El Naggar & Bentley, 2000; Gerolymos & Gazetas, 2005c; Kaynia & Andersen, 2015). Furthermore, the frequencies of the expected excitations applied to OWTs are less than 1 Hz, as shown in Figure 2.17 (Tarp-Johansen et al., 2009). Andersen (2010) demonstrated that radiation damping can often be neglected due to relatively slow loading conditions in offshore environments.

Material damping

Material damping occurs due to the soil's plasticity during medium to large strains (Ishihara, 1997). The stress-strain hysteresis loops occur due to nonlinear stress path experienced during repeated load cycles (Vucetic & Dobry, 1991). Figure 2.20 illustrates the typical hysteretic behaviour of soil under large symmetrical loads, including the energy dissipated per cycle.

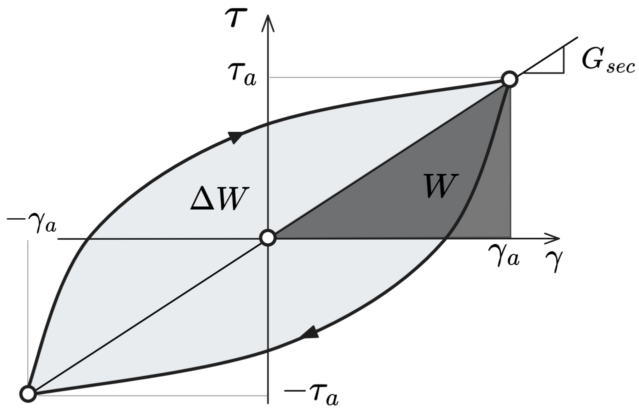

Figure 2.20: Typical hysteretic behaviour of soil under large symmetrical loads, including the energy lost (ΔW) and energy stored (W) per cycle

The shape of the hysteresis can depend on many factors, including the stress history, strain rate, number of cycles, and pore pressure (Andersen, 2015; Gerolymos & Gazetas, 2005a; Hardin & Drnevich, 1972b; Vucetic & Dobry, 1988). It can also demonstrate the gapping phenomena in pile-soil models (Abadie et al., 2019; Allotey & El Naggar, 2008; Swane & Poulos, 1984; Williams et al., 2021). However, it is common practice for simplified models to capture the energy dissipation due to material damping by using a viscous dashpot in combination with a linear spring, taking the form of an equivalent visco-elastic model (Damgaard et al., 2013). The damping coefficient is designed such that the elliptical area of the dashpot (Figure 2.18c) is equal to the area expected inside the hystereses formed by the soil's nonlinear stress path (Anoyatis & Lemnitzer, 2017a; Mylonakis, 2001a).

It should be noted that material damping is a function of the strain amplitude and the corresponding damping coefficient may not be the same for each complete load cycle. Therefore, material damping is a function of the strain history rather than an intrinsic property of the soil material. It is not possible to encapsulate the complex plastic behaviour of soils with a single damping coefficient informed from in-situ or laboratory testing, especially when the system is loaded asymmetrically. To add, utilising a linear spring model to consider the nonlinear stiffness properties of the soil is unrepresentative of the physical problem, and highly limiting when more complex geotechnical phenomena are involved.

An alternative approach to modelling material damping is to explicitly define the stress path and calculate the change in stiffness over time within each cycle using a nonlinear spring. While effective at modelling complex geotechnical behaviors under large, irregular loading, this method can be computationally expensive due to time-domain simulations, requiring a substantial number of iterations to converge to a solution (Kontoe et al., 2008). This is discussed in more detail in Section 2.3.5.

2.3.4 Other forms of damping

Other forms of damping in OWT structures include:

- Structural: energy dissipation due to the internal friction of the structure's components and elastic deformation of the structural material
- Hydrodynamic: energy dissipation due to the interaction of the structure with the surrounding fluid
- Aerodynamic: energy dissipation due to the interaction of the structure with wind

These forms of energy losses are not considered in detail herein, as the focus is on the soil-structure interaction and the energy dissipation mechanisms associated with the hysteretic behaviour of the soil. However, they can be encapsulated in an idealised way.

Rayleigh damping is a common approach to define the equivalent damping coefficient that represents the combined effect of all the aforementioned damping mechanisms. The model assumes the damping coefficient can be described as a linear combination between the mass and stiffness of the system according to Equation 2.29.

$$c = \alpha_1 m + \alpha_2 k \tag{2.29}$$

where α_1 and α_2 are the Rayleigh damping coefficients proportional to the mass and stiffness, respectively. The coefficients are calculated as:

$$\alpha_1 = \frac{2\zeta_t \omega_1 \omega_2}{\omega_1 - \omega_2} \tag{2.30}$$

$$\alpha_2 = \frac{2\zeta_t}{\omega_1 + \omega_2} \tag{2.31}$$

where ζ_t is the target damping ratio of the system, and ω_1 and ω_2 are the two frequencies defining the frequency range over which the damping is approximately constant at ζ_t. Clearly, this is an oversimplification to the complex dissipation associated with the dynamic behaviour of OWTs. The Rayleigh damping model is a simple approach to define the equivalent damping coefficient, and is commonly used to idealise complex dissipative mechanisms such as hystereses and radiation damping (Bathe & Wilson, 1976; Chopra, 2013; Ishihara, 1997; Tedesco, 1999). This form of damping is also relevant for nonlinear systems to aid in obtaining stable solution estimates (Vaiana et al., 2019).

2.3.5 Hysteresis modelling

Earthquakes have caused widespread destruction to buildings and infrastructure, impacting the lives of countless people. These disasters have highlighted the need for geotechnical earthquake engineers to develop more accurate predictions of dynamic soil-structure interaction under intense earthquake conditions (Fan et al., 1991; Kagawa & Kraft, 1980; Lam & Martin, 1986). The sudden rise in commercial availability of computational power in the 1980s facilitated the inaugural shift towards more complex models to capture the dynamic nonlinear behaviour of soil. This mainly involved implementing theory derived earlier in the century into complex nonlinear time-domain algorithms (Iwan, 1967; Masing, 1926). This section discusses some important advancements in modelling the hysteretic stress-strain response of samples, and its application to pile soil-structure interaction and dynamic *p*-*y* models.

Original masing rules

Elastic perfectly-plastic stress-strain models enable fast response estimations due to their simplicity, and are commonly used in multi-directional dynamic FEA when modelling seismic activity in soils (Kohgo et al., 1993; Sun et al., 2003, 2007). However, the elasticity range of soils is extremely small, and plastic deformations can be expected for strains as small as 0.001% (Ishihara, 1997). Curvilinear or piecewise-linear models enable a more appropriate representation of the soil's nonlinear behaviour over many strain ranges (Iwan, 1967; Masing, 1926; Vucetic & Dobry, 1988, 1991; Wen, 1976), but require more complex algorithms to solve.

Hysteretic models involve two main components to represent the stress path of a complete cycle: (i) the initial stress-strain curve from rest (referred to as the backbone curve herein) and (ii) the subsequent unload/reload curves that embody the stress-strain response due to changes in direction of motion. Masing (1926) proposed a methodology to capture this behaviour by taking a representative monotonic backbone curve and transforming the function when a reversal occurs accordingly. The general function of the transformation theory is described in Equation 2.32.

$$\begin{aligned} \frac{\tau - \tau_i}{C} &= f\left(\frac{\gamma - \gamma_i}{C}\right) \\ \tau &= Cf\left(\frac{\gamma - \gamma_i}{C}\right) + \tau_i \end{aligned} \tag{2.32}$$

where τ_i and γ_i indicate the stress-strain coordinates of the hysteretic reversal points h_i. C is the generalised scaling factor applied to the piecewise functions that form the hysteresis shape. Originally, Masing (1926) proposed that, after the initial loading sequence, the subsequent unload and reload paths take the form of the backbone curve, and are scaled by a factor of 2. In other words; $h_0 = (0, 0)$ and $C = 1$ for the initial loading curve, whereas the subsequent unload/reload paths follow that $h_{i+1} = (\tau_a, \gamma_a)$ and $C = 2$, where τ_a and γ_a are the stress and strain amplitudes of the soil's response, respectively. This is illustrated in Figure 2.21 and is known as the Original Masing Rules (OMRs).

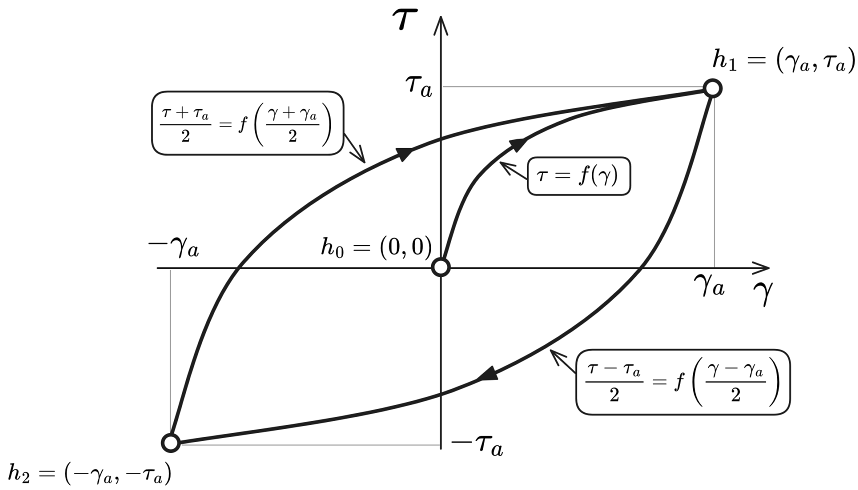

Figure 2.21: Original Masing rules for capturing the hysteretic stress-strain response of soils (Masing, 1926)

The OMR methodology enables a simplified analytical approach to computing the energy dissipated per cycle for symmetrical loading. The area within the enclosed hysteresis loop in Figure 2.21 can be determined by integrating the backbone function and subtracting the energy stored ($W = \frac{1}{2}\gamma_a f(\gamma_a)$) at γ_a. Multiplying the crescent-like shape by eight gives the total area within the hysteresis loop, and therefore the energy dissipated per cycle ΔW. The expected damping ratio from the OMR model is given in Equation 2.33.

$$\zeta = \frac{\Delta W}{4\pi W} = \frac{8\left[\int_0^{\gamma_a} f(\gamma)d\gamma - W\right]}{4\pi W} = \frac{2}{\pi}\left[\frac{2\int_0^{\gamma_a} f(\gamma)d\gamma}{\gamma_a f(\gamma_a)} - 1\right] \tag{2.33}$$

Equation 2.33 estimates the material damping for a symmetrically loaded soil sample, if a backbone function $\tau = f(\gamma)$ is defined. The monotonic response of most materials can be used to describe the backbone function if the expected load rate is sufficiently slow (Ishihara, 1997). However, this approach has been shown to overestimate the anticipated material damping for soils when compared to lab experiments (Kondner & Zelasko, 1963; Matasović & Vucetic, 1993; Yi, 2010).

Typically, the backbone function includes parameters that represent the initial (maximum) stiffness and the ultimate resistance. Many models have been defined using a hyperbolic relationship taking the form described in Equation 2.34, such as Duncan and Chang (1970), Hardin and Drnevich (1972b), Kondner and Zelasko (1963), and Vucetic and Dobry (1988).

$$\tau = \frac{G_0\gamma}{1 + \frac{\gamma}{\gamma_r}} \tag{2.34}$$

where γ_r is the reference strain. Kondner and Zelasko (1963) suggested a hyperbolic backbone where $\gamma_r = \tau_{ult}/G_0$, which has shown a good match to cohesionless soil tests at medium strain amplitudes (when $\gamma < 0.001\%$). However, Ishihara (1997) demonstrated that, when the hyperbolic function is applied to Equation 2.33, and $\gamma_r = \tau_{ult}/G_0$, the damping ratio determined from the area within the hysteresis is $\zeta = 2/\pi = 0.637$ for large strain amplitudes (when $\gamma > 0.001\%$). This is much higher than the material damping measured experimentally, which typically ranges between 0.05 and 0.3 (Hardin & Black, 1968; Hardin & Drnevich, 1972b; Seed et al., 1986; Vucetic & Dobry, 1991). Matasović and Vucetic (1993) proposed modifications to the γ_r definition to generalise the function for additional types of sand, improving the ζ estimation using experimental results.

The hyperbolic model therefore involves two parameters, G_0 and τ_{ult}, to determine the backbone function, and by extension the area within Masing-type hysteresis loop. However, the initial stiffness and the ultimate resistance are not completely indicative of the anticipated degree of material damping. Material properties such as saturation, void-ratio, density and grain size can have a significant influence on the hysteretic response of soils (Carswell et al., 2015; Gazetas & Dobry, 1984b; Hardin & Drnevich, 1972b; Seed et al., 1986). Furthermore, external factors, such as the loading configuration, load rate, stress history and confining pressure may also influence response (Ambrosini, 2006; Ashmawy et al., 1995; Vucetic, 1990).

In light of this, it is convenient to encapsulate the overlapping factors that influence the hysteretic response of soils into parameters that directly control the geometrical shape of the hysteresis loop. The Ramberg-Osgood (RO) backbone function facilitates this with two additional shape parameters, and is defined in Equation 2.35.

$$\tau = \frac{G_0 \gamma}{1 + \alpha \left| \frac{\tau}{\tau_{ult}} \right|^{r-1}} \tag{2.35}$$

where α and r are empirically derived coefficients that best match test data. Note that Equation 2.35 is a modification of the original RO model for soils, as recommended by Idriss et al. (1978). The RO model is used extensively across multiple disciplines when calibrating model behaviour to experimental results (Desai & Zaman, 2013; Giardina, 2017; Pugasap, 2006; Sireteanu et al., 2014; Ueng & Chen, 1992). α and r are chosen such that the area within the hysteresis loop (energy dissipated) matches well with experimental damping results, which typically leads to appropriate representation of the stress path (Sireteanu et al., 2014).

The OMRs offer a convenient analytical approach to calibrating the backbone function to the dynamic behaviour of τ-γ and p-y systems under simple harmonic motion. However, the initial rules established by Masing (1926), where unload/reload functions are scaled with a factor of $C = 2$, cannot facilitate irregular load signals due to inappropriate backbone scaling for varied cycling amplitudes. As such, the OMRs are often used to characterise dashpots that encapsulate the anticipated energy dissipation due to material damping for convenience in dynamic analyses, rather than explicitly defining the stress path in a hysteretic spring.

Extended masing rules

When large-strain dynamics is of concern in geotechnical systems, the input force is seldom simply harmonic, for example seismic loading and storm events. In such cases, equivalent dashpots or symmetrically hysteretic springs are not adequate to capture the system's true response to irregular load signals. This is particularly true for soils (Baber & Noori, 1986; Pyke, 1979; Vucetic, 1990; Wen, 1976).

Masing's theory was derived from an experiment where a brass bar was symmetrically loaded, which will have extremely different rheological behaviour to soil (Masing, 1926). As such, Pyke (1979) outlined two crucial features of the OMRs which defined the first two rules of the methodology, and added two additional rules to comply with the expected cyclic behaviour of soil. The rules are as follows:

1. The tangent stiffness after an unload/reload sequence is equal to the initial stiffness.

2. The unload/reload function is the same shape as the backbone curve, and is scaled appropriately.

3. When the unload/reload curve exceeds the maximum past strain and intersects the backbone curve, the stress-strain path follows that of the backbone curve until the next reversal point.

4. If the unload/reload curve intersects the curve from the previous cycle, the stress-strain path follows that of the previous cycle.

Note that if rule 2 is followed, rule 1 is implicit. These rules are commonly applied in modelling hysteresis loops of soils with *non-degrading* behaviour, primarily due to their capability to retain the maximum stress experienced by the soil in the past (Vucetic & Dobry, 1991). Figure 2.22 illustrates the four rules and demonstrates their application in the Extended Masing Rules (EMRs) for constitutive models of a non-degrading hysteresis, as introduced by Vucetic (1990).

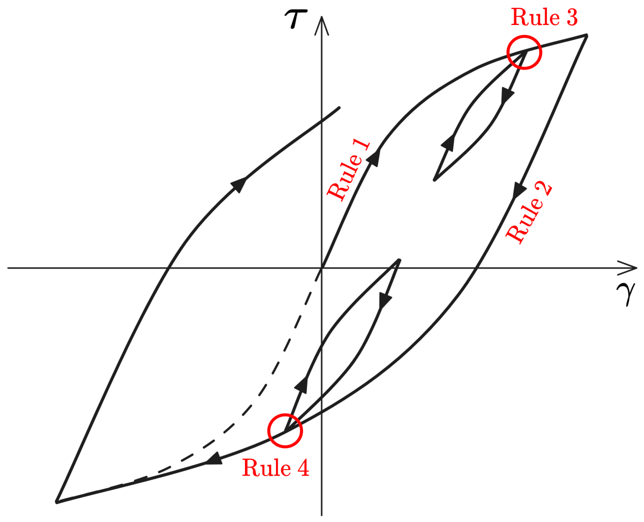

Figure 2.22: EMR illustration for an irregular stress sequence

When subjected to irregular cyclic loading, it is expected that the reversal points $h_i = (\gamma_i, \tau_i)$ will vary from cycle to cycle. If the OMR is used to define the reload curves (where $C = 2$), then the stress path will likely exceed the ultimate stress of the soil, which is problematic. To overcome this, Pyke (1979) suggested a generalising equation for the unload/reload scaling factor C, and is defined in Equation 2.36.

$$C = \left| \mathrm{sgn}(\dot{\gamma}) - \frac{\tau_i}{\tau_{ult}} \right| \tag{2.36}$$

where $\dot{\gamma}$ is the shear strain velocity of the system, $\mathrm{sgn}(\dot{\gamma})$ is the signum function of $\dot{\gamma}$ (i.e. ± 1 for positive or negative $\dot{\gamma}$, respectively), τ_i is the shear stress of the previous load reversal, and τ_{ult} is the ultimate shear stress of the soil. The τ_i/τ_{ult} term is important, as it ensures that the current stress path is scaled to fit between the stress of the previous reversal ordinate τ_i and the ultimate stress τ_{ult}. As a consequence, Equation 2.36 enables a more realistic stress-strain path for soils subjected to irregular cyclic loading, as a certain 'memory' of the soil's ultimate state is captured in the scaling factor. Figure 2.23 illustrates the effect of Equation 2.36 on the stress-strain path of a system subjected to irregular cyclic loading and demonstrates its ability to capture the EMRs.

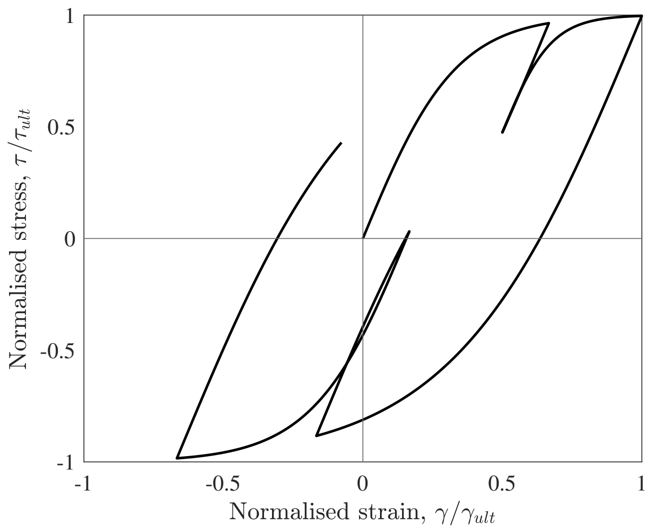

Figure 2.23: Arbitrary irregular loading signal applied to a Masing model informed using Pyke's rule (Equation 2.36)

Whilst Pyke's rule does not explicitly capture rules 3 and 4 of the EMRs by closing the loop, it can be argued that the modelled response is more indicative of the observed behaviour of reloaded soils in sample tests (Barnes, 2010). Subsequent reload curves are scaled using Equation 2.36 such that the stress path is bound within τ_{ult} and $-\tau_{ult}$.

This approach offers a practical method to define the unload/reload curves of a system subjected to irregular cyclic loading (Amjadi & Johari, 2022; Beck & Pei, 2022; Restrepo & Taborda, 2018). However, 'overshooting' is a common issue for hysteresis models that compose subsequent reload functions in real-time, whereby small loops develop erroneous stress paths that do not sensibly follow the previous cycle. Figure 2.24 shows that the reload curves in the small hystereses do not close the loop, which lead to stress paths exceeding the desired response.

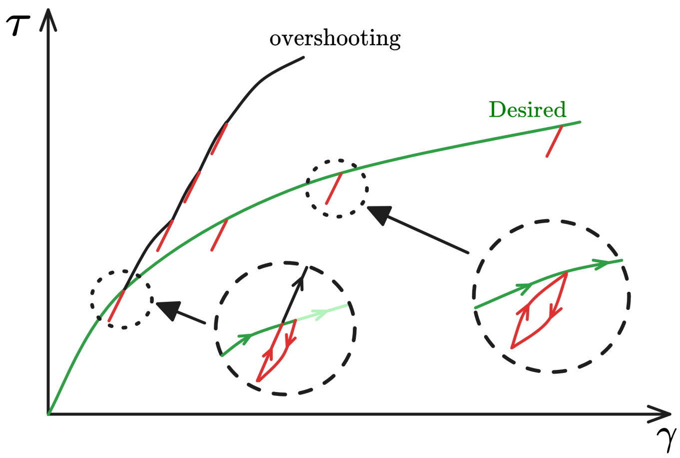

Figure 2.24: Overshooting due to Equation 2.36 for small reload cycles

This issue is typically countered using pre-simulation signal filtering to remove low amplitude, high frequency load reversals (Norén-Cosgriff et al., 2015), or complex modifications to the EMR algorithm in order for the system to 'memorise' previous stress-paths and recognise when they are intersected (Benz, 2007). Regardless, Pyke's rule is a simple and effective method to define the reload curves of a system subject to low frequency, high amplitude irregular cyclic loading, and is used extensively in the literature (Basarah et al., 2019; Konstandakopoulou et al., 2020; Su et al., 2020).

It is possible to model more advanced stress paths that facilitate certain soil-structure interaction phenomena using the Masing algorithm. Beck and Pei (2022) demonstrated that including a hardening spring in parallel with the nonlinear Masing spring can encapsulate changes in pore pressure. Other researchers directly modified C to simulate certain behaviours. For example, Williams et al. (2022) demonstrated a simple methodology to modify C when loaded in a certain direction to encapsulate ratcheting effects. Vucetic (1990) suggested a degradation model, where C is a function of the number of cycles. Pile-soil gapping is also possible (Damgaard et al., 2013; Klinkvort & Hededal, 2013; Williams et al., 2021).

Modifying C is a powerful approach to encapsulating more advanced hysteretic behaviour and degradation. However, C directly scales both the x and y axes, which was suggested in the above examples. It is postulated here that it is possible to uncouple the direction of scaling such that both degradation (vertical curve scaling) and ratcheting (horizontal curve scaling) can be calibrated independently. Equation 2.37 describes a more generalised form of the Masing algorithm, where C_x and C_y are the horizontal and vertical scaling factors, respectively.

$$\tau = C_y f\left(\frac{\gamma - \gamma_i}{C_x}\right) + \tau_i \tag{2.37}$$

Iwan model

An alternative method for modelling the hysteretic behaviour of soil is to use a series of bilinear springs which, when arranged in parallel, emulate the response of the EMRs for a given initial load curve. Known as the Iwan model, the elastic perfectly-plastic springs are back-derived from a backbone function by piecewising the curve into linear segments[1]. Figure 2.25 demonstrates the decomposition of a backbone function to form the Iwan spring elements for $N_s = 4$ bilinear springs. The total response of the bilinear hysteretic springs described in Figure 2.25b is

[1]The model is described with reference to forces (F) and displacements (x), in accordance with the original literature.

shown in Figure 2.26.

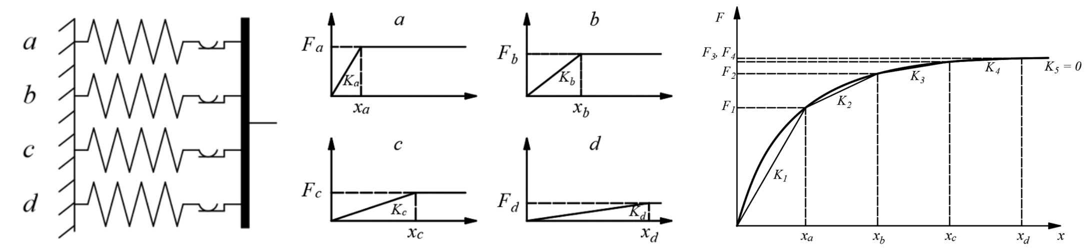

(a) Springs in parallel (b) Bilinear springs (c) Global Iwan spring

Figure 2.25: Iwan model for $N_s = 4$ springs

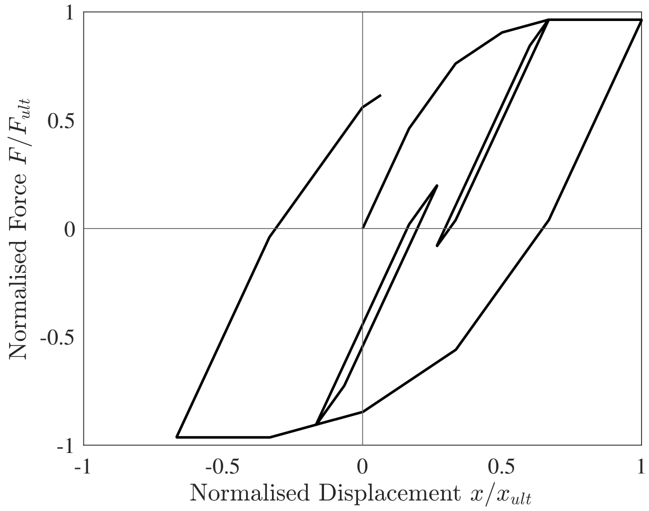

Figure 2.26: Iwan hysteresis model response to arbitrary loading ($N_s = 4$)

It is clear from Figure 2.26 that the EMRs are strictly followed, as previous load cycle stress paths are continued and internal loops are closed. Because of this, overshooting is not an issue with the Iwan model. The parallel springs are evident in the global Iwan model due to the polygonal shape. Note that the hysteresis is continuous when $N_s \to \infty$. Section 4.2.3 demonstrates that $N = 20$ is sufficient for smooth hysteretic stress paths.

Similar to the Masing methodology, the Iwan model is capable of modifications to facilitate complex geotechnical behaviour. Kaynia (2019) demonstrated that describing intermediate bilinear springs as nonlinear-elastic developed a 'pinching' effect in the global Iwan spring, which is akin to soil-structure separation behaviour in piles. Markou and Kaynia (2018) suggested parametrised micro-elements which enable a calibration for the expected material damping in OWTs. Whyte et al. (2020) developed an Iwan model for undrained clays, which applies spring-wise scaling factors derived from three-dimensional FEA calibration tests to estimate pile-soil element strength degradation due to large amplitude cyclic loading, and similar work was done by Prevost (1985). Mostaghel (1999) suggested a differential equation description for piecewise-type hysteresis with degrading characteristics, such as those proposed by Kaynia (2019) and Whyte et al. (2020). Ratcheting behaviour is also possible with appropriate modifications to the reload stiffness in the bilinear springs (Park, 1988). However, it has not been applied to the context of OWT monopiles.

Bouc-Wen model

The Bouc-Wen (BW) model offers an alternative approach to defining the hysteretic stress path by utilising a first order differential equation. Originally proposed by Bouc (1971), and later modified by Wen (1976), the model is described as a linear and hysteresis spring in parallel[2]. The linear spring defines a post-yielding stiffness, which can be neglected, and both springs are described in Equation 2.40. Figure 2.27 illustrates the springs.

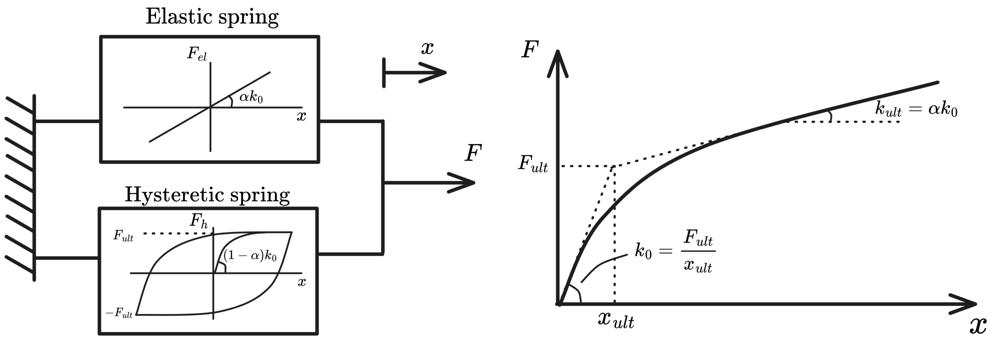

(a) Springs in parallel (b) Initial total response

Figure 2.27: Bouc-Wen spring combination describing total hysteretic response

$$F_{el} = \alpha \frac{F_{ult}}{x_{ult}} x \tag{2.38}$$

$$F_h = (1-\alpha) F_{ult} z(t) \tag{2.39}$$

$$F = F_{el} + F_h \tag{2.40}$$

where α is a post-yielding stiffness parameter, x_{ult} is the ultimate strain and F_{ult} is the ultimate stress. $z(t)$ is the hysteresis parameter that is computed by solving the differential equation described in Equation 2.41.

[2]The model is described with reference to forces (F) and displacements (x), in accordance with the original literature.

$$\dot{z}(t) = \frac{1}{x_{ult}} \dot{x}(t) \left[A - |z(t)|^n \left(\beta - \gamma \mathrm{sgn}(\dot{x}(t) z(t)) \right) \right] \tag{2.41}$$

where A, n, β and γ are parameters which control the shape of the hysteresis. Equation 2.41 is a nonlinear first order differential equation, which can be described as a two-dimensional slope field in the F-x domain, where the solution is the spring state. The β and γ parameters modify the slope direction to develop unique shapes in the stress path, and n controls the curvature between the initial and post-yielding stiffness (bilinear behaviour when $n \to \infty$). Typically, A is taken as unity such that F_{ult}/x_{ult} in Equation 2.38 becomes the small-strain elastic stiffness (Badoni & Makris, 1996; Constantinou et al., 1987). Note that the signum function in Equation 2.41 governs the direction of the slope field, which therefore controls the direction of the hysteresis loop. When $\dot{x}$ is negative, the slope field is reversed such that the new solution $z(t)$ forms the unload curve.

It is difficult to explicitly define an analytical expression for the stress path due to its nonlinear form when $n > 1$ and non-integer. The ordinary differential equation described in Equation 2.41 is therefore typically solved using numerical integration approaches, such as the fourth order Runge-Kutta algorithm (Butcher, 1996). Figure 2.28 shows the effect of β and γ on the hysteresis loop for the arbitrary load sequence used in Figures 2.23 and 2.26.

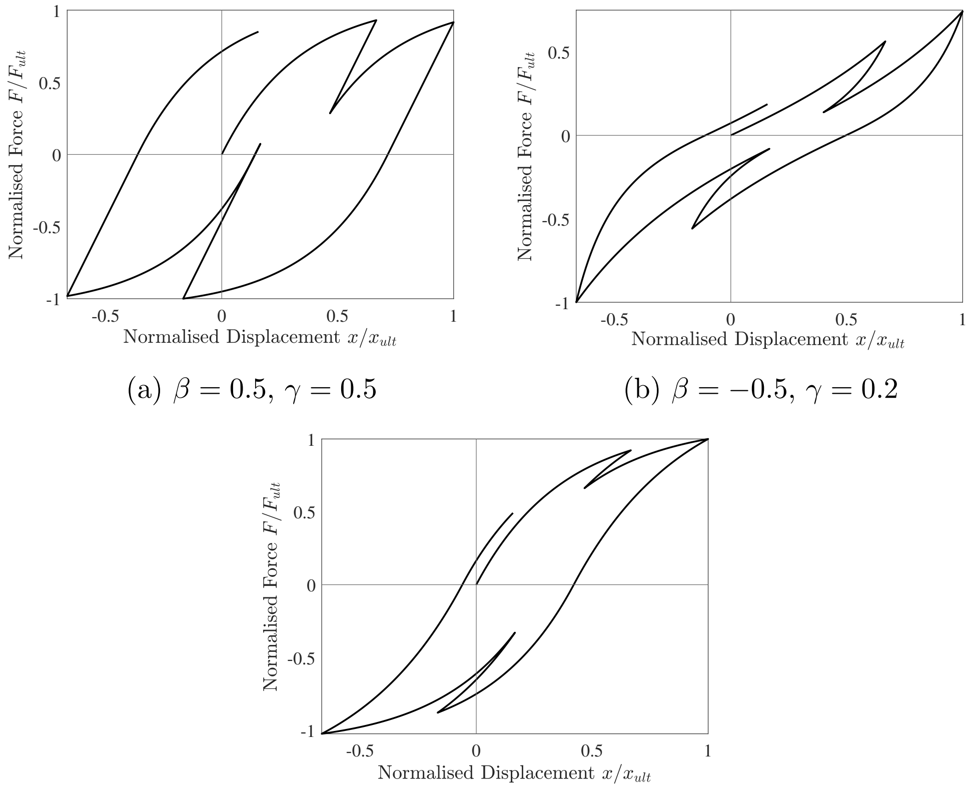

(a) $\beta = 0.5$, $\gamma = 0.5$

(b) $\beta = -0.5$, $\gamma = 0.2$

(c) $\beta = 0.8$, $\gamma = 0.1$

Figure 2.28: BW model for different β and γ parameters ($n = 1$)

The BW function can facilitate complex hysteresis shapes with simple parametrisation and demonstrates similar behaviour to Pyke's rule when capturing the 4 EMRs in Figure 2.28a. However, note that rule 1 is often compromised for this type of model. The first reloading sequence in Figure 2.28a does not have the same initial stiffness as the first loading sequence. For this reason, the BW hysteresis is commonly used in other structural engineering applications rather than soil-structure interaction modelling (Pelliciari et al., 2020; Sengupta & Li, 2013). However, Badoni and Makris (1996) directly applied the BW model to piles under earthquake excitations, and derived a method to directly inform Equation 2.41 using ultimate capacity and stiffness parameters defined in the API design codes, such as Equation 2.4 and 2.9 (API, 2014). The results compared well with numerous earthquake case studies.

Although the Masing rules are not strictly followed, the hysteresis geometry of the BW spring is similar to those defined by Pyke's equation demonstrated in Figure 2.23, but offers further control of the hysteresis shape. This can serve as a powerful model when more complex system behaviour is expected; such as liquefaction, densification or general evolution of the constitutive soil-structure properties. The stress path of the BW model is not informed by a backbone function, which makes empirical calibration difficult using tried methods such as the OMRs formulation. However, Gerolymos and Gazetas (2005c) used the BW model to describe the nonlinear seismic response of a rigid concrete caisson. The hysteresis model was applied to both the dashpots (p-$\dot{y}$) and springs (p-y) and showed good results, but required extensive and arduous calibration (Gerolymos & Gazetas, 2005d). Separation and gapping behaviour is also possible (Baber & Noori, 1985; Gerolymos & Gazetas, 2005b).

Due to similar structural geometries in the models, this model was also applied to OWT monopiles, as large concrete caissons also exhibit diameter effects with low L/D ratios (Kassas & Gerolymos, 2016). These effects were considered in the model proposed by Gerolymos and Gazetas (2005c). Baber and Noori (1986), Kottari et al. (2014), and Pelliciari et al. (2020) proposed that the shape parameters in Equation 2.41 can be modified as a function of time or displacement, such that the shape of the hysteresis evolves. Sivaselvan and Reinhorn (2001) suggested multiple hysteretic springs in parallel to describe gapping and degradation independently.

More advanced analysis is also possible with the BW due to its fully analytical definition. Miguel et al. (2020) suggested a method to determine characteristic parameters of the BW model through analysing the frequency spectrum of the displacement signal. Defining the nonlinear characteristics of dynamic soil-structure interaction using simple diagnostics, such as accelerometers, is a promising approach to determining the system's nonlinear behaviour in-situ, and may be a valuable tool for SHM of OWTs when observing lifetime degradation (Alexander, 2010; Alexander & Bhattacharya, 2011; Huang et al., 2018).

Hysteresis models for pile-soil interaction

Pile-soil interaction can be modelled using a variety of different methods to describe the stress paths. Typically, to simplify the problem, the OWT substructure is encapsulated using a lateral, rotational and coupling spring at the ground line (Arany et al., 2017; Carswell et al., 2015; Krathe & Kaynia, 2016). Whilst convenient for fast analysis and simple integration with superstructural models, the local response of individual soil layers cannot be considered, which can have a significant impact on the system's response (Di Laora et al., 2013; Gazetas & Dobry, 1984a; Tott-Buswell et al., 2022; Yang & Jeremić, 2005). A system with multiple degrees of freedom would be required to capture the full stratum, which requires a significant increase in computational power and time to solve for nonlinear systems.

Badoni and Makris (1996) used numerous hysteresis springs and frequency dependent dashpots to model the lateral soil reaction of a slender pile subject to earthquake motion. The model was informed using simple geotechnical parameters and compared to case study base excitations, which showed excellent results. Rovithis et al. (2009) also used p-y-type models to replicate centrifuge tests which demonstrated promise. However, it is important to address that models consisting of large numbers of degrees of freedom and hysteretic springs are computationally expensive, as they require small time steps to accurately capture the system's response. This is particularly true for nonlinear systems, as the stiffness is not constant. More degrees of freedom lead to additional modal vibrations of higher natural frequencies (Bathe & Wilson, 1976; Tedesco, 1999), which can result in profound instabilities for nonlinear systems due to excessive motion reversals (Chopra, 2013), and may invoke erroneous stress paths in discrete hysteresis models.

2.3.6 Summary

This section has discussed the different methods used to define the hysteretic response of soils. The OMRs are a convenient approach to defining the stress paths of a system subject to harmonic loading. This method is often used to define the material damping behaviour of dashpots in dynamic soil-structure interaction models, but is highly dependent on the governing backbone function and its experimental calibration. Furthermore, The OMRs (where $C = 2$) were not suitable for irregular cyclic loading, and therefore the EMRs were proposed by Pyke (1979). Pyke's modification enables a more realistic stress path for soils by calculating the anticipated stress for the current irregular loading configuration, but can exhibit erroneous behaviour. However, the Iwan model implicitly follows the EMRs by piecewising backbone functions into elastic perfectly-plastic spring elements arranged in parallel. Reversals are therefore determined on a local yielding criteria, rather than explicit hysteresis reversal coordinates. Both of these models are capable of modification to facilitate more complex hysteretic behaviour, such as ratcheting, gapping and degradation, however the BW methodology encompasses such behaviour with simple parametrisation.

Each methodology has been used to model dynamic pile-soil interaction in literature. However, there has been no comparative review on the stability and accuracy of the algorithms, particularly when computational efficiency is of importance. OWTs are undergoing rapid development, and therefore the ability to accurately and efficiently model the system's response is crucial. SHM systems are also becoming more common in OWTs due to the harsh environment and the need to ensure the structural integrity over long periods. If the nonlinear dynamic response of a system can be accurately predicted, then a SHM system can be used to monitor and estimate operational fatigue damage and encourage data-driven decision making. Such a model would also appropriately model the material damping effects in the dynamic soil-structure interaction, which is a prominent component in large OWTs subject to resonance and high intensity storm events.

Chapter 3

Static multi-spring model: development and analysis

This chapter aims to build upon the traditional p-y model by accounting for the diameter effects experienced in low L/D monopiles. The static model developed in this chapter is compared to laterally loaded monopile field tests performed in sand at Blessington (Murphy et al., 2018) and Dunkirk (McAdam et al., 2020). The field tests were not part of the work contributing to this thesis. The Blessington pile tests are described in the following section and the problem definition is underlined through a brief performance review on CPT-based p-y-only models in comparison to the API sand p-y approach.

The objective is to derive soil reaction curves for each type of spring element that is informed using cone tip resistance q_c data. This will facilitate analysis procedures that lead to quick preliminary designs of monopile foundations by improving the traditional p-y methodology. The chapter concludes with a discussion on the model's limitations and potential improvements for future work.

3.1 Blessington pile test database

Lateral load tests were performed in two regions of the Blessington site, Dublin, and are described herein. Blessington Lower quarry (BL) comprised three monopile configurations with L/D = 3, 4.5, and 6; and one pile from Blessington Upper quarry (BU) with L/D = 13. Full details on pile dimensions are given in Table 3.1. The CPT investigations for each quarry demonstrate notable uniformity across their respective site (Figure 3.1). Due to the lack of pile-specific CPT data, the average q_c profile is used. The water table is reported to be 13 m below ground level for BU and >10 m below ground level for BL. The site contains dense, fine sand with relative density close to 100% and bulk unit weight of 19.8 kNm^{-3}. All piles were installed via driving. Detailed descriptions of the ground conditions at the Blessington sites have been reported by Doherty et al. (2012), Gavin and Lehane (2007), and Tolooiyan and Gavin (2011). Minimum, maximum, and average CPT profiles, including the G_0 profile, are plotted in Figure 3.1 for both BL and BU sites.

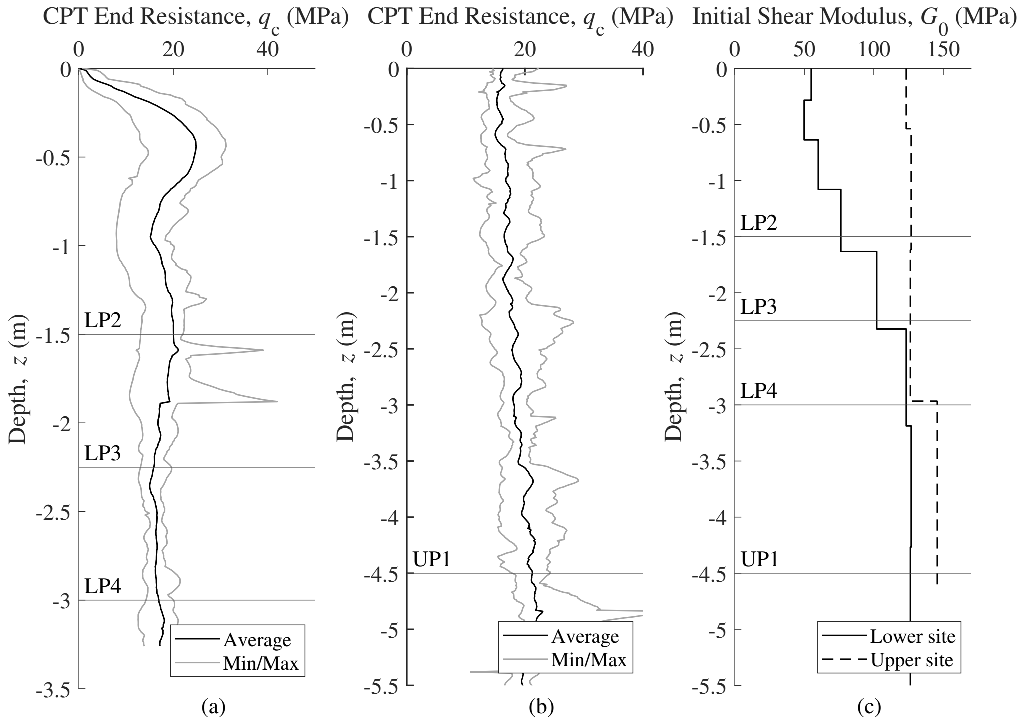

Figure 3.1: (a) minimum, maximum and average q_c profiles for Blessington Lower quarry (b) minimum, maximum and average q_c profiles for Blessington Upper quarry (c) G_0 profile used for Blessington Upper and Lower quarry

Table 3.1: Monopile geometries at Blessington site (Murphy et al., 2018)

Pile Name	**Embedment** L (mm)	**Diameter** D (mm)	**Ratio** L/D	**Thickness** t (mm)	**Eccentricity** h (mm)
LP2	1500	510	3.0	10	1000
LP3	2250	510	4.5	10	1000
LP4	3000	510	6.0	10	1000
UP1	4500	340	13.0	14	400

3.2 CPT-based *p-y* models

The performance of the API sand and CPT-based *p-y* functions described in Table 2.5 are compared with the Blessington pile pushover tests outlined in Table 3.1. The CPT-based *p-y* functions are informed using the q_c profiles shown in Figure 3.1. For the API *p-y* function, the friction angle is assumed to be 40° and a unit weight of 19kNm^{-3}. The *p-y* model is developed in MATLAB's coding environment, and details for model assembly and validation can be found in Appendices A and B, respectively. The results are shown in Figure 3.2. Timoshenko beam theory is used to model the elastic properties of a pile, particularly accounting for internal shear forces that arise when rigid elements, such as monopile substructures, undergo deflection (Gupta & Basu, 2018). E_p=200 GPa, G_p=80.77 GPa, ρ=7850 kgm^{-3}, $\kappa = 0.5$ are assumed for all piles.

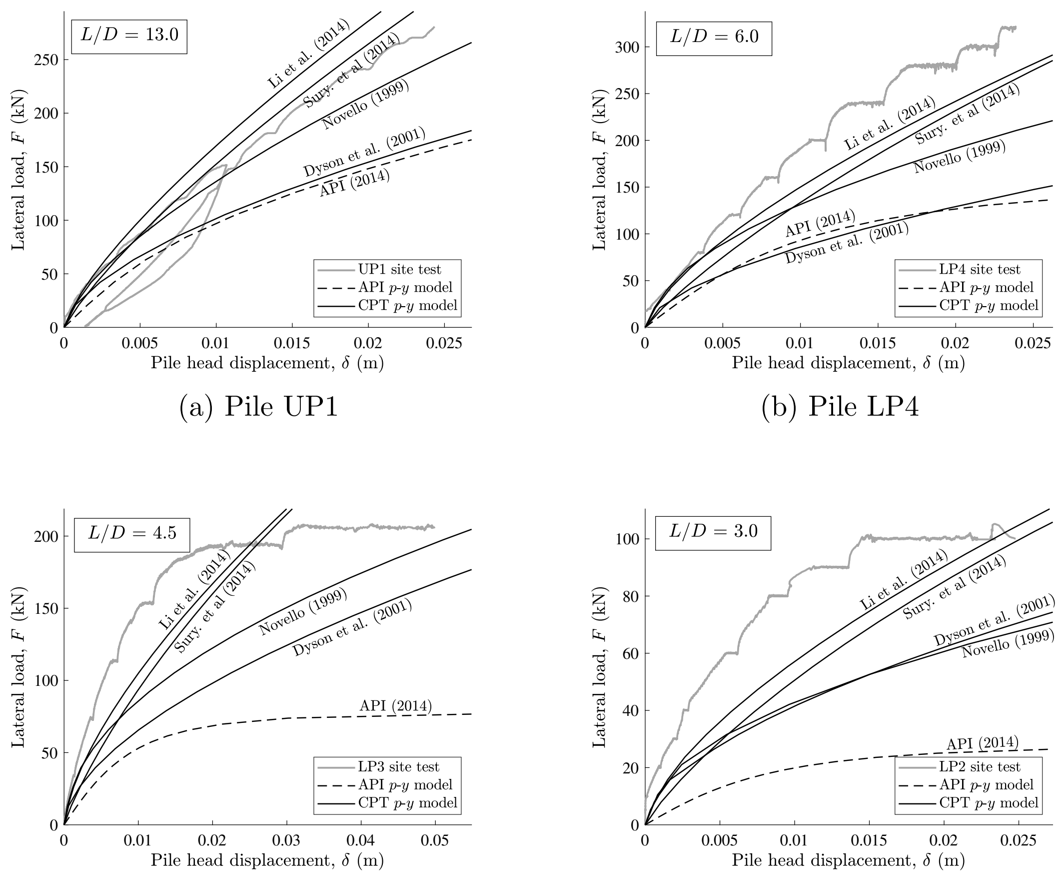

(a) Pile UP1 (b) Pile LP4

(c) Pile LP3 (d) Pile LP2

Figure 3.2: Comparison of CPT-based *p-y* functions with API sand *p-y* function against Blessington's monotonic lateral pushover tests

The results in Figure 3.2 show that the API sand function overestimates pile head deflections and underestimates the ultimate capacity for all pile geometries.

This is because the API sand function is calibrated for piles of L/D ratios near 34 (Reese et al., 1974), therefore the parameters defined in Figure 2.3 and Figure 2.4 cannot be applied to the pile geometries tested at Blessington. Figure 3.2a shows that most CPT models capture pile head deflection with reasonable accuracy. The CPT-based models proposed by Dyson and Randolph (2001), Li et al. (2014), Novello (1999), and Suryasentana and Lehane (2014) (see Table 2.5) all have considerably lower L/D calibration spaces compared to the API function, therefore UP1 ($L/D = 13$) is captured with reasonable accuracy. Li et al. (2014), Novello (1999), and Suryasentana and Lehane (2014)'s models are in general a good fit, whereas Dyson and Randolph (2001)'s *p*-*y* model overestimates the most out of the CPT-based models for all piles.

UP1 and LP4 site tests do not reach capacity when laterally loaded, and demonstrate a similar trend that is indicative of a similar failure mechanism. The power law relationships describing the Li, Novello and Dyson estimate this shape well (see Table 2.5), but have no consideration for the capacity in the formulation. This is evident in relatively rigid pile tests LP3 and LP2, as the pile head reaches maximum lateral load but the CPT functions do not show any indication of reaching an ultimate value. It should be noted that the function developed by Suryasentana and Lehane (2014) implicitly includes parameters that consider the ultimate capacity of the pile (Equation 2.16). However, the model still fails to estimate the capacity of LP3 and LP2 site tests, likely due to original calibration space of the function. Conversely, the similar response shape to LP3 and LP2 and the API-defined *p*-*y* models suggests that the hyperbolic tangent formulation (Equation 2.3) is an appropriate model for rigid piles. Currently, no CPT-based model exists that uses a hyperbolic relationship.

The relative performance for all *p*-*y* models are the same for each pile test; however, the model's deflections become increasingly overestimated as the L/D ratio decreases. This is in part due to further extrapolation of the calibration ranges, and the transition from slender pile to rigid pile behaviour (see Section 2.1.4). Murphy et al. (2018) demonstrated that, for increasingly lower slenderness ratios, the relative contribution of the *p*-*y* spring to the applied overturning moment reduces from approximately 90% to 80% for $L/D = 6$ and 3, respectively. This trend is in line with what is observed in Figure 3.2, and suggests that additional resistance mechanisms are required to appropriately capture the behaviour of rigid piles.

To summarise, Figure 3.2 demonstrates that CPT-based *p*-*y* functions can capture the general response of laterally loaded piles with $L/D \geq 13$, but are restricted to more confining pile geometry calibration spaces. The overestimated deflections for lower L/D ratios for all functions suggests that there are residual soil resistances unaccounted for in the traditional p-y spring element. It is a core objective of this chapter to develop a model that can capture the behaviour of low L/D monopiles, by incorporating additional CPT-based resistance mechanisms that are not considered in traditional p-y models.

3.3 CPT-based multi-spring model development

Diameter effects have been addressed in various models in literature using multi-spring models. Lai et al. (2021), Wang et al. (2020), and Zhang and Andersen (2019) propose two-spring models in clay, where the p-y elements are accompanied by a single rotational spring at the global rotation point of the pile that encapsulates the lateral and rotational resistances at the tip. Wang et al. (2022a) further simplified the approach by encapsulating all resistances using a single rotational spring at the rotation point. Fu et al. (2020) proposed a three-spring model that added a distributed moment and base shear mechanism; and Cao et al. (2021) suggested a three-spring model with only lateral, base shear and base moment springs, assuming the utilised p-y functions implicitly account for the distributed moments. Burd et al. (2020b) and Zhang et al. (2023) proposed a four-spring model that considers all resistances separately with respective spring types. Among these models, the four-spring model system can comprehensively simulate the expected resistances of a near-rigid pile under lateral load.

Figure 3.3 illustrates the four anticipated resistances for a rigid monopile when laterally loaded at the pile head. The horizontal pile displacement y mobilises lateral soil pressures p, and the local rotations θ induce shear tractions along the pile-soil interface that generate a distributed moment m. The pile base is also subject to a moment M_b and shearing V_b due to the bearing stresses q_b at the tip. Assuming Winkler's theory, the soil-structure reaction mechanisms can be treated as uncoupled and take the form of a p-y model with additional springs (Winkler, 1867), as shown in Figure 3.3b.

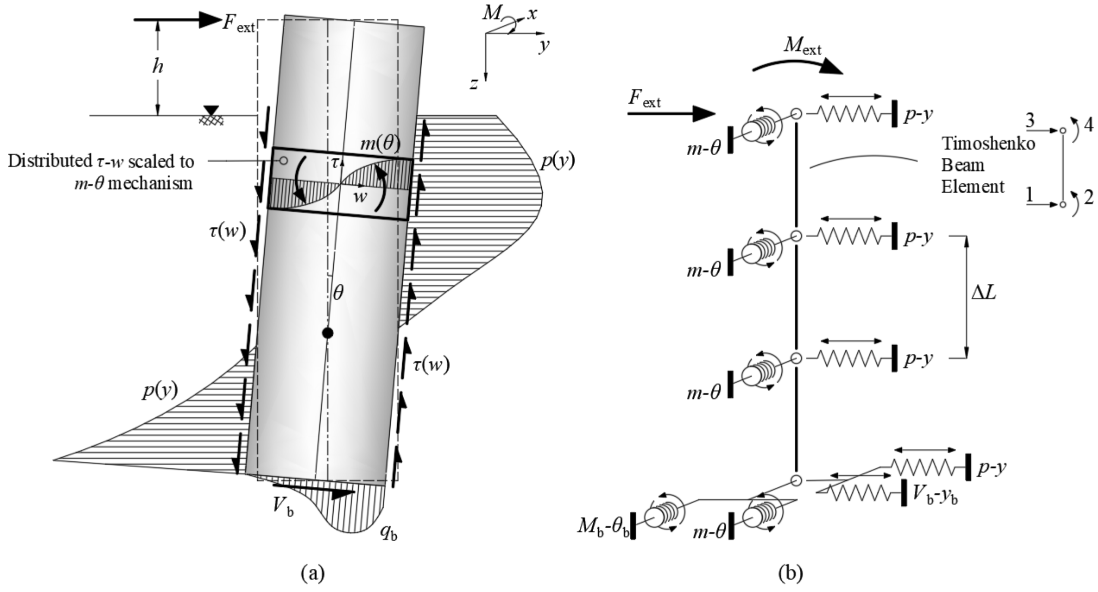

Figure 3.3: (a) Resistances for monopiles under lateral loading and (b) schematic of discretised multi-spring model

Using the Direct Stiffness Method (see Appendix A), the system can be discretised into elements and solved for, where the nonlinear soil elements are described by updating the secant modulus of the reaction curves. The lateral soil pressure is captured using a traditional p-y definition, and the distributed moment due to soil-pile interface friction is modelled as distributed m-θ spring elements. The monopile is modelled using four degree-of-freedom elastic beam elements, where each node is supported by lateral and rotational springs. Timoshenko beam theory is used to capture internal shear deflections within the pile section that are expected for low L/D monopiles (Gupta & Basu, 2018). Axial forces within the monopile are neglected. A lateral and rotational spring is added to the pile base to encapsulate tip resistances resulting from large diameter effects. The lateral base shear spring (V_b-y_b) models the lateral shearing due to the pile annulus and internal soil, and the base rotation spring (M_b-θ_b) represents the moment resistance incurred due to soil bearing stress q_b.

The CPT-based reaction curves for each new spring element are derived in the following sections.

3.3.1 Lateral p-y springs

p-y functions are commonly derived from site test data or finite element calibration procedures that are specific to a particular pile-soil configuration. This means that these functions are typically only suitable for use within a limited range of pile dimensions and soil profiles for which they were originally derived or calibrated (Jeanjean et al., 2011; Lehane & Suryasentana, 2014; Murphy et al., 2018; O'Neill & Murchison, 1983; Reese et al., 1975). When choosing a *p*-*y* function to inform the lateral resistance elements of a multi-spring model, it is necessary to isolate the lateral soil pressure p to prevent an overlap with other mechanical resistances that could be implicitly defined within the *p*-*y* relationship. Additionally, the *p*-*y* function must exhibit an appropriate consideration of the flexural rigidity of the pile, which can have a significant influence on the lateral resistance (Ashford & Juirnarongrit, 2003; Fan & Long, 2005; Poulos & Hull, 1989).

The power law *p*-*y* relationship proposed by Li et al. (2014) was derived using open-ended circular steel piles installed in siliceous sands, with L/D ratios ranging between 6.5 and 20. As slenderness ratios as low as 6.5 were considered, resistance mechanisms from the aforementioned diameter effects may be inherently included in its parametrisation space. Murphy et al. (2018) showed that, when $L/D = 6$, *p*-*y* springs can contribute to $\sim$ 90% by evaluating percentage contribution to resisting the applied overturning moment for each spring type. It is therefore assumed that the *p*-*y* relationship derived by Li et al. (2014) isolates the lateral soil pressure p when used in a multi-spring framework, as the L/D ratio of the most rigid pile in the calibration space is above $L/D = 6$ (Li et al., 2014). The intended L/D ratio for the *p*-*y* relationship is also low enough that appropriate pile flexibility may be assumed accounted for. To add, the function was derived for piles with the cross-sectional properties of a monopile. The *p*-*y* function was described in Table 2.5, and is repeated in Equation 3.1 for convenience.

$$p = 3.6D(\gamma' D)\left(\frac{q_c}{\gamma' D}\right)^{0.72}\left(\frac{y}{D}\right)^{0.66} \tag{3.1}$$

where γ' is the effective unit weight of sand.

It should be noted that Li's *p*-*y* function cannot be used to model the ultimate lateral capacity of piles due to the power law relationship, which was demonstrated in Figure 3.2. As such, the multi-spring model is limited to small to medium range deflections and cannot fulfil ULS design. However, it may still be used to estimate the initial response and deflection range of a monopile within typical operational deflections, as loading conditions that reach the designed ultimate capacity are seldom experienced during OWT operation.

3.3.2 Rotational m-θ springs

The distributed moment m due to vertical soil-pile interface friction becomes more significant as the diameter of the monopile increases (Byrne et al., 2015; Lam, 2013). This is due to the pile radius acting as a lever arm as the pile rotates. This is not explicitly captured in traditional p-y models. The moment-rotation relationship of this spring element can be informed by scaling vertical shear-displacement reaction curves (τ-w) to a moment-rotation function (m-θ), as demonstrated in Figure 3.4. The τ-w curve is well defined in CPT-based axial capacity design methodologies (Lehane et al., 2020b), therefore a CPT-based m-θ function can be derived.

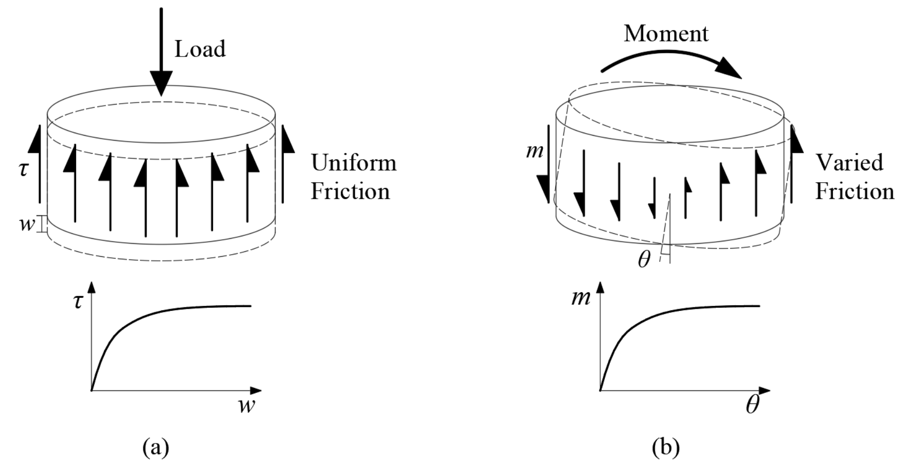

Figure 3.4: (a) Axial model with uniform friction and (b) rotational model with varied friction

Lehane et al. (2020a) suggested a parabolic τ-w relationship, originally proposed by Randolph (2003), because of its close match with the τ/τ_f against w/w_f load-transfer curve recommended in API (2014). The τ-w relationship is as follows:

$$\tau = G_0 \left(\frac{w}{2D}\right) \left[1 - \frac{w}{2w_f}\right] \tag{3.2}$$

where w_f is the local ultimate displacement and is defined as $4D\tau_f/G_0$, G_0 is the initial shear modulus of the soil and τ_f is the local maximum vertical shaft shear resistance. G_0 and τ_f are the only parameters required for full definition of the τ-w relationship and can be estimated using CPT q_c values in the absence of appropriate site test data. For example, G_0 can be approximated with q_c using empirical scaling relationships such as those proposed by Baldi et al. (1989) as recommended in the ICP-05 design method (Jardine et al., 2005). See Section 2.1.2.

It is expected that dilation and plugging effects can be present for small-scale steel open-ended circular piles, which may have a marked effect on pile-soil interface shearing capacities (Gavin et al., 2013; Lehane & Gavin, 2001; Lehane et al., 2005). As such, it is important that scaling effects are accounted for when comparing the model to scaled monopile site tests. The UWA CPT-based design methodology estimates the pile shaft friction at approximately 14 days after driving and is shown in Equation 3.3 (Lehane et al., 2020b).

$$\tau_f = \left(\frac{f_t}{f_c}\right)(\sigma'_{rc} + \Delta\sigma'_{rd}) \tan\delta_f \tag{3.3a}$$

$$\sigma'_{rc} = (q_c/44)\, A_{re}^{0.3} \left[\max\left(1, \frac{H}{D}\right)\right]^{-0.4} \tag{3.3b}$$

$$\Delta\sigma'_{rd} = \left(\frac{q_c}{44}\right)\left(\frac{q_c}{\sigma'_v}\right)^{-0.33}\left(\frac{d_{\mathrm{CPT}}}{D}\right) \tag{3.3c}$$

where f_t/f_c is the loading configuration ratio, A_{re} is the effective area ratio, H is the distance from the pile tip to the soil horizon of interest, σ'_v is the effective vertical stress ($\gamma' z$), d_{CPT} is the diameter of the standard CPT probe (35.7mm), and δ_f is the interface friction angle (defined as 29° in Lehane et al. (2020a)). f_t/f_c is taken as 0.8 for general applications, as suggested by O'Neill (2001). Equation (3.3b) represents the radial effective stress induced by plugging, where $A_{re} = 1 - \mathrm{PLR}(D_i/D)^2$ and PLR is the Plug Length Ratio (defined as $\mathrm{PLR} = \tanh(0.3(D_i/d_{\mathrm{CPT}})^{0.5})$). D_i is the internal diameter of the pile. Equation 3.3c represents the increase in radial effective stress due to dilation. Both σ'_{rc} and $\Delta\sigma'_{rd}$ are inversely proportional to the pile diameter, therefore the function can be extrapolated to larger pile configurations where plugging effects are less pronounced (Lehane et al., 2020b).

Figure 3.5 illustrates how the friction forces vary around the pile circumference with respect to the polar angle ψ. The relative local vertical deflection w can be described using Equation 3.4.

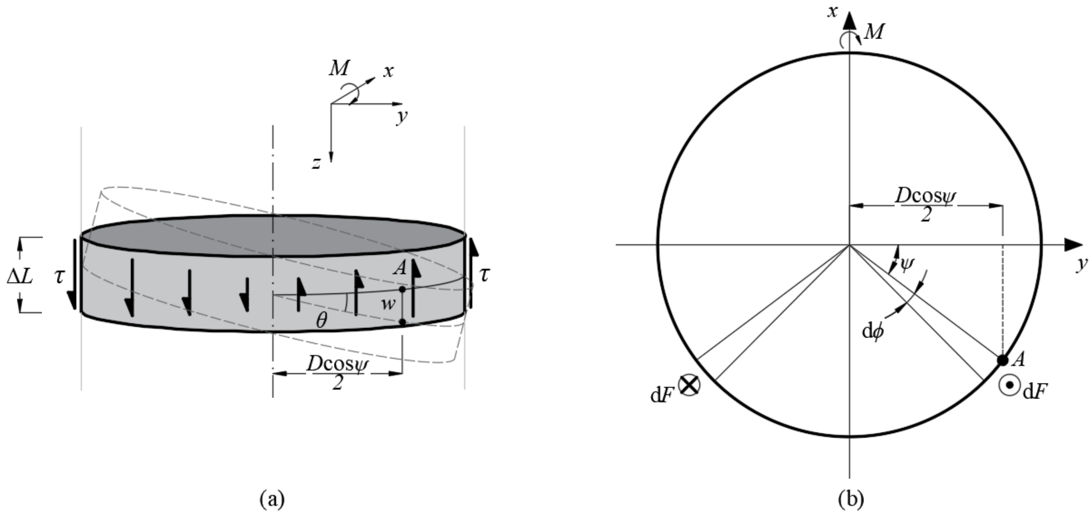

Figure 3.5: (a) section side view under rotation (b) section plan view with varying shear force (modified from Fu et al. (2020))

$$w = \frac{\theta D}{2} \cos \psi \tag{3.4}$$

The distributed moment per unit of resistance is:

$$m = 2 \int_{-\pi/2}^{\pi/2} \frac{D}{2} \cos \psi dF \tag{3.5}$$

It is important to note that the factor 2 assumes a symmetrical distribution of frictional forces about the pile, meaning the shear stiffness of the sand is assumed isotropic around the circumference of the pile. Fu et al. (2020) results suggest that the shallow active side of the pile has no resistance due to soil-structure separation at large deflections, and a reduced resistance on the active side at greater depths, and Zhang et al. (2023) assumed only passive side resistance for conservatism. Burd et al. (2020b) and Byrne et al. (2020a) coupled the local moment resistance with local lateral resistances from the *p*-*y* springs. This was possible due to the use of a 3D finite element calibration process which isolated element reaction curves (Taborda et al., 2020; Zdravković et al., 2020b). However, it is likely that semi-empirical *p*-*y* functions derived from field tests, such as Li et al. (2014), may include this side-friction resistance implicitly. Coupling is therefore neglected in this model.

Symmetrical interface shearing becomes less accurate as deflections increase. The assumption is made that the alterations in the generated moments on either side of the pile section are somewhat preserved when moments are calculated around the axis of rotation of the pile. It is presumed that the resultant moment remains constant despite the increasing interface shear on the passive side and decreasing interface shear on the active side. As such, any interface gaps and notable asymmetry in soil stresses surrounding the pile section are considered insignificant within the range of small to medium deflections under study.

Substituting $dF = \tau dA$ (where $dA = 0.5Dd\psi$) into Equation (3.5) gives m as a function of $\tau(w)$.

$$m = \frac{D^2}{2}\int_{-\pi/2}^{\pi/2} \tau(w)\cos\psi d\psi \tag{3.6}$$

Substituting Equation 3.3 into 3.2 and subsequently Equation 3.2 into 3.6, then solving the integral gives the total moment per unit length m as a parabolic function of θ:

$$m(\theta) = \begin{cases} a\theta - b\theta^2 & \theta < \theta_f \\ m_f & \theta \geq \theta_f \end{cases} \tag{3.7a}$$

$$a = \frac{G_0 D^2 \pi}{16} \tag{3.7b}$$

$$b = \frac{G_0^2 D^2}{96\tau_f} \tag{3.7c}$$

where m_f is the ultimate moment capacity per unit length and θ_f is the rotation at capacity. Full parametrisation of the m-θ function is shown in Table 3.2, including the initial stiffness k_θ. The function is illustrated in Figure 3.6.

Table 3.2: Key parameters of the m-θ function

Parameter	Definition
Maximum moment, m_f	$a^2/4b = \frac{3}{32}\pi^2 D^2 \tau_f$
Failure rotation, θ_f	$a/2b = 3\pi\tau_f/G_0$
Initial rotation stiffness, k_θ	$a = \pi D^2 G_0/16$

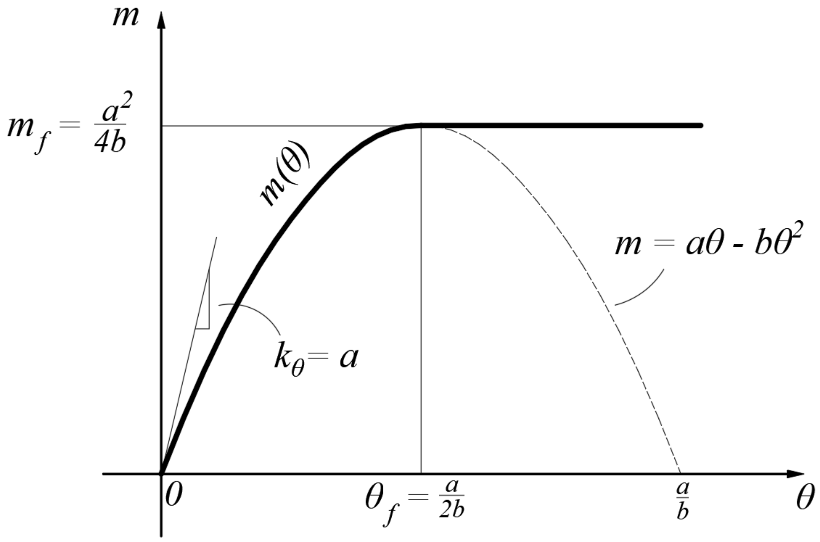

Figure 3.6: m-θ relationship as a parabolic function of θ

k_θ enables the m-θ spring to be defined in terms of the initial shear modulus of the soil, G_0, and the pile diameter, D, and can be implemented in small-strain analysis models such as those described in Section 2.3.2. This may help to improve natural frequency estimations for low L/D monopiles (Prendergast & Gavin, 2016).

It should be noted that the ultimate distributed moment per unit length (m_f) is defined without the consideration of gapping or asymmetrical normal stresses around the pile. However, the chosen CPT-based p-y function already disregards this condition for a ULS-type design process as Li's model is not capable of modelling lateral capacity (Figure 3.2).

3.3.3 Base moment M_b-θ_b spring

Pile tip resistances are not explicitly captured in traditional p-y models, and recent modifications to address the diameter effects at the base of the pile involves utilising macro spring elements that encapsulate base moment and shear mechansims (Cao et al., 2021; Fu et al., 2020; Wang et al., 2020; Zhang & Andersen, 2019). However, it is difficult to correlate macro element parameters with CPT end resistance values that represent local soil conditions. The base moment spring is therefore assumed decoupled from the base shear resistance.

CPT-based correlations to estimate the moment resistance at the pile tip due to overturning is not well-defined in literature, therefore cautious estimates are made herein. A residual bearing stress $q_{b,res}$ at the pile base exists post-installation (Byrne et al., 2018) and can resist rotation at the pile base. This can have a significant influence on the lateral resistance of low L/D monopiles (Burd et al., 2017). Byrne et al. (2018) investigated the impact of $q_{b,res}$ on the driveability of piles by estimating the residual stress as a function of the cone tip resistance local to the base ($q_{c,r}$). Defined as $q_{b,res} = \alpha q_{c,r}$, the parameter α was varied to achieve a best fit to the performance of driven pile site tests. It was found that residual bearing stresses exist even for large diameter piles installed with no plugging effects (Byrne et al., 2018).

$q_{c,r}$ should be chosen in a way that accounts for the variation in the local q_c values near the pile tip. In this study, $q_{c,r}$ is taken as the average q_c over a range above and below the pile tip. This range is set as a function of L/D, as monopiles with smaller L/D values tend to be more sensitive to variations in soil strength near the tip. This way the range is proportional to the slenderness ratio and will appropriately decrease for low L/D monopiles. It is important to note that the range will become disproportionately large for piles with a high L/D, but the influence of the tips will become insignificant in this case. The range is taken as $0.25L/D$ above and below the pile tip, which was deemed appropriate for the piles and CPT profiles used in this study. However, this value is at the discretion of the user.

A bilinear relationship is proposed to simplify the quantification of the anticipated nonlinear relationship. For simplicity, the restoring moment of the rotating pile base is assumed to act over a semi-circular area on the pile base. The maximum moment at the base is described in Equation 3.8.

$$M_{b,f} = q_{b,res} \frac{\pi D^2}{8} d \tag{3.8}$$

where d is the lever arm taken and is taken as $2D/3\pi$, which defines the distance from the centroid of the loaded semicircular area to the centre of the pile cross-section.

The PISA one-dimensional model has underlying similarities to the multi-spring model presented herein (Burd et al., 2020a; Burd et al., 2020b; Byrne et al., 2020a). Each spring is characterised using a dimensionless conic function that provides a convenient means to calibrate soil reactions to relevant displacement/rotation variables (Burd et al., 2020b). The function's ultimate soil reaction, initial stiffness, and displacement/rotations are derived based on three-dimensional finite element analysis calibration procedures of piles in dense sand (Burd et al., 2020b), informed from soil sample tests extracted from the Dunkirk site test (Zdravković et al., 2020a). All normalisation parameters for the conic function were determined based on a calibration space of $2 \leq L/D \leq 6$ and

$45\% \leq D_r \leq 90\%$. From calibration procedures described in Burd et al. (2020b), the failure rotation for a moment-rotation spring at the pile tip is given as:

$$\theta_{b,f} = \frac{\bar{\theta}_b \sigma'_b}{G_0} \tag{3.9}$$

where σ' is the vertical effective stress at the pile base and $\bar{\theta}_b$ is the calibrated ultimate rotation dimensionless parameter, taken as 44.98 (Burd et al., 2020b). Note that $\bar{\theta}_b$ is determined for piles with slenderness ratios between 2 and 6, therefore its application to piles with $L/D > 6$ is uncertain. However, it is expected that the moment induced at the pile tip will be increasingly insignificant for smaller diameters (higher L/D ratios) due to the D^3 term implicit in Equation 3.8.

3.3.4 Base shear V_b-y_b spring

For large diameter monopiles, the soil within the annulus of the cross-section will undergo horizontal shearing when the pile head is laterally loaded. It is assumed that the residual bearing stress $q_{b,res}$ acts as the confining stress, such that the horizontal shear at the base ($\tau_{b,f}$) can take a Mohr-Coulomb assumption. CPT-based correlations that estimate the friction angle within the pile at the tip are limited, therefore 35° is assumed for dense soil post-installation (Byrne et al., 2018). $\tau_{b,f}$ is therefore approximated as $q_{b,res} \tan 35°$. The M_b-θ_b and V_b-y_b spring at the pile tip are both a function of the bearing stress post-installation.

The V_b-y_b load-displacement function assumes a bilinear relationship, where the capacity V_b is defined as the maximum shear force at the pile tip. Zhang and Andersen (2019) suggested that the scoop-like shearing mechanism expected at the tip of a rotating pile can be simplified to a horizontal shear across the pile cross-section for large pile diameters. The shearing surface of the pile tip scoop and the pile tip area become increasingly similar as the diameter increases, therefore the shear force $\tau_{b,f}$ can be assumed to act over the area of the cross-section (Zhang & Andersen, 2019). The expected maximum shear force is therefore proposed as:

$$V_{b,f} = \frac{\pi D^2}{4} q_{b,res} \tan 35° \tag{3.10}$$

The failure displacement $y_{b,f}$ for the bilinear lateral base spring is informed based on the PISA methodology (Burd et al., 2020b) and is as follows:

$$y_{b,f} = \frac{2\bar{y}_{b,f} D \sigma'_b}{G_0} \tag{3.11}$$

$$\bar{y}_{b,f} = \bar{y}_{b,f1} + \bar{y}_{b,f2}\left(\frac{L}{D}\right) \tag{3.12}$$

where $\bar{y}_{b,f1} = 0.52 + 2.88D_r$ and $\bar{y}_{b,f2} = 0.17 - 0.70D_r$ and D_r is the relative density ($D_r = 0.75$ as recommended by Burd et al. (2020b)).

Equation 3.11 and 3.12 are calibrated based on three-dimensional finite element analysis procedures and are used to define the normalised conic spring function that models local horizontal soil reactions at the pile tip. $\bar{y}_{b,f}$ is intended for $2 \leq L/D \leq 6$ and $45\% \leq D_r \leq 90\%$ (Burd et al., 2020b).

According to Equation 3.12 it is possible for the initial stiffness of the bilinear base shear spring (i.e. $V_{b,f}/y_{b,f}$) to be negative or have an extremely large value for monopiles with large slenderness ratios. An arbitrary upper and lower limit of $L/D = 6$ and $L/D = 2$ are applied to Equation 3.12 to remain within the calibration space and to prevent inadmissible stiffness values. Due to the second order power law relationship with respect to D in Equation 3.10, small diameters (high L/D ratios) will reduce the expected shear force and consequently minimise the significance of these limits, but will not affect monopile geometries where base shearing is expected.

3.3.5 Calculation procedure

The pile deflections are computed using the Direct Stiffness Method (Tedesco, 1999), where $\{x\} = [K]^{-1}\{F\}$. The secant stiffness matrix $[K]$ is assembled from the individual secant stiffnesses of the spring elements and the elastic Timoshenko beam elements represent the pile. Details of the matrix assembly can be found in Appendix A. The nodal displacements $\{x\}$ are solved for using an iterative procedure where $[K]$ is updated with the secant stiffness of the spring elements until convergence is achieved. $\{F\}$ contains the force applied at the pile head, including the anticipated applied moment M at the ground line due to eccentricity h ($M = Fh$). The length of each beam element is set to $\Delta L = 0.05$ m. The elastic modulus, shear modulus, density and Poisson ratio is taken as 200 GPa, 80.77 GPa, 7850 kgm^{-3} and 0.3, respectively.

The CPT q_c profile is averaged at depth increments of 0.05 m, which is the same as the length of the beam element. The average q_c value is then used to inform the respective p-y and m-θ spring. $q_{b,res}$ is estimated as a percentage (α) of the average q_c value $0.25L/D$ above and below the pile tip. $\Delta L = 0.05$ m is a sufficiently small length to capture the spatial variability of the CPT profiles used in this study, and reducing the value shows a negligible influence on results. The numerical model is developed in MATLAB, and the pile tests described in the following sections are replicated using the multi-spring model and their respective CPT profile. The deflections at the ground line node are recorded for each applied load step and the results are compared to the field data.

The influence of the residual bearing stress $q_{b,res}$ on both the moment and shearing spring mechanisms at the pile tip remains uncertain and warrants further investigation. The subsequent analyses will evaluate the performance of the multi-spring model by comparing it to site tests conducted on laterally loaded piles. The parameter α is varied to identify an appropriate value for $q_{b,res}$ that aligns with the performance of site investigations. A maximum value of 0.1 is used, as recommended by Byrne et al. (2018).

3.4 Analysis and results

A wide range of monotonic push-over tests were performed at a site in Blessington, Ireland, investigating the influence of slenderness ratio for open-ended circular steel piles. Notable uniformity is demonstrated across the site (Doherty et al., 2012), therefore the average CPT profile is used to inform the multi-spring model. Site tests performed in Dunkirk, France, also investigated the performance of laterally loaded scaled monopiles, including local CPT q_c profiles for each pile's location (Zdravković et al., 2020a), enabling an improved investigation on the spatial variation sensitivity in CPT-based *p*-*y* models. Both site tests were performed in dry sand, therefore the influence of groundwater was not considered.

The SLS design philosophy for OWTs requires that the ground line rotations remain within 0.25° (DNV, 2021). However, only the ground line displacement was measured at the site tests used in this study. For this reason, it is assumed that 0.25° rotation is equivalent to $0.01D$ displacement at the ground line. This can be justified by assuming the rotation point of a laterally loaded rigid pile is located at $2/3L$ below the ground line (Arany et al., 2017; Chortis et al., 2020). Figure 3.7 illustrates the rigid pile assumption, and the following calculations justify that $0.25° \equiv 0.01D$ for low L/D ratios.

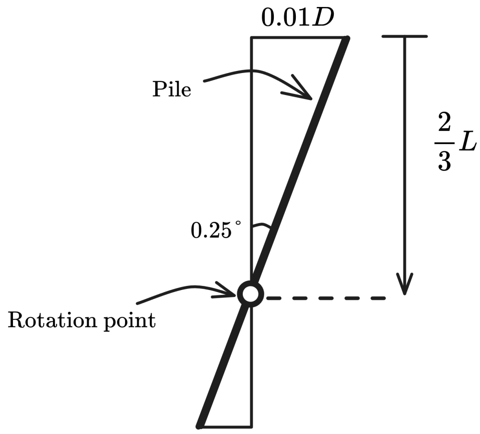

Figure 3.7: Rigid pile assumption for lateral pile analysis

$$\tan(0.25°) = \frac{0.01D}{2L/3} = \frac{0.01}{\frac{2}{3}\left(\frac{L}{D}\right)} \tag{3.13}$$

$$\frac{L}{D} = \frac{0.01}{\frac{2}{3}\tan(0.25°)} \simeq 3.44 \tag{3.14}$$

Therefore, under the rigidity and rotation depth assumptions, 0.25° rotation is equivalent to $0.01D$ displacement at the ground line if the slenderness ratio (L/D) is approximately 3.44. This is inline with the slenderness ratio of the site tests reviewed in this chapter. To add, the rigidity assumption is deemed appropriate for piles/caissons of this L/D (i.e. Gerolymos and Gazetas (2005e) and Grecu et al. (2021)). However, it is important to note that this assumption becomes increasingly more invalid as the slenderness of the pile increases due to bending. It was observed that no piles demonstrated this behaviour in the model during the analysis.

The field tests used in this investigation were incrementally loaded to capacity, therefore creep is evident in the ground line responses. However, the creep effects are expected to be minimal within the SLS deflection range.

3.4.1 Blessington benchmark

The piles described in Table 3.1 are replicated using the multi-spring model and the springs are informed using the average CPT and G_0 profile shown in Figure 3.1. Three different permutations of the multi-spring model are simulated to demonstrate the individual spring-type contributions to lateral resistance. These permutations include the traditional p-y-only method, p-y + m-θ, and the full multi-spring model, which incorporates both rotational and lateral pile tip spring elements. The results are shown in Figure 3.8. Two configurations of the multi-spring model are plotted: one with $q_{b,res} = 0.1q_{c,r}$ and the other corresponding to the $q_{b,res}$ value that provides the best fit to the site response.

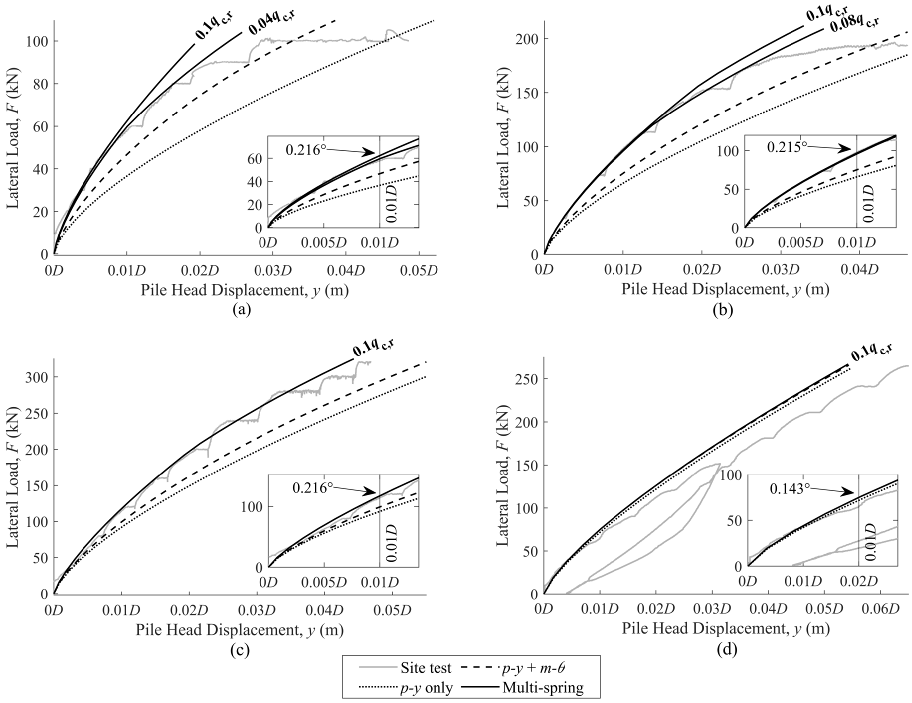

Figure 3.8: Model performance compared to Blessington pile tests (a) LP2, $L/D = 3.0$ (b) LP3, $L/D = 4.5$ (c) LP4, $L/D = 6.0$ (d) UP1, $L/D = 13.0$

The multi-spring model compares well with the site tests for all piles at deflections below $0.01D$ when $q_{b,res} = 0.1q_{c,r}$, which can be improved for larger deflections if an appropriate $q_{b,res}$ value is identified. Notably, the response of different spring model permutations demonstrate that the influence of each spring type diminishes as the slenderness ratio increases. For example, the difference between the deflection estimated in the p-y +m-θ model and the p-y-only model is greater for piles with low L/D ratios, such as piles LP2 and LP3 in Figs. 3.8a and 3.8b, respectively. This is indicative of the contribution of the distributed m-θ springs, and reduces for the more flexible piles such as LP4 and UP1, as shown in Figure 3.8c and 3.8d, respectively. Pile UP1 indicates that, when L/D is high, the additional spring mechanisms become negligible and the multi-spring model collapses to the traditional p-y method. This is suggested in Figure 3.8d, as the difference between the p-y and multi-spring model is minor, and demonstrates that the diameter effects present in low L/D monopiles are captured effectively in the proposed model. It is worth noting that the apparent underestimation of ground line deflections in UP1 could potentially be attributed to the use of a site-averaged CPT profile.

The p-y function proposed by Li et al. (2014) is a power law relationship and is calibrated for piles with $L/D \geq 6.5$, therefore it is not suitable for the prediction of low L/D piles loaded to failure. This is evident in Figs. 3.8a and 3.8b, as the p-y -only model does not capture the yielding behaviour of piles LP2 and LP3. A more appropriate p-y function should be applied if ULS analysis is required. The issue is further exaggerated by the significant creep experienced at large ground line deflections, which is not considered in the proposed model.

When $q_{b,res} = 0.1q_{c,r}$, the multi-spring model offers a satisfactory match to all the pile tests conducted at Blessington for small deflections below $0.01D$, and are within the ground line rotation limit of 0.25°. However, the ground line deflection at higher loads is underestimated for low L/D piles, giving a conservative design estimate. Notably, LP2, LP3, and LP4 require different $q_{b,res}$ values ($0.04q_{c,r}$, $0.08q_{c,r}$, and $0.1q_{c,r}$, respectively) to improve large head deflection estimates. This observation suggests that $q_{b,res}$ increases with the L/D ratio. However, determining precise correlations for parameters localised near the pile tip remains challenging due to the many factors that influence ground line deflections. Furthermore, the utilisation of an average CPT profile across the site limits the ability to directly investigate such correlations. It is also important to address that changing the p-y function will influence the appropriate value of $q_{b,res}$ required for large deflection estimates, suggesting different α values are required for different p-y functions.

Accurate measurements of residual base stresses on open-ended piles in sand are scarce. For instance, Gavin and O'Kelly (2007) found that the residual base stress was linked to the Incremental Filling Ratio (IFR) during driving, pile diameter, and end resistance values. Similarly, Paik et al. (2003) reported a residual base stress of approximately 1.7MPa, or around 6% of the q_c value at the pile tip, for a pile with a diameter of 0.356m and an IFR of 75% at the end of driving. Another study by Gavin and Igoe (2021) measured very low residual stresses during the initial driving stages of a 0.34m diameter pile when the IFR was high. Towards the end of installation, with an IFR value of 40%, a residual base stress of 4MPa was mobilised, approximately 20% of the q_c value at the pile tip. Considering the substantial diameter of offshore monopiles, significant plugging during installation is unlikely. Therefore, it is recommended that residual stresses are conservatively estimated, and designers should exercise caution.

3.4.2 Dunkirk benchmark

The PISA project conducted a series of lateral push-over tests in Dunkirk (France) and Cowden (UK) to assess piles loaded in soil deposits similar to those encountered in offshore environment (Burd et al., 2020b; McAdam et al., 2020; Zdravković et al., 2020a). Twelve open-ended circular steel piles with various L/D ratios ranging from 3 to 8 were investigated. For this study, seven pile tests were selected, and are detailed in Table 3.3.

CPT investigations were conducted at each pile location and the profiles are shown in Figure 3.9a. This enables a meaningful evaluation of the influence of spatial variability on the CPT-based multi-spring model. The water table was found to be at a depth of $z = 5.4$ m below ground level, with bulk unit weights of $\gamma = 17.1$ kNm^{-3} and 19.9 kNm^{-3} above and below the water table, respectively. Figure 3.9b presents the G_0 profile, which was computed using a combination of triaxial tests and seismic CPTs. Additional site-specific information is available in Zdravković et al. (2020a).

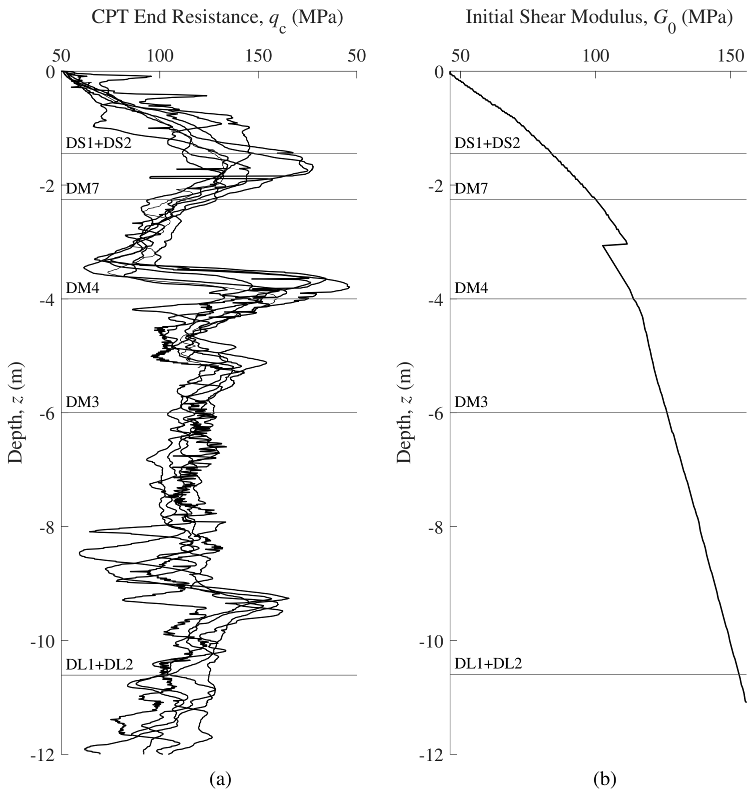

Figure 3.9: (a) q_c profiles and (b) G_0 profile for the Dunkirk site (Zdravković et al., 2020a)

Table 3.3: Monopile geometries at Dunkirk site (McAdam et al., 2020)

Pile name	**Embedment** L (mm)	**Diameter** D (mm)	**Ratio** L/D	**Thickness** t (mm)	**Eccentricity** h (mm)
DM3	6000	762	8.00	25	10000
DM4	4000	762	5.25	14	10000
DM7	2250	762	3.00	10	10000
DS1	1450	273	5.25	7	5000
DS2	1450	273	5.25	7	5000
DL1	10600	2000	5.25	38	9900
DL2	10600	2000	5.25	38	9900

The majority of pile tests were subject to incremental loading at an average rate of 0.91 mm/min. DS2 was loaded continuously at a rate of 325 mm/min to investigate the influence of load rate on pile response. Notably, DS1 and DS2 share the same pile geometry but differ in terms of the load application rate. DS2 is included in Section 3.4.3 to assess the influence of CPT profiles for identical pile geometries. It's worth noting that the proposed multi-spring model remains independent of load rate, which adds interest to evaluating the extent to which CPT variations influence pile response. Finally, DL1 and DL2 are included in this analysis for the same reason, and are included in Section 3.4.3. Figure 3.10 shows the results.

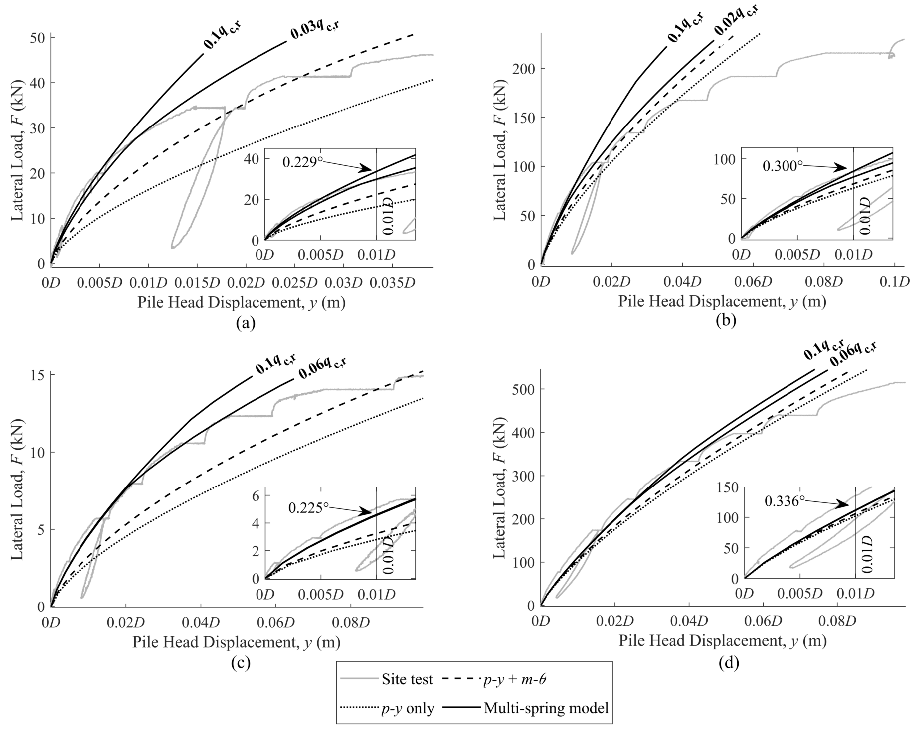

Figure 3.10: Model performance compared to Dunkirk pile tests (a) DM7, $L/D = 3.0$ (b) DM4, $L/D = 5.25$ (c) DS1, $L/D = 5.25$ (d) DM3, $L/D = 8.0$

Similar to the Blessington site tests, the multi-spring model compares well with the site tests for all piles at deflections below $0.01D$ when $q_{b,res} = 0.1q_{c,r}$. Figure 3.10a and 3.10c suggest that piles DM7 and DS1 exhibit an improvement in estimating the response when additional spring components are included, and an appropriate $q_{b,res}$ value can be identified to improve medium to large-strain deflections. Furthermore, these piles demonstrate that low L/D piles benefit from low α values to improve estimates for large displacements, which is a similar trend that was observed in the Blessington site tests.

Figure 3.10d and 3.10b show that all spring model permutations exhibit a superficially stiff response in comparison to the DM3 and DM4 site tests. Notably, the estimated ground line deflections do not improve when more spring elements are added. This suggests that the issue is not entirely related to the additional resistance mechanisms proposed in this study. Figure 3.9a shows that piles DM3 and DM4 are subject to excessive variability in q_c along the depth of the pile. In contrast, other pile tests, including those from the Blessington site, have either partially constant or linearly increasing CPT end resistance profiles. To add, DS1 and DM4 both have a slenderness ratio of 5.25. Aside from differences in scale between the two pile geometries, a key distinction between DS1 and DM4 lies in the variability of the q_c inputs, as shown in Figure 3.9. This suggests that high variations in q_c can lead to artificially large stiffness in p-y-only models. The q_c

discretisation method proposed may not adequately account for the horizontal shear load transfer between sand layers and localised failures at regions carrying locally elevated loads. This may be a limitation with CPT-based p-y models in general.

According to Figure 3.10c, pile DS1 exhibits a significant contribution from the base spring components, as the difference between the deflections estimated from the multi-spring model ($q_{b,res} = 0.1q_{c,r}$) and the p-y $+m$-θ model is large. This may be a consequence of the linearly-increasing CPT profile evident in Figure 3.9, which ultimately causes a high stiffness in the base springs relative to the other reaction elements.

The initial deflections are captured reasonably well regardless of the issues associated with high CPT variation and uncertainty associated around $q_{b,res}$. It can be concluded that the CPT-based multi-spring model works best for relatively uniform CPT end resistance profiles, as a high degree of spatial variability leads to superficially stiff springs.

3.4.3 Sensitivity to CPT profiles

DS1, DS2, DL1 and DL2 offer an opportunity to investigate the influence of CPT profile variations for identical pile geometries. For the following analysis, $q_{b,res} = 0.1q_{c,r}$ is taken for piles DL1 and DL2, and $q_{b,res} = 0.06q_{c,r}$ for piles DS1 and DS2, as suggested by Figure 3.10c.

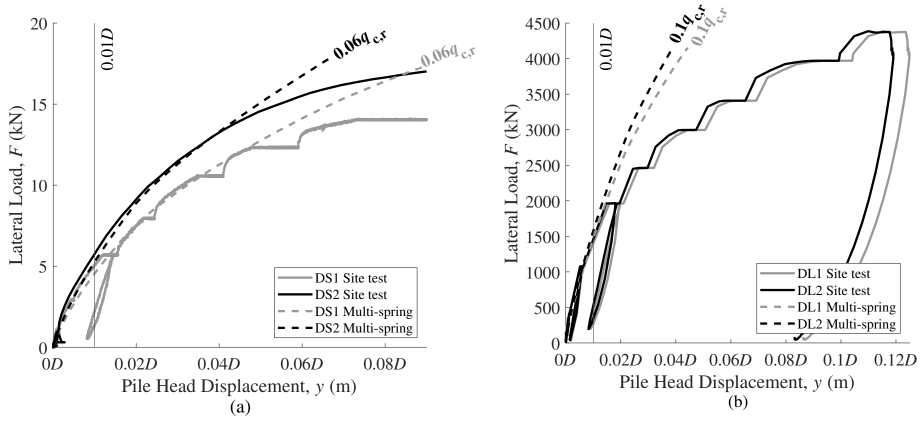

Figure 3.11: Multi-spring model performance against pile tests DS1 and DS2 (b) Multi-spring model performance against pile tests DL1 and DL2

As DS1 and DS2 were loaded at different rates (0.91 mm/min and 325 mm/min, respectively), it was originally concluded that the apparent stiffness difference between DS1 and DS2 can be attributed to the isotach behaviour of soil (McAdam et al., 2020). However, in Figure 3.11a, it is observed that the multi-spring model provides reasonable ground line deflection estimates for both DS1 and DS2. More importantly, the model captures the apparent increase in stiffness in DS2. This suggests that the difference in load rate alone does not account for the observed change in resistance between piles DS1 and DS2. The multi-spring model is independent of load rate, which implies that these differences may be attributed, at least in part, to the local variations present in each CPT profile.

Figure 3.11b shows that the multi-spring model underestimates ground line deflections beyond $0.01D$ and does not adequately capture the response of both DL1 and DL2. Again, this is likely due to substantial depth variations in the CPT profiles demonstrated in Figure 3.9, leading to a superficially high stiffness in the model. Moreover, it is possible that the embedded depth of the pile tests may influence the model response. For example, the lateral bearing stresses experienced along DS1 and DS2 are expected to be relatively low due to shallow embedment depth of 1450 mm. In contrast, DL1 and DL2 are embedded at a depth of 10600 mm, which would lead to larger lateral bearing stresses and potentially a reduced influence on CPT end resistance fluctuations. This is a limitation with the proposed model, as it does not account for the influence of pile embedment depth on the model response. Regardless, the model performs reasonably well for displacements below $0.01D$, and captures the relative difference between the deflections of DL1 and DL2.

3.4.4 Spring Contributions

The contributions of each type of spring element to the total lateral resistance are shown in Figure 3.12 for the Dunkirk site tests and the varying contribution for different L/D ratios is demonstrated. The Moment Contribution Ratio (MCR) is defined as the ratio of the moment resistance provided by each spring type (M_{int}) to the total external moment applied ($M_{ext} = F_{ext}h$). M_{int} is calculated as force multiplied by the eccentricity of the spring element from the rotation point. The rotation point is calculated as the point at which the lateral displacement of the pile is zero, and linear interpolation is used to estimate the rotation point between the two closest nodes.

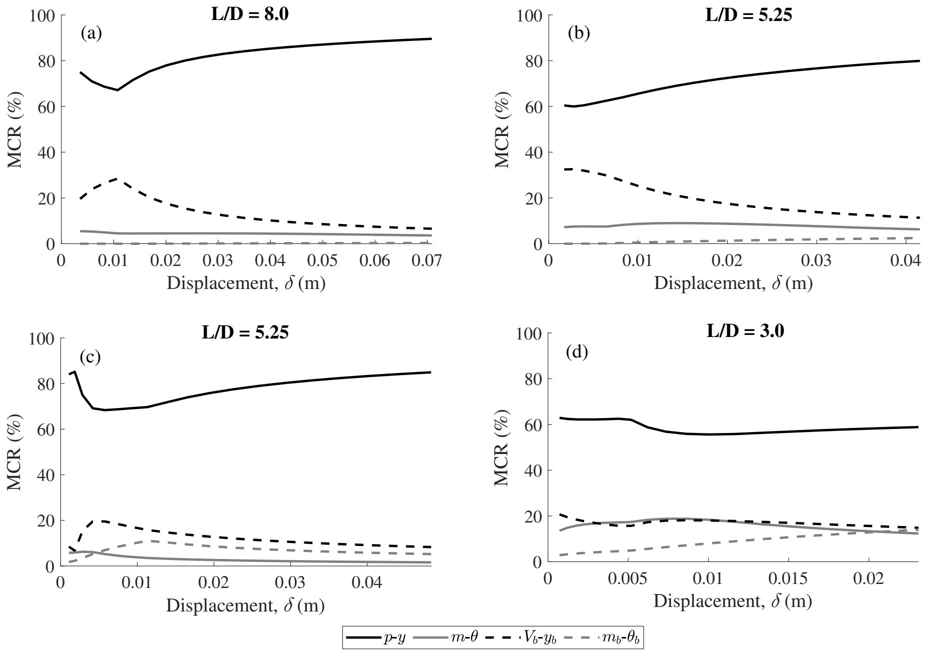

Figure 3.12: Spring contributions for Dunkirk site tests (a) DM3, L/D= 8.0; (b) DM4, L/D= 5.25; (c) DS1, L/D= 5.25; (d) DM7, L/D= 3.0

Figure 3.12a shows that the pile with the highest L/D ratio, DM3, has the highest contribution percentage of approximately 90% from the p-y springs, which is expected as the pile is more flexible and the resistance is dominated by the lateral soil pressure p. Notably, at initial pile head displacements, the V_b-y_b springs contribute approximately 30% of moment resistance, and plateaus towards $\sim$ 10% as displacement increases. The sudden redistribution of stresses is indicative of the bilinear V_b-y_b relationship described in Section 3.3.4. When the horizontal displacement of the pile base exceeds $y_{b,f}$ (Equation 3.11), the secant stiffness of the V_b-y_b spring begins to reduce and the contributing resistances from the p-y springs increases as a consequence. DM3 shows that the contribution from the M_b-θ_b spring is negligible, which is indicative of zero rotation at the pile tip. This is expected from flexible pile behaviour.

In general, the percentage contribution from the lateral springs reduces as the L/D ratio reduces. Figure 3.12d illustrates that when $L/D = 3$, the lateral springs contribute to $\sim$60% and the additional springs contribute to $\sim$40% of the total moment resistance. Two pile tests for $L/D = 5.25$ are shown in Figure 3.12b and 3.12c (DM4 and DS1, respectively). Both plots demonstrate similar contributions from the lateral springs; however, the contributions from the additional spring mechanisms vary. This variance indicates the influence of CPT profiles on the model response. Therefore, the analysis may not be exhaustive, as it does not fully account for the nuanced behaviour associated with the variability between the CPT profiles in the Moment Contribution Ratio (MCR) calculations. However, despite these limitations, the presented analysis provides valuable insights into the behaviour of the structural system under consideration, and is in agreement with similar analyses conducted in the literature (Murphy et al., 2018).

3.5 Conclusions

A one-dimensional CPT-based multi-spring Winkler model has been developed, where each soil element is informed using discretised q_c data. The traditional p-y method is modified by incorporating additional spring mechanisms that encapsulate the expected resistances induced by diameter effects in low L/D monopiles. CPT-based axial capacity methods are repurposed to approximate distributed moment-resistances along the monopile, which arise from the rotation of large-diameter sections. Pile tip resistances are estimated by decoupling the expected base moment and horizontal shear mechanisms and utilising a rotational and lateral bilinear spring positioned at the pile base. The capacity of each base spring is informed by averaging q_c values $0.25L/D$ above and below the pile tip to estimate the post-installation residual bearing stress, $q_{b,res}$. The following conclusions are made:

1. The proposed model captures initial ground line deflections below $0.01D$ well when $q_{b,res} = 0.1q_{c,r}$, which is in agreement with SLS design criteria. It is not suitable for analysing large strains or predicting ultimate failure loads.

2. Determining an appropriate value for residual bearing stress ($q_{b,res}$) is challenging, and a conservative estimate of $q_{b,res} = 0.1q_{c,r}$ is recommended.

3. The m-θ, V_b-y_b, and M_b-θ_b springs successfully encapsulate diameter effects for low L/D monopiles, and become negligible as the slenderness ratio increases.

4. The model works well for CPT profiles that are uniform or linearly increasing with depth, such as those measured in the Blessington site.

5. Minor variations in CPT profiles are captured by the model. However, a high degree of spatial variability leads to a superficially stiff response.

6. A more appropriate p-y function is required to capture the ultimate capacity of the pile.

It is difficult to establish a $q_{b,res}$ for lateral pile analysis using ground lines deflection estimates, as there are many overlapping factors that influence the ground line response of a laterally loaded pile. Additionally, the underlying assumptions of uncoupled springs may not be suitable for CPT profiles of high variability, as the horizontal shearing between laterally loaded soil layers is not captured. This may be significant for neighbouring soil horizons with large differences in q_c. It is postulated that utilising site-average q_c profiles may be more appropriate than CPT profiles local to the pile, as the model performed better in general for Blessington tests compared to Dunkirk tests. Averaging may reduce the degree of fluctuation within the input data and improve the model's performance. However, more data from site tests is required to support this claim.

The proposed model is a step towards a more comprehensive CPT-based model for laterally loaded monopiles. However, further work is required to improve the estimated ultimate capacity of the pile. This may be achieved by defining a more suitable p-y relationship that is a function of horizontal effective stress. This was not within the scope of this investigation, however the multi-spring model offers a modular framework to replace the current definition, should a more appropriate CPT-based p-y definition be proposed. To add, some underlying assumptions will require further modification. For example, the m-θ soil element assumes no gapping at large pile deflections and vertical interface shear stresses remain symmetrical about the central axis of the pile section. This can be improved by coupling the m-θ element with the p-y element, as the confining stress imposed by the lateral soil pressure p will have an influence on the amount of vertical shear experienced. These are topics of interest for future research.

Chapter 4

Dynamic p-y model: development and analysis

This chapter describes the development of a dynamic nonlinear model that facilitates irregular load sequences that can be expected in offshore environments. OWTs are dynamically sensitive structures, therefore it is imperative that energy dissipation is adequately modelled. The model is developed using time-domain approaches, which involves solving for the dynamic equilibrium of the system at each step in time. To achieve this, Time Marching Algorithms (TMA) are employed. These algorithms are capable of facilitating nonlinear Multi-Degree of Freedom (MDOF) models, and therefore can be used to estimate the response of the dynamic soil-structure interaction of an embedded pile. Hysteresis algorithms are used to establish distinct stress paths for discrete layers as nonlinear springs.

As discussed in Section 2.3, a time-domain analysis of an OWT-monopile system is essential for capturing its dynamic response. This is because the system is subject to irregular load sequences, therefore load histories should be randomly generated from wind and wave frequency spectra of various sea states and wind speeds to form realistic simulations of anticipated environmental excitations. The guidelines provided by IEC (2009) suggest that the dynamic response of the system is evaluated for a range of sea states and wind speeds to ensure that the structure is safe and reliable, each with a unique frequency spectrum. To add, it is common practice to generate numerous wind and wave load profiles from the same spectrum, to explore all potential load scenarios in OWT design simulations. This compounds the multitude of potential simulations required for a comprehensive analysis of the dynamic response of the OWT, therefore a full design for a single OWT-monopile configuration can take many hours. It is therefore essential that the dynamic model is computationally efficient to facilitate the large number of simulations required, especially when considering the nonlinear soil-structure interaction.

This chapter will emphasise the importance of time-domain analysis, the efficacy of various hysteresis reaction models, and the sensitivity of numerical integration methods for both linear and nonlinear systems. Achieving this requires appropriate modifications to the hysteresis algorithms, including considerations for gapping, liquefaction, and ratcheting. Consequently, the model serves the purpose of a digital twin, enhancing structural safety and reliability through data-driven decision-making.

It is important to note that this chapter does not intend to evaluate the performance of specific hysteresis modifications. The primary aim is to create a robust and efficient dynamic nonlinear MDOF model that enables the exploration of such effects. Figure 4.1 illustrates the modified *p*-*y* model from Chapter 3 for dynamic analysis. Each spring is defined with a distinct hysteretic *p*-*y* relationship representing the dynamic nonlinear properties of the corresponding soil layer.

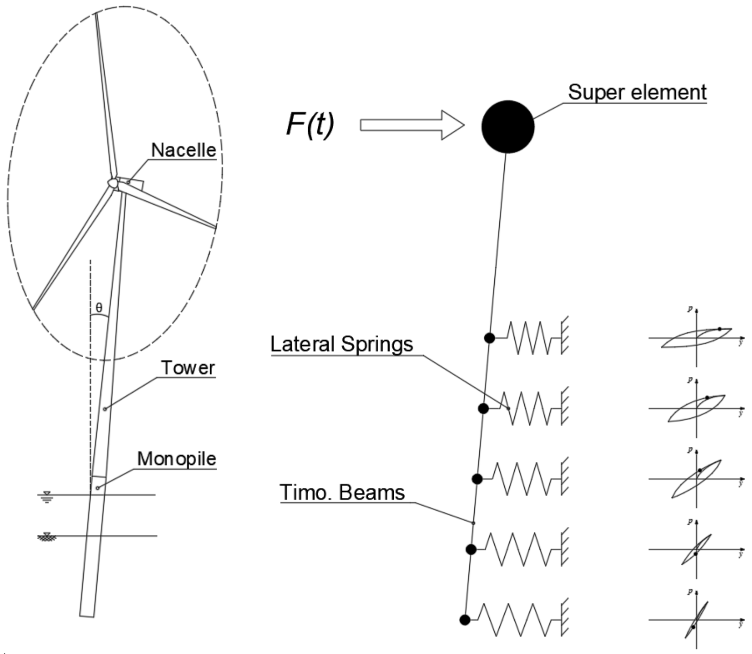

(a) OWT-monopile structure

(b) Nonlinear hysteresis model

Figure 4.1: MDOF dynamic nonlinear model of an OWT-monopile structure

The spring stiffness is defined as the tangent modulus rather than the secant type in static *p*-*y* models, as shown in Figure 2.2b (Chopra, 2013). The mass matrix is informed using a consistent-mass technique (Tedesco, 1999), which is detailed in Appendix A. $F(t)$ is the load history applied that encompasses external environmental excitations (Figure 2.17). The super element in Figure 4.1b is a simplified structural reduction methodology used to describe the superstructure with a point mass and cantilever, such that the dynamic properties are unchanged (Branlard et al., 2020). The study of super elements is not within the scope of this thesis and is therefore omitted in the analyses herein, but is a common approach to reducing the complexity and computational spend of high MDOF structures without compromising accuracy.

TMAs will be reviewed using a Single Degree of Freedom (SDOF) oscillating linear mass-spring system. This is to establish a confidence in the simplistic case of the algorithms before extending to a MDOF system. The model illustrated in Figure 4.1b can be sensitive to both the TMA and the hysteresis representation (Kontoe et al., 2008). It is important that the model converges to the true solution and achieves stability (Wood, 1990). Therefore, this chapter will:

1. Investigate the stability and accuracy of TMAs in simple SDOF linear systems, therefore identifying the most appropriate method for the dynamic *p*-*y* model.

2. Investigate the robustness of alternative hysteresis models in a controlled simulation, and identify the most appropriate model for the dynamic *p*-*y* model.

3. Review the performance of the dynamic *p*-*y* model by applying realistic wind and wave load histories to an integrated OWT superstructure appended to the dynamic *p*-*y* foundation model.

4.1 Time marching algorithms

Figure 4.2 shows the SDOF model of an oscillating mass on a nonlinear spring with linear viscous dashpot. The three internal forces are illustrated in 4.2b. Note that k is a function of x, indicating a nonlinear system.

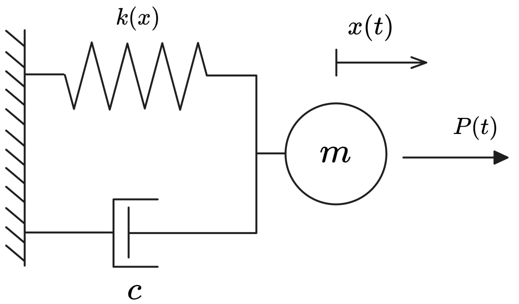

(a) SDOF mass on nonlinear spring and viscous dashpot

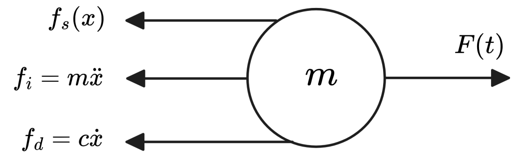

(b) Free body diagram of particle, where f_s, f_d and f_i are the spring, damping and inertial forces respectively

Figure 4.2: Illustration of the SDOF system and the forces applied to a dynamic particle

The equation of motion for a driven oscillator with mass m and spring force f_s (Figure 4.2) can be described by Equation 4.1.

$$F(t) = m\ddot{x}(t) + c\dot{x}(t) + f_s(x) \tag{4.1}$$

where $F(t)$ is the externally applied load history, $\ddot{x}$ is the object's acceleration, $\dot{x}$ is the object's velocity, x is the object's displacement and $f_s(x)$ is the nonlinear spring force. c is the viscous damping coefficient that encapsulates the energy dissipation other than material damping. Material damping is captured using nonlinear restoring force of the spring $f_s(x)$, as discussed in Section 2.3.3. Closed form solutions of $x(t)$ exist for harmonically driven damped oscillators with one degree of freedom and elastic properties (Bathe & Wilson, 1976; Chopra, 2013; Tedesco, 1999). However, it is difficult to define analytical solutions for irregular force-time histories, and even more so for MDOF nonlinear systems (Kovacic & Brennan, 2011).

According to D'Alembert's principle, the equation of motion can be solved for using the concept of dynamic equilibrium (Chopra, 2013). At any point in time, a fictitious inertial force acting in the direction opposing the acceleration can be established to balance the system's applied forces and ensure equilibrium. Thus, at any instance in time, a free body diagram can be derived and the principles of static equilibrium can be directly applied (Figure 4.2b). This is the primary concept of TMAs when solving Equation 4.1, which can estimate the solution $x(t)$ to the second order differential equation (Equation 4.1) using numerical integration methods.

TMA approximate the solution of the equation of motion with a set of algebraic equations which are evaluated in a step-by-step manner. The continuous form of the equation of motion is therefore discretised into time steps at Δt intervals, whereby dynamic equilibrium is solved for to compute the system's kinematics (x, $\dot{x}$ and $\ddot{x}$) at each step in time. The variation of the kinematic forces are therefore assumed within the time step, which depend on the type of numerical integration method used. Many numerical integration methods exist in literature (Bathe & Wilson, 1976; Hilber & Hughes, 1978; Newmark, 1959; Wilson et al., 1972), which impose different kinematic assumptions within Δt. This can have a significant impact on the accuracy and stability of the simulation, as equilibrium is assumed to only be achieved at Δt intervals.

The following section will review the most common TMAs for linear SDOF systems ($f_s(x) = kx$), and will discuss their relative merits based on accuracy, stability, efficiency and dissipative qualities. Both explicit and implicit TMA methods are explored, where the former is typically less accurate but more efficient, and the latter is accurate but computationally expensive. If i is the time step count, explicit methods estimate the kinematics at t_{i+1} based on the current kinematics at t_i, which can be a source of instability if Δt is large relative to the natural period T_n of the system. Implicit methods solve for the response at t_{i+1} by implying equilibrium at t_{i+1}. This is favourable for linear systems, as the restoring force is easily computed at t_{i+1} ($f_s(x) = k(x_{i+1} - x_i)$). However, nonlinear restoring forces ($f_s = f(x)$) require further iteration within time steps to achieve equilibrium, or sufficiently small time steps to mitigate the error.

Most TMAs enable parametric modifications to control stability and algorithmic dissipation. This enables certain higher frequency modes in the estimated displacement signal to be filtered out during the simulation, and is particularly useful for nonlinear systems. The restoring force in hysteretic systems can be highly dependent on the displacement history at large strains, therefore erroneous oscillations should be mitigated. The derivation of TMAs and the importance of their respective parameters are detailed herein.

4.1.1 Central difference method

The Central Difference Method (CDM) is based on the finite difference approximation of the kinematic derivatives outlined in Equation 4.2, where derivative of any function $f(x)$ can be approximated. If h is the generalised discrete step size, then:

$$f'(x) \simeq \frac{f(x+h) - f(x-h)}{2h} \tag{4.2}$$

The first and second derivatives of displacement ($\dot{x}$ and $\ddot{x}$, respectively) can therefore be estimated using the same principles, and are illustrated in Figure 4.3 and described in Equations 4.3 to 4.5.

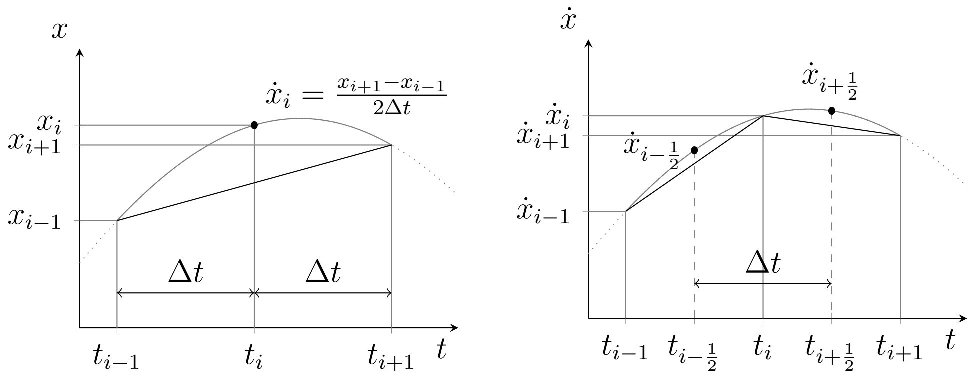

(a) Estimation for $\dot{x}$ at time t_i

(b) CDM for $\ddot{x}$

Figure 4.3: Assumptions of the Central Difference Method for estimating $\dot{x}$ and $\ddot{x}$

$$\dot{x}_i = \frac{x_{i+1} - x_{i-1}}{2\Delta t} \tag{4.3}$$

In order to compute $\ddot{x}_i$, the velocity at times $t_{i-\frac{1}{2}} = t_i - \frac{1}{2}\Delta t$ and $t_{i+\frac{1}{2}} = t_i + \frac{1}{2}\Delta t$ are required. These can be estimated using Equation 4.3 at $t_{i-\frac{1}{2}}$ and $t_{i+\frac{1}{2}}$ respectively, as illustrated in Figure 4.3b.

$$\dot{x}_{i-\frac{1}{2}} = \frac{x_i - x_{i-1}}{\Delta t} \quad \dot{x}_{i+\frac{1}{2}} = \frac{x_{i+1} - x_i}{\Delta t} \tag{4.4}$$

Equation 4.2 is then applied to find $\ddot{x}_i$ using $\dot{x}_{i-\frac{1}{2}}$ and $\dot{x}_{i+\frac{1}{2}}$.

$$\begin{aligned}
\ddot{x}_i &= \frac{\dot{x}_{i+\frac{1}{2}} - \dot{x}_{i-\frac{1}{2}}}{\Delta t} \\
\ddot{x}_i &= \frac{\dfrac{x_{i+1} - x_i}{\Delta t} - \dfrac{x_i - x_{i-1}}{\Delta t}}{\Delta t} \\
\ddot{x}_i &= \frac{x_{i+1} - 2x_i + x_{i-1}}{\Delta t^2}
\end{aligned} \tag{4.5}$$

Equations 4.3 and 4.5 can be substituted directly into the equation of motion at $t = t_i$ (Equation 4.1) and refactored to give a more convenient form to determine the displacement at the next time step x_{i+1}.

$$x_{i+1} = \frac{\hat{F}_i}{\hat{k}} \tag{4.6}$$

where

$$\hat{k} = \frac{m}{\Delta t^2} + \frac{c}{2\Delta t} \tag{4.7}$$

and

$$\hat{F}_i = F_i - \left[\frac{m}{\Delta t^2} - \frac{c}{2\Delta t}\right] x_{i-1} - \left[k - \frac{2m}{\Delta t^2}\right] x_i \tag{4.8}$$

where $\hat{k}$ is the effective stiffness and $\hat{F}_i$ is the effective force. Both terms include the dynamic properties of the system, but simplify the approximation of x_{i+1} to resemble a static problem. $\hat{k}$ and $\hat{F}_i$ do not require the kinematic properties at time t_{i+1}, therefore this method is explicit.

According to Equation 4.8, $x_{i-1} = x(t-\Delta t)$ is required to compute the effective force $\hat{F}_i$. This is problematic, as the conditions of the system at $t = 0 - \Delta t$ are typically unknown. The CDM is therefore not self-starting without appropriate estimations at $t = -\Delta t$, which was one of the fundamental characteristics required for a successful TMA according to Hilber and Hughes (1978).

4.1.2 Newmark-β Method

The Newmark-β methodology uses a Taylor series expansion, where $\dot{x}_{i+1}$ and $\ddot{x}_{i+1}$ are estimated using polynomials to calculate x_{i+1} and $\dot{x}_{i+1}$ at $t = t_i$, respectively (Newmark, 1959).

$$x_{i+1} = x_i + \dot{x}_i \Delta t + \frac{1}{2}\ddot{x}_i \Delta t^2 + \frac{1}{6}\dddot{x}_i \Delta t^3 + ... + \mathcal{O}(\Delta t^4) \tag{4.9}$$

$$\dot{x}_{i+1} = \dot{x}_i + \ddot{x}_i \Delta t + \frac{1}{2}\dddot{x}_i \Delta t^2 + ... + \mathcal{O}(\Delta t^3) \tag{4.10}$$

where $\dddot{x}(t_i)$ is the first derivative of acceleration with respect to time and $\mathcal{O}(\Delta t^4)$ and $\mathcal{O}(\Delta t^3)$ are the truncation errors due to the infinite series. Newmark (1959) proposed that the Mean Value Theorem can be applied to approximate $\dddot{x}(t_i)$, i.e.:

$$x_{i+1} = x_i + \dot{x}_i \Delta t + \frac{1}{2}\ddot{x}_i \Delta t^2 + \beta \dddot{x}_i \Delta t^3 \tag{4.11}$$

$$\dot{x}_{i+1} = \dot{x}_i + \ddot{x}_i \Delta t + \gamma \dddot{x}_i \Delta t^2 \tag{4.12}$$

where $\beta \in [0, 1]$ and $\gamma \in [0, 1]$ such that Equations 4.11 and 4.12 are true. These parameters enable control of the stability, accuracy and dissipative properties of the algorithm and encapsulate the truncation error of the Taylor series expansion. Eliminating the $\dddot{x}_i$ term gives:

$$x_{i+1} = x_i + \Delta t \dot{x}_i + \left(\frac{1}{2} - \beta\right) \Delta t^2 \ddot{x}_i + \beta \Delta t^2 \ddot{x}_{i+1} \tag{4.13}$$

$$\dot{x}_{i+1} = \dot{x}_i + (1 - \gamma) \Delta t \ddot{x}_i + \gamma \Delta t \ddot{x}_{i+1} \tag{4.14}$$

which define the general governing kinematic equations for the Newmark-β algorithm. Similar to the derivation of the CDM equations, the effective equilibrium equation $\hat{F}_{i+1} = \hat{k} x_{i+1}$ can be determined by rearranging Equation 4.13 for $\ddot{x}_{i+1}$, substituting into Equation 4.14 then substituting both definitions of $\dot{x}_{i+1}$ and $\ddot{x}_{i+1}$ into the equation of motion at time $t = t_{i+1}$ (Equation 4.1). The effective force and stiffness is therefore:

$$\begin{aligned}\hat{F}_{i+1} = F_{i+1} &+ \left[\frac{1}{\beta\Delta t^2}m + \frac{\gamma}{\beta\Delta t}c\right]x_i \\ &+ \left[\frac{1}{\beta\Delta t}m + \left(\frac{\gamma}{\beta} - 1\right)c\right]\dot{x}_i \\ &+ \left[\left(\frac{1}{2\beta} - 1\right)m + \Delta t\left(\frac{\gamma}{2\beta} - 1\right)c\right]\ddot{x}_i\end{aligned} \tag{4.15}$$

and

$$\hat{k} = k + \frac{\gamma}{\beta\Delta t}c + \frac{1}{\beta\Delta t^2}m \tag{4.16}$$

Note that $\hat{k}$ in Equation 4.16 requires the stiffness of the system k. Solving $\hat{F}_{i+1} = \hat{k}x_{i+1}$ is trivial for SDOF systems. However, for nonlinear MDOF systems (where k updates at each time step), a stiffness matrix inversion is required and can be computationally expensive. This is a major advantage of the CDM, as undamped MDOF systems with a lumped mass configuration can be solved for without the need for stiffness matrix inversion, as shown in Equations 4.6 and 4.7.

β and γ capture underlying assumptions in the Newmark-β theory, which by extension controls different qualities of the algorithm. Furthermore, depending on the selection of β and γ, the method can be either implicit or explicit. According to Newmark (1959), the method is explicit if $0 \leq \beta < \frac{1}{4}$, with varying stability and accuracy characteristics. When $\beta \geq \frac{1}{4}$, the system is implicit.

γ controls the stability conditions of the system, and unconditional stability is guaranteed if $\gamma \geq \frac{1}{2}$ and $\beta \geq 0.25(0.5+\gamma)^2$. Unconditional stability is a favourable property of TMAs, as there is no prerequisite for Δt in order to ensure an estimated solution that does not grow without bound. This is discussed in more detail in Section 4.1.5. If the Newmark-β algorithm is conditionally stable, the maximum time step for stability (Δt_{cr}) is given by:

$$\Delta t_{cr} = \frac{1}{\pi\sqrt{2}}\frac{1}{\pi\sqrt{\gamma - 2\beta}}T_n \tag{4.17}$$

It is also possible to exhibit dissipative behaviour for higher modes, which can be achieved if $2\beta \geq \gamma > \frac{1}{2}$ (Hughes, 2000; Kontoe et al., 2008). Common derivations for β and γ are derived herein.

Constant Average Acceleration

The Constant Average Acceleration (CAA) method assumes that the acceleration within the time step is constant and computed as the average of $\ddot{x}_i$ and $\ddot{x}_{i+1}$. This is shown in Figure 4.4, where τ denotes the variation of time within a time step. The assumption is defined in Equation 4.18.

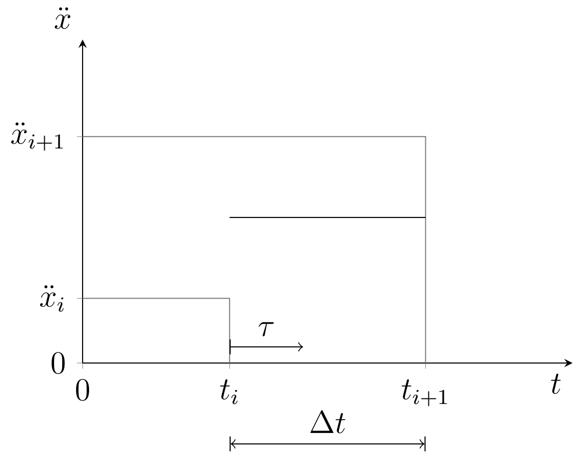

Figure 4.4: Variation of acceleration within a time step for the CAA method

$$\ddot{x}(\tau) = \frac{1}{2}(\ddot{x}_{i+1} + \ddot{x}_i) \tag{4.18}$$

where $\dfrac{d\ddot{x}}{d\tau} = \dddot{x}(\tau) = 0$. Therefore, substituting Equation 4.18 and $\dddot{x}(\tau) = 0$ into Equation 4.9 and 4.10 for $\tau = \Delta t$ gives the following expressions:

$$x_{i+1} = x_i + \Delta t \dot{x}_i + \frac{1}{4}\Delta t^2 \ddot{x}_i + \frac{1}{4}\Delta t^2 \ddot{x}_{i+1} \tag{4.19}$$

$$\dot{x}_{i+1} = \dot{x}_i + \frac{1}{2}\Delta t \ddot{x}_i + \frac{1}{2}\Delta t \ddot{x}_{i+1} \tag{4.20}$$

Comparing Equation 4.19 with Equation 4.13 and Equation 4.20 with Equation 4.14 shows that the CAA method is equivalent to the general Newmark equations when $\gamma = \frac{1}{2}$ and $\beta = \frac{1}{4}$. The CAA method is therefore implicit, as $\beta \geq \frac{1}{4}$. Dahlquist (1963) demonstrated that the CAA method is the most accurate unconditionally stable implicit scheme.

Linear Acceleration

The Linear Acceleration (LA) method assumes that the acceleration within the time step is varies linearly between $\ddot{x}_i$ and $\ddot{x}_{i+1}$. This is shown in Figure 4.5, where τ denotes the variation of time within a time step. Equation 4.21 defines the assumption.

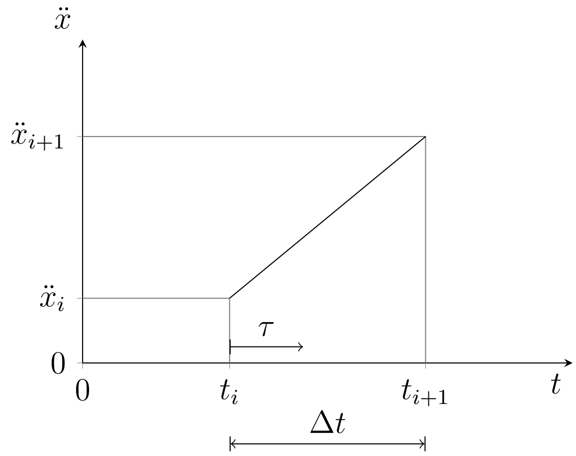

Figure 4.5: Variation of acceleration within a time step for the Linear Acceleration method

$$\ddot{x}(\tau) = \ddot{x}_i + \frac{\tau}{\Delta t}(\ddot{x}_{i+1} - \ddot{x}_i) \tag{4.21}$$

where $\frac{d\ddot{x}}{d\tau} = \dddot{x}(\tau) = \frac{\ddot{x}_{i+1} - \ddot{x}_i}{\Delta t}$. Again, substituting Equation 4.21 and $\dddot{x}(\Delta t)$ into Equation 4.9 and 4.10 gives the following expressions:

$$x_{i+1} = x_i + \Delta t\dot{x}_i + \frac{1}{3}\Delta t^2\ddot{x}_i + \frac{1}{6}\Delta t^2\ddot{x}_{i+1} \tag{4.22}$$

$$\dot{x}_{i+1} = \dot{x}_i + \frac{1}{2}\Delta t\ddot{x}_i + \frac{1}{2}\Delta t\ddot{x}_{i+1} \tag{4.23}$$

Comparing Equation 4.22 with Equation 4.13 and Equation 4.23 with Equation 4.14 shows that the LA method is equivalent to the general Newmark equations when $\gamma = \frac{1}{2}$ and $\beta = \frac{1}{6}$. As $\beta < \frac{1}{4}$, the LA method is explicit and conditionally stable.

Other variations of Newmark-β

Argyris and Mlejnek (1991) showed that, if $\beta = 0$ and $\gamma = \frac{1}{2}$, then Equations 4.13 and 4.14 can be rearranged to form the CDM method equations in Equations 4.3 and 4.5, if equilibrium is solved for at $t = t_i$. In this light, it is shown again that the CDM meets the conditions for an explicit algorithm but is conditionally stable (since $\beta < \frac{1}{4}$ and $\beta < 0.25(0.5{+}\gamma)^2$). Equation 4.17 demonstrates a stability condition of $\frac{1}{\pi}\Delta t$. The β and γ parameters clearly have a strong influence on the underlying assumptions made when estimating how the kinematics vary within a time step, including the stability of the algorithm (Dahlquist, 1963). Fung (2003) demonstrated that many more permutations of β and γ are possible that exhibit dissipative properties with unconditional stability. The family of common Newmark-β algorithms and their stability conditions are summarised in Table 4.1.

Table 4.1: Summary of Newmark-type algorithms and their stability conditions

Algorithm	β	γ	**Stability Condition**
Central Difference Method (CDM)	0	$\frac{1}{2}$	$\Delta t_{cr} = \frac{1}{\pi} T_n$ (conditional)
Linear Acc. (LA)	$\frac{1}{6}$	$\frac{1}{2}$	$\Delta t_{cr} = 0.551 T_n$ (conditional)
Constant Average Acc. (CAA)	$\frac{1}{4}$	$\frac{1}{2}$	$\Delta t_{cr} = \infty$ (unconditional)

4.1.3 Wilson-θ Method

The Wilson θ method assumes that the acceleration is linear during the time interval t_i to $t_i + \theta\Delta t$ (where $\theta \geq 1$), as shown in Figure 4.6. When $\theta \geq 1$, equilibrium is solved for after $t = t_{i+1}$, which causes dissipative behaviour in the approximated solution for certain frequencies (Wilson et al., 1972). Equation 4.24 describes how acceleration varies over the time step.

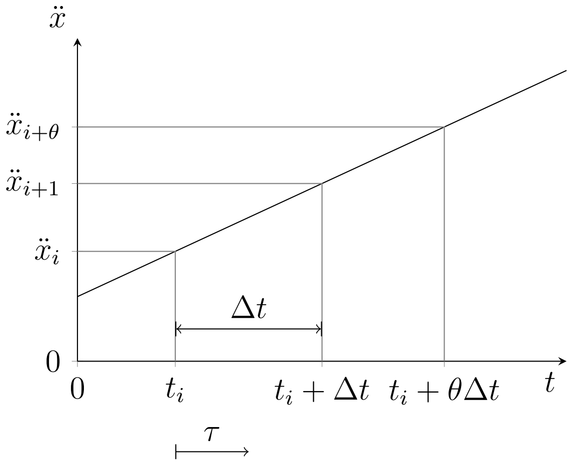

Figure 4.6: Wilson θ method acceleration assumption

$$\ddot{x}(\tau) = \ddot{x}_i + \frac{\tau}{\theta\Delta t}(\ddot{x}_{i+\theta} - \ddot{x}_i) \tag{4.24}$$

where τ is the time variable within the time step, and $\dot{x}_{i+\theta} = \ddot{x}(t_i + \theta\Delta t)$. The θ parameter controls the stability and accuracy of the algorithm. When $\theta = 1$, Equation 4.24 collapses to Equation 4.21 and takes the form of the Newmark-β LA method. Integrating Equation 4.24 twice and letting $\tau = \theta\Delta t$, the displacement and velocity can be calculated as follows:

$$x_{i+\theta} = x_i + \theta\Delta t\dot{x}_i + \frac{\theta^2\Delta t^2}{6}(\ddot{x}_{i+\theta} + 2\ddot{x}_i) \tag{4.25}$$

$$\dot{x}_{i+\theta} = \dot{x}_i + \frac{\theta\Delta t}{2}(\ddot{x}_{i+\theta} + \ddot{x}_i) \tag{4.26}$$

where $\dot{x}_{i+\theta} = x(t + \theta\Delta t)$ and $\ddot{x}_{i+\theta} = \ddot{x}(t + \theta\Delta t)$. The equation of motion is satisfied at $t = t_i + \theta\Delta t$. However, since a linear projection of acceleration is assumed (Figure 4.6), then a linearly projected force vector is also required to satisfy equilibrium (Tedesco, 1999). The equation of motion becomes:

$$m\ddot{x}_{i+\theta} + c\dot{x}_{i+\theta} + kx_{i+\theta} = F_i + \theta(F_{i+\theta} - F_i) \tag{4.27}$$

Equations 4.25 and 4.26 can be substituted into Equation 4.27 to obtain the effective stiffness and effective force, which are as follows:

$$\hat{k} = k + \frac{6}{\theta^2\Delta t^2}m + \frac{3}{\theta\Delta t}c \tag{4.28}$$

$$\begin{aligned} \hat{F}_{i+\theta} &= F_i + \theta(F_{i+\theta} - F_i) \\ &+ \left[\frac{6}{\theta^2\Delta t^2}m + \frac{3}{\theta\Delta t}c\right]x_i \\ &+ \left[\frac{12}{\theta^2\Delta t^2}m + 2c\right]\dot{x}_i \\ &+ \left[2m + \frac{\theta\Delta t}{2}c\right]\ddot{x}_i \end{aligned} \tag{4.29}$$

The Wilson-θ method is unconditionally stable when $\theta \geq 1.37$, and is a single-parameter algorithm that enables dissipative behaviour (Wilson et al., 1972). Goudreau and Taylor (1973) demonstrated that, when Δt is large, the Wilson-θ algorithm exhibits overestimated estimations of the solution for the first few time steps, then eventually converges towards the exact solution. This is due to the linear extrapolation of $\ddot{x}_{i+1+\theta}$ when $\theta \geq 1$ (see Figure 4.6), resulting in an over prediction of the kinematics. Hilber and Hughes (1978) suggested a TMA called the Collocation Method, which combined Wilson-θ and the Newmark-β's dissipative properties. This method enabled further control of the algorithm's properties and addressed the initial overestimation problem of the Wilson-θ method. For brevity, the Collocation method is not discussed in this comparative study.

4.1.4 α-Family Methods

α-family algorithms extend the Newmark-β method by applying α factors to different kinematic terms in the equation of motion. The Hilbert Hughes Taylor (HHT) approach (Hilber & Hughes, 1978) and the Wood Bossak Zienkiewicz (WBZ) approach (Wood et al., 1980) are two such methods that introduce α factors to the stiffness and inertial terms, respectively, which were generalised by amalgamating the two algorithms into the Generalised-α method (Chung & Hulbert, 1993).

Similar to the θ term in the Wilson-θ algorithm, the α terms introduce dissipation into the algorithm by evaluating kinematic forces within the time-stepped interval via linear interpolation. This modification enables a method of controlled algorithmic dissipation that can target certain modal frequencies in the estimated solution, which will be discussed in more detail in Section 4.1.5. The HHT and WBZ methods are individually described herein, followed by their combination into the Generalised-α method.

WBZ Method

The WBZ method introduces α_m to control the evaluation of the inertial term in the equation of motion (Wood et al., 1980), and is illustrated in Figure 4.7. The equation of motion is modified and described in Equation 4.30.

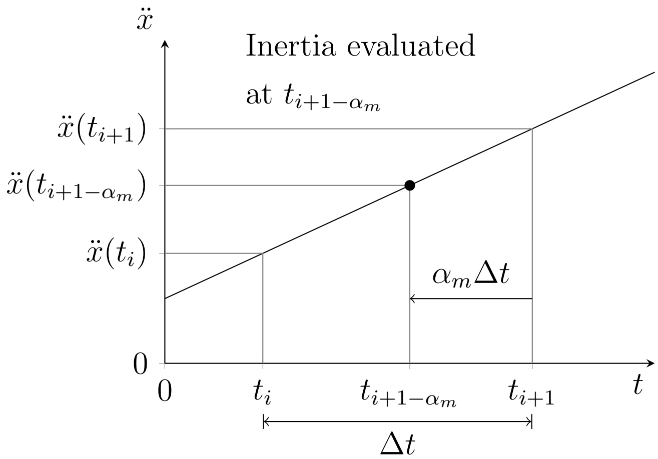

Figure 4.7: WBZ Linear interpolation of the inertial term within a time step

$$F_{i+1} = m\ddot{x}_{i+1-\alpha_m} + c\dot{x}_{i+1} + kx_{i+1} \tag{4.30}$$

where $t_{i+1-\alpha_m}$ is the time at which the evaluation of the inertial term takes place. The linear interpolation of $\ddot{x}$ is calculated in Equation 4.31.

$$\ddot{x}_{i+1-\alpha_m} = (1-\alpha_m)\ddot{x}_{i+1} + \alpha_m \ddot{x}_i \tag{4.31}$$

where $\ddot{x}_{i+1-\alpha_m} = \ddot{x}(t_{i+1-\alpha_m})$. Note that only the inertial term is evaluated within the time-stepped interval when the WBZ method is used.

HHT Method

The HHT method evaluates the stiffness and damping terms in the equation of motion by applying a factor α_f to the displacement and velocity terms, respectively. The interpolation of each term is illustrated in Figure 4.8.

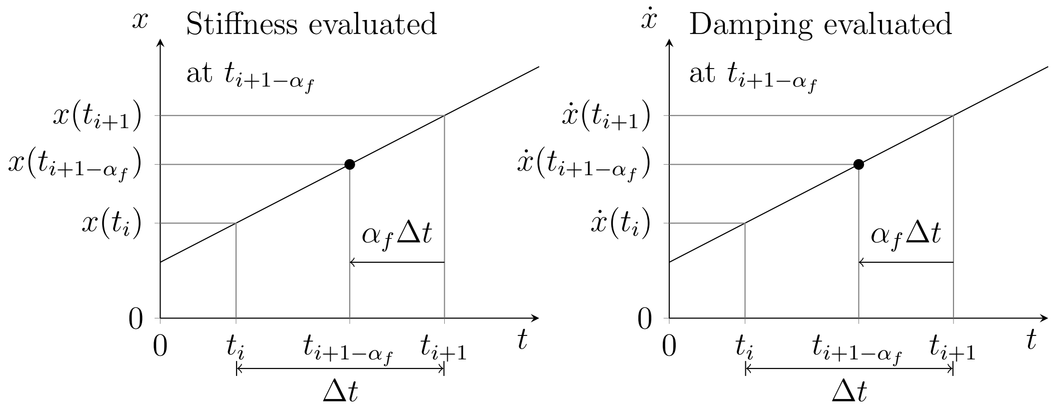

(a) HHT stiffness term evaluation (b) HHT damping term evaluation

Figure 4.8: HHT method acceleration assumptions

The stiffness and damping terms are evaluated at $t_{i+1-\alpha_f} = t_i + (1-\alpha)\Delta t$. Similar to the WBZ method, the equation of motion is updated based on the linear interpolation illustrated in Figure 4.8 and is as follows:

$$F_{i+1-\alpha_f} = m\ddot{x}_{i+1} + c\dot{x}_{i+1-\alpha_f} + kx_{i+1-\alpha_f} \tag{4.32}$$

where

$$\begin{aligned} x_{i+1-\alpha_f} &= (1-\alpha_f)x_{i+1} + \alpha_f x_i \\ \dot{x}_{i+1-\alpha_f} &= (1-\alpha_f)\dot{x}_{i+1} + \alpha_f \dot{x}_i \\ F_{i+1-\alpha_f} &= (1-\alpha_f)F_{i+1} + \alpha_f F_i \end{aligned} \tag{4.33}$$

Note that for the HHT method the inertial term in Equation 4.32 is still evaluated at $t = t_{i+1}$.

Generalised-α Method

Chung and Hulbert (1993) combined the HHT method and WBZ method to form the Generalised-α algorithm, and derived a more detailed description of the dissipative properties for the parameters. The Generalised-α method is described in Equation 4.34, which is notably a simple combination of Equations 4.30 and 4.32, where both α_m and α_f are applied to the equation of motion.

$$F_{i+1-\alpha_f} = m\ddot{x}_{i+1-\alpha_m} + c\dot{x}_{i+1-\alpha_f} + kx_{i+1-\alpha_f} \tag{4.34}$$

where

$$\begin{aligned} F_{i+1-\alpha_f} &= (1-\alpha_f)F_{i+1} + \alpha_f F_i \\ x_{i+1-\alpha_f} &= (1-\alpha_f)x_{i+1} + \alpha_f x_i \\ \dot{x}_{i+1-\alpha_f} &= (1-\alpha_f)\dot{x}_{i+1} + \alpha_f \dot{x}_i \\ \ddot{x}_{i+1-\alpha_m} &= (1-\alpha_m)\ddot{x}_{i+1-\alpha_m} + \alpha_m \ddot{x}_i \end{aligned} \tag{4.35}$$

The Generalised-α method collapses to the HHT method when $\alpha_m = 0$ and to the WBZ method when $\alpha_f = 0$. The algorithms are therefore generalised using the α parameters, as the name suggests. As the Generalised-α method is an extension to the Newmark-β method, Equations 4.13 and 4.14 are employed to determine the displacement and velocity, respectively, at $t = t_{i+1}$. Chung and Hulbert (1993) showed that the β and γ parameters can be defined such that unconditional stability and second order accuracy (see Section 4.1.6) is guaranteed. These parameters can be expressed as functions of α_m and α_f as follows:

$$\beta = \frac{1}{4}(1-\alpha_m+\alpha_f)^2, \quad \gamma = \frac{1}{2} - \alpha_m + \alpha_f \tag{4.36}$$

It is clear that, when $\alpha_m = \alpha_f = 0$, the algorithm collapses to the Newmark CAA method, as $\beta = 1/4$ and $\gamma = 1/2$.

The effective force $\hat{F}_{i+1}$ and effective stiffness $\hat{k}$ can be determined when Substituting Equations 4.35, 4.13 and 4.14 into Equation 4.34, and are defined as follows:

$$\hat{k} = (1-\alpha_m)m\left(\frac{1}{\beta\Delta t^2}\right) + (1-\alpha_f)c\left(\frac{\gamma}{\beta\Delta t}\right) + (1-\alpha_f)k \tag{4.37}$$

$$
\begin{aligned}
\hat{F}_{i+1} =&(1-\alpha_f)F_{i+1} + \alpha_f F_i \\
&+ \left[(1-\alpha_m)m\left(\frac{1}{\beta\Delta t^2}\right) + (1-\alpha_f)c\left(\frac{\gamma}{\beta\Delta t}\right)\right] x_i \\
&+ \left[(1-\alpha_m)m\left(\frac{1}{\beta\Delta t}\right) - (1-\alpha_f)c\left(1-\frac{\gamma}{\beta}\right) - \alpha_f c\right] \dot{x}_i \\
&+ \left[(1-\alpha_m)m\left(\frac{1}{2\beta}-1\right) - (1-\alpha_f)c\left(1-\frac{\gamma}{2\beta}\right)\Delta t - \alpha_m m\right] \ddot{x}_i
\end{aligned}
\tag{4.38}
$$

The displacement at t_{i+1} is therefore $x_{i+1} = \hat{F}_{i+1}/\hat{k}$.

The α terms allow for effective control over the dissipative properties of the algorithm, as high frequency mode may be erroneous in the estimated solution and can be targeted and filtered out based on appropriate parametrisation (Chung & Hulbert, 1993). This is demonstrated in the following section.

4.1.5 Spectral Analysis

Spectral analysis enables a comprehensive review on the stability and dissipative qualities of a particular algorithm for different values of Δt. To investigate the stability characteristics of an integration scheme for linear systems, it is common practice to consider the modes of a system independently with a common time step Δt (Bathe, 2006). Therefore, it is possible to evaluate the performance of TMAs applied to a linear MDOF model by observing the behaviour of a simple SDOF system. Consider the linear homogenous case of Equation 4.1 where $F(t) = 0$ and $f_s(x) = kx$. A TMA can be generalised in the following form to estimate the governing kinematics at the next time step t_{i+1}:

$$
\begin{Bmatrix} x_{i+1} \\ \dot{x}_{i+1} \\ \ddot{x}_{i+1} \end{Bmatrix} = [A] \begin{Bmatrix} x_i \\ \dot{x}_i \\ \ddot{x}_i \end{Bmatrix}
\tag{4.39}
$$

where $[A]$ is the amplification matrix and contains the algebraic description of the TMA. The eigenvalues of $[A]$ are used to determine the stability and numerical dissipation of a system. Known as the spectral radius, $\rho([A])$ is defined as the maximum eigenvalue of $[A]$, i.e.:

$$
\rho([A]) = \max(|\lambda_1|, |\lambda_2|, |\lambda_3|)
\tag{4.40}
$$

where λ_1, λ_2, and λ_3 represent the three eigenvalues of matrix $[A]$. The TMA is considered stable if $\rho([A]) \leq 1$ and unstable otherwise. An example of the spectral radius for the Newmark CAA is shown in Figure 4.9 (Section 4.1.2). In this Figure, $\rho([A])$ is plotted against the normalised frequency $f_n\Delta t$ (or alternatively, $\Delta t/T$)

when the damping ratio is $\zeta = 0$ and $\zeta = 0.5$.

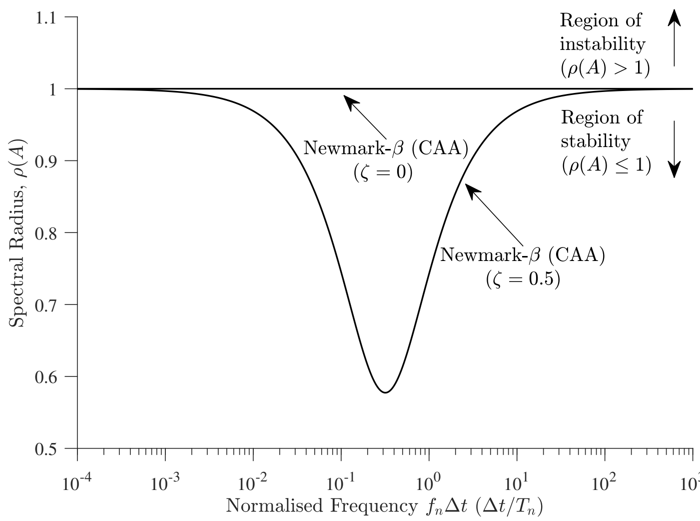

Figure 4.9: Example spectral radius for Newmark's Method (Constant Average Acceleration) with and without damping

Note that, for both algorithms, $\rho([A])$ values for all normalised frequencies are below or equal to unity, indicating that this TMA is unconditionally stable for all values of Δt. The spectral radius can be considered as a dissipating metric for a particular frequency in the estimated response signal, where $\rho([A]) = 1$ indicates no numerical dissipation and 0 indicates strong dissipation. In this light, Figure 4.9 shows that the CAA method can capture all frequency modes in the estimated response (i.e. no algorithmic dissipation). However, it is shown that viscous damping ($\zeta = 0.5$) in the CAA algorithm dissipates a certain frequency bandwidth (approximately $10^{-3} < f\Delta t < 10^{2}$) as there is a drop in $\rho([A])$. Chopra (2013) suggests that including viscous damping is an appropriate method for aiding stability in nonlinear simulations, as high frequency modes can cause unwanted behaviour (Kontoe et al., 2008; Vaiana et al., 2019). However, as is shown in Figure 4.9, the higher frequencies that are considered to have no engineering significance in dynamic soil-structure interaction (i.e. $f\Delta t > 10^{2}$) are unaffected by the presence of viscous damping, which are often the root cause of instabilities in nonlinear simulations (Fung, 2003; Hughes, 1983; Kontoe et al., 2008; Wood, 1990). An algorithm with dissipative qualities is therefore desirable. The inaccuracies associated with higher modal vibrations in MDOF systems are reviewed in Appendix C.1.

4.1.5.1 Demonstrating algorithmic dissipation and instability

An integration scheme is considered stable if the estimated solution does not grow without bound (Bathe, 2006). Unconditionally stable algorithms demonstrate stability for all values of Δt, whereas conditionally stable algorithms are only stable when Δt is sufficiently small. The condition for stability varies between algorithms and can be dependent on its parametrisation. Conditionally stable TMAs require Δt to be below a certain critical value Δt_{cr}, which is a function of the system's smallest natural period T_n of the system (Bathe & Wilson, 1976; Chopra, 2013; Hilber & Hughes, 1978; Tedesco, 1999). For large MDOF systems, the smallest natural period is typically very small due to the many vibrational modes, which directly affects the Δt_{cr} value required to achieve stability, thereby requiring small values of Δt. This can lead to long computation times, therefore unconditionally stable algorithms are preferred for large systems.

The spectral radius enables a graphical representation of stability for various Δt values, and is therefore a useful tool for comparing the stability of TMAs. However, to understand spectral analysis, it is helpful to first evaluate a TMA that demonstrates all algorithm characteristics with simple parametrisation. For this reason, the Wilson-θ method is briefly reviewed, as the concept of the algorithmic dissipation and stability condition can be conveniently demonstrated with different values of a single parameter, θ.

Recalling from Section 4.1.3, the Wilson-θ method collapses to Newmark-β LA approach if $\theta = 1$, which has a stability condition of $0.551\frac{\Delta t}{T_n}$ (see Table 4.1). Otherwise, the Wilson-θ algorithm is unconditionally stable if $\theta \geq 1.37$. This is demonstrated in Figure 4.10 by calculating $\rho([A])$ using the amplification matrix $[A]$ for different values of θ (see Appendix D).

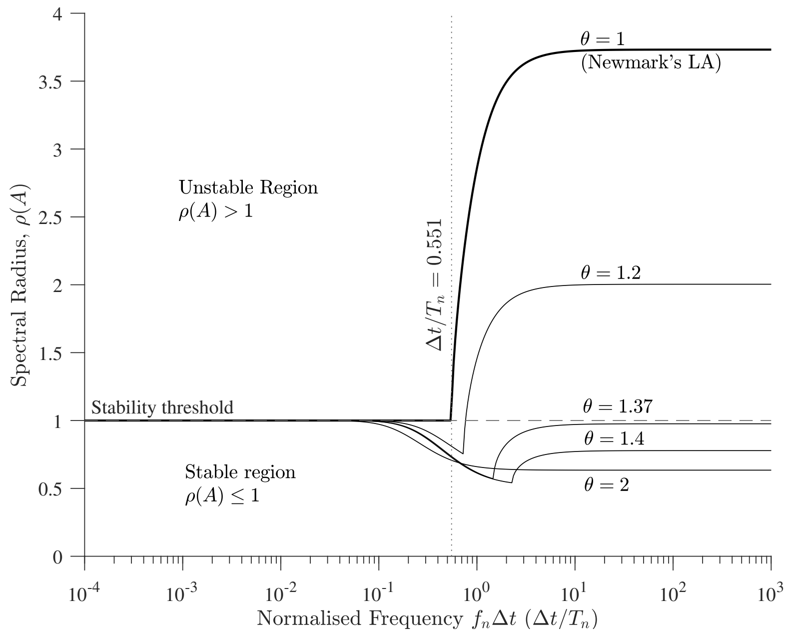

Figure 4.10: Spectral analysis of the Wilson-θ algorithm for different values of θ

Note that, when $\theta = 1$, the Wilson-θ method coincides with Newmark LA's spectral radius, and $\rho([A]) \geq 1$ when $\frac{\Delta t}{T_n} > 0.551$. The instability of the Wilson-θ algorithm (and Newmark LA) can therefore be observed graphically. When $1 \leq \theta < 1.37$, the stability condition also increases as θ increases from 1. This is demonstrated when $\theta = 1.2$, as the intersection with the stability threshold has increased (i.e. $\Delta t_{cr} > 0.551T_n$). Also note that, for $\theta = 1.2$, a normalised frequency range of approximately $0.1 < f_n\Delta t < 0.9$ has $\rho([A]) < 1$. This is indicative of the dissipative properties of the algorithm. If Δt is selected such that $f_n\Delta t \in [0.1, 0.9]$, the algorithm will dampen the system's frequency modes within this range. It is clear then, that further increasing θ will increase the bandwidth of normalised frequencies that are algorithmically damped.

When $\theta \simeq 1.37$, $\rho([A]) \leq 1$ for all frequencies, meaning no condition is required for stability, as there are no intersections with the stability threshold. The algorithm is unconditionally stable. When $\theta = 2$, $\rho([A])$ achieves an asymptotic value of $\rho([A]) = 0.63$ as $f_n\Delta t \to \infty$. Termed ρ_∞ herein, this is a favourable quality of TMAs in general, as the consequence of all erroneous high frequency modes in the estimated solution are minimised. In this light, a TMA that demonstrates a steep $\rho([A])$ curve such that the line quickly approaches a low ρ_∞ value is desired, as high modal frequencies of no engineering significance will be quickly dissipated in the time domain. However, recalling Figure 4.6, the physical meaning of θ indicates the time at which the inertial term is evaluated after t_{i+1}. Careless values of θ are therefore prone to error due to an unrepresentative equilibrium approximation, regardless of the dissipative properties exhibited (Hilber & Hughes, 1978). As will be shown later in Section 4.1.6, the Wilson-θ method demonstrates the largest numerical errors. It is recommended in literature that $\theta = 1.4$ as a compromise between output accuracy and dissipative qualities when using the Wilson-θ method (Bathe & Wilson, 1976; Goudreau & Taylor, 1973).

The consequence of instability in the time domain is demonstrated in Figure 4.11. $\theta = 1$ is used to estimate the response of an undamped SDOF system under free vibrations with a natural period of $T_n = 1$ and initial conditions of $x_0 = 1$, and $\dot{x}_0 = 0$, $\ddot{x}_0 = -\omega_n^2$ and $F(t) = 0$. The exact closed-form solution is therefore $x(t) = \cos(\omega_n t)$, where ω_n is the natural circular frequency $2\pi f_n$. $\frac{\Delta t}{T_n} = 0.5$ and one where $\frac{\Delta t}{T_n} = 0.6$ are simulated to demonstrate the stability limit of the Wilson-θ method when $\theta = 1$. The time-domain solution estimations are shown as insets in Figure 4.11, including the true solution of $x(t)$ in grey.

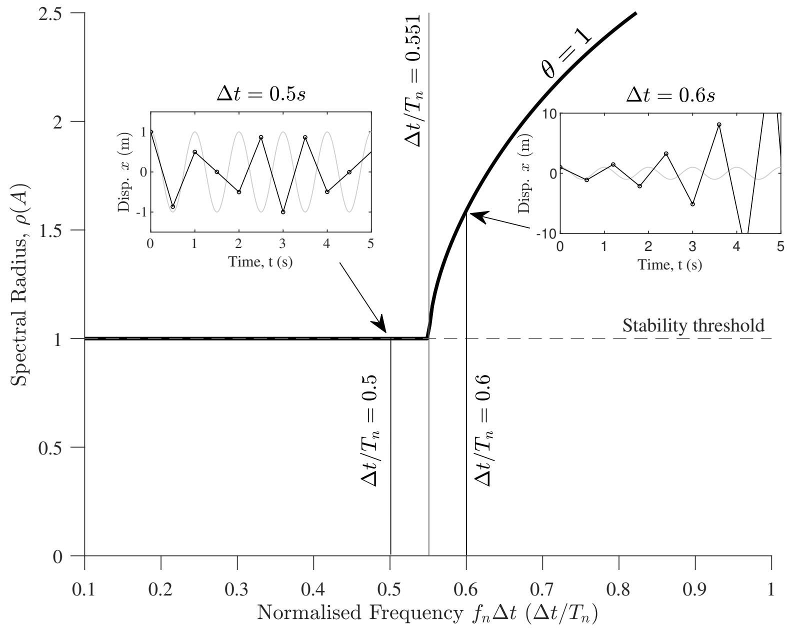

Figure 4.11: Stability demonstration for the Wilson-θ algorithm in the time domain

When $\Delta t = 0.5$ s, the estimated response remains stable but inaccurately estimates the deflections. This is due to the inherent numerical errors associated with relatively large time steps, indicating a period elongation error. This will be discussed in detail in Section 4.1.6. When $\Delta t = 0.6$ s, the estimated response increases without bound, which is obviously undesirable and indicative of instability.

Indeed, numerical errors that become apparent during the simulation at $\Delta t =$ 0.5 s are problematic, naturally suggesting a reduction in the time step size as an effective approach to address the exhibited computational inaccuracies. However, it is important to understand the stability conditions (if any) are imperative to adhere to for both linear and nonlinear MDOF systems. Conditionally stable TMAs are often suitable for SDOF systems, as ensuring a TMA adheres to one modal frequency of a linear system is trivial. However, for MDOF systems, the number of natural periods is equal to the number of degrees of freedom, and the stability condition becomes increasingly more difficult to satisfy. The largest frequency mode is used to determine the stability condition, meaning $T_n = \frac{1}{f_n}$ is often extremely small and therefore requires an even smaller time step. For this reason, it is sensible to use unconditionally stable algorithms for MDOF systems, such as the Wilson-θ method with $\theta \geq 1.37$. However, as shown in this analysis, the Wilson-θ method does not offer much control on the dissipative properties, and has inherent theoretical issues.

4.1.5.2 Comparing spectral radii for different algorithms

It is possible to describe the α parameters in the Generalised-α algorithm as a function of ρ_∞. Chung and Hulbert (1993) shown that α_m and α_f in Equation 4.34 can be expressed as follows:

$$\alpha_m = \frac{2\rho_\infty - 1}{\rho_\infty + 1}, \quad \alpha_f = \frac{\rho_\infty}{\rho_\infty + 1} \tag{4.41}$$

Equation 4.41 can be directly substituted into the Generalised-α method's definition for β and γ (Equation 4.36), such that β and γ are also functions of ρ_∞ in the Newmark-β algorithm. Therefore, the following analysis evaluates the performance of $\rho_\infty = 0, 0.25, 0.5, 0.75$ and 1 for both the Newmark-β and Generalised-α algorithms. The spectral radii for each simulation configuration are shown in Figure 4.12, including the Wilson-θ method for different θ values.

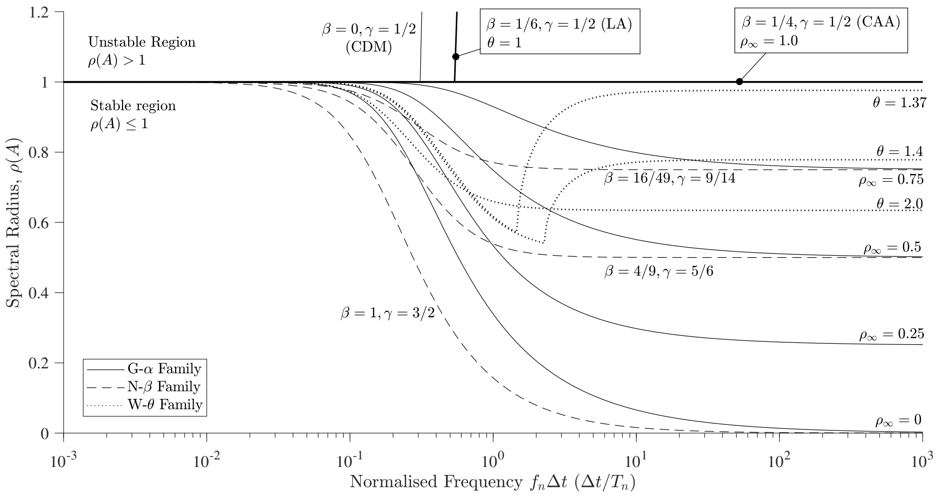

Figure 4.12: Comparative spectral analysis study of different family of algorithms

The CDM algorithm is unstable when $f_n\Delta t \geq \frac{1}{\pi} \simeq 0.318$, as described in Section 4.1.2, which is evidently a stricter stability condition than the Newmark-β LA method. Moreover, Figure 4.12 shows that the Wilson-θ family of algorithms have limitations regarding the range of potential algorithmic dissipation when compared to other algorithms. The Newmark-β family shows that a steep spectral radius is possible for defined parametrisations. For instance, taking $\beta = 1$ and $\gamma = 3/2$ provides a ρ_∞ of zero, and Figure 4.12 suggests that normalised frequencies of approximately 15 and higher are completely filtered out. However, it is worth noting that, at $f_n\Delta t \simeq 10^{-2}$, the spectral radius starts to deviate from unity, which may lead to numerical dissipation in the fundamental modal frequency of the estimated response if Δt is too large. Given that the frequencies of interest for an OWT system subjected to wind and wave loads are typically ≤ 1 Hz, ensuring that the relevant vibration modes are not dissipated would require a considerably small Δt.

For the same ρ_∞, Figure 4.12 suggests that the Generalised-α algorithm reduces $\rho([A])$ at a higher $f_n\Delta t$ compared to an equivalent Newmark-β parametrisation for ρ_∞, but with the same rate of change. This is due to the α factors applied to the kinematic terms in the equation of motion, and directly addresses the concern posed by the Newmark family where low normalised frequencies experience algorithmic damping. In general, this permits larger Δt values without compromising accuracy of the fundamental modal frequency of the system. Also note that, when $\rho_\infty = 1$, the Generalised-α method collapses to the Newmark CAA method ($\beta = 1/4$, $\gamma = 1/2$, see Equation 4.36), which is recognised as the most accurate unconditionally stable scheme (Dahlquist, 1963).

The Generalised-α presents itself as a promising choice for MDOF dynamic soil-structure interaction simulations due to the minimal requirements for setting up a computationally efficient simulation prior to analysis. To demonstrate, consider the dynamic *p*-*y* model in Figure 4.1b. Two parameters need be specified by the user: Δt and ρ_∞. The modal frequencies of the system can be quickly identified via an eigenanalysis (Section 2.3.2), allowing for a direct comparison with the normalised frequencies outlined in the spectral radius plot provided in Figure 4.12. The user can then select a Δt that is sufficiently small to ensure erroneous modes are dissipated without compromising the first or second mode. ρ_∞ can then be selected in accordance with the modal characteristics of the system. This process is notably straightforward and can be applied to any MDOF system, and is amenable to automation through pre-simulation scripting.

It is important to note that estimated solutions using numerical integration methods are still prone to numerical errors that are heavily dependent on the size of the time step. It is therefore crucial that the anticipated numerical error for a given normalised frequency is recognised and minimised. The following section discusses how to quantify the numerical errors inherent with TMAs, and compares the accuracy of the Generalised-α method with other TMAs.

4.1.6 Numerical error in TMAs

A TMA is considered accurate if the approximated solution is close to the exact solution, and is said to be convergent when the approximation approaches the exact solution as Δt tends to zero. The numerical error is proportional to $(\Delta t/T_n)^\epsilon$, where ϵ is the order of accuracy, and Hilber and Hughes (1978) suggested that algorithms that exhibit $\epsilon = 2$ are suitable for structural dynamics problems. Second-order accuracy is, therefore, a desirable property of TMAs.

Establishing the anticipated numerical error can provide a method to optimise computational efficiency without compromising simulation accuracy. Numerical errors in TMAs can be quantified in two forms: Amplitude Decay (AD) and Period Elongation (PE). Figure 4.13 shows a SDOF response signal of an undamped oscillator subject to free vibrations compared with a numerical estimation to the system's response using a TMA. The exact solution is $x(t) = \cos\left(\frac{2\pi}{T_n}t\right)$.

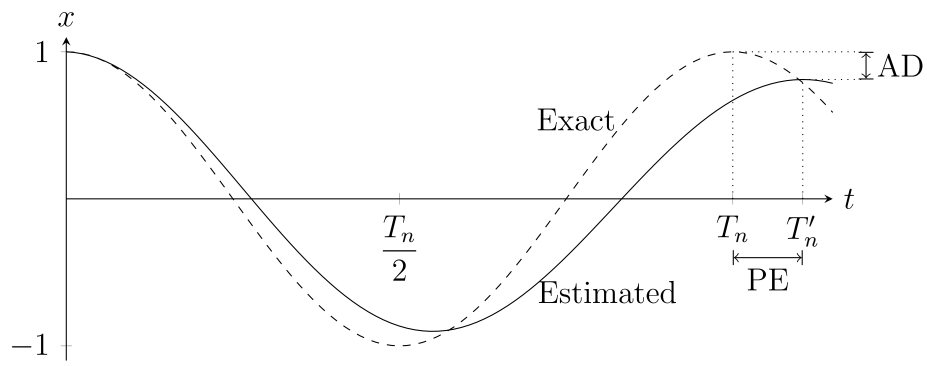

Figure 4.13: Amplitude decay and period elongation of a numerical solution compared to the exact solution $x(t) = \cos(\omega_n t)$

The difference in the responses after one full cycle indicates the numerical error, which can be quantified with reference to Figure 4.13. The PE can be determined as the percentage error between true and estimated natural period (T_n and T'_n, respectively), and is defined in Equation 4.42.

$$\mathrm{PE} = \frac{T'_n - T_n}{T_n} \tag{4.42}$$

AD resembles an energy loss due to mechanical properties such as viscous damping, but is a consequence of computational error embedded in the numerical integration algorithm and is therefore artificial. As discussed previously, this can be a favourable quality as erroneous modal frequencies can be targeted to achieve a stable solution in nonlinear systems (Chung & Hulbert, 1993; Kontoe et al., 2008; Wood, 1990). An artificial damping ratio ζ' can be determined using Equation 4.43 (Hilber et al., 1977).

$$\zeta' = \frac{-\ln(\mathrm{Re}^2 + \mathrm{Im}^2)}{2\omega'_n} \tag{4.43}$$

where Re is the real part and Im is imaginary part of the complex eigenvalues $\lambda_{1,2}$ of the amplification matrix $[A]$, which are complex conjugates. ω'_n is the circular natural frequency of the numerical approximation ($\omega' = 2\pi/T'_n$). A full derivation of the numerical approximation function can be found in Hilber et al. (1977).

In hysteretic systems, maximum displacement occurs when there is a large change in material properties (for example, a stiffness reset in the Masing rules). This can have significant implications if not estimated accurately, as careless values of Δt could result in incorrect estimations of the nonlinear stiffness due to a miss-approximation in maximum displacements. It is therefore important to understand the relationship between the Δt and the amplitude decay of the numerical solution.

Equations 4.42 and 4.43 depend on the first full oscillation cycle of the numerical estimation T'_n, which corresponds to the location of maximum displacement location along the time axis (Figure 4.13). However, for large Δt values, the resolution of the estimated displacement signal becomes compromised, making it challenging to accurately identify the exact time in the simulation where maximum displacements occur. To circumvent this, T_n' is computed by utilising a discrete Fourier analysis on a displacement signal that was estimated using numerical integration after many cycles. By leveraging the frequency spectrum generated through this analysis, an approximate value for the natural frequency of the system from the TMA f_n' can be obtained. f_n' is subsequently utilised to ascertain T_n', ensuring a more precise estimation even in simulations where poor resolution could otherwise impede accurate reversal determination.

The following analysis utilises this frequency domain approach to approximate T_n' for the different TMA families and a range of parameters. Initial conditions to the undamped freely-oscillating SDOF system are $x_0 = 1$, $\dot{x}_0 = 0$, and $\ddot{x}_0 = -\omega_n^2$, such that the true solution is $x(t) = \cos(\omega_n t)$ and the estimated response is comparable. The algorithmic damping ratio is computed using Equation 4.43. The results are shown in Figure 4.14.

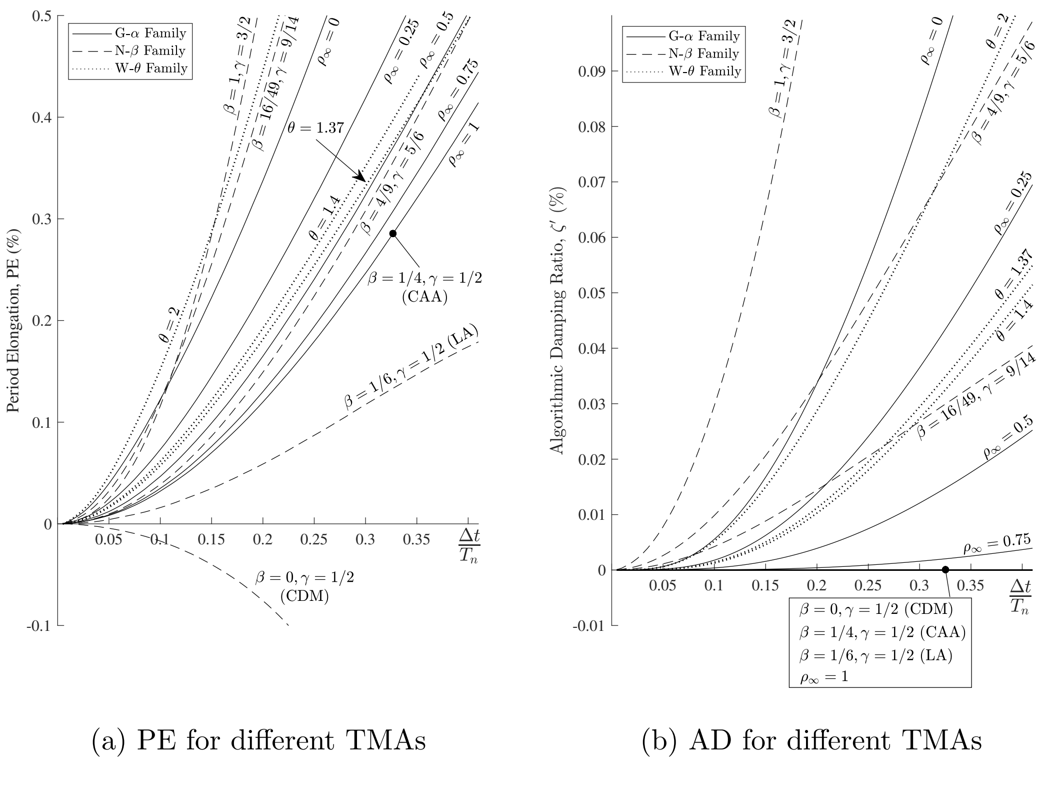

(a) PE for different TMAs (b) AD for different TMAs

Figure 4.14: Comparative error analysis for different families of TMAs

Figure 4.14a suggests that all TMAs exhibit period elongation, and the Newmark family of algorithms exhibit the highest sensitivity to period error depending on the β and γ parameters. The Newmark LA method ($\beta = 1/6$, $\gamma = 1/2$) is the least susceptible to period elongation errors, but is conditionally stable as shown in the spectral analysis in Figure 4.12. When $\beta = 1$ and $\gamma = 3/2$, the spectral analysis shown that the algorithm offers the strongest dissipative properties. However, it is evident in Figure 4.14a that this parametrisation of the Newmark-β method introduces extremely large elongation errors for small increases in normalised frequencies. The same goes for the Wilson-θ method when $\theta = 2$, which shows a high PE value in general for all acceptable values of θ. Figure 4.14a indicates that the Generalised-α algorithm is generally less susceptible to period elongation errors for a range of ρ_∞ values. The CDM algorithm is the only method that exhibits a period 'shrinkage'.

Notably, when $\gamma = 1/2$, Newmark-β algorithms demonstrate no amplitude decay for all normalised frequencies (including Generalised-α when $\rho_\infty = 1$). When $\gamma \neq 1/2$, it is shown that algorithmic damping is observed when $\Delta t/T_n$ is very small. In contrast, when $\rho_\infty = 0$ for the Generalised-α algorithm, begins to dissipate when $\Delta t/T_n \geq 0.05$. This limit improves as ρ_∞ is increased. In general, the Generalised-α algorithm demonstrates lower numerical dissipation for low normalised frequencies when compared to the equivalently parametrised Newmark-β algorithm. The artificial damping ratio for Wilson-θ family of algorithms is in general low, but is subject to its own theoretical issues, as discussed previously, and has extremely limited parametrisation.

4.1.7 Summary

The characteristics of various TMAs and how their parameters influence the numerical estimation have been evaluated. The underlying assumptions of numerical integration schemes have significant implications on their performance when Δt is relatively large. This is especially true for nonlinear MDOF models, which makes such analyses necessary. The response of a linear SDOF system was estimated using various TMAs to identify the most appropriate method to be applied to the MDOF model. This is possible as the overall response of a linear system can be represented as the superposition of individual vibration modes, therefore reviewing TMAs applied to one mode (i.e. a SDOF) is sufficient (Bathe & Wilson, 1976; Chopra, 2013). However, including nonlinear spring elements requires further investigation, and involves complex analyses which is bespoke to the type of nonlinearity (Chen & Ricles, 2008).

The spectral analysis provided a graphical representation of stability conditions and demonstrated how modal frequencies can be targeted depending on the TMA used. Results show that all algorithms can exhibit favourable properties for nonlinear simulations (particularly in dissipating high modal frequencies), but certain algorithms are constrained by their parametrisation. Newmark-β and Generalised-α show similar capabilities, however Generalised-α demonstrated less artificial damping to lower frequency modes. This is important for OWT systems, as the first and second modal frequencies are typically below 1 Hz (Prendergast et al., 2018; Tarp-Johansen et al., 2009).

This was further reinforced with the numerical error analysis, as the algorithmic damping ratio ζ' is less pronounced for lower normalised frequencies in the Generalised-α method compared to the Newmark-β method. This permits larger time steps in simulations without significant loss of information, as the algorithmic decay doesn't affect vibration modes of engineering significance. Period elongation errors are also minimal, as ρ_∞ has a smaller influence on expected errors compared to other algorithm families and their parametrisations. This is ideal for slender structures such as OWTs, as the natural frequencies of the system are typically as low as 0.25 Hz.

The Generalised-α method collapses to Newmark's CAA ($\beta = 1/4$ and $\gamma = 1/2$) when $\rho_\infty = 1$ (See Equation 4.36). According to Dahlquist (1963), The CAA is considered as the most accurate unconditionally stable methodology. Combining this fact with the strengths demonstrated in the spectral and numerical error analyses, the Generalised-α TMA is selected for the nonlinear MDOF model. The development and analyses of the TMAs presented thus far do not consider the implications of a hysteretic nonlinear restoring force, which is the focal point of the following section.

4.2 Hysteresis models

The hysteretic behaviour of soil can be encapsulated in the direct integration method by computing and updating the nodal restoring force $f_s(x)$ of the spring element at each time step. However, this will require significant modifications to the TMA. The Masing, Iwan and Bouc-Wen hysteresis models will be investigated using the Generalised-α algorithm, which was deemed the most appropriate TMA for the application of soil-structure interaction and nonlinear MDOF systems.

Due to the system's nonlinearity, it is not possible to perform a numerical error analysis similar to Section 4.1.6. This is due to the absence of a closed-form analytical solution for displacement which would otherwise serve as a benchmark. Therefore, simulation robustness will be assessed by scrutinising the sensitivity of the estimated response to variations in Δt, ρ_∞, and different load histories in an MDOF configuration.

Each hysteresis model will adopt a similar backbone description to ensure a meaningful comparison in the force-displacement domain over time. The backbone function, denoted as $f_{bb}(x)$, takes the generalised form described in Equation 4.44, which is inspired by the hyperbolic function found in API sands (Equation 2.3). Equation 4.44 enables simple parametrisation, and is as follows:

$$f_{bb}(x) = F_{ult} \tanh\left(\frac{k_0 x}{F_{ult}}\right) \tag{4.44}$$

where F_{ult} is the ultimate spring force and k_0 is the initial stiffness. It is important to note that this section will provide a qualitative study towards nonlinear dynamics. Hence, the specific values assigned to Equation 4.44 hold no significance. The objective is to ensure comparability between nonlinear models and determine appropriate parameter values for each hysteresis-type. The physical value is therefore unimportant.

Nonlinear simulations (both SDOF and MDOF) require considerable modifications to TMAs derived for linear systems. The following section will describe the modifications necessary to the Generalised-α algorithm such that it is appropriate for nonlinear systems. The Masing, Iwan and Bouc-Wen hysteresis models will then be investigated using the Generalised-α algorithm for SDOF systems. The most effective parameters for each model will be identified to enforce similarity. Each hysteresis model is then applied to an MDOF system to determine the most appropriate model for the application of dynamic soil-structure interaction in OWT monopiles.

4.2.1 Generalised-α for nonlinear systems

The implicit TMAs described in section 4.1, including the Generalised-α method, compute the displacements at $t = t_i + \Delta t$ by deriving an effective stiffness $\hat{k}$ and effective force $\hat{F}$ such that $x_{i+1} = \hat{F}_{i+1}/\hat{k}$. This notation is advantageous due to its resemblance to simple static linear spring mechanics. However, the linear approximation $\hat{F}_{i+1}/\hat{k}$ is no longer valid for nonlinear systems. Instead, it is convenient to solve $x_{i+1} = x_i + \Delta x$, such that $\Delta x = \Delta\hat{R}/\hat{k}_T$, where $\hat{R}$ is the residual force within the time step required to achieve equilibrium and $\hat{k}_T$ is the tangent stiffness of the system. After the initial linear approximation to x_{i+1}, there exists an imbalance within the internal kinematic forces of the system at $t = t_{i+1}$ that must be resolved. An iterative scheme is therefore required to achieve equilibrium.

Equilibrium iterations within each time step reduces the residual out-of-balance forces $\Delta\hat{R}$. The Modified Newton Raphson (MNR) approach is used to iterate towards equilibrium using the system properties at $t = t_i$. The MNR iteration scheme, as well as the concept of force imbalance, is illustrated in Figure 4.15.

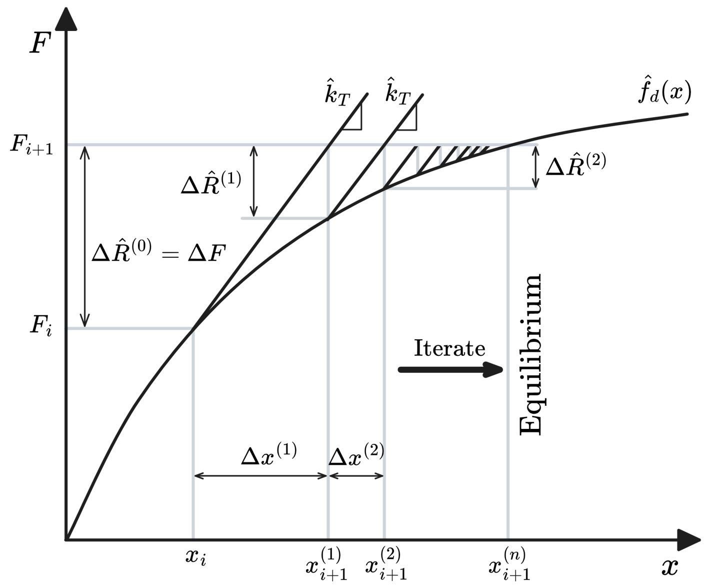

Figure 4.15: Force imbalance in nonlinear systems and the Modified Newton Raphson iteration scheme within a time step

The dynamic restoring force $\hat{f}_d$ shown in Figure 4.15 encapsulates the internal forces (inertial, damping and nonlinear restoring force) of the system. It is clear then, that an effective residual force $\Delta\hat{R}^{(1)}$ between the applied external force F_{i+1} and internal forces $\hat{f}_s$ will exist after the first estimation of x_{i+1} using $\Delta x = \Delta F/\hat{k}_T$. Using the effective tangent stiffness $\hat{k}_T$, the effective residual force is iteratively reduced until equilibrium is achieved after n number of iterations within the time step, such that $\hat{f}_s(x_{i+1}) = F_{i+1}$.

It now stands to reason that, similar to Equations 4.37 and 4.38; $\hat{f}_d$, $\hat{k}_T$ and $\hat{F}$ must be defined in terms of the Generalised-α algorithmic parameters α_m, α_f, β and γ. Recalling that the Generalised-α method evaluates equilibrium within the time stepped interval and not at the end of the time step, the equilibrium condition is satisfied when:

$$\hat{f}_d(x_{i+1}) = (1 - \alpha_f)F_{i+1} + \alpha_f F_i \tag{4.45}$$

Therefore, the updated MNR iteration scheme for the nonlinear Generalised-α algorithm is shown in Figure 4.16, and the restoring force is described in Equation 4.46.

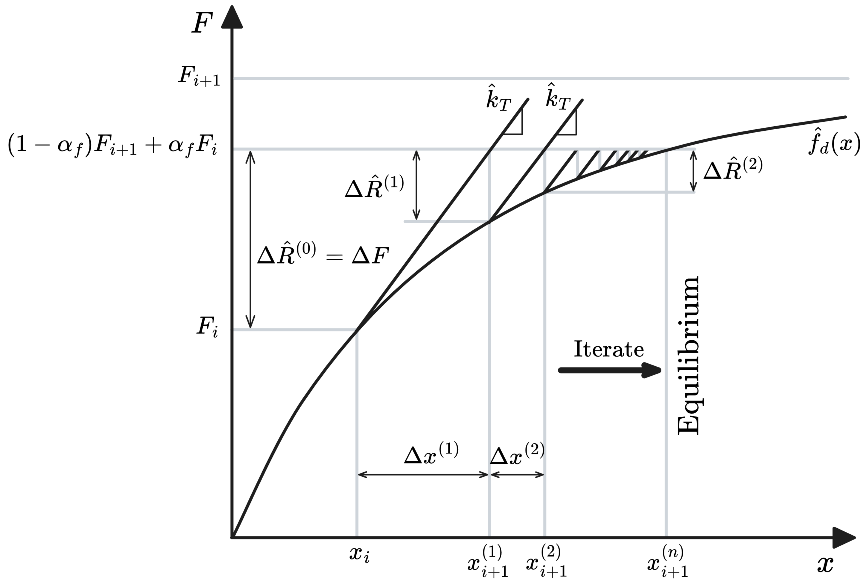

Figure 4.16: Modified Newton Raphson iteration scheme for the Generalised-α algorithm

$$\begin{aligned}\hat{f}_d(x) = &(1 - \alpha_m)m\ddot{x}_{i+1} + \alpha_m m\ddot{x}_i \\ &+ (1 - \alpha_f)c\dot{x}_{i+1} + \alpha_f c\dot{x}_i \\ &+ (1 - \alpha_f)f_s(x_{i+1}) + \alpha_f f_s(x_i)\end{aligned} \tag{4.46}$$

By encapsulating the kinematic forces in an equivalent force $\hat{f}_d(x_{i+1})$, the system can be solved for using the method illustrated in Figure 4.15.

$\hat{k}_T$ is described as the first derivative of Equation 4.46 with respect to x_i, i.e.:

$$\hat{k}_T = \frac{\partial \hat{f}_d(x_i)}{\partial x_i} = (1-\alpha_m)m\frac{\partial \ddot{x}_{i+1}}{\partial x_i} + (1-\alpha_f)c\frac{\partial \dot{x}_{i+1}}{\partial x_i} + (1-\alpha_f)\frac{\partial f_s(x_{i+1})}{\partial x_i} \tag{4.47}$$

Figure 4.16 shows that $\hat{k}_T$ is constant for each iteration within the time step. The traditional Newton Raphson method recalculates $\hat{k}_T$ for each iteration j, which is acceptable for SDOF systems due to the faster conversion towards equilibrium. However, for MDOF models, this would require multiple inversions of the tangent stiffness matrix within a time step, which can become computationally expensive for long simulations that are highly nonlinear. Keeping $\hat{k}_T$ constant within a time step requires only one inversion of the stiffness matrix at the start, which is computationally faster. For this reason, the $\frac{\partial f_s(x_{i+1})}{\partial x_i}$ term in Equation 4.47 is taken as the tangent stiffness of the spring k_T at x_i instead of $x_{i+1}^{(j)}$.

The derivatives of the inertial and damping terms in Equation 4.47 can be determined from the Newmark-β Equations 4.13 and 4.14:

$$\frac{\partial \ddot{x}_{i+1}}{\partial x_i} = \frac{1}{\beta \Delta t^2} \qquad \frac{\partial \dot{x}_{i+1}}{\partial x_i} = \frac{\gamma}{\beta \Delta t} \tag{4.48}$$

Therefore, $\hat{k}_T$ can be rewritten as:

$$\hat{k}_T = (1-\alpha_m)m\left(\frac{1}{\beta \Delta t^2}\right) + (1-\alpha_f)c\left(\frac{\gamma}{\beta \Delta t}\right) + (1-\alpha_f)k_T \tag{4.49}$$

To compute x_{i+1}, $\dot{x}_{i+1}$ and $\ddot{x}_{i+1}$ must be eliminated from Equation 4.46, which can be done by rearranging the original Newmark-β formulations described in Equations 4.13 and 4.14.

$$\dot{x}_{i+1} = \frac{\gamma}{\beta \Delta t}(x_{i+1} - x_i) + \left(1 - \frac{\gamma}{\beta}\right)\dot{x}_i + \Delta t\left(1 - \frac{\gamma}{2\beta}\right)\ddot{x}_i \tag{4.50}$$

$$\ddot{x}_{i+1} = \frac{1}{\beta \Delta t^2}(x_{i+1} - x_i) - \frac{1}{\beta \Delta t}\dot{x}_i - (\frac{1}{2\beta} - 1)\ddot{x}_i \tag{4.51}$$

According to Figure 4.16, $\Delta \hat{R}^{(j)} = (1-\alpha_f)F_{i+1} + \alpha_f F_i - \hat{f}_d(x_{i+1}^{(j)})$. Therefore, substituting Equations 4.50 and 4.51 into Equation 4.46 yields:

$$\begin{aligned} \Delta \hat{R}^{(j)} &= (1-\alpha_f)F_{i+1} + \alpha_f F_i + a_1 x_i - a_2 \dot{x}_i - a_3 \ddot{x}_i ... \\ &- (1-\alpha_f) f_s(x_{i+1}^{(j)}) - \alpha_f f_s(x_i) - a_1 x_{i+1}^{(j)} \\ &= \hat{F}_{i+1} - \hat{f}_s(x_{i+1}^{(j)}) \end{aligned} \tag{4.52}$$

where

$$
\begin{aligned}
\hat{F}_{i+1} &= (1-\alpha_f)F_{i+1} + \alpha_f F_i + a_1 x_i - a_2 \dot{x}_i - a_3 \ddot{x}_i \\
\hat{f}_s(x_{i+1}^{(j)}) &= (1-\alpha_f) f_s(x_{i+1}^{(j)}) + \alpha_f f_s(x_i) + a_1 x_{i+1}
\end{aligned}
\tag{4.53}
$$

and

$$
\begin{aligned}
a_1 &= (1-\alpha_m)m\left(\frac{1}{\beta\Delta t^2}\right) + (1-\alpha_f)c\left(\frac{\gamma}{\beta\Delta t}\right) \\
a_2 &= -(1-\alpha_m)m\left(\frac{1}{\beta\Delta t}\right) + (1-\alpha_f)c\left(1-\frac{\gamma}{\beta}\right) + \alpha_f c \\
a_3 &= -(1-\alpha_m)m\left(\frac{1}{2\beta}-1\right) + (1-\alpha_f)c\Delta t\left(1-\frac{\gamma}{2\beta}\right) + \alpha_m m
\end{aligned}
\tag{4.54}
$$

The MNR iteration scheme is complete once $\Delta\hat{R}^{(j)}$ is reduced to a sufficiently small value. The condition for convergence is taken as $\Delta\hat{R}^{(j)} \leq 10^{-6}$. It should be noted that, for nonlinear systems with hysteretic properties, there would exist a condition where equilibrium would not be achievable within the time step when utilising MNR. This is due to a restoring force reversal in $\hat{f}_d$ existing between F_i and F_{i+1} (referring to Figure 4.15). As a consequence, $\hat{k}_T$ derived at x_i would not permit convergence without an updated $\hat{k}_T$ at $x_{i+1}^{(j)}$. This is known as the Original Newton Raphson (ONR) iteration scheme. For this reason, when a reversal is detected (change in velocity signage), the iteration scheme is switched from MNR to ONR, which simply involves updating $\hat{k}_T$ during the equilibrium iteration process.

The full time marching algorithm for the Generalised-α method applied to nonlinear systems, including the equilibrium iteration process, is summarised in Appendix C.2. The following analyses are produced in MATLAB.

4.2.2 Masing model

The Masing model informs the unload and reload stress paths of the hysteresis by transforming and scaling the initial reaction function $f_{bb}(x)$ (Masing, 1926). As discussed in Section 2.3.5 the Masing model can be generalised using Pyke's formulation described in Equation 2.36 (Pyke, 1979). The general spring force can therefore be described as:

$$
\begin{aligned}
f_s &= C f_{bb}\left(\frac{x-x_r}{C}\right) + f_r \\
&= C F_{ult}\tanh\left(\frac{k_0(x-x_r)}{C F_{ult}}\right) + f_r
\end{aligned}
\tag{4.55}
$$

where x_r and f_r are the coordinates of reversal points of the hysteresis in the force-displacement domain[1]. C is the scaling coefficient defined in Equation 2.36 that enables asymmetrical loading (Pyke, 1979), and scales the reload function such that it does not exceed the ultimate resistance F_{ult}. For nonlinear MDOF systems, it is required that the tangent stiffness k_T is determined at each time step to inform the global stiffness matrix of the system (see Section 4.2.1). The tangent stiffness can be determined by differentiating Equation 4.55.

$$\begin{aligned} k_T &= \frac{df_s}{dx} = f'\left(\frac{x - x_r}{C}\right) \\ &= k_0 \operatorname{sech}^2\left(\frac{k_0(x - x_r)}{CF_{ult}}\right) \end{aligned} \tag{4.56}$$

$f_{bb}(x)$ in Equation 4.44 allows for a simple analytical expression for the tangent stiffness for any reloading configuration by computing the first derivative as follows:

$$k_T = f'_{bb}(x) = k_0 \operatorname{sech}^2\left(\frac{k_0 x}{F_{ult}}\right) \tag{4.57}$$

However, the derivative for some backbone definitions may not be as trivial to acquire. In such cases, k_T can be determined using the finite difference approach described in Equation 4.2 if the closed form solution for $f'_{bb}(x)$ is undefined.

It is important to note that the constitutive equations that form the Masing model are dependent on the reversal coordinates (x_r, f_r) in the force-displacement domain. This is problematic, as the reversal coordinates are not known a priori, and can only be detected if there is a change in sign of velocity. The reversal coordinate error is demonstrated in Figure 4.17, and shows how the error would accumulate for each reversal. Notably, this error would become more pronounced with larger Δt values. One solution is to reduce the time step size to ensure that the reversal point is captured with sufficient accuracy. However, this can be computationally expensive, particularly for large MDOF systems when multiple hysteretic springs are simulated.

[1]The following hysteresis models are described in the context of force-displacement rather than p-y. However, the application is analogous.

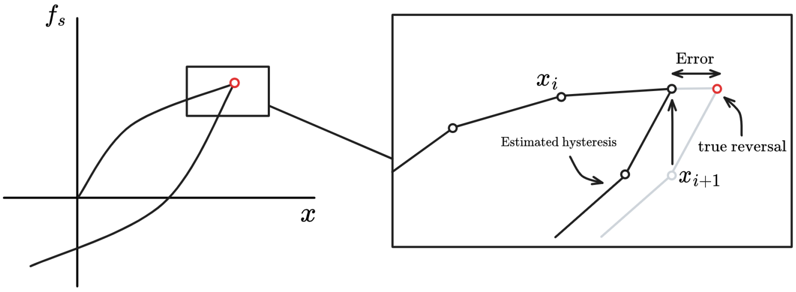

Figure 4.17: Reversal estimation error in the Masing model

An alternative approach that does not compromise a coarse resolution of time is proposed herein. As $\dot{x} = 0$ during a reversal event, the moment of this occurrence can be estimated through linear interpolation between the velocities at the time steps just before and after the detection of the reversal, which happens when the velocity's sign changes during the algorithm's computation. This is illustrated in Figure 4.18. The parameter α is introduced to determine the time at which the velocity is 0 along the time stepped interval Δt. The reversal occurs at $t = t_i + \alpha\Delta t$.

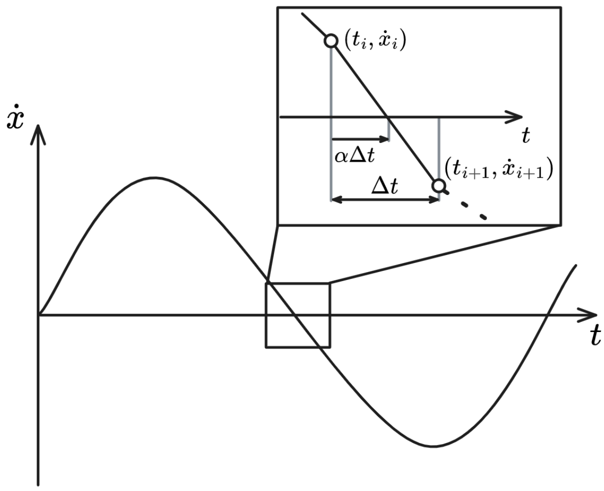

Figure 4.18: Linear interpolation to determine the time at which a reversal occurs between time steps

The velocity and displacement at the start and end of the time step are known, therefore α can be determined using Equation 4.58.

$$\alpha = \frac{|\dot{x}_i|}{|\dot{x}_i| + |\dot{x}_{i+1}|} \tag{4.58}$$

Figure 4.19 illustrates the method in the displacement-time domain. It can be assumed that a quadratic relationship can provide a better estimate to the turning point behaviour within the time step interval. The quadratic function is informed using the kinematics at $t = t_i$ and $t = t_{i+1}$ as boundary conditions. The general second order polynomial to be defined at each reversal point is described in Equation 4.59 as $g(\tau)$, where τ is the variation of time along Δt.

$$g(\tau) = a\tau^2 + b\tau + c \tag{4.59}$$

$$g'(\tau) = 2a\tau + b \tag{4.60}$$

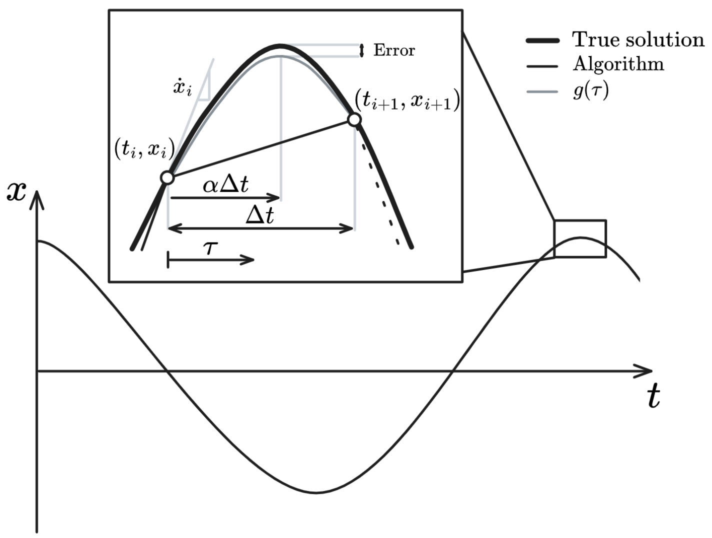

Figure 4.19: Quadratic estimation of the turning point within the time step using α

Note that the first derivative in Equation 4.60 defines the straight line approximation shown in Figure 4.18. a, b and c are coefficients to be determined using the current kinematics as boundary conditions; i.e. $g(0) = x_i$, $g(\Delta t) = x_{i+1}$ and $g'(0) = \dot{x}_i$. Substituting these boundary conditions into Equations 4.59 and 4.60 yields the following definition for the general quadratic curve used to estimate the turning point at any reversal event:

$$x = \frac{x_{i+1} - x_i - \dot{x}_i\Delta t}{\Delta t^2}\tau^2 - \dot{x}_i\tau + x_i \tag{4.61}$$

According to Figure 4.18, the reversal occurs at $\tau = \alpha\Delta t$. Therefore, substituting Equation 4.58 into the above equation yields the displacement at the reversal point, which is described in Equation 4.62.

$$x_r = \alpha^2 x_{i+1} + (1 - \alpha^2)x_i - \alpha(1 - \alpha)\dot{x}_i\Delta t \tag{4.62}$$

The turning point in a discrete displacement-time signal has therefore the estimated coordinate of (t_r, x_r), where $t_r = t_i + \alpha\Delta t$. The hysteresis reversal point in the force-displacement domain can be estimated by calculating the force as $f_r = f_s(x_r)$, where $f_s(x)$ is the force-displacement relationship of the Masing-type hysteretic spring described in Equation 4.55.

It is not possible to evaluate the numerical error by means of PE and AD assessment as done in Section 4.1.6, as there is no analytical solution to define a benchmark. Furthermore, assessing stability conditions is also complicated for nonlinear systems, and depends on the type of nonlinearity in the system (Chen, 2000; Chen & Ricles, 2008). Currently, no stability criteria exist in literature for TMAs applied to nonlinear systems of the hysteretic-type. For this reason, the 'true solution' is considered as a response estimation whereby a sufficiently small time step is applied, and smaller time steps have negligible effect on the system's response. Δt is then increased until the response of the system diverges from the true solution.

Figure 4.20 compares the performance of the default Masing model compared with the optimised Masing model. The SDOF system is subjected to harmonic excitation at a frequency of 0.05 Hz and an amplitude of 1 N. The mass is set to m = 10 kg and backbone function is arbitrarily defined with parameters set as F_{ult} = 1 N and k_0 =15 N/m. $\zeta = 0$ and the simulation is run for 100 seconds. Without the reversal estimator, the reversal displacement is taken as the displacement at the start of the time step at which a change in velocity signage was detected. Simulations ranging from $\Delta t = 0.01$ s and $\Delta t = 2.5$ s are shown in Figure 4.20 for both Masing model configurations.

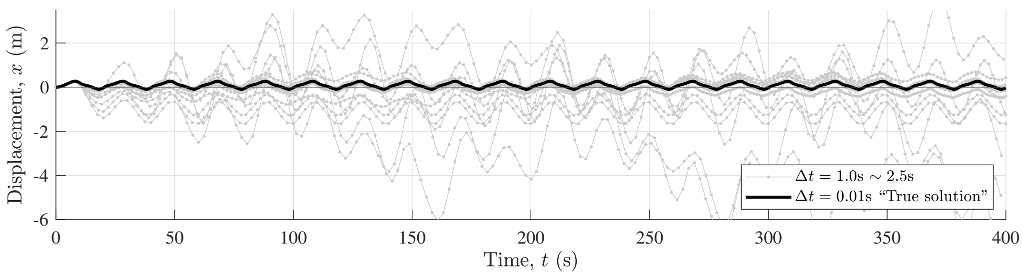

(a) Masing model response without reversal improvements

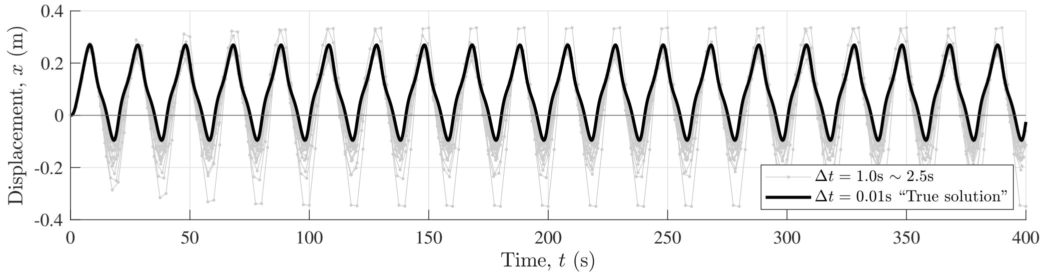

(b) Masing model response with Equation 4.62

Figure 4.20: Response of a harmonically-driven Masing-type hysteretic system with and without the proposed reversal estimation method

Figure 4.20a demonstrates the poor performance of the Masing model for large time steps if no improvements are made to the reversal estimation. Simulations with the largest Δt value diverge the most from the true solution, and show varying peak displacements. This is due to the error in the reversal estimation, which is amplified with larger time steps and accumulated for each reversal.

Figure 4.20b shows that the stability of the estimated solution is significantly improved for all values of Δt and remains bound. However, the maximum displacement increases with increase in Δt, which may be a consequence of the small error inherent with the quadratic estimation, as shown in Figure 4.19. In general, the estimated solution for all investigated time steps compares well with the 'true solution'. Stability is evidently achieved as the estimated solutions remains bounded for all time steps throughout the simulation.

It should be noted that the large Δt values investigated in Figure 4.20 are not practical for simulations, and are only used to demonstrate the efficacy of the reversal estimation method. Δt will typically be sufficiently small enough to ensure that this error is negligible.

4.2.3 Iwan model

The Iwan model requires an initial backbone function $f_{bb}(x)$ and is used to back-calculate the bilinear springs as shown in Figure 4.23a. The combined response of

N_s number of bilinear hysteretic springs result in a global cyclic behaviour akin to the unload/reload behaviour expected in nonlinear dynamic soil-structure interaction. One major advantage of the Iwan model is that the reversal coordinates are not required to define the subsequent stress path, which is a notable cause for stability in the Masing model. Instead, the reversal behaviour is implicitly defined in the global spring due to the yielding conditions of the individual bilinear springs. No reversal location estimation is required.

Figure 4.21 shows the individual bilinear spring models that constitute the Iwan model for $N_s = 3$.

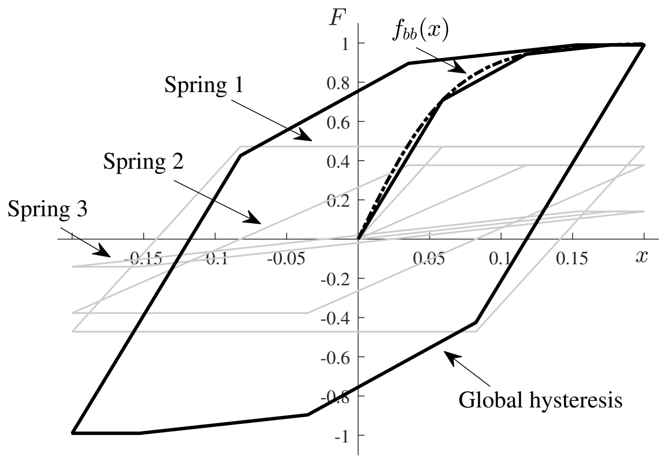

Figure 4.21: Individual Iwan springs and the global effective spring for $N_s = 3$

The global spring characteristics at x_{i+1} is determined by computing the individual bilinear spring states at x_{i+1}, and summing their reaction forces and tangent stiffnesses. The parameters of the bilinear spring model is shown in Figure 4.22, and Figure 4.23 illustrates the piecewising methodology for determining F_n and K_n using the backbone function $f_{bb}(x)$. n is the bilinear spring number. The process is defined in Table 4.2.

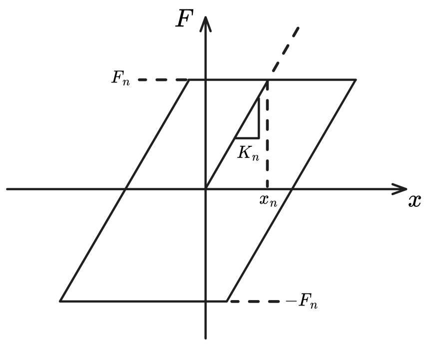

Figure 4.22: Parameter notation for individual bilinear springs in the Iwan model

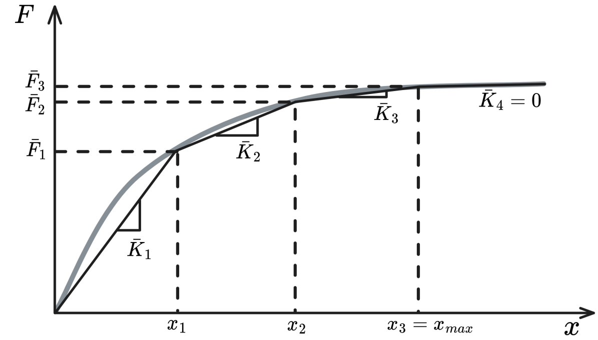

(a) Computing the piecewise backbone function from the original backbone function $f_{bb}(x)$

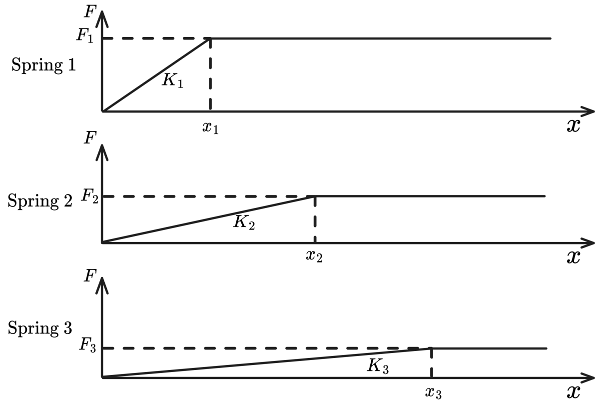

(b) Individual bilinear spring backbone functions

Figure 4.23: Piecewising the backbone function into N_s number of parallel springs

Table 4.2: Methodology for piecewising the backbone function into N number of parallel springs

Defining Iwan Springs

1. Determine backbone yield displacement x_{ult}
2. Calculate space yield displacements such that $x_n = \dfrac{x_{ult}}{N_s} n$
3. Find forces along backbone function $\bar{F}_n = f_{bb}(x_n)$ for each x_n
4. Determine piecewise stiffnesses along backbone $\bar{K}_n = \Delta \bar{F}_n / \Delta x_n$
5. Compute stiffnesses of bilinear springs $K_n = \Delta \bar{K}_n$
6. Determine yield forces $F_n = K_n x_n$

The influence of the number of bilinear springs, N_s, on simulating nonlinear systems is examined herein. The system is described using the same properties as the Masing analysis in Section 4.2.2. The time step is set to $\Delta t = 0.01$s such that it is sufficiently small and does not introduce algorithmically-induced errors. Five Iwan models are trialled; where $N_s = 3, 5, 10, 20$ and 50. The results are presented in Figure 4.24.

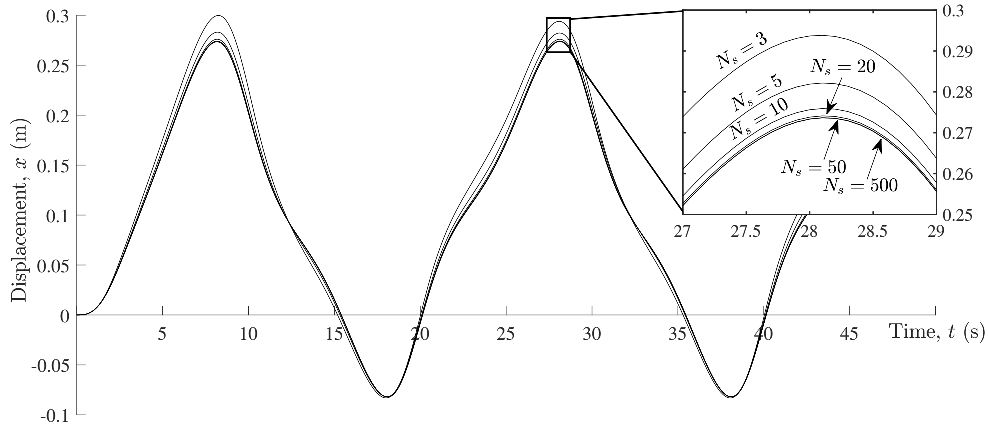

Figure 4.24: Sensitivity of the Iwan model to the number of bilinear springs N_s

Figure 4.24 shows that the spring system converges to a solution as N_s increases. This is expected, as the piecewise backbone function approaches the original backbone function as $N_s \to \infty$. N_s also influences the system's maximum displacement, which is likely due to the low resolution of the piecewise discretisation process. For example, when $N_s = 3$, Figure 4.23a shows that there is a significant under-approximation of the initial stiffness (i.e. $\bar{K}_1 < f'_{bb}(0)$). As a consequence, the initial stiffness of the global spring is reduced and the restoring force is initially much less than if N_s was large. Increasing N_s reduces this initial stiffness deficit, therefore the nonlinear systems with more bilinear springs will demonstrate a stiffer response, as shown in Figure 4.24. Considering the importance of the reversal stiffness as outlined in the Original Masing Rules in Section 2.3.5, the initial stiffness must be accurately represented in the piecewise backbone function (Vucetic & Dobry, 1991).

It is shown that there is a negligible difference between $N_s = 50$ and $N_s = 500$, therefore $N_s = 50$ provides a reasonable degree of convergence towards the 'true solution', which is when $N_s \to \infty$. However, for large MDOF systems, the number of nonlinear spring elements in the system is effectively increased by a factor N_s, which can be computationally expensive. Minimising the value of N_s is therefore ideal. An alternative solution is to implement a non-uniform piecewise discretisation for the yield displacements x_n, such that the initial stiffness of the global Iwan spring is more accurately represented for lower N_s values. This would require changes to Step 2 in Table 4.2. However, in the interest of simplicity, N_s is taken as 20 for all implementations of the Iwan model herein, as Figure 4.24 shows that the difference between $N_s = 20$ and $N_s = 500$ is minor.

4.2.4 Bouc-Wen model

The Bouc-Wen model does not require a backbone function or explicit reversal coordinate estimates to define subsequent nonlinear stress paths. Instead, the Bouc-Wen method encapsulates the unload/reload characteristics by means of a slope field in f_s-x space, where β, γ and $\hat{n}$ control the shape (See Section 2.3.5). The differential equation is:

$$\frac{dz}{dt} = \frac{1}{x_{ult}}\dot{x}[1 - |z|^n(\beta + \gamma \text{sgn}(\dot{x}z))] \tag{4.63}$$

where z is the hysteretic function to be solved for that governs the stress path. The equation to determine the hysteretic force $f_s(x)$ is described in Equation 2.40, and α is taken as zero herein to remove post-yielding stiffness properties (i.e. $F_{el} = 0$). f_s and k_T are therefore as follows:

$$f_s(x) = F_h = F_{ult}z \tag{4.64}$$

$$\frac{df_s}{dx} = k_T = F_{ult}\frac{dz}{dx} \tag{4.65}$$

$\frac{dz}{dx}$ can be determined from the chain rule:

$$\frac{dz}{dx} = \frac{dz}{dt}\frac{dt}{dx} = \frac{dz}{dt}\frac{1}{\dot{x}} \tag{4.66}$$

therefore the velocity term in Equation 4.63 is eliminated and the differential equation to solve for is simply:

$$\frac{dz}{dx} = \frac{1}{x_{ult}}[1 - |z|^n(\beta + \gamma \text{sgn}(\dot{x}z))] \tag{4.67}$$

In order for the Bouc-Wen model to be in a comparative form to the Masing and Iwan model, the shape parameters controlling the differential equation must be defined such that the shape of the stress paths resemble the backbone function when monotonically loaded, and the unload/reload behaviour should demonstrate the EMR. This can be achieved by deriving an analytical solution to Equation 4.63 under specific conditions. It is recommended by Gerolymos and Gazetas (2005a) that taking $\beta = \gamma = 0.5$ can resemble Masing-type behaviour as established by the rules in Section 2.3.5. Figure 4.25 illustrates the various regions along the hysteretic function $z(x)$ for different signs of $\dot{x}$ and z when $\beta = \gamma = 0.5$. n controls the bilinearity of the solution.

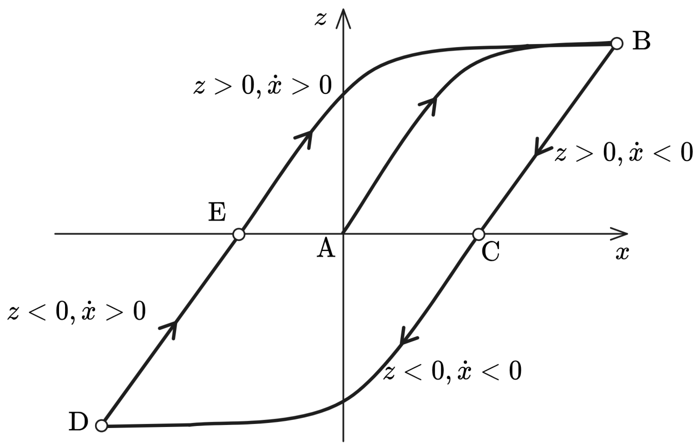

Figure 4.25: Regions of interest in the Bouc-Wen function when $\beta = \gamma = 0.5$

The signage of z and $\dot{x}$ are crucial for determining the direction of the slope field. It is shown in Figure 4.25 that the initial monotonic reaction occurs in region AB when both z and $\dot{x}$ are greater than zero. Similarly, regions BC and DE are considered the initial reversal regions that satisfy the OMR criteria.

Taking the conditions pertaining to region AB, the differential Equation 4.63 can be simplified. Notably, when $n = 2$, Equation 4.63 is simplified further, making it amenable to analytical solutions. Therefore, when $\beta = \gamma = 0.5$, $n = 2$, $z > 0$ and $\dot{x} > 0$, Equation 4.67 is simplified and takes the form:

$$\frac{dz}{dx} = \frac{1}{x_{ult}}(1 - z^2) \tag{4.68}$$

Separation of variables leads to:

$$\int \frac{1}{1 - z^2} dz = \frac{1}{x_{ult}} \int dx \tag{4.69}$$

where both sides can be integrated and rearranged for $z(x)$, which yields:

$$z = \frac{Ae^{2x/x_{ult}} - 1}{Ae^{2x/x_{ult}} + 1} \tag{4.70}$$

where A is an integration constant and can be determined by applying the initial conditions $z = 0$ and $x = 0$, giving $A = 1$. Therefore, the solution to the differential equation is:

$$z = \frac{e^{2x/x_{ult}} - 1}{e^{2x/x_{ult}} + 1} \tag{4.71}$$

If the numerator and denominator are multiplied by $e^{-x/x_{ult}}$, the solution can be simplified to the hyperbolic tangent function, i.e.:

$$z(x) = \frac{e^{x/x_{ult}} - e^{-x/x_{ult}}}{e^{x/x_{ult}} + e^{-x/x_{ult}}} = \tanh\left(\frac{1}{x_{ult}}x\right) \tag{4.72}$$

Note that, according to Figure 2.27b, $x_{ult} = F_{ult}/k_0$. Therefore, substituting Equation 4.72 into Equation 4.64 gives the general backbone function $f_{bb}(x)$ described in Equation 2.34. The solution of the Bouc-Wen differential equation under monotonic conditions $z > 0$ and $\dot{x} > 0$ is therefore a hyperbolic tangent function when $\beta = \gamma = 0.5$ and $n = 2$, and is in a comparative form to the Masing and Iwan models. This is validated in Appendix C.4 by comparing the monotonic response of the three dynamic hysteretic theories informing a dynamic pile model by slowly increasing the head load.

A solution estimate for the Bouc-Wen differential equation is computed at each time step using the fourth order Runge-Kutta (RK4) method, which is a numerical integration technique that is commonly used to solve first order ordinary differential equations (Butcher, 1996). The RK4 method approximates the solution of a differential equation by considering multiple intermediate points within each step, and then using a weighted average of each intermediate point to estimate the final solution.

4.3 Dynamic p-y models

This section aims to provide a comparative assessment of the performance of hysteresis algorithms in a dynamic p-y model using the Generalised-α numerical integration method. A sensitivity study is first conducted to evaluate the performance of the Masing, Iwan and Bouc-Wen models, where idealised two-way and one-way load and moment profiles are applied to a monopile-only model. The objective of this investigation is to discern the strengths and vulnerabilities inherent with each hysteresis model within an MDOF framework by evaluating the stability and computational efficiency for different loading conditions and algorithm parameters.

The investigation is then extended to include an integrated 3.6MW OWT superstructure on top of the dynamic p-y model. The superstructure ensures that the vibration modes are adequately representative of an OWT system supported by a pile, and inertial loads imposed on the substructure are realistic. Wind and wave load histories are applied to the OWT system to encourage realistic soil-structure interaction mobilisation. Finally, optimal algorithmic parameters are determined that facilitate a stable and efficient model for the OWT system supported by a dynamic p-y model.

4.3.1 MDOF hysteresis sensitivity study

A simplified reference monopile model is used for this sensitivity analysis. The monopile properties are described in Table 4.3 and the model is illustrated in Figure 4.26. The monopile is assumed to be fully cored, therefore the soil mass within each pile section is considered as a lumped mass applied to the nodes for that respective layer.

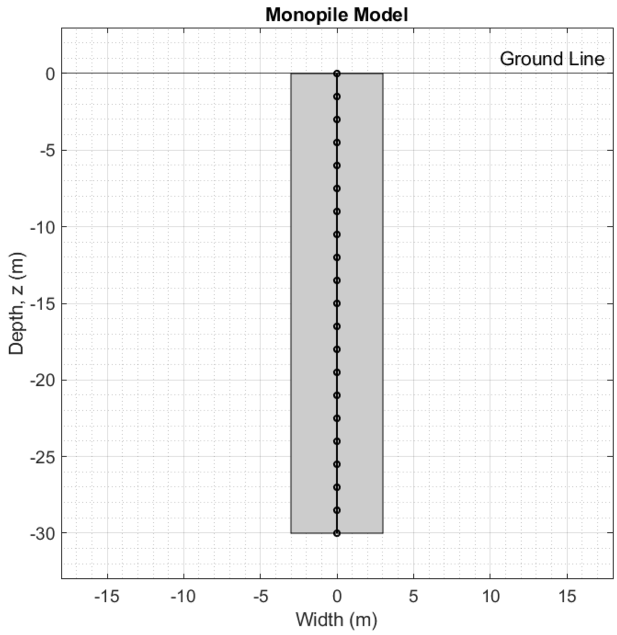

Figure 4.26: MDOF hysteresis model for sensitivity study with $N = 20$ (from MATLAB GUI)

Table 4.3: Reference monopile geometry for the MDOF analyses

Parameter	**Value**	**Unit**
diameter, D	6	m
wall thickness, t	0.08	m
Embedment, L	30	m
Density, ρ	7850	kg/m^3
Young's Mod., E	210,000	MPa
Eccentricity, h	0	m
Num. springs, N	20	-
Damping ratio, ζ	0.2	%
Natural Frequency, f_n	9.43	Hz

The Rayleigh method is used to define the viscous damping (Section 2.3.4). All spring models are informed using the API sand model for convenience, where $\gamma = 20$ kPa and $\phi' = 35°$.

Figures 4.27a and 4.27b display the spectral radii corresponding to different ρ_∞values alongside the first five normalised modal frequencies of the MDOF system for time steps of $\Delta t = 0.01$ s and $\Delta t = 0.05$ s, respectively. The normalised modal frequencies are obtained through eigenanalysis of the MDOF system using the global mass and initial stiffness matrices (Section 2.3.2), multiplied by Δt.

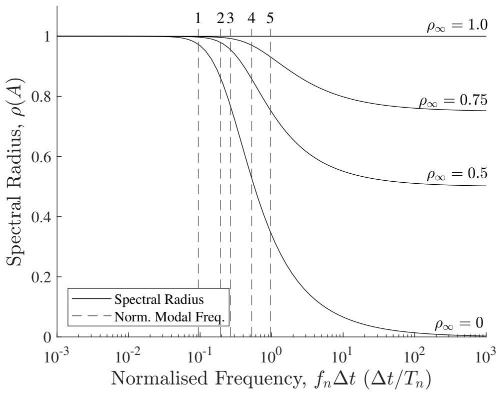

(a) $\Delta t = 0.01$ s

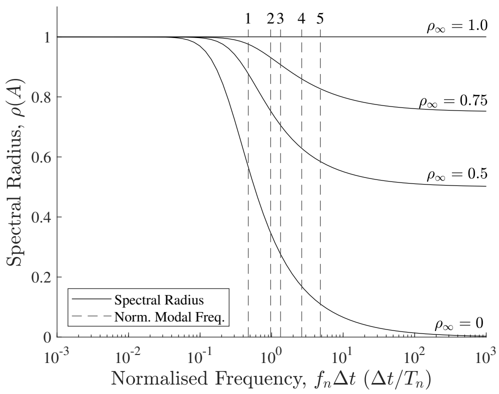

(b) $\Delta t = 0.05$ s

Figure 4.27: Spectral radius diagram for the first 5 normalised modal frequencies of the MDOF system

It is clear from Figure 4.27 that, when $\rho_\infty \leq 1$, the spectral radius decreases as the normalised frequency increases. This is indicative of the numerical dissipation inherent with the Generalised-α algorithm, which is more effective for the higher modes of the system. Varying Δt shifts the normalised modal frequencies and changes the corresponding $\rho([A])$, therefore the discretisation of time also has a significant influence on the anticipated numerical dissipation in the estimated solution.

Figure 4.27a shows that, when $\rho_\infty = 1$, 0.75 and 0.5, the spectral radius $\rho([A])$ is 1 for the first natural frequency when $\Delta t = 0.01$ s. Higher modes have lower $\rho([A])$, therefore are dissipated. Higher modes of vibration in MDOF systems are known to be highly dependant on the constitutive model properties of the finite element model (Bathe & Wilson, 1976; Kontoe et al., 2008). This is observed in Appendix C.1. Furthermore, $\rho(A) \leq 1$ for all values of Δt and ρ_∞values, which is indicative of unconditional stability for all parameters in the Generalised-α algorithm. As such, any observed instabilities will therefore be a consequence of the hysteresis models, and not the numerical methods used. The generalised-α method is validated in Appendix C.3.

When $\rho_\infty = 1$, The Generalised-α method collapses to the CAA Newmark method (see Section 4.1), which is the most common TMA for linear MDOF dynamic analyses due to its modal retention shown in Figure 4.27 (Chopra, 2013; Goudreau & Taylor, 1973; Kampitsis et al., 2013; Markou & Kaynia, 2018; Tsaparli et al., 2017). This algorithm configuration therefore provides a benchmark for the following nonlinear analyses, and will also be evaluated.

A two-way simple sine load and moment history are applied to the ground line node. This is a strategic simplification to evaluate the performance of the hysteresis models in a controlled environment, and is not representative of the complex loading conditions experienced by OWT foundations. To add, the natural frequency of the pile is 9.43 Hz (Table 4.3), which is a superficially high value for monopile systems. It is important to note that the water, turbine tower, and nacelle mass are neglected in this study. The superstructure will have a marked affect on natural vibrations of the system, including the anticipated load history applied at the mudline due to inertial effects. However, the objective of this investigation is to qualitatively evaluate the performance of the hysteresis models in the context of a MDOF system under ideal loading conditions. They are therefore neglected at this stage.

The load and moment functions are described in Equation 4.73.

$$F(t) = \Psi F \sin(\omega t), \qquad M(t) = \Psi M \sin(\omega t) \tag{4.73}$$

where Ψ is the load factor, F is the load amplitude, M is the moment amplitude, and ω is the circular frequency of the external load and moment ($\omega = 2\pi f$). The frequency is $f = 0.1$ Hz as an approximation to the general loading history caused by a combination of wind and wave loads (see Figure 2.17). F and M are derived to be consistent with SLS design compliance such that the load and moment histories are assumed to resemble normal turbine operating conditions. The computed horizontal load and overturning moment at the ground line are 1155 kN and 93225 kN m, respectively. For full derivation, see Prendergast et al. (2018). The load factor Ψ is an arbitrary constant to encourage different degrees of mobilisation such that the unload-reload behaviour of each hysteresis model can be reviewed.

The sensitivity study involves adjusting simulation parameters to assess potential instability or divergence in hysteresis models. Initially, the TMA parameters are set at $\rho_\infty = 1$ and $\Delta t = 0.05$ s, providing a benchmark for subsequent modifications. The load factor is then arbitrarily increased, and the ρ_∞ and Δt value required to maintain stability is documented. This approach provides a practical and systematic methodology for evaluating the sensitivity of each hysteresis model to TMA parameters, aiding in the selection of the most robust and stable model for application to fully-integrated OWT-monopile models. Simulations are run for $t = 1200$s such that convergence can be observed. This corresponds to 120,000 time steps for $\Delta t = 0.01$ s, 24,000 time steps for $\Delta t = 0.05$ s, and 120 load cycles for $f = 0.1$ Hz.

4.3.1.1 Analysis and results

A low-amplitude sinusoidal load history is applied to study the behaviour of the hysteresis model under small strains. The load factor is set to $\Psi = 1$, therefore the maximum load and moment are within serviceability limits and mobilisation is expected to be minimal. The performance of each model is shown in Figures 4.28 to 4.30. The p-y hystereses for three different springs are plotted to provide an overall understanding of the entire response of the pile.

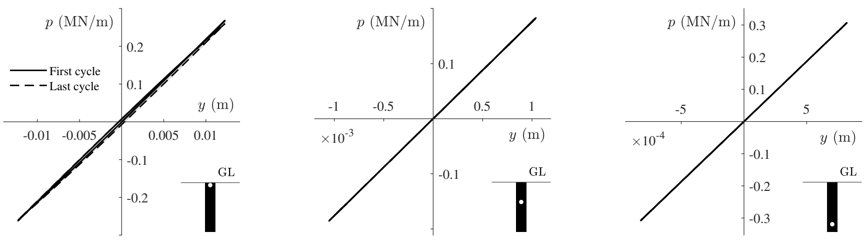

(a) Depth = 1.5m (b) Depth = 12m (c) Depth = 25.5m

Figure 4.28: Masing model response for $\Psi = 1$, $f = 0.1$ Hz, $\Delta t = 0.05$ s and $\rho_\infty = 1$

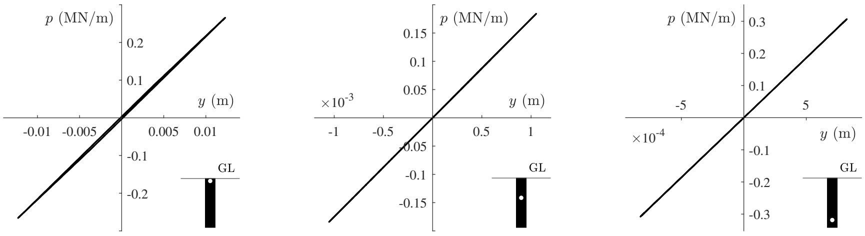

(a) Depth = 1.5m (b) Depth = 12m (c) Depth = 25.5m

Figure 4.29: Iwan model response for $\Psi = 1$, $f = 0.1$ Hz, $\Delta t = 0.05$ s and $\rho_\infty = 1$

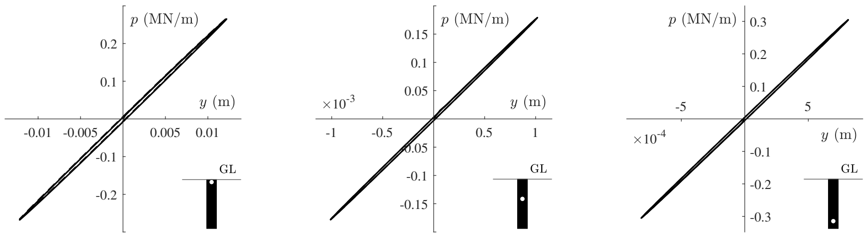

(a) Depth = 1.5m (b) Depth = 12m (c) Depth = 25.5m

Figure 4.30: Bouc-Wen model response for $\Psi = 1$, $f = 0.1$ Hz, $\Delta t = 0.05$ s and $\rho_\infty = 1$

All models show minimal mobilisation in each spring, which is expected for low-amplitude load profiles derived from SLS conditions. Minor hystereses are observed for each model at $z = 1.5$m, but become linear at greater depths due to the API sand model and an attenuation in lateral pile displacement. Figure 4.28a shows a slight shift in the p-y cycle at the end of the simulation, but is not present in the deeper layers. This is likely due to the Masing model's constitutive laws defining the reload curves. The hyperbolic tangent function describing the backbone curve does not exhibit an initial linear region, therefore nonlinear behaviour is expected regardless of displacement magnitude. In contrast, the Iwan model discretises the backbone into linear sections, therefore small strains are definitively linear. The Bouc-Wen model exhibits minor p-y loop cycles at all depths, but the response is in general elastic and stable. All models have comparable p-y responses and exhibit stability.

4.3.1.2 Two-way loading

The following simulations increase the amplitude factor to $\Psi = 15$ to encourage hysteresis mobilisation. The p-y responses are presented in Figures 4.31 to 4.33 for each model. $\Delta t = 0.05$s and $\rho_\infty = 1$ (CAA) are used for this analysis.

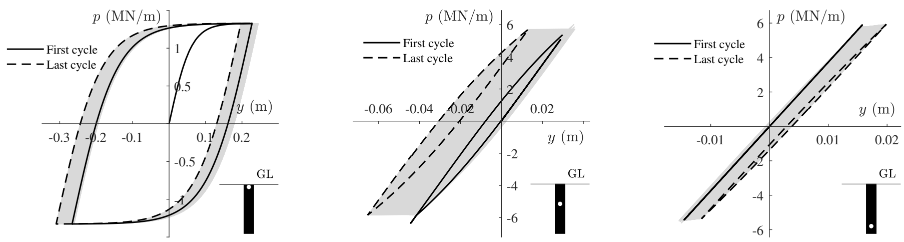

(a) Depth = 1.5m (b) Depth = 12m (c) Depth = 25.5m

Figure 4.31: Masing model response for $\Psi = 15$, $\Delta t = 0.05$ s and $\rho_\infty = 1$

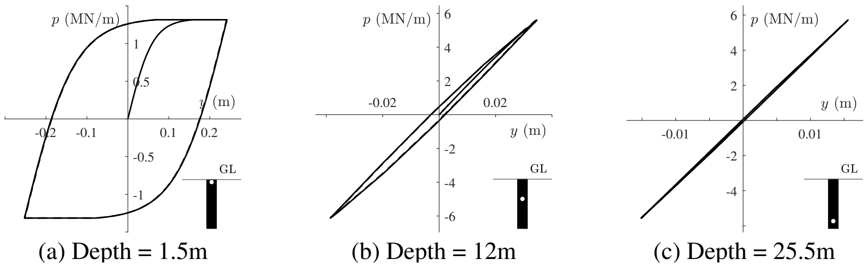

Figure 4.32: Iwan model response for $\Psi = 15$, $\Delta t = 0.05$ s and $\rho_\infty = 1$

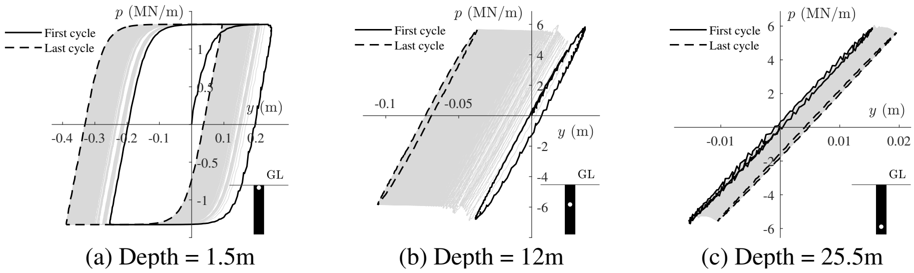

Figure 4.33: Bouc-Wen model response for $\Psi = 15$, $\Delta t = 0.05$ s and $\rho_\infty = 1$

All hysteresis models demonstrate a high degree of mobilisation when $\Psi = 15$ near the ground line due large pile deflections in weaker soil layers near the ground line. Figure 4.31 and Figure 4.33 shows that the Masing and Bouc-Wen model experiences a cyclic drift at all depths, and suggest an accruing global counter-clockwise pile rotation. Considering that the sinusoidal load is applied symmetrically at the pile head and no empirical soil-structure damage model is implemented, this behaviour is erroneous and a consequence of the hysteresis model. Figure 4.32 shows that the Iwan model does not exhibit global pile rotation. The reversal laws defined by the Masing and Bouc-Wen are dependent on the velocity of the node. Subsequent reaction curves of the Masing hysteresis model depend on the p-y coordinate of the node's maximum displacement (Equation 2.36). Additionally, the governing differential equation for the Bouc-Wen model (Equation 4.63) is a function of the velocity. The velocity of the node is a critical parameter in the Masing and Bouc-Wen models. The high natural frequency of the monopile (9.43 Hz) leads to small vibrations during the initial loading sequence, which can cause unwanted oscillations in the p-y response. This transience arises from inappropriate initial conditions where the model's starting conditions do not precisely match the system's equilibrium within the first time step, resulting in a significant acceleration that triggers vibration modes (Bathe & Wilson, 1976). This behaviour is mostly evident in the Bouc-Wen model's response in Figure 4.33, where the first cycle exhibits spurious noise due to the initial load transience at all depths. The Iwan model does not exhibit this behaviour, as the reversal laws are defined based on a yield criterion of individual bilinear springs (Figure 4.21), which is independent on the velocity of the node. In general, the transience is eventually dissipated in part due to Rayleigh damping and the energy dissipation inherent with the hysteresis model.

Transience is a common issue for large MDOF dynamical systems and can be resolved by increasing the damping ratio to quickly dissipate problematic vibrations (Hilber & Hughes, 1978; Wilson et al., 1972). However arbitrarily increasing the damping ratio can result in an overestimation of the idealised dissipation effects encapsulated by the Rayleigh viscous damping model. Decreasing ρ_∞ is therefore investigated. To add, given that $T_n = 1/f_n \simeq 0.1$s and $\Delta t = 0.05$s, the time discretisation resolution is not sufficiently small enough to sample the high frequency transience experienced in the first loop. Decreasing Δt is another solution, therefore $\Delta t = 0.01$s is also investigated. The results are shown Figure 4.34 and Figure 4.35.

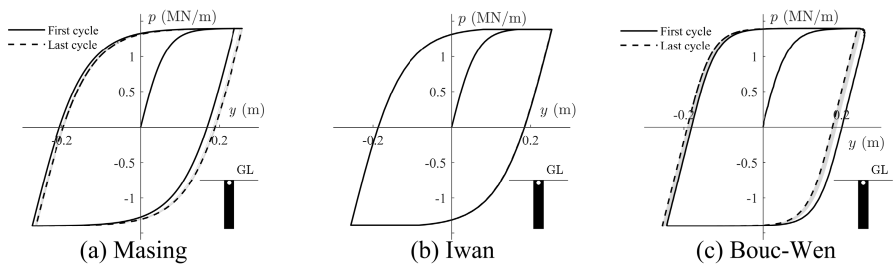

Figure 4.34: Masing, Iwan and Bouc-Wen model responses for $z = 1.5$ m, $\Psi = 15$, $\rho_\infty = 1$, and $\Delta t = 0.01$ s

Evidently, decreasing the time step limits the drift in the Masing and Bouc-Wen models. The Masing model converges within the first cycle, whereas the Bouc-Wen model still exhibits minor drifting characteristics without convergence after $t = 1200$ s. The Iwan model is unaffected by the change in Δt.

The stability of the rate-dependent hysteresis models has improved. However, this is at the expense of computational spend, as the number of required steps in time (and therefore the number of operations) has increased by a factor of five. The effect of decreasing ρ_∞ to add numerical dissipation (whilst $\Delta t = 0.05$ s) is shown in Figure 4.35.

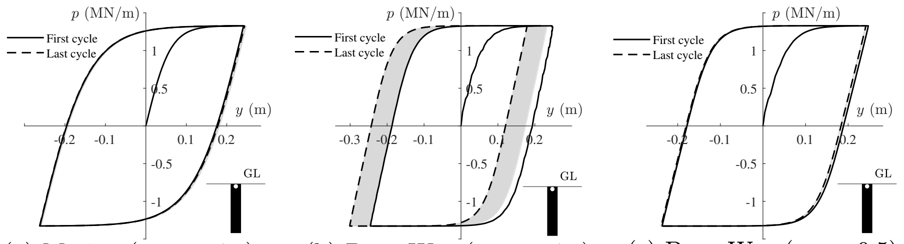

(a) Masing ($\rho_\infty = 0.75$) (b) Bouc-Wen ($\rho_\infty = 0.75$) (c) Bouc-Wen ($\rho_\infty = 0.5$)

Figure 4.35: Masing and Bouc-Wen model response for $z = 1.5$ m, $\Psi = 15$, and $\Delta t = 0.05$ s

Figure 4.35a shows that, when $\rho_\infty = 0.75$, the Masing model exhibits no drift and converges to the same solution as the Iwan model when $\rho_\infty = 1$ (Figure 4.32). However, hysteretic drift is only mitigated in the Bouc-Wen model, but still present when $\rho_\infty = 0.75$ (Figure 4.35b). Figure 4.35c shows that further decreasing ρ_∞ to 0.5 suppresses the lateral shift in the p-y response. When the drift is removed, the Masing and Bouc-Wen model converge to the same solution as the Iwan model when $\rho_\infty = 1$ shown in Figure 4.32a.

It is important to note that the degree of numerical dissipation for the first five modes of the model when $\rho_\infty = 0.75$ and $\Delta t = 0.05$s are shown in Figure 4.27b. Both cases indicate that the spectral radius is less than one for the first mode, and is therefore being dissipated by the TMA. Whilst it can achieve a stable hysteresis, it may not be representative of the true physical behaviour of the monopile. This is investigated in more detail in Section 4.3.2. The data in Figure 4.35 suggest that the Bouc-Wen model is the most sensitive to the transient response of the MDOF system.

It is shown in Figure 4.34 that the general shape of the Bouc-Wen hysteresis is fundamentally different to the Iwan and Masing model. This is due to differences in the constitutive laws governing the unload/reload behaviour. Unlike the Masing model, the Bouc-Wen differential equation does not explicitly adhere to the criteria defined by the Extended Masing Rules. After a change in direction, the stress path exhibits a linear relationship until crossing the displacement axis, followed by the hyperbolic tangent function (as discussed in Section 4.2.4). This behaviour is clearly illustrated in Figure 4.36, where the tangent stiffness of each hysteresis model is plotted against time at depth $z = 1.5$ m. Only the first three cycles are plotted for clarity.

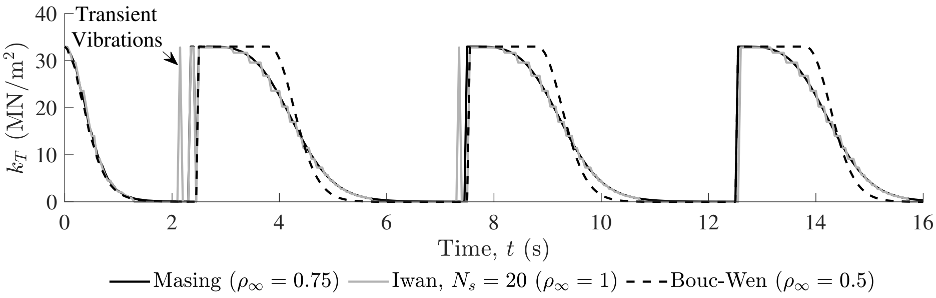

Figure 4.36: Tangent stiffnesses for $z = 1.5$ m, $\Psi = 15$, and $\Delta t = 0.05$ s for each Hysteresis model

The Bouc-Wen model briefly maintains its initial stiffness before decreasing, which is not representative of the highly nonlinear nature of soil behaviour (Hardin & Black, 1968; Idriss et al., 1978; Vucetic & Dobry, 1991). Under specific conditions (see Figure 4.25), the stress path reverts to a hyperbolic function if the model is parametrised using $\beta = \gamma = 0.5$ and $n = 2$. Consequently, the rate of change of k_T is comparable to that of the Masing and Iwan model, taking the same shape.

All models adhere to the second extended Masing rule, where the stress path returns to the initial stiffness upon reversing direction, as discussed in Section 2.3.5. In Figure 4.36, it is evident that the Iwan model exhibits a piecewise-linear behaviour, with its tangent stiffness taking a stepped form of the Masing model's k_T. Moreover, during directional reversals caused by higher modal frequencies, the Iwan model briefly returns to the initial stiffness. Despite having $\rho_\infty = 1$ (indicating that natural modal vibrations are not numerically dissipated), the Iwan model still maintains stability, highlighting its robustness as a hysteresis model when compared to the Bouc-Wen and Masing models.

4.3.1.3 One-way loading

The dynamic *p*-*y* models are exposed to force and moment histories representative of one-way loading conditions to observe the performance under asymmetrical loading conditions. The load factor is taken as $\Psi = 10$, and the load and moment functions are described using the following Equations:

$$F(t) = \Psi F(1 - e^{-t})\sin(\omega t), \qquad M(t) = \Psi M(1 - e^{-t})\sin(\omega t) \tag{4.74}$$

where the exponential term serves as a ramping function to gradually increase the load and moment profile to one-way conditions. The force applied at the ground line is plotted in Figure 4.37. The load and moment profiles are applied to each hysteresis model for $t = 1200$ s at $f = 0.1$ Hz (120 cycles). Each hysteresis model is parametrised using the TMA values that achieved stability and convergence in the two-way loading sensitivity analysis. The p-y responses are shown in Figures 4.38 to 4.40.

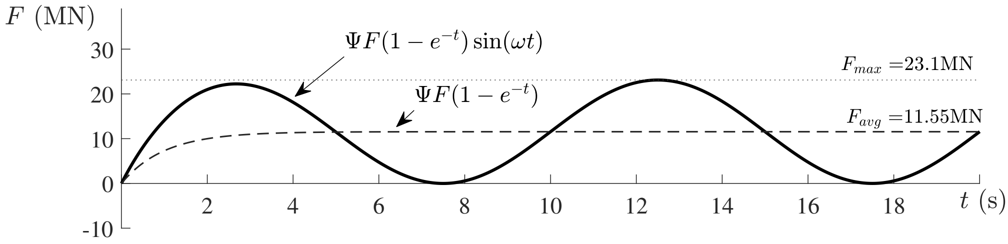

Figure 4.37: One-way load profile applied at the ground line (first 20 seconds)

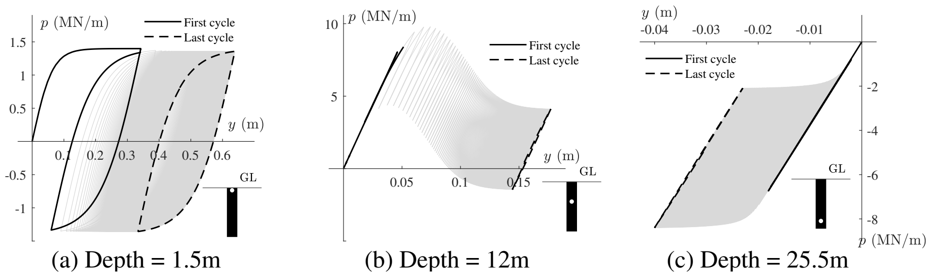

Figure 4.38: Masing model response for $\Psi = 10$, $\Delta t = 0.05$s and $\rho_\infty = 0.75$

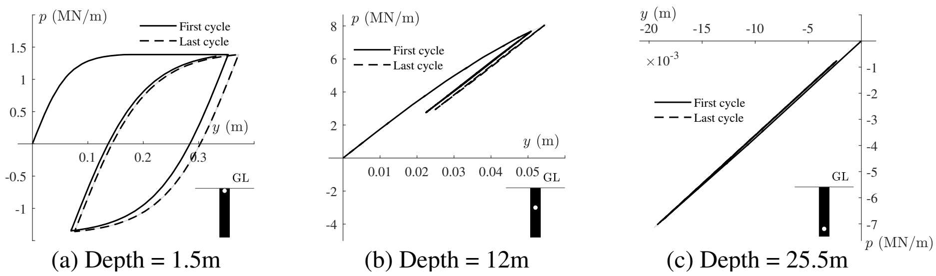

Figure 4.39: Iwan model response for $\Psi = 10$, $\Delta t = 0.05$s and $\rho_\infty = 1$

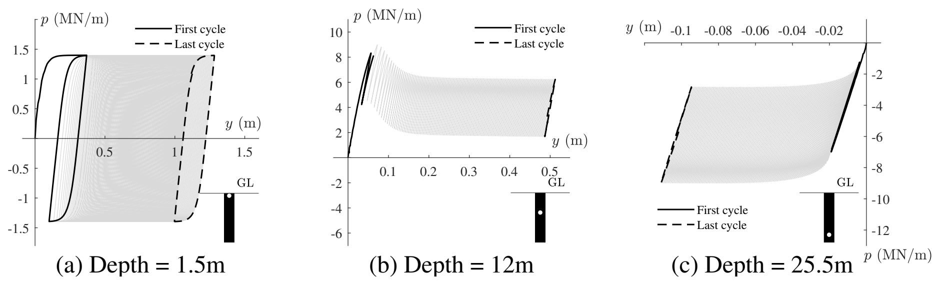

Figure 4.40: Bouc-Wen model response for $\Psi = 10$, $\Delta t = 0.05$s and $\rho_\infty = 0.5$

Figures 4.38 and 4.40 demonstrate excessive hysteresis drift when one-way loading conditions are applied to the Masing and Bouc-Wen models, regardless of the TMA parameters. The evident strain accumulation in the Masing model is due to Pyke's scaling coefficient C, which is used to estimate the scale of the subsequent stress path. Equation 2.36 suggests that C is a directionally-dependent function of the ratio between the soil pressure at the previous reversal event p_{rev} and the ultimate soil pressure p_{ult} (p_{rev}/p_{ult}). Figure 4.41 isolates the problem using idealised oscillations bound between y_{min} and y_{max}.

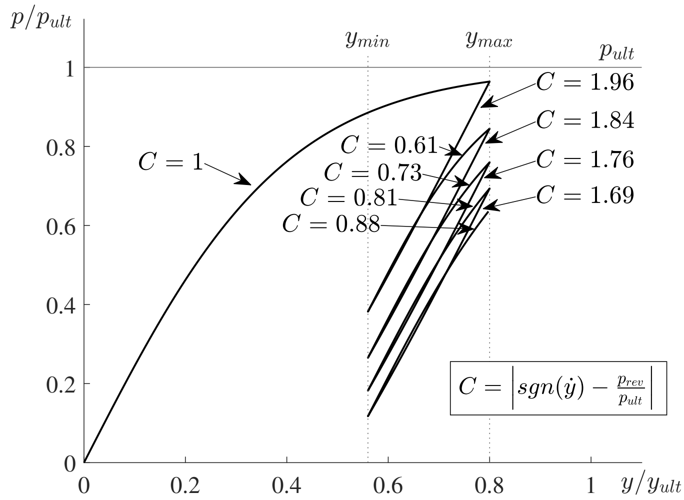

Figure 4.41: Example of Pyke's scaling coefficient C for one-way loading conditions

It is clear that C is a function of the velocity signage, and is therefore highly dependent on the direction of movement. Initial loading conditions correspond to $C = 1$, and the following magnitudes of C after reversals fluctuate significantly depending on the direction of motion. The first full load cycle therefore cannot close the hysteresis loop, and a drift is observed. The tangent stiffness of the stress path is therefore weaker when the velocity is positive, generating a superficial ratchet-type behaviour in the foundation model, which is clearly observed in Figure 4.38b. The Masing model is therefore not suitable for one-way loading conditions, unless appropriate modifications are made to the fundamental scaling laws describing the the unload-reload curves.

Figure 4.40 shows that the Bouc-Wen model exhibits a similar behaviour. Recall from Figure 4.25 that the Bouc-Wen p-y loop exhibits a linear stiffness when $(z < 0, \dot{y} > 0)$ or $(z > 0, \dot{y} < 0)$, and a hyperbolic tangent when $(z < 0, \dot{y} < 0)$ or $(z > 0, \dot{y} > 0)$ (if $\beta = \gamma = 0.5$ and $n = 2$). This was observed in Figures 4.34 and 4.36. This can lead to significantly different stress paths depending on the direction of motion, as the tangent stiffness can be linear in one direction and nonlinear in the other. The corresponding effect is a superficial ratcheting behaviour in the p-y response, as observed in Figure 4.40b. The Bouc-Wen model is therefore not suitable for one-way loading conditions.

The Iwan model is independent of velocity, therefore the stress path will not change depending on the direction of motion. The response to one-way loading is shown in Figure 4.39, and demonstrates a fast convergence after the first cycle. It is likely that the first cycle is different to subsequent cycles due to large inertial forces within the pile when initially loaded.

Exhibiting no numerical drift is an extremely important quality for hysteretic OWT models, as the loading conditions are typically one-way (Leblanc et al., 2010b; Page et al., 2021). A hysteresis that can facilitate asymmetrical loading conditions without numerically-induced accumulated displacements can serve as a basis for well-informed empirical ratcheting models, as the source of ratcheting will be a function of the soil layer parameters and not the constitutive hysteresis model.

4.3.1.4 Summary

A sensitivity study evaluated the performance of the Masing, Iwan and Bouc-Wen hysteresis models under small-strain and large-strain loading conditions. The Generalised-α algorithm was used to solve dynamic equilibrium for the nonlinear MDOF system, and the influence of the ρ_∞ parameter was investigated for hysteretic systems. It was found that the Masing and the Bouc-Wen models are sensitive to the initial high-frequency transience, and their stability is compromised unless numerical dissipation is applied or the time discretisation is sufficiently small. Adjusting the numerical dissipation is favourable, as increasing the number of time steps is computationally expensive. However, it can lead to over-dissipation for the first frequency, which may not be physically representative. It is unclear from this study if the stability condition is a function of the natural modes of the system, which is investigated further in Section 4.3.2.

The Masing and Bouc-Wen models may not be suitable for one-way loading conditions, as the stress path is highly dependent on the direction of motion. The Iwan model was found to be the most robust, as it was stable for all values of ρ_∞, Δt and types of loading. The study showed that the modal frequencies of the model monopile did not affect the efficacy of the Iwan hystereses, therefore $\rho_\infty = 1$ (Newmark-β CAA method) is sufficient for dynamic p-y models of this type.

The constitutive laws describing the hysteresis stress path in the Iwan model are independent of velocity, therefore no superficial ratcheting is observed in the p-y response. This is an important quality for hysteretic OWT models, as empirically-derived ratcheting models can be used to inform the source of ratcheting in the p-y response with confidence. Monopiles supporting OWTs experience a high degree of mobilisation during storm events, which typically leads to one-way loading conditions (Arany et al., 2017; Byrne & Houlsby, 2003; Leblanc et al., 2010b). Ratcheting is a common phenomenon in one-way loading conditions, and is caused by asymmetrical stress paths and the plasticity of the soil layers (Abadie et al., 2019; Houlsby et al., 2017; Ren et al., 2021; Williams et al., 2022). The Iwan model is therefore selected for application to the fully-integrated OWT-monopile model in Section 4.3.2.

It has been established from the sensitivity study that the a dynamic p-y model informed with Iwan springs can be sufficiently solved for using the classical Newmark-β algorithm ($\rho_\infty = 1$), as all vibration modes were captured and did not compromise the stability. However, high frequency modes may arise from many sources, such as noise in sensors when determining load histories. Out-of-phase wind and wave time series may also activate higher vibration modes. It is therefore important to investigate the consequence of high modal frequencies in the dynamic p-y model under realistic loading configurations.

4.3.2 Integrated dynamic p-y model

An OWT tower and nacelle structure is attached to the top of the monopile model described in Figure 4.26. Only the Iwan hysteresis model is investigated herein, as it was deemed the most robust soil-structure model in Section 4.2. The monopile is extended above the Mean Sea Level (MSL), and the length of the beam elements vary along the superstructure in the interest of minimising the number of degrees of freedom. The integrated model is illustrated in Figure 4.42, and the properties are summarised in Table 4.4.

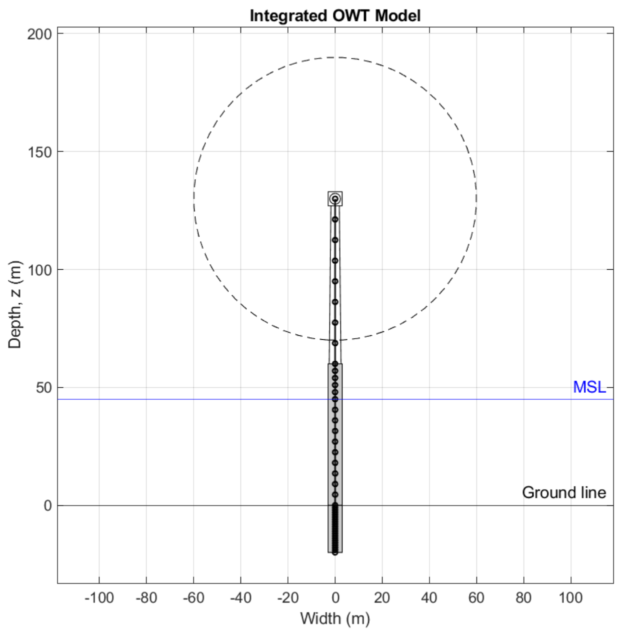

Figure 4.42: Integrated OWT-Monopile model (from MATLAB GUI)

Table 4.4: Properties of the integrated OWT-Monopile model

Section	**Length (m)**	**# elements**	**Dia. (m)**	**Thickness (m)**
Tower	70.0	8	5 to 3.5	0.045
Pile above MSL	15.0	5	6.0	0.080
Pile below MSL	45.0	10	6.0	0.080
Pile embedded	20.0	20	6.0	0.080

The section and material properties of the monopile can be found in Table 4.3. The monopile is extended 15m above MSL and the embedment depth is reduced to 20 m. A turbine tower of length 70m is attached to the top of the monopile. The tower is modelled using eight tapered beam elements, where the diameter varies from 5m to 3.5m. The stiffness and mass properties of the transition piece is neglected for simplicity. The nacelle is modelled by applying a lumped mass at the top horizontal and rotational node of the tower structure, where the mass and rotational inertia are taken as 230,000 kg and 3.5×10^{7} $\mathrm{kg\,m^{2}}$, respectively. The blade catchment diameter is taken as 120m. Eccentricities due to the offset of the nacelle mass from the vertical and the gyroscopic motion of the blades is not considered in this study. The Young's modulus and Poisson's ratio of the tower is 210 GPa and 0.3, respectively. The density of the tower is 7850 $\mathrm{kg\,m^{-3}}$. The submerged monopile section includes lumped masses to model the inertial effects of the hydrodynamic (external) and entrapped (internal) sea water. The lumped mass is calculated using the following Equation:

$$m_w = C_a \rho_w \frac{\pi D^2}{4} L_b 2 \tag{4.75}$$

where m_w is the added mass acting over a submerged monopile beam element, C_a is the coefficient of added mass multiplying the area of fluid displaced by the monopile, ρ_w is the density of sea water (1025 $\mathrm{kg\,m^{-3}}$).

4.3.2.1 Storm load design

Irregular wind and wave load profiles are applied to the nacelle and MSL, respectively. The load time series for each load type is generated by superimposing a number of linear sine waves with different amplitudes, frequencies and phases. The amplitude and frequencies are derived from appropriate power density spectra. The general equation used to describe the wind and wave load time series is as follows:

$$h(t) = \sum_{i=1}^{N} A_i \sin(2\pi f_i t + \phi_i) \tag{4.76}$$

where N is the number of linear waves, i denotes the ith wave, A_i is the amplitude, f_i is the frequency and ϕ_i is the phase. A_i and f_i are informed using the appropriate wave spectra for wind and wave loading as recommended by the IEC 61400-3 standard (IEC, 2009), and the phase of each wave ϕ_i is randomly generated between 0 and 2π. The spectral density $S(f)$ for a given wave spectrum can be converted to the wave amplitude A_i using the following equation:

$$A_i = \sqrt{2S(f_i)\Delta f} \tag{4.77}$$

where Δf is the frequency bandwidth and $S(f)$ is the frequency spectrum describing the stochastic frequency content of a wind speed or wave elevation amplitude. The time series for the wind and wave loads are derived in the following sections.

Wind Force Time Series

The wind speed $U(t)$ is described as the sum of the mean wind speed $\bar{U}$ and the random turbulence $u(t)$, as shown in Equation 4.78.

$$U(t) = \bar{U} + u(t) \tag{4.78}$$

$\bar{U}$ is determined using the wind shear power law described in Equation 4.79 for a given reference height z_r.

$$\bar{U} = U_r \left(\frac{z}{z_r}\right)^{\alpha} \tag{4.79}$$

where U_r is the reference wind speed at height z_r and α is the shear exponent taken as $\alpha = 0.12$ for open seas (Wilson, 2003). The random turbulence $u(t)$ is generated by superimposing a number of linear sine waves with different amplitudes, frequencies and phases, as described in Equation 4.76. The wind speed amplitudes for a given frequency of the individual sine waves are described using the Kaimal spectrum (IEC, 2009), and the wind speed power spectral density function is defined as follows:

$$S_u(f) = \frac{4\sigma_u^2 f}{(1+6f)^{5/3}} \tag{4.80}$$

where σ_u is the standard deviation of the wind speed spectrum, and can be defined $\sigma_u = I\bar{U}$. I is the intensity of the storm (IEC, 2009). The wind speed amplitude spectrum is computed using Equation 4.77 for a given frequency, and the phase of each sine wave is randomised before superposition to achieve $u(t)$. The wind thrust time series can then be computed using the following expression:

$$F_u(t) = \frac{1}{2}\rho_a C_T \frac{\pi D_r^2}{4}\bar{U}^2 + \frac{1}{2}\rho_a C_T \frac{\pi D_r^2}{4} u(t)^2 \tag{4.81}$$

where ρ_a is the density of air (1.225kg m^{-3}), D_r is the turbine catchment diameter, and C_T is the thrust coefficient, approximated as $C_T = 7/\bar{U}$ (Arany et al., 2015).

Wave force time series

Similarly to the wind load, the sea wave elevation $\eta(t)$ is defined by superimposing linear waves with different amplitudes, frequencies and phases, of which the amplitudes and frequencies are informed using the JONSWAP spectrum (DNV, 2021; IEC, 2009). The wave elevation power spectral density function is defined as follows:

$$S_w(f) = \frac{\alpha g^2}{(2\pi)^4 f^5} \exp\left(\left(-\frac{5}{4}\left(\frac{f_p}{f}\right)^4\right)\right)\gamma^r \tag{4.82}$$

$$\alpha = 0.076\left(\frac{\bar{U}_{10}}{Xg}\right)^{0.22} \qquad f_p = \frac{22}{2\pi}\left(\frac{g^2}{\bar{U}_{10}^2 X}\right)^{1/3}$$

$$r = e^{\left(-\frac{(f-f_p)^2}{2\sigma_w^2 f_p^2}\right)} \qquad \sigma_w = \begin{cases} 0.07 & f \le f_p \\ 0.09 & f > f_p \end{cases}$$

where $\gamma = 3.3$, $\bar{U}_{10}$ is the wind speed after 10 minutes of measurement, X is the storm fetch, and σ_w is the standard deviation of the wave spectrum. The amplitudes of the sea waves are determined using Equation 4.77, and subsequently directly applied to Equation 4.76.

Under linear wave theory, it is assumed that the sum of forces due to the individual sine waves gives the force time series of the total wave elevation over time. The Morison equation can therefore be applied to compute the inertial and drag forces acting on the monopile for a given sine wave, and superimposed to determine the total wave force time series acting on the monopile. The Morison equations for the inertial and drag forces of the waves are as follows:

$$F_D = \frac{1}{2} C_d \rho_w D \left| v(s,z,t) \right| v(s,z,t) \tag{4.83}$$

$$F_I = C_m \rho_w \frac{\pi D^2}{4} \dot{v}(s,z,t) \tag{4.84}$$

where C_m and C_d are the inertial and drag coefficients, respectively. $v(s,z,t)$ and $\dot{v}(s,z,t)$ is the horizontal velocity and acceleration of the water particle, respectively, for a given water depth z and horizontal displacement s. The wave particle kinematics can be estimated using Airy's theory using Equations 4.85 and 4.86.

$$v(s,z,t) = \frac{H_i}{2} \omega_i \frac{\cosh(k_i(z+d))}{\sinh(k_i d)} \cos(ks - \omega_i t) \tag{4.85}$$

$$\dot{v}(s,z,t) = \frac{H_i}{2} \omega_i^2 \frac{\cosh(k_i(z+d))}{\sinh(k_i d)} \sin(ks - \omega_i t) \tag{4.86}$$

where $\omega_i = 2\pi f_i$, d is the water depth, and H_i is the wave height, which is double the amplitude determined from the JONSWAP wave model described in Equation 4.82 ($H_i = 2A_i$). k is the wave number and can be computed using the dispersion relation:

$$\omega_i^2 = g k_i \tanh(k_i d) \tag{4.87}$$

Equation 4.87 is an implicit function of k_i, therefore needs to be solved numerically. However, an explicit approximation can be used to estimate k for a given f_i and d using the following equation:

$$k_i = \frac{\omega^2}{g \left(\tanh\left(\frac{2\pi\sqrt{d/g}}{T_i} \right)^{3/2} \right)^{2/3}} \tag{4.88}$$

where $T_i = 1/f_i$ is the wave period. The total inertial and drag force produced by each sine wave can be computed by integrating Equations 4.83 and 4.84 over the submerged length of the monopile and ignoring time variations. Assuming a horizontal distance from the monopile of 0 ($s = 0$), and using 4.87, the maximum inertial force $\hat{F}_I$ and maximum drag force $\hat{F}_D$ are as follows:

$$\begin{aligned}\hat{F}_D =& \rho_w g \frac{C_d D}{2} \int_{-d}^{\eta(t)=0} v(s,z,t)\,|v(s,z,t)|\,dz \\ =& \rho_w g \frac{C_d D}{2} \left(\frac{H_i}{2}\right)^2 \left[\frac{1}{2} + \frac{k_i d}{\sinh(2k_i d)}\right]\end{aligned} \tag{4.89}$$

$$\begin{aligned}\hat{F}_I &= \rho_w g C_m \frac{\pi D^2}{4} \int_{-d}^{\eta(t)=0} \dot{v}(s,z,t)dz \\ &= \rho_w g C_m \frac{\pi D^2}{4} \frac{H_i}{2} \tanh(k_i d)\end{aligned} \tag{4.90}$$

Note that the wave elevation $\eta(t)$ is taken as zero to simplify the integral and represents a force distribution from MSL to the seabed along the monopile. According to Equations 4.85 and 4.86, the particle velocity is a cosine function of time and the acceleration is a sine function of time. The maximum inertial and drag forces therefore occur at a phase difference of $\pi/2$. Since $\cos t = \sin(t + \pi/2)$, the total wave force time series can be expressed as follows:

$$F_w(t) = \sum_{i=1}^{N} \left[\hat{F}_{I,i} \sin(\omega_i t + \phi_i) + \hat{F}_{D,i} \cos(\omega_i t + \phi_i)\right] \tag{4.91}$$

where ϕ_i is the random phase angle between 0 and 2π. The total wave force time series is then applied to the MSL of the monopile model.

Storm parameters

A fictitious storm event lasting for 20 minutes is generated using the methodology outlined above. The wave time series of the storm event is characterised by the JONSWAP spectrum and models waves for an average wind speed of $\bar{U} = 65$ m s^{-1} and a fetch of 150 km. Notably, this wind speed exceeds the turbine's cut-out threshold of 25 m s^{-1}, rendering the rotor idle in practice. Therefore, it is assumed that the wind load time series expected from a 65 m s^{-1} wind speed storm for an idle rotor is equivalent to that of a Kaimal spectrum with a mean wind speed of 25 m s^{-1} during operation. For a wind intensity of $I = 20\%$, the Kaimal wind spectrum and JONSWAP wave spectrum are shown in Figure 4.43.

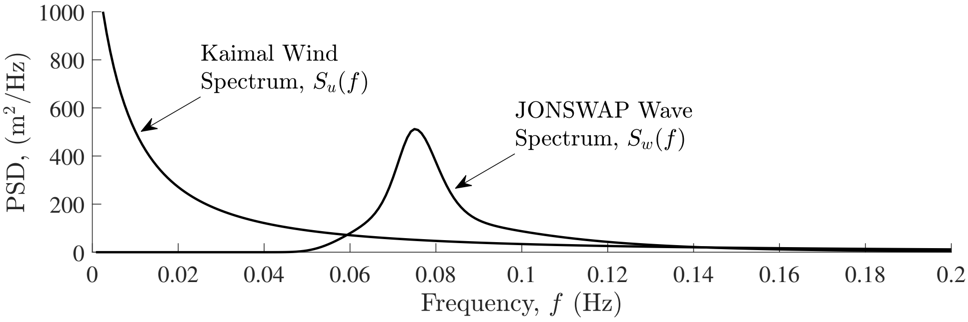

Figure 4.43: Frequency content of the Kaimal wind spectrum and JONSWAP wave spectrum

The Kaimal spectrum is sampled at 300 frequencies between 0.01 Hz and 0.1 Hz, and the JONSWAP spectrum is sampled at 300 frequencies between 0.01 Hz and 0.5 Hz, generating 300 sinusoidal wind speed and sea elevation sine waves. The superimposed wind and wave time series are shown in Figure 4.44.

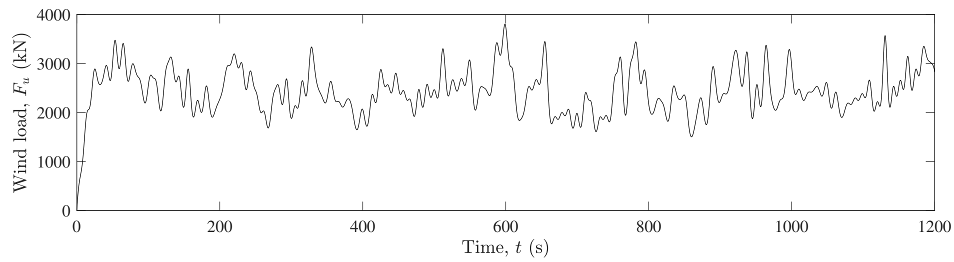

(a) Wind force time series

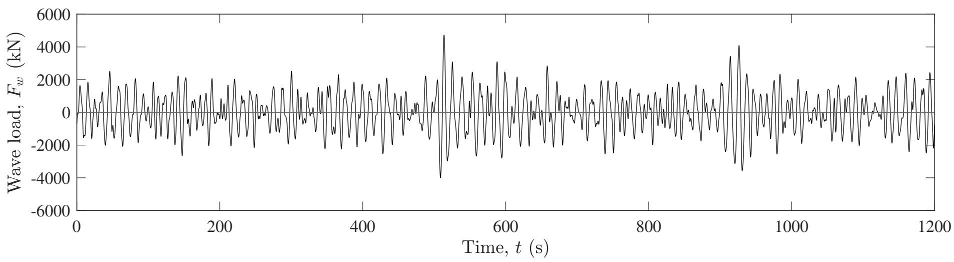

(b) Wave force time series

Figure 4.44: Wind and wave force time series for a 20 minute storm event

Similar to the one-way load history derived in Figure 4.37, an exponential ramping factor is applied to the wind and wave load time series to reduce the transient behaviour in the model due to large sudden loading. Figure 4.44a shows that the wind load is gradually increased to maximum after the first thirty seconds.

Large wave

An arbitrary large wave is superimposed on to the wave force time series to observe the response of the dynamic *p*-*y* model under extreme loading conditions.

Known as a constrained wave, the free surface elevation history of the wave loads is designed to include a singular wave of a determined height at a particular moment in time. The free surface elevation of the random waves cab be naturally blended into the free surface elevation of the large wave (Rainey & Camp, 2007). A simplified approach is adopted herein, where the large wave is modelled in the time domain using a Gauss-like distribution function described in Equation 4.92, and superimposed on the random free surface elevation.

$$F_L(t) = \hat{F}_L \exp\left(-\frac{(t-t')^2}{2\beta^2}\right) \tag{4.92}$$

where $\hat{F}_L$ is the maximum force of the large wave, t' is the time at which the large wave occurs, and β is a parameter that describes the duration. The large wave is applied at $t' = 500$ s, and the duration parameter is taken as $\beta = 3$. The maximum force of the large wave is arbitrarily taken as $\hat{F}_L = 9.6$ MN, which is approximately 2 times the maximum wave force expected from the storm event. The large wave force time series is shown in Figure 4.45.

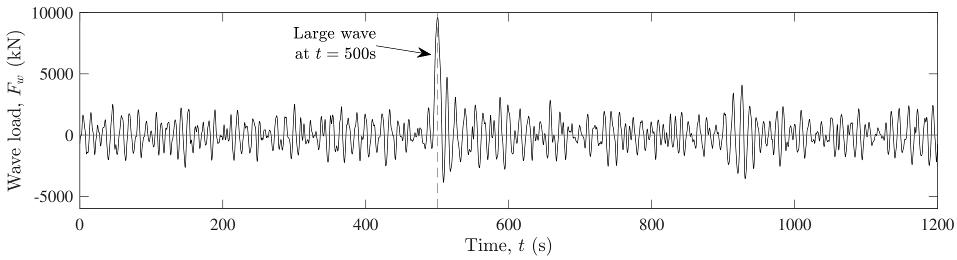

Figure 4.45: Wave force time series at $t = 500$ s

The force time series shown in Figures 4.44a and 4.45 are applied to the nacelle and MSL of the dynamic *p*-*y* model, respectively, and the time required to complete the simulations are noted. The blade-passing excitations are not considered in this analysis.

4.3.2.2 Analysis and results

$\Delta t = 0.01$s is chosen such that the resolution of the estimation is sufficiently small and errors are mitigated, and $\rho_\infty = 1$ such that high frequency modes of the model are captured. The ground line displacements is shown in Figure 4.46. Three hystereses at various depths are shown in Figure 4.47.

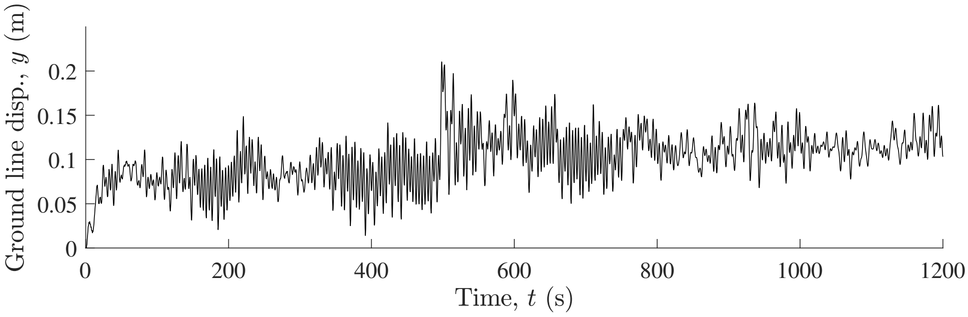

Figure 4.46: Ground line displacements for $\Delta t = 0.01$s and $\rho_\infty = 1$ (CAA)

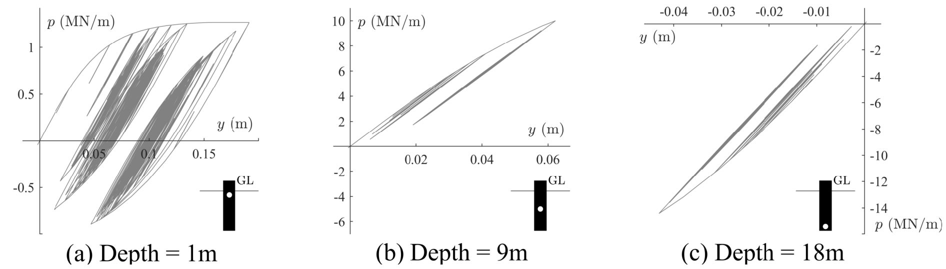

Figure 4.47: Iwan hystereses at various depths for $\Delta t = 0.01$s and $\rho_\infty = 1$

The response is predominantly one-way due to the lever arm imposed by the wind loads applied at the nacelle. Initially, the average displacement is approximately 0.075 m before the large wave, which then increases to approximately 0.1 m due to impact. This suggests permanent deformation due to high spring mobilisation. This behaviour is also evident in Figure 4.47, where the p-y response continues to mobilise along the API sand backbone function. Subsequent hysteresis loops occur due to the irregular loading sequence from both the wind and wave time series. The p-y loops successfully close upon completing load cycles and return to the previous stress path, as shown in Figure 4.47a at spring depth $z = 1$ m, in accordance with the Extended Masing Rules.

The wave impact is also evident at spring depths $z = 9$ m and $z = 18$ m, however the magnitude of the spring mobilisation and displacements are significantly smaller due to the stiffness distribution described by the API sand model. The p-y responses at different depths suggest that the hysteresis model is exhibiting a permanent global monopile rotation. The frequency content of the ground line response is shown in Figure 4.48, including the modal frequencies calculated by an eigenanalysis described in Equation 2.26.

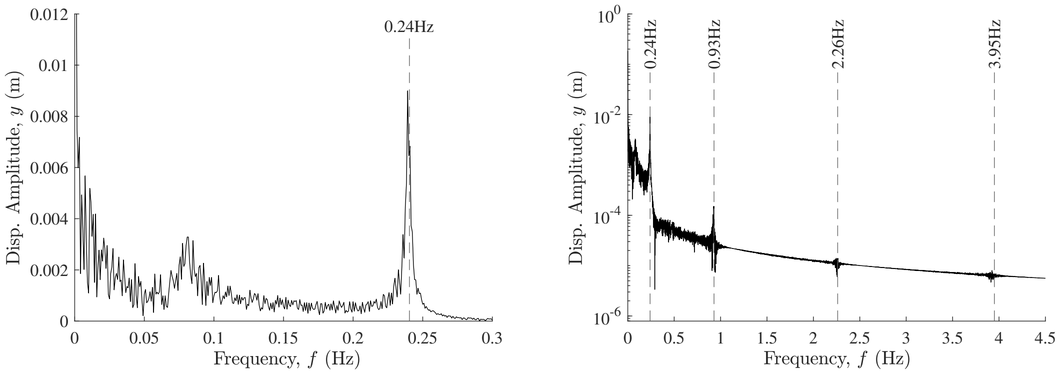

(a) Linear scale

(b) Log scale

Figure 4.48: Frequency content of the ground line displacements for $\Delta t = 0.01$ s and $\rho_\infty = 1$

Note that the Kaimal and JONSWAP spectra are observable in Figure 4.48a. The wave time series resonates with the first mode of the model at 0.24 Hz. The one-way behaviour is a consequence of the wind loads, whilst the wave load is responsible for the large displacements due to resonance, highlighting the dynamic sensitivity of OWT structures. It is important to note that the API sand model used to characterise the lateral springs may not be suitable for monopiles with low L/D ratios, as discussed in detail in Chapter 3. Consequently, the stiffness of the foundation model is considerably weaker, and will therefore produce a lower natural frequency than expected.

The second, third and forth modal frequencies are also displayed in Figure 4.48b and are captured well by the TMA due to the small Δt value used and minimal period elongation errors. However, it is postulated here that the presence of high-frequency modes contribute to erroneous reversal events in the *p*-y domain. Hysteresis reversals cause the tangent stiffness to revert to the initial value, resulting in a momentary increase in stiffness that can encourage transient behaviour. Furthermore, increasing the time step to reduce computational spend can compromise the accuracy of the higher modes. Figure 4.49 illustrates the influence of the time step size on the modal accuracy of the monopile model. The time required to complete the simulation on a standard computer with an AMD Ryzen$^{\text{TM}}$ 7 7745HX Processor (3.60 GHz) is recorded in Table 4.5.

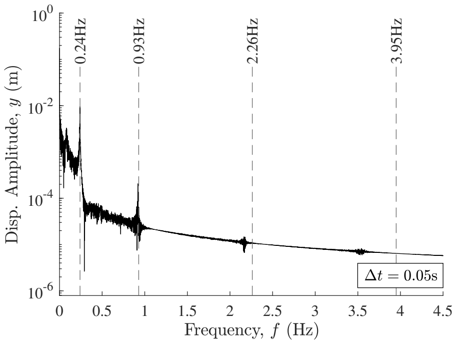

(a) $\Delta t = 0.05$s

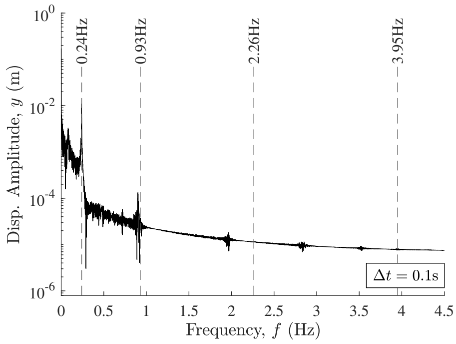

(b) $\Delta t = 0.1$s

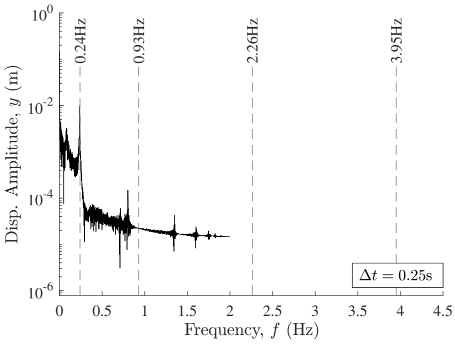

(c) $\Delta t = 0.25$s

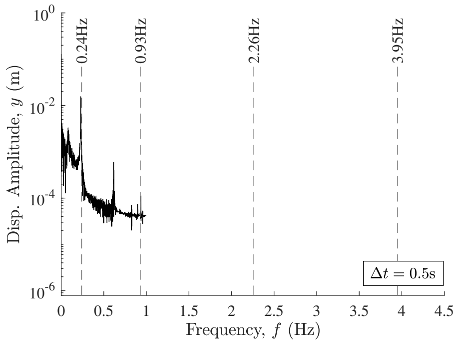

(d) $\Delta t = 0.5$s

Figure 4.49: Frequency content of ground line displacements for various time step sizes

Table 4.5: Simulation time for the integrated OWT-Monopile model at various time step sizes for 1200 seconds of simulation time

Time step size (s)	**Simulation time (s)**
0.05	9.906
0.1	4.877
0.25	1.999
0.5	0.979

As Δt is increased, the TMA becomes less effective at capturing the higher modes of vibration due to the period elongation expected for large normalised frequencies (Figure 4.14a). Obviously, this results in a quicker simulation time, and a linear relationship is observed in Table 4.5. The algorithm demonstrates reasonable accuracy in capturing the first two modes When Δt is less than or equal to 0.1 s. This is particularly important since the first two modes of an OWT system are widely recognised as holding the most engineering significance for OWT systems (Carswell et al., 2016; Prendergast et al., 2018; Tarp-Johansen et al., 2009). Higher values of Δt lead to a significant loss in accuracy for all frequencies.

$\Delta t = 0.1$ s is a suitable time step size for the proposed integrated dynamic p-y model, as it is sufficiently small to capture the first two modes of the system and can provide computationally efficient simulation. However, when $\rho_\infty = 1$, the TMA does not dissipate the poorly estimated high frequency modes evident in Figure 4.49b. An appropriate ρ_∞ value is therefore investigated for the dynamic p-y model at $\Delta t = 0.1$ s. Figure 4.50 shows the spectral radius for modal frequencies (normalised with $\Delta t = 0.1$ s) and various values of ρ_∞.

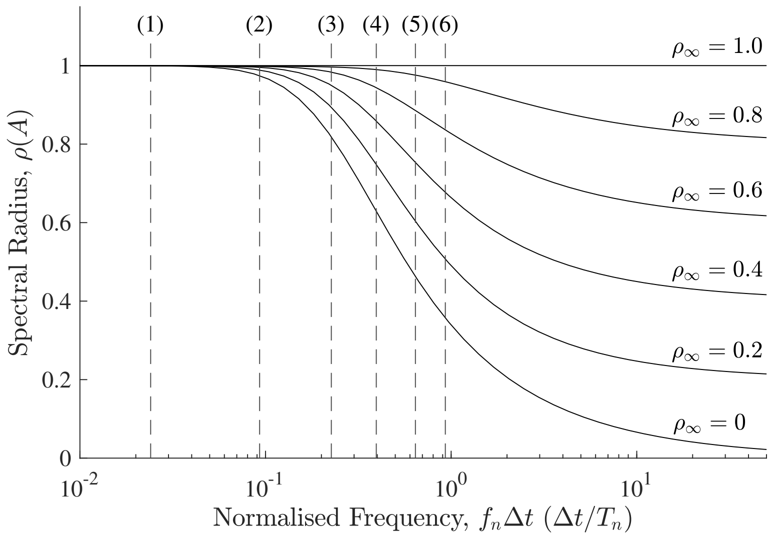

Figure 4.50: Spectral radius of different ρ_∞ values for the first six modal frequencies normalised at $\Delta t = 0.1$ s

Figure 4.50 suggests that, when $\Delta t = 0.1$ s, the preservation of the first and second vibration modes occurs when ρ_∞ is greater than 0.4. The frequency content of simulation with $\rho_\infty = 0.8$, 0.7, 0.6 and 0.5 are shown in Figure 4.51, and are compared with the frequency content of the simulation with $\rho_\infty = 1$. Only the second, third and fourth modal frequencies are shown for clarity.

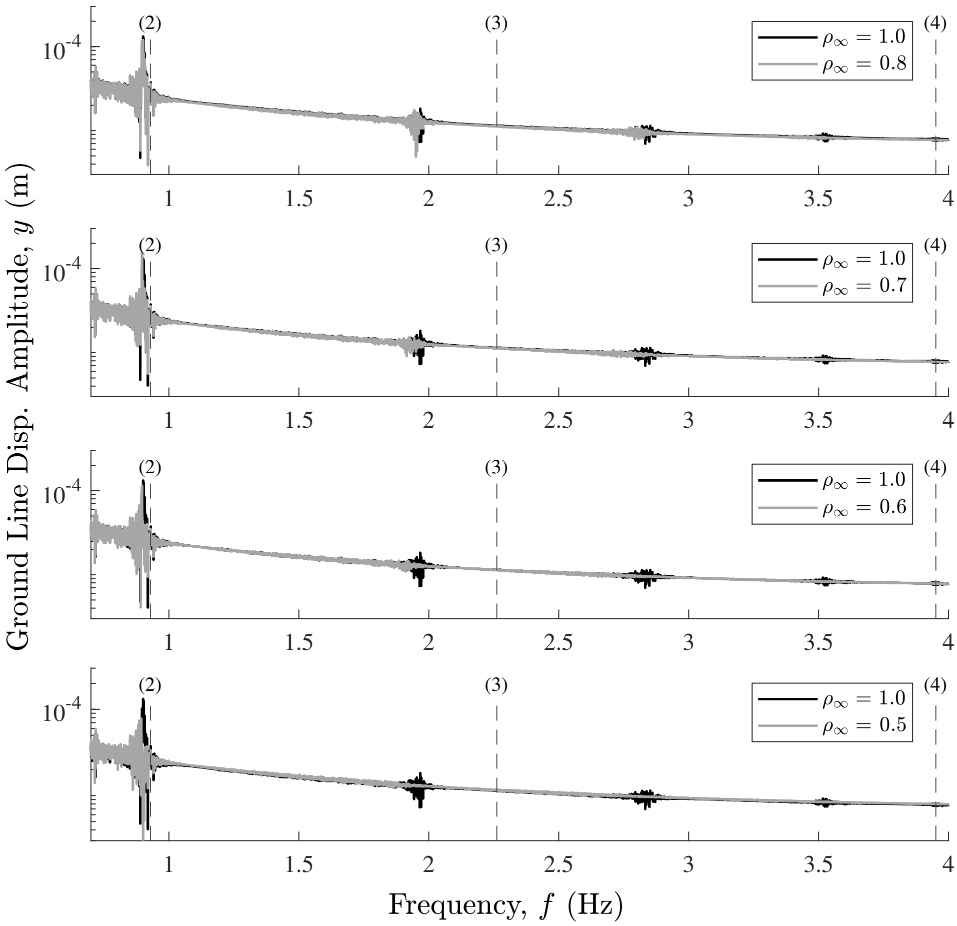

Figure 4.51: Frequency content of the ground line displacements for various ρ_∞ values when $\Delta t = 0.1$ s

The frequency content of the third and fourth mode are successfully dissipated when ρ_∞ is decreased. Notably, Figure 4.51 shows that, when $\rho_\infty = 0.5$, the third and fourth mode are completely filtered out by the TMA, and the second mode is partially dissipated. $\rho_\infty = 0.6$ preserves the amplitudes of the second modal frequencies, whilst also dissipating the third and fourth modes. $\rho_\infty = 0.7$ and $\rho_\infty = 0.8$ do not demonstrate sufficient dissipation of the third and fourth modes, and therefore $\rho_\infty = 0.6$ is chosen as the appropriate value for ρ_∞.

Figure 4.14a shows the period elongation error for the Generalised-α algorithm. Notably, the percentage error increases with ρ_∞ for a given normalised frequency. This is evident in Figure 4.51. When $\rho_\infty = 0.5$, the second mode has minor period elongation error, whereas for $\rho_\infty = 0.8$, the period elongation is negligible. The ground line displacements for $\rho_\infty = 1$ when $\Delta t = 0.1$ s and $\Delta t = 0.01$ s, as well as $\rho_\infty = 0.6$ when $\Delta t = 0.1$s are shown in Figure 4.52. The insets show 20 second intervals along the 1200 second response signal at different points of interest.

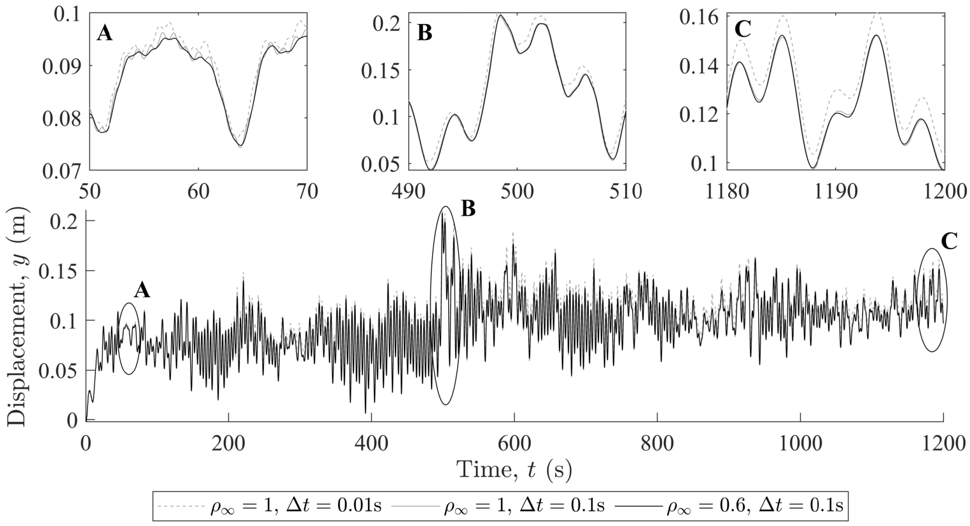

Figure 4.52: Ground line displacements when $\Delta t = 0.01$s and $\rho_\infty = 1$, $\Delta t = 0.1$ s and $\rho_\infty = 1$, and $\rho_\infty = 0.6$ and $\Delta t = 0.1$ s

Inset A demonstrates the transient response of higher modes due to initial loading conditions. Erratic high frequency oscillations are present when $\rho_\infty = 1$, but are dissipated quickly when $\rho_\infty = 0.6$. Notably, the difference in estimated response between $\rho_\infty = 1$ and $\rho_\infty = 0.6$ is negligible at all points in time. This demonstrates that the erroneous frequency modes evident in Figure 4.51 are inconsequential to the overall response of the model, and the simulation response is dominated by the first and second vibrational modes.

Inset B shows the impact of the large wave at $t = 500$ s, and marks when the difference between the $\Delta t = 0.1$ s and $\Delta t = 0.01$ s simulations becomes most pronounced. The large wave causes a significant increase in the ground line displacement, and the difference between the $\Delta t = 0.1$ s and $\Delta t = 0.01$ s is approximately 0.01m thereafter. This difference is also evident in inset C, suggesting that the highly nonlinear response, as demonstrated in the spring stress paths in Figure 4.47, has caused a degree of permanent displacement that is dependent on the time step size. Considering that there is no difference between $\rho_\infty = 1$ and $\rho_\infty = 0.6$, it is postulated that the difference in permanent displacement is not due to the erroneous high frequency modes, but rather the inherent numerical errors associated with the time step size and nonlinear systems. This is difficult to quantify in the presented analysis.

It is important to note that, when $\Delta t = 0.01$s, it is not possible to evaluate the influence of the first and second mode. This is because the normalised modal frequencies (i.e. $f_n\Delta t$) are too low for meaningful ρ_∞ values to affect the response in a comparative way. This is illustrated in Figure 4.53.

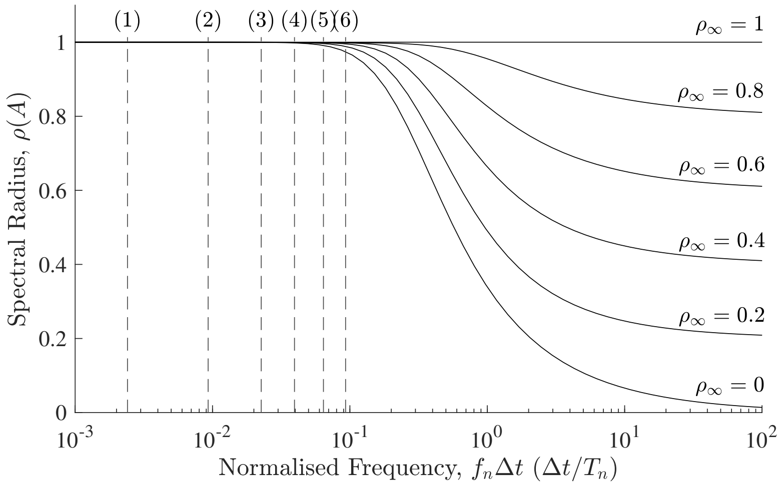

Figure 4.53: Spectral radius of different ρ_∞ values for the first six modal frequencies normalised at $\Delta t = 0.01$ s

Note that the majority of the meaningful vibration modes have a spectral radius of unity when $\rho_\infty = 0$. This means that the Generalised-α method cannot dissipate erroneous frequency modes for systems with low natural frequencies and relatively small time step sizes.

4.3.2.3 Summary

An integrated dynamic p-y model has been developed to simulate the response of a monopile under intense wind and wave loading. The soil elements are informed using the Iwan hysteresis method and the backbone function is characterised using the API sand model. A qualitative review on the performance of the model has shown that the Iwan model is capable of capturing the nonlinear response of the soil for highly irregular one-way loading configurations without instabilities. It was shown that the Newmark-β CAA algorithm is suitable for such models. However, it is good practice to filter out the erroneous modes present for larger Δt values. A value of $\rho_\infty = 0.6$ preserves the first two modal frequencies when $\Delta t = 0.1$ s (which are the most important for OWTs), and successfully filters out the higher modes. This investigation showed that the first two modes are most dominant in nonlinear analyses, as the difference between $\Delta t = 0.1$ s simulations when $\rho_\infty = 1$ and $\rho_\infty = 0.6$ is negligible. Further investigation is required to review the model's dependence on the time step size when the degree of nonlinearity in the soil elements is high.

4.4 Conclusions

A dynamic *p-y* model has been investigated by applying a strategically simplified load and moment time series to evaluate the response of a monopile hysteresis model in a controlled environment for different hysteresis definitions. It was found that, when regular cyclic loading is applied to the pile head the Iwan model is the most robust, whereas the Masing and Bouc-Wen models were unstable due to their dependence on velocity. ρ_∞ and Δt were found to have a significant influence on the dynamic response of the rate dependent hysteresis models, and therefore must be carefully selected to ensure the model is stable and accurate.

The Iwan model was used to define the nonlinear soil resistance in a dynamic *p-y* model with an appended OWT superstructure, and the backbone was informed using the API sand model. A wind and wave load time series was derived from design code spectra for an intense storm event. The dynamic response of the model was evaluated using the Generalised-α method and the influence of the time step size and spectral radius on the dynamic response of the model was investigated.

Wind and wave load time series are derived using the Kaimal and JONSWAP spectra, respectively, to simulate an intense storm event. The load histories are applied to the appropriate points along the superstructure to ensure the ground line excitations are inline with the anticipated response of a commissioned monopile during a storm. The influence of the time step size and spectral radius on the dynamic response of the model is investigated.

It was found that, for this model configuration, a ρ_∞ value of approximately 0.6 is recommended to preserve the first two modal frequencies of the system and filter out erroneous high frequency modes. However, ρ_∞ will also be dependent on the natural frequency of the system. The inaccurate modal frequencies for large Δt values demonstrated to have a negligible influence on the overall response of the model, suggesting that the first two modes dominate the response of the nonlinear system. The analysis suggests that Newmark-β CAA method is suitable for dynamic *p-y* models for OWTs. However, the Generalised-α method can be more efficient and stable. It is good practice to use the Generalised-α method, especially when dealing with loading sequences that may induce high-frequency excitations, such as seismic loading. This was not within the scope of this study. The displacements under highly nonlinear behaviour are dependent on the size of the time step, and not the transient response of higher modes. However, this is difficult to quantify in the presented analysis.

Future work will include characterising the soil element function with a more appropriate soil model that is representative of the dynamic soil-structure interaction of monopiles. The API sand model was used in this investigation, which is derived from static loading conditions. This analysis was therefore qualitative, and comparison to empirical data is not meaningful. Diameter effects from low L/D monopiles was also not considered in this analysis, which will have a marked influence on the stiffness of the foundation model, as discussed in Chapter 3. Furthermore, it is possible to modify the spring elements to capture more advanced geotechnical behaviour, such as gapping, ratcheting and liquefaction. In its current form, the model offers a framework for the implementation of these phenomena, and it was demonstrated that the proposed model does not exhibit superficial ratcheting behaviour. An empirical ratcheting model can therefore be applied with confidence. However, the relationship between highly nonlinear behaviour and the size of the time step needs to be reviewed further.

A dynamic p-y model implicitly computes the local mobilisation of each soil layer due to irregular load histories applied to the pile head. This means that the degree of degradation for each layer can be quantified if an appropriate soil degradation model is applied, such as the cyclic contour diagrams discussed in Section 2.2. This is a topic of interest in the offshore wind industry, as the amplitude and frequency of irregular time series can have a marked influence on the fatigue life of the structure (Andersen, 2009; Page et al., 2021; Zhang et al., 2017; Zhang & Andersen, 2019).

Chapter 5

Pseudostatic model: development and analysis

The one-dimensional beam-spring model configuration is a popular methodology for pile analysis due to its fast computational simulations and versatility in application. So far, this thesis has focused on the development of a static and dynamic p-y model for OWT monopiles. It is possible to extend the dynamic time-domain p-y model to consider seismic effects by imposing motion on the boundary conditions of each spring, but this approach is computationally expensive. Typically, the peak bending moment of a pile is the governing design parameter for seismic loading during earthquake events, which can be estimated using a static p-y model if the loading configurations due to seismic excitation are appropriately represented.

This chapter details the development and performance of a pseudostatic p-y model for a single pile and a pile group embedded in a two-layered soil profile. These tests were performed by associates at University of Cambridge (Garala, 2020), therefore experimental data curation and analysis were not conducted by the author of this thesis, but are detailed in this chapter for the purpose of clarity. The results of this chapter are published in Soil Dynamics and Earthquake Engineering (Tott-Buswell et al., 2022).

5.1 The pseudostatic p-y model

Conventional pile design involves estimating the axial load capacity and satisfying the serviceability criteria in terms of allowable settlements and durability under static loads. In addition to axial loads, pile foundations are subjected to lateral dynamic loads during an earthquake due to: (i) the oscillation of the superstructure, which induces inertial loads at the pile head, and (ii) the ground deformation during the passage of seismic waves, which induce kinematic loads along the pile. Traditionally, kinematic loads are neglected in pile foundation seismic design as they are assumed insignificant in comparison to inertial loads applied at the ground line. However, the significance of kinematic loads has been highlighted by various post-earthquake reconnaissance reports (Mizuno, 1985; Nikolaou et al., 2001) and thus, several revised seismic codes recommend the consideration of kinematic loads in the seismic design of pile foundations under certain conditions (EC8, 2000). Nevertheless, there are no specific methodologies recommended for the seismic design of pile foundations in design codes, resulting in various design approaches being followed by practitioners. These design approaches can range from very simplistic methods, such as the pseudostatic methodology, to complex computer analyses, such as time-domain simulations (Poulos, 2017).

Despite recent developments in two- and three-dimensional dynamic finite element models including advanced soil constitutive behaviour, one-dimensional finite element or finite difference-based methods, Winkler models are still commonly employed for seismic soil-pile-structure interaction analysis due to their simplicity. The p-y method is widely employed for monotonic analysis, utilising a nonlinear relationship between soil resistance p and lateral displacement of the pile y (as shown in Chapters 3 and 4). However, it can be modified to encapsulate the maximum stress conditions within the pile imposed by seismic activity (Tabesh & Poulos, 2001). Alternatively, the variation in response of the pile foundation with time-varying earthquake characteristics (intensity and frequency of excitation) can be evaluated using time-domain dynamic analyses and appropriate soil element hysteresis models (Kampitsis et al., 2013; Naggar & Bentley, 2000; Rovithis et al., 2009). Such methods are computationally expensive and can be impractical for design purposes, especially when the capacity of the pile is required. The pseudostatic method offers a practical approach to estimating the maximum bending moment if the applied loads are appropriately characterised based on the anticipated seismic activity (Poulos, 2017).

Similar to the traditional p-y method, the pseudostatic model takes advantage of the simplicity in pile-soil interaction representation by considering only one dimension. This method uses a beam-spring configuration under static loading to estimate the maximum bending moment that occurs during an earthquake event without the need for computationally expensive time-domain simulations. As is the case with the p-y approach, the model assumes that discrete soil layers behave as nonlinear spring. The pseudostatic methodology assumes a point load at the pile head that is representative of the inertial force imposed by the superstructure. This is estimated using a static inertial force with a magnitude equal to the mass of the system times the acceleration of the excitation. The kinematic soil forces induced by the ground accelerations are encapsulated with non-homogenous boundary conditions on nonlinear springs. The pseudostatic model, including the idealised forces, are shown in Figure 5.1.

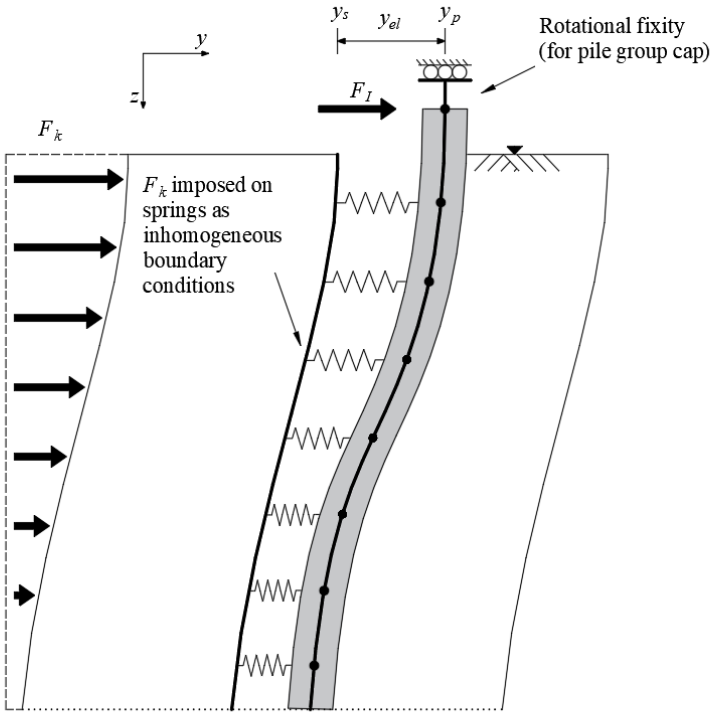

Figure 5.1: Schematic of pseudostatic p-y model for a single pile, including inertial loading and non-homogenous boundary conditions

Note that the spring elements are now described with a p-y_{el} relationship, where $y_{el} = y_p - y_s$. y_p and y_s is the displacement of the pile and the free field soil displacement, respectively. The depth and value of the maximum bending moment can be calculated using the gradient matrix, which can be derived from elastic beam theory (Bathe, 2006). See Appendix A.2.4.

A typical pseudostatic analysis for seismic loading involves two steps: (i) performing a seismic ground response analysis to obtain the maximum free-field soil displacement profile along the pile's length, and (ii) imposing a static force (peak inertial load) at the pile head and non-zero boundary conditions along the embedded pile informed by discretising the maximum free-field soil displacements (kinematic load). Abghari and Chai (1995) presented the first pseudostatic analysis approach for piles in non-liquefying soils by considering the inertial force acting at the pile head as the product of the cap-mass times a spectral acceleration as recommended by Dowrick (1977). To this end, an approximation is necessary to compute the associated natural period by considering the lateral pile head stiffness (Tabesh & Poulos, 2001). By comparing the results of pseudostatic analysis with dynamic finite element analysis, the above authors concluded that 25% of the peak inertial force should be combined with the peak kinematic displacement for computing the peak pile deflection. Similarly, for computing the peak pile bending response, 50% of peak inertial force should be combined with peak kinematic displacement. Later, Tabesh and Poulos (2001) contradicted this finding and recommended that imposing the total inertial force at the pile head can result in good agreement between the pseudostatic approach and dynamic analysis. Castelli and Maugeri (2009) considered both kinematic and inertial loads and highlighted the suitability of pseudostatic approaches for the seismic analysis of single piles and pile groups.

In this chapter, the pseudostatic methodology is adopted to estimate the bending moment profile of single and group piles in two-layered soils of high stiffness contrasts. The soil-structure interaction is modelled using the well-established API reaction curves, which were originally derived for the p-y methodology for slender piles under monotonic loading (API, 2014; Murchinson & O'Neill, 1986; O'Neill & Murchison, 1983; Reese et al., 1974). The efficacy of these design curves for seismic loading in layered soils is evaluated by comparing the results of the pseudostatic model with centrifuge test results. Model corrections to facilitate soil layer and pile group effects are also investigated.

5.2 Description of centrifuge tests

The following sections describe the centrifuge experiments conducted by associates at University of Cambridge (Garala, 2020) to investigate the seismic response of single and group piles in two-layered soil profiles. Centrifuge experiments were performed for single and group piles in dense sand underlying soft clay at 60g (g = gravitational acceleration) under various sinusoidal and earthquake excitations. The experimental setup, model instrumentation and soil strata are detailed herein. The acceleration response of soil strata and pile foundations during the various base excitations are also discussed.

5.2.1 Model pile instrumentation and preparation

The centrifuge experiments were conducted at 60g using the Turner beam centrifuge (Schofield, 1980) facilities at the Schofield Centre, University of Cambridge, UK. In this series of experiments, the soil models were prepared with a dense, poorly graded, fraction-B Leighton Buzzard sand underlying soft Speswhite kaolin clay to maintain significant stiffness contrast between the soil layers. The properties of fraction-B Leighton Buzzard sand and Speswhite kaolin clay can be found in Garala et al. (2020). For model pile foundations, a single pile and a 1 x 3 row pile group were fabricated using an aluminium (Alloy 6061 T6) circular tube of outer diameter (D) 11.1 mm and thickness (t) 0.9 mm. A centre-to-centre spacing of 3 diameters is adopted between piles in the pile group. The bottom of the tubular piles is closed with an aluminium plug to restrict the entry of soil into the piles during pile installation. Further, the single pile and end piles of the pile group were strain gauged to measure the bending moments during earthquakes. Figure 5.2 shows the schematic view of the pile foundations used in the study along with the location of strain gauges.

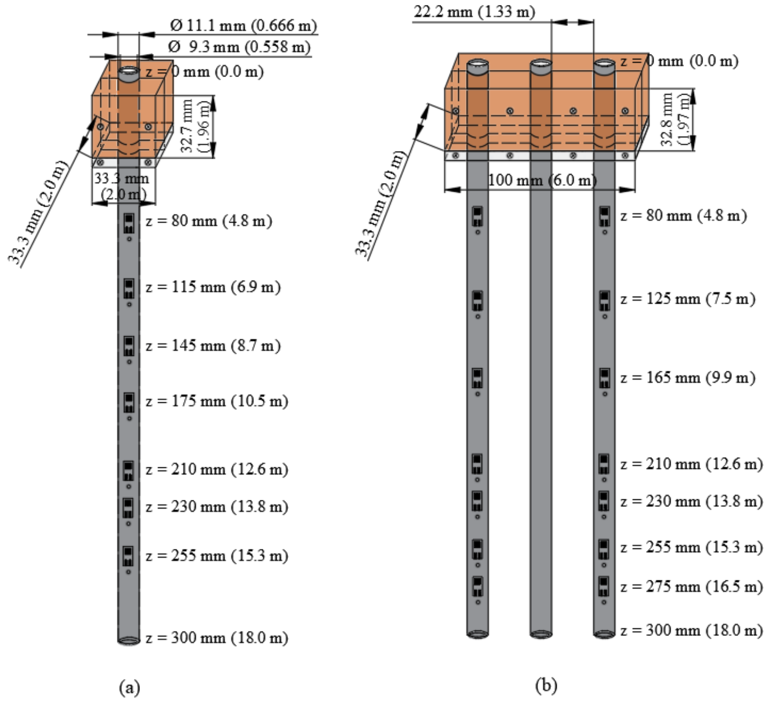

Figure 5.2: Schematic view of tested pile foundations: (a) single pile and (b) pile group (prototype dimensions in parentheses) (Garala, 2020)

The mass of the plexiglass caps for single pile and the pile group are 11 grams and 24 grams at model scale, respectively. These masses are less than half the self-weight of the pile foundations (each model pile weighs 24 grams without strain gauges) and are negligible compared with the axial load-carrying capacity of the single pile (0.57 kg at model scale). Hence, the pile accelerations and bending moments measured during K flight (kinematic loads only, not cap mass) can be considered as the effect of kinematic loads alone. In K+I flight (including inertial effects from cap mass), the brass caps will induce a static vertical force of 167.75

N and 503.25 N at model scale (0.604 MN and 1.812 MN at prototype scale) for the single pile and the pile group, respectively; therefore, the vertical load acting per pile is the same for both the single pile and the pile groups.

5.2.2 Centrifuge preparation and instrumentation

The centrifuge models were prepared from bottom to top, first by pouring the sand at the required relative density using an automatic sand pourer (Madabhushi et al., 2006), followed by saturating the sand layer with de-aired water and then filling the model container with kaolin slurry for consolidation (Garala, 2020). An air hammer device, a small actuator that can act as a source to induce waves within the soil model (Ghosh & Madabhushi, 2002), was placed at the bottom of the model on a 10-15mm thick sand layer during sand pouring. The detailed model preparation procedure and equivalent prototype characteristics of a single pile can be found in Garala (2020) and Garala and Madabhushi (2020). The unit weight of the saturated clay and the sand is 16.2 kNm^{-3} and 20.4 kNm^{-3}, respectively. Figure 5.3 shows the sectional view of the model along with the location of various instruments used. Piezoelectric accelerometers were used to measure the accelerations in the soil model at different depths, micro-electro mechanical system accelerometers were used on top of pile caps to measure the accelerations, and pore pressure transducers were used to measure the pore-water pressures at different depths. Further, each centrifuge experiment was carried out in two flights, with acrylic plexiglass used as pile caps in flight-01 (hereafter referred to as K flight) and pile caps made from brass in flight-02 (hereafter referred to as K+I flight), to examine the effects of kinematic and inertial loads individually.

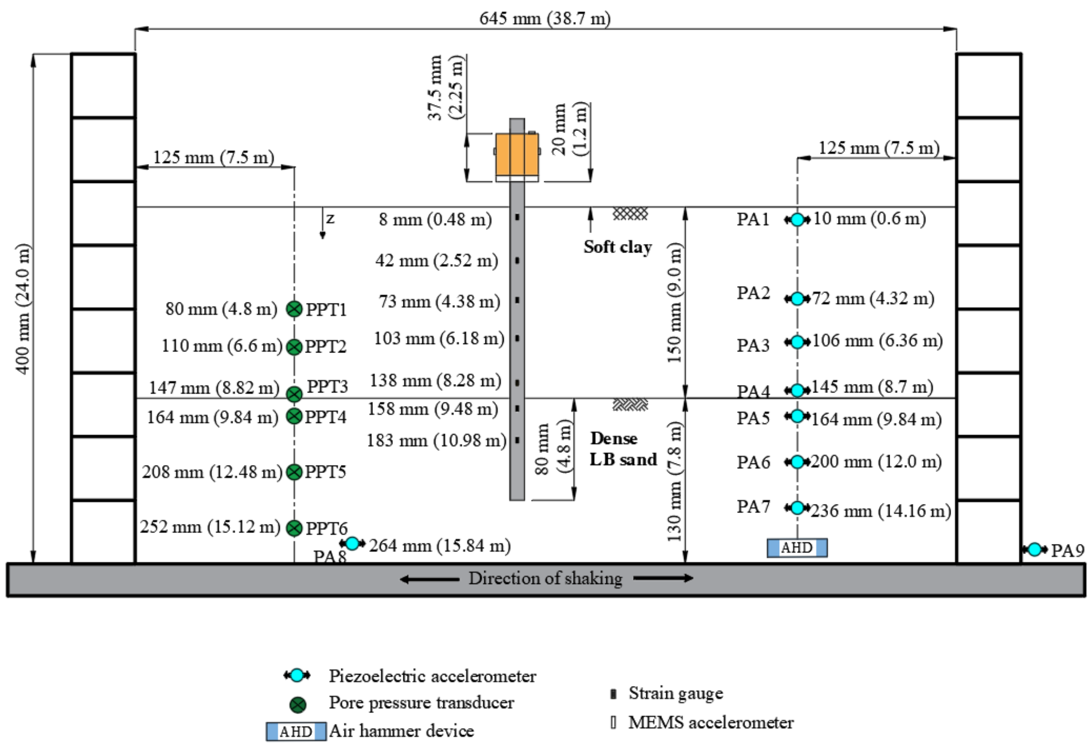

Figure 5.3: Sectional view of the centrifuge model with instruments and pile foundation (prototype dimensions in parentheses) (Garala, 2020)

A T-bar 40 mm wide and 4 mm in diameter was used to determine the undrained shear strength (c_u) of the clay layer. To measure the soil stiffness, the air hammer device was activated and the propagation of shear waves through the soil profile was measured using an array of piezo-electric accelerometers placed above the air hammer device (see Figure 5.3). Figures 5.4a and 5.4b show the c_u profile of the clay layer determined from in-flight T-bar tests and the small-strain shear modulus (G_0) of the soil layers determined from the air hammer device, respectively, before subjecting the model to base excitations. G_0 values determined from published expressions (Hardin & Drnevich, 1972a; Oztoprak & Bolton, 2013; Viggiani & Atkinson, 1995) are also shown in Figure 5.4b. By considering an average G_0 of 23 MPa and 184 MPa for the clay and sand layers (at a depth of $4D$-$5D$ above and below the interface), respectively, a sharp stiffness contrast between the two soil layers is obtained, referring to a small-strain shear modulus ratio ($G_{0,sand}/G_{0,clay}$) equal to 8. Further, a quite large $G_{0,clay}/c_u$ ratio around 2300 was obtained for the clay layer.

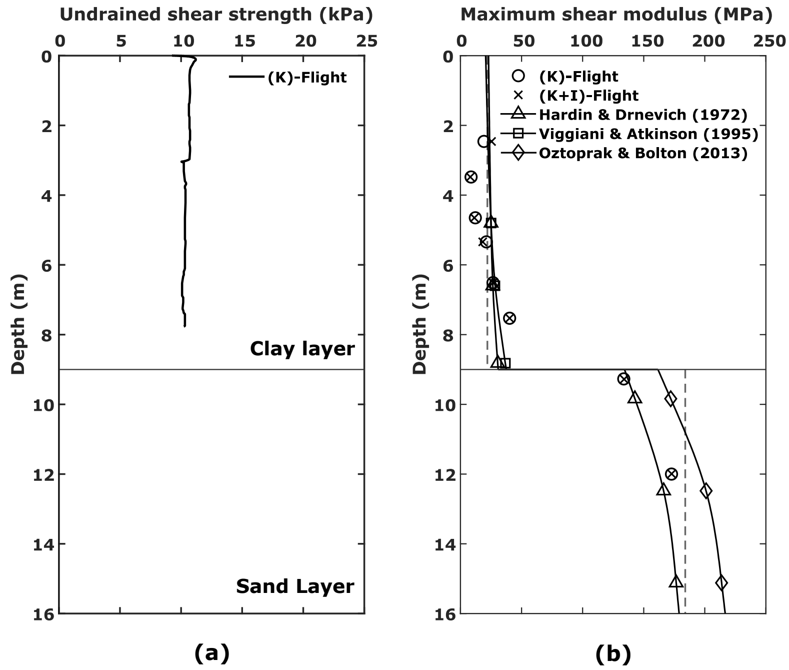

Figure 5.4: (a) Undrained shear strength of clay layer from T-bar test and (b) Maximum shear modulus of soil layers from air-hammer tests (Garala, 2020)

5.2.3 Acceleration response of soil strata and pile foundations

Figure 5.5 shows the acceleration time-histories of the Base Excitations (BE) considered in this study, including sinusoidal excitations of different driving frequencies (BE1-BE4) and increasing intensity along with a scaled 1995 Kobe earthquake motion (BE5).

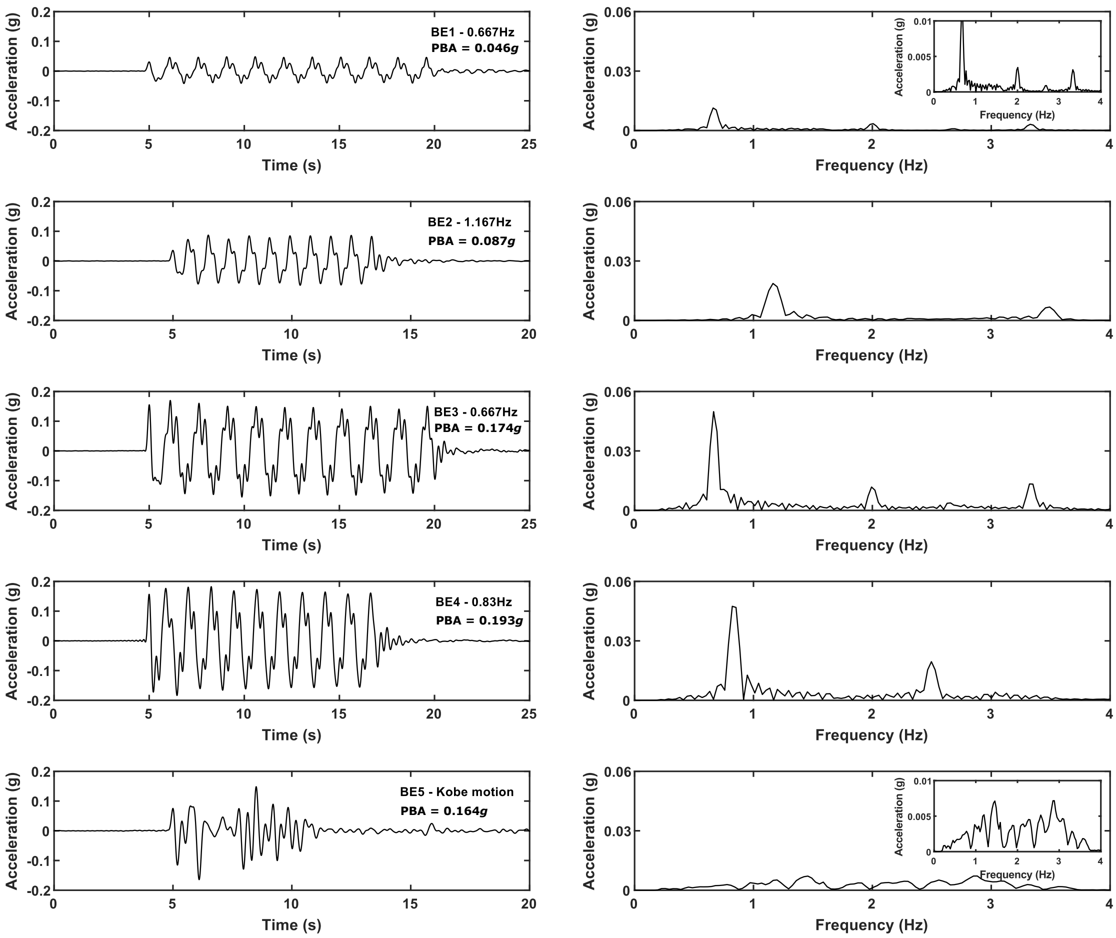

Figure 5.5: Acceleration time-histories and corresponding fast Fourier transforms of base excitations BE1 to BE5 (Garala, 2020)

Figure 5.6a shows the peak acceleration measured at different depths of soil strata during each base excitation (BE1-BE5) in K and K+I centrifuge flights. The peak soil displacement profile, determined by double integration of the recorded soil accelerations, is shown in Figure 5.6b. The amplification of motion as shear waves propagate from the dense sand layer to the surface of the soft clay layer can be clearly seen in Figures 5.6a and 5.6b. More details about the dynamic response of tested soil-strata and the comparison of response from centrifuge soil-strata with one-dimensional seismic ground response analysis can be found in Garala and Madabhushi (2021).

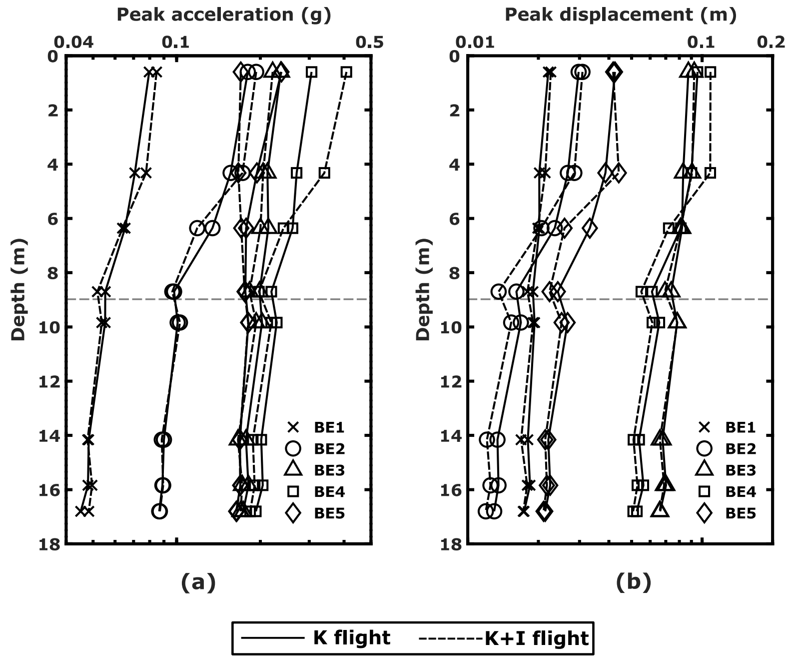

Figure 5.6: (a) peak accelerations and (b) peak displacements along the soil depth (Garala, 2020)

Figure 5.7 shows the acceleration response at the soil surface and the pile-cap as recorded during the two flights of centrifuge testing (see Figure 5.3 for accelerometer locations). The soil-strata responded similarly in both flights, except for BE4 excitation. As expected, the pile accelerations are different in K flight and K+I flight, with the pile acceleration amplitude being larger in K+I flight compared to K flight in most cases due to the presence of inertial loads in K+I flight. However, for the single pile, the pile accelerations in K+I flight are smaller than in K flight at some loading cycles during BE2, BE4 and BE5 excitations. This is due to the phase difference between the kinematic and inertial loads. For the same tested pile foundations, Garala and Madabhushi (2020) has shown that there is a significant phase difference between the kinematic and inertial loads for the single pile during BE2, BE4 and BE5 excitations and hence the pile accelerations in K+I flight are smaller than those in K flight. For all other cases, the kinematic and inertial loads act together or with smaller phase differences, leading to larger pile accelerations in K+I flight compared to K flight. The significant phase difference between the kinematic and inertial loads also leads to lower pile bending moments as the piles are vibrating with smaller acceleration amplitudes. More details about the phase difference between the kinematic and inertial loads and its influence on pile accelerations and bending moments can be found in Garala and Madabhushi (2020).

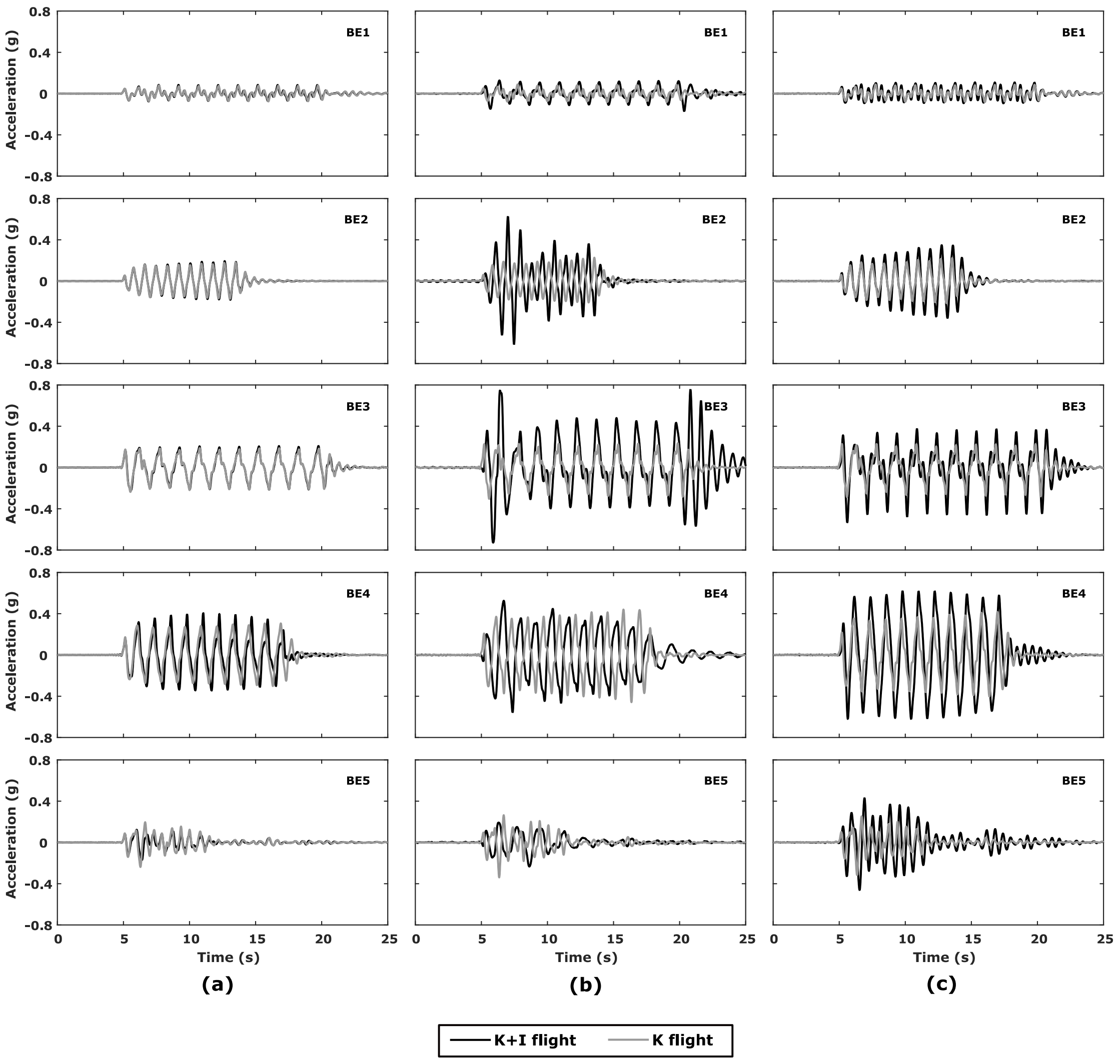

Figure 5.7: Acceleration time histories of (a) soil surface, (b) single pile, and (c) pile group during different excitations in K and K+I flights (Garala, 2020)

5.3 Development of the pseudostatic model

The pseudostatic model employed herein is presented in Figure 5.8 following Tabesh and Poulos (2001). The beam-spring model consists of a series of linear-elastic beam elements supported on nonlinear p-y spring elements at discrete points to represent the pile and soil respectively. Euler-Bernoulli beam theory is used in this theory due to the relatively slender pile model geometries (Figure 5.2) (Gupta & Basu, 2018). The general ordinary differential equation of a beam on a Winkler foundation is given by:

$$E_p I_p \left(\frac{d^4 y_p}{dz^4} \right) - p(y_{el}) - F_I = 0 \tag{5.1}$$

where E_pI_p is the flexural stiffness of the pile, y_p is the pile displacement, p is the soil pressure function, y_{el} is the spring element's displacement, referring to the relative displacement between the free-field soil displacement y_s and the pile deflection y_p (i.e. $y_{el} = y_p - y_s$), and F_I is the inertial load.

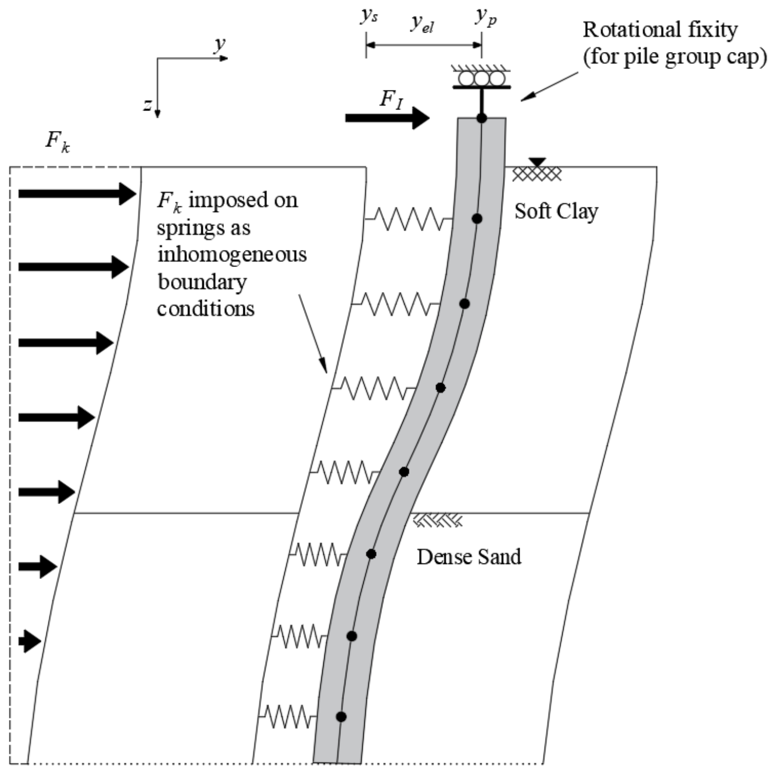

Figure 5.8: pseudostatic p-y_{el} model illustration of a capped pile in a multi-layered soil strata

The continuous form of the equilibrium equation can be solved using the Direct Stiffness Method by discretising the physical system appropriately (Appendix A). The pseudostatic model considers both kinematic and inertial loading in the following manner:

1. Kinematic loading F_k induced from the free field soil lateral displacement y_s is modelled through imposing y_s as non-homogeneous boundary conditions on the spring elements as informed through the maximum soil displacements recorded in the centrifuge tests for a given base excitation. It should be noted that the maximum soil displacements at each depth may have occurred at different times. Values are linearly interpolated where necessary for nodal displacement values within the discretised Winkler model.

2. Inertial loading $F_I = M_{cap}(\ddot{y}_s)$ due to the pile cap mass is modelled as a single point load applied at the pile head, where M_{cap} is the mass of the

pile cap and $\ddot{y}_s$ can be either the peak ground acceleration or the peak spectral acceleration recorded in the centrifuge at soil surface for a given base excitation.

A rotational fixity is assumed at the pile head location for the pile group to simulate pile cap boundary conditions and for the single pile case the pile head is free to rotate. The lateral soil pressure p is computed based on y_{el}. The function used to describe the p-y_{el} element depends on the layer in which the corresponding spring resides. For the present study, the API methodology is applied for both the sand and clay layers, assuming $y = y_{el}$ (API, 2014). It should be noted that the p-y curves in API (2014) were developed for laterally loaded pile foundations using full-scale monotonic and cyclic pile head lateral load field tests on long piles in different soil conditions. For these reasons, the p-y functions may not be suitable for pile response analysis under dynamic loading. However, as there are no dynamic p-y_{el} curves recommended in the codes, cyclic p-y relationships are used in this study as defined by API design codes for simplicity, which are discussed in detail in Section 2.1.2.

5.3.1 API p-y model for each soil layer

The p-y_{el} curves for the clay layer are hereby denoted as the first layer with subscript 1. The API clay methodology proposed by Matlock (1970) suggests that the lateral pressure of the first layer p_1 is function of the ultimate lateral resistance ($p_{u,1}$) and the lateral pile displacement at one-half the ultimate lateral resistance (y_c), calculated as $y_c = 2.5\epsilon_c D$ (Matlock, 1970). Due to the absence absence of experimental stress-strain curves, a representative value for ϵ_c can be adopted in terms of c_u (Sullivan et al., 1980). For an average c_u of 11 kPa (Figure 5.4), Sullivan et al. (1980) recommended $\epsilon_c = 0.02$ (see Table 2.4).

The sand layer's p-y_{el} curves are denoted as the second layer herein, with subscript 2. The API sand methodology proposed by O'Neill and Murchison (1983) defines the lateral soil pressure of the second layer p_2 using the hyperbolic tangent relationship described in Equation 2.3.

Full details on the spring element definitions can be found in Section 2.1.2.

5.3.2 Soil layering effects

Design standards for laterally loaded piles do not explicitly advise any specific p-y curves to account for layered soils or any suggestions to modify the above p-y curves of homogeneous soils for use with layered soils (API, 2014). Therefore, in the presence of layered soils, underlying soil spring element functions must be modified accordingly to account for the change in vertical stresses imposed by upper soil layers. For soft clay underlain by dense sand, it is expected that the sand's strength would be less than what API's hyperbolic definition suggests (Equation 2.3), as the lighter clay imposes a lower overburden pressure at the soil interface depth than what would be expected in a fully homogeneous dense sand deposit. Therefore, the p-y_{el} functions describing the sand's lateral resistance to pile motion must be modified. In the present study, the upper layer of soft clay is modelled by using the API functions for clay under cyclic loading (Matlock, 1970) without any modifications. Two methods are used to modify the sand's p-y_{el} curves.

Method A: Georgiadis' approach

The effective depth at which API functions for sand are computed from is modified by calculating an equivalent height (h_2) above the interface depth H_1 that would provide a lateral capacity equivalent to the original overlying soil layer, as recommended by Georgiadis (1983). Using $z_2 = H_1 - h_2$ as the effective ground line depth for API sand functions in Equations 2.3 to 2.4 ensures that the lateral capacity above $z = H_1$ is fully considered when deriving the spring functions below the interface depth. This method is illustrated in Figure 5.9 and demonstrates the lateral capacities of the pile-soil interaction which are defined by the areas within the respective p_u functions in Equations 2.8, 2.9, 2.4b and 2.4c. Equating the two hatched areas defined by the failure criteria of sand and clay above the interface depth H_1, the appropriate effective depth h_2 can be calculated.

Denoting the hatched area in Figure 5.9 as F_1, the lateral capacity of the soft clay can be expressed analytically as follows:

$$F_1 = \int_0^{z_r} p_{us,1} dz + \int_{z_r}^{H_1} p_{ud,1} dz = \int_0^{h_2} p_{u2} dh \tag{5.2}$$

where h_2 is the effective depth of sand to be solved for. Note that the clay layer below z_r has constant ultimate lateral resistance proportional to the undrained shear strength, as defined by Equation 2.9. It is also important to note that h_2 varies depending on the failure function (either Equation 2.4b or 2.4c) for the ultimate resistance of the sand, as shown in Figure 5.9a and 5.9b. As it was not specified in Georgiadis (1983) which failure definition should be considered for the given stratum, therefore both shallow and deep failure definitions are evaluated for the underlying dense sand layer.

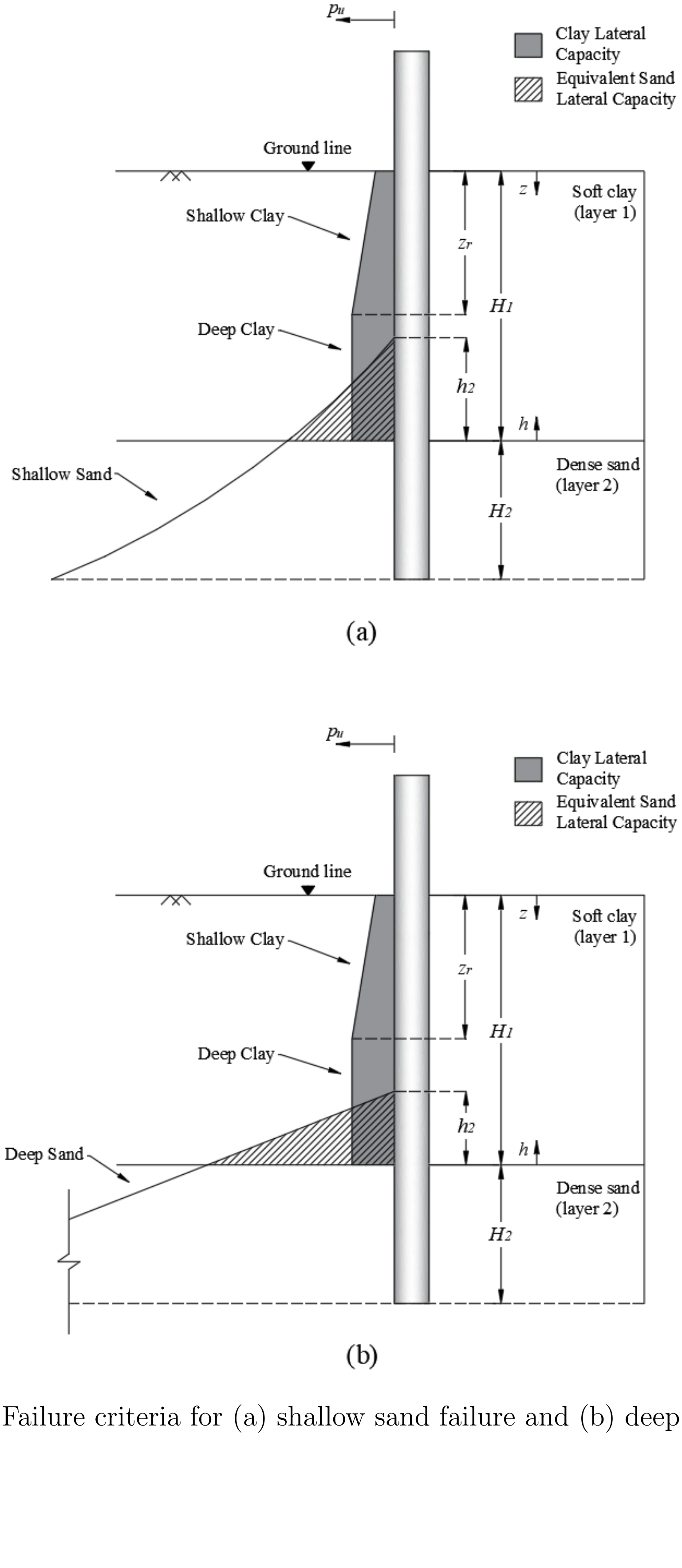

Figure 5.9: Failure criteria for (a) shallow sand failure and (b) deep sand failure

To determine the equivalent depth h_2 above the sand layer (Figure 5.9), the total force acting on the pile at the bottom of clay layer (the layer transition depth H_1) is to be determined first. Therefore, the transition depth z_r at which the wedge failure criteria changes to deep failure criteria in the soft clay layer is to be determined. For the given experimental set up as desribed in Section 5.2; substituting $\gamma' = 6.5\ \mathrm{kN\,m^{-3}}$, average $c_u = 11$ kPa, pile diameter $D = 0.666$ m and $J = 0.5$ (for soft clays), the transition depth z_r is computed as 4.47 m, as per Equation 2.7.

Substituting Equation 2.8 and 2.9 into Equation 5.2 for the clay layer, and Equation 2.4b and 2.4c for either shallow failure of sands, respectively, gives:

$$\int_0^{4.47} \left(3 + \frac{\gamma'}{C_u}z + \frac{J}{b}z\right) c_u D dz + \int_{4.47}^{9} 9 c_u D dz = \begin{cases} \int_0^{h_2} (C_1 z + C_2 D)\gamma' z dz \\ \int_0^{h_2} C_3 D \gamma' z dz \end{cases}$$

Parameters for the API sand equations can be found in equation 2.3. Solving Equation 5.2 using the expression above gives $h_2 = 3.07$ m for the shallow sand failure criterion using Equation 2.4b, and $h_2 = 1.40$ m for the deep failure criterion using Equation 2.4c.

Method B: Adjusting the overburden pressure

In method B, the layering effect is considered by imposing the upper clay layer as an overburden stress on the lower sand layer through a modification in Equations 2.4b and 2.4c such that the sand's ultimate resistance increases (i.e. $\sigma'_{v2} = \gamma'_2 z_2 + \gamma'_1 H_1$) and the effective depth z_2 of the lower layer springs is now measured from the interface depth. This method will result in a lower bound value for the ultimate resistance of the sand layer, as suggested by Georgiadis (1983).

5.3.3 Model assembly

The model is solved under both kinematic and inertial loading through non-homogenous boundary conditions and a nodal point load, respectively. The modulus of subgrade reaction (E_{py}) for each spring element is computed as the secant stiffness of the p-y_{el} reaction curves (p/y_{el}). The global stiffness matrix is populated by computing the spring stiffness $k = E_{py}\Delta L$ and Euler-Bernoulli beam elements. The details on this process are available in Appendix A and Appendix B.1. 60 clay spring elements and 30 sand spring elements are evenly spaced across

H_1 and H_2, respectively. A sensitivity study showed that additional springs had negligible influence on the global response of the pile.

5.4 Pseudostatic model performance

Each permutation of the centrifuge configuration described in Section 5.2 is compared with equivalent pseudostatic models described in Section 5.3. The kinematic response and the combined kinematic and inertial response are investigated.

5.4.1 Kinematic bending moments - single pile

Strain gauges distributed along the pile continuously measure the bending moments during different base excitations for both the single and pile group in the centrifuge experiments (end piles only, see Figure 5.2) for both flights. The measured bending moments in the K flight are considered as the kinematic pile bending moments. Bending at the pile tip is assumed to be zero for both the single pile and end piles in the group for both flights and only the response measured by one end pile in a group is used for the numerical comparison.

The bending moment profile is determined from the pseudostatic model using Method A and Method B by considering no inertial load at the pile cap location. Figure 5.10 shows the comparison of peak bending moment profiles from centrifuge data and the pseudostatic model for the single pile.

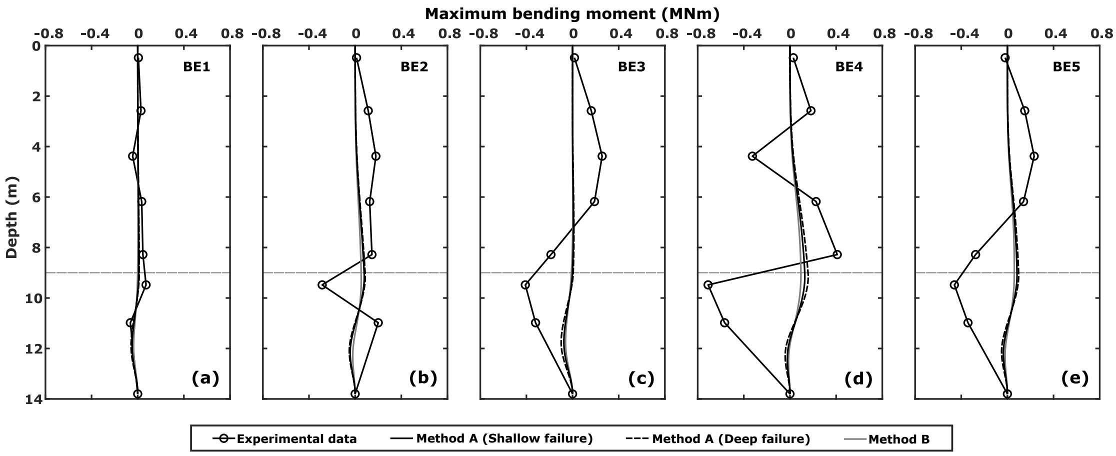

Figure 5.10: Comparison of kinematic pile bending moments obtained from centrifuge experiment and numerical study for a single pile

In Figure 5.10b and 5.10d, there are discontinuities in the bending moment profile generated from the experimental data. This is indicative of the maximum moments occurring at different points in time during the centrifuge tests, which is a principle assumption made in the pseudostatic methodology (Abghari & Chai, 1995; Tabesh & Poulos, 2001). Experimental results suggest that the maximum moment occurs at the interface of the layered soils. This is also evident in the numerical analysis, albeit the numerical model underestimates the peak moment of the single pile for each base excitation. All tests suggest that the numerical studies based on Method B underestimate the bending moment more than Method A, and the deep failure criteria of Method A gives a larger bending moment. This is expected, as the ultimate capacity of the sand spring will be greater for the deep failure definition, leading to a larger stiffness contrast between soil layers and a large moment at the interface. Figure 5.10d shows that BE4 experiences the largest peak bending moment during the K flight centrifuge test, which demonstrated to have the largest peak accelerations for single piles in Figure 5.7.

5.4.2 Kinematic pile bending moments - group pile

Figure 5.11 shows the bending moment profiles of the numerical models and the centrifuge experiments for the pile group. Pile group effects are simulated in the numerical model by applying a rotational fixity at the pile cap. No p-multipliers were used for pile groups as group effects are usually neglected for the kinematic loads (Fan et al., 1991; Nikolaou et al., 2001).

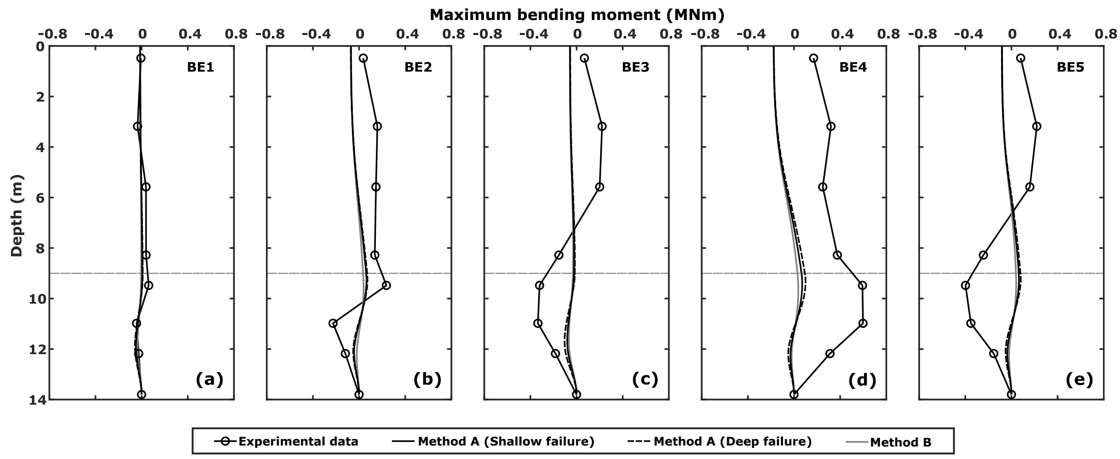

Figure 5.11: Comparison of kinematic pile bending moments obtained from centrifuge experiment and numerical study for group piles (p-multiplier = 1.0)

Again, the maximum moment occurs near the interface of the layered soils, and the numerical analysis underestimates the bending moment profile, especially for the larger intensity base excitations. This indicates that the earthquake intensity critically governs the accuracy of the pseudostatic results when considering kinematic loads. When a pile cap rotational constraint is considered, the difference between Method A and Method B is negligible for larger intensity earthquakes. Notably, the rotation fixity results in a significant bending moment at the ground line, which is near zero for single piles due to the free head boundary condition. Figure 5.11 suggests that the pseudostatic model can predict the magnitude of the bending moment at the ground line for the pile group. Regardless, the local maximum bending moment at the interface of the layered soils is still underestimated for all base excitations.

It is clear from Figures 5.10 and 5.11 that the pseudostatic method highly underestimates the kinematic pile bending moments for both the single pile and pile group and the difference increases with the intensity of the excitation. This is to be expected as the adopted code-based p-y curves are not developed for seismic kinematic loads. For evaluating pile bending under seismic kinematic loads, several simplified procedures and analytical solutions have been proposed in the literature. Margason and Halloway (1977) assumed that the pile foundation follows the surrounding soil motion during earthquakes and evaluated the pile bending response based on the free-field soil curvatures using the finite-difference method. Despite its simplicity, the Margason and Halloway (1977) method showed satisfactory performance in predicting the pile head moment in homogeneous or two-layer soils with the soil interface at deeper depths (Di Laora et al., 2013; Sanctis et al., 2010). Nevertheless, the Margason and Halloway (1977) method is not useful for a layered soil profile with sharp stiffness contrast between the layers. In this case, Di Laora and Rovithis (2015), Di Laora et al. (2012), Dobry and O'Rourke (1983), Mylonakis (2001b), Nikolaou et al. (1995), and Nikolaou et al. (2001), among others, have proposed closed-form solutions for evaluating the peak bending moment experienced along the pile based on beam on Winkler foundation or finite element analyses. Garala et al. (2020) evaluated the accuracy of these analytical and numerical solutions by comparing with experimental centrifuge data, and revealed that only a few methods in the literature can reasonably estimate the peak bending moment. The importance of considering soil nonlinearity effects and accurate shear strains at the interface of soil layers for a reliable assessment of the kinematic pile bending moment from the methods in existing literature is also highlighted in Garala et al. (2020).

5.4.3 Kinematic and inertial bending moments - single pile

The inertial force acting at the pile head can be computed by determining a representative acceleration in two different ways: (i) by considering the maximum soil surface acceleration from the centrifuge experiments, and (ii) by considering the peak spectral acceleration. In the case of liquefiable soils, Abghari and Chai (1995) found that considering the spectral acceleration for the inertial force resulted in the overestimation of pile response. On the other hand, Tabesh and Poulos (2001) recommended to consider either peak ground acceleration or peak spectral acceleration depending on the relevance between the dominant period of the pile-cap-soil system and the frequency content of the surface motion. According to Tabesh and Poulos (2001), the former may be approximated by the expression $T = 2\pi\sqrt{M_{cap}/K_x}$, where K_x is the lateral head stiffness of the pile. However, the above expression involving a crude approximation of reducing the mass of the supporting structure to a pile-cap mass should be used with caution as any eccentricity of the superstructure mass may have an important effect on the response. In this regard, the above authors suggested that for the case of relatively small pile-cap masses, the natural frequency of pile-cap-soil system may not be within the dominant frequencies of the ground surface motion, denoting negligible inertial effects. For such cases, the free-field soil motion governs pile behaviour, and the pseudostatic analysis can be performed by considering the peak ground acceleration at soil surface. For larger pile-cap masses that can have dominant frequencies close to the dominant frequencies of surface motion, inertial effects may be significant. Under these circumstances, Tabesh and Poulos (2001) recommended to consider the peak spectral acceleration rather than the maximum soil surface acceleration as considering peak spectral acceleration can yield a conservative result. The recommendations of Tabesh and Poulos (2001) suggest that the ground natural frequency and that of the pile cap-structure govern whether kinematic or inertial loads dominate.

The studies of Adachi et al. (2004) and Tokimatsu et al. (2005) also recommend that whether kinematic and inertial loads dominate is a function of the relevance between the natural frequencies of the soil and the pile-supported superstructure. However, Garala and Madabhushi (2020) concluded that whether kinematic or inertial loads dominate pile response is independent of the natural frequency of the soil and the phase relationship between the kinematic and inertial loads follows the conventional force-displacement phase variation for a viscously damped simple oscillator excited by a harmonic force.

In this study, to keep the analysis simple, the kinematic and inertial loads are assumed to act together on the pile foundations, indicating in-phase loading conditions. Further, due to the uncertainty in choosing the peak soil surface acceleration or the peak spectral acceleration for computing the inertial force in pseudostatic analysis, both are considered in this study and the difference between the two is evaluated by comparing the results with centrifuge data.

First, the maximum soil surface acceleration from centrifuge experiments is considered to compute the pseudostatic inertial force. Figure 5.12 shows the comparison of centrifuge data and the pseudostatic model for the single pile.

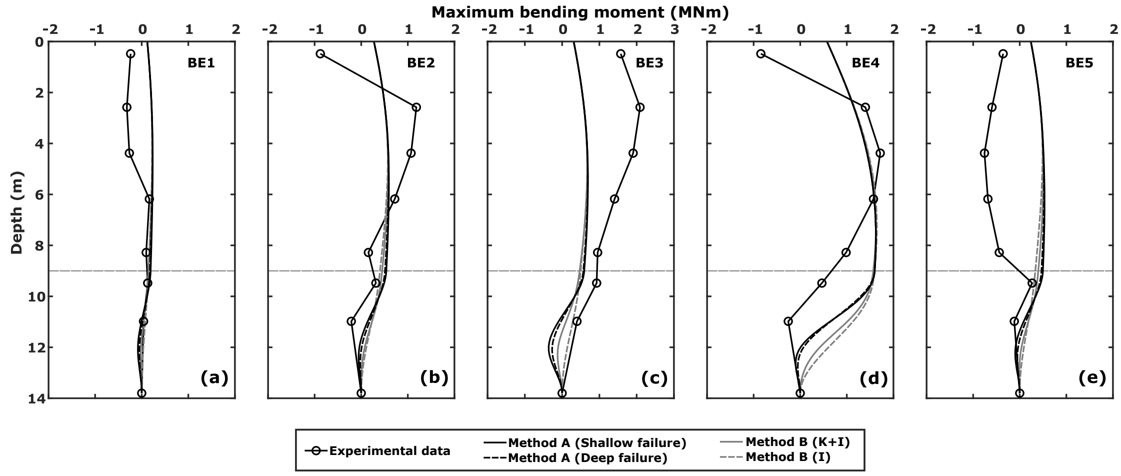

Figure 5.12: Comparison of pile bending moments obtained from centrifuge experiment and numerical study for single pile

Note that the bending moment profiles produced by the pseudostatic model for K+I and I are similar. This is indicative of the negligible kinematic forces when the bending moment profile is estimated, and suggests that the effects of poor kinematic bending moment profiles presented in Section 5.4.1 are minimised in K+I analyses. To add, according to Figure 5.12, the pseudostatic analysis still underestimates the peak bending moment during all base excitations when peak ground accelerations is used to inform the inertial load due to the pile cap for single piles. However, BE4 and BE5 demonstrates a close prediction in the peak bending moment. It was highlighted in Section 5.2 that there was a marked phase difference between the kinematic and inertial loads during the single pile tests for BE4 and BE5, which would lead to vibrations with smaller acceleration amplitudes and lower bending moments. Considering that BE4 and BE5 are regarded as intense excitations, it is likely that this phase difference resulted in lower bending moments in the experimental data evident in Figure 5.12d and 5.12e, and therefore a closer match between the numerical and experimental results. The pseudostatic model assumes in-phase loading conditions, therefore the peak bending moments would be overestimated for BE4 and BE5. It can therefore be deduced that the kinematic forces are poorly represented in the pseudostatic model for all base excitations, and is likely the cause for the contrasting peak bending moments.

The maximum bending moment profile estimated using Method A and Method B for layering effects is also shown in Figure 5.12. Results suggest that there is no significant difference in peak bending moment predicted by considering either the top-layer as overburden or an equivalent depth for the bottom layer, following Georgiadis (1983) procedure with shallow or deep failure criteria to account for soil-layering effects. Notably, Figure 5.12c and Figure 5.12d show the bending moment profiles differ in the lower sand layer due to the different failure criteria and strength definitions used across Method A and Method B. However, the difference in peak bending moment between Method A and Method B is still negligible. It should be noted that this might be valid only for the case of soils with significant stiffness contrast between the layers. Additionally, The pseudostatic model estimates the depth of the peak bending moment close to the transition depth between the two soil layers, whereas the centrifuge tests suggest that the peak bending moment occurs somewhere higher in the clay layer. This may be due to a poor representation of the stiffness and dynamic properties of the API soil reaction curves.

5.4.4 Kinematic and inertial bending moments - group pile

For the case of the pile group, the reduced stiffness and ultimate capacity is accounted for through p-multipliers, as discussed earlier and in Section 2.1.2. Table 2.6 shows the p-multipliers proposed by various researchers for pile groups under non-dynamic lateral loads in sands and clays. As a single row pile group is tested in the centrifuge experiments, an average conservative value of the p-multiplier of 0.7 is considered for both the clay and sand layers from Table 2.6, given that p-multipliers depend primarily on pile spacing rather than soil layering (Castelli et al., 2010). More details on the application of p-multipliers in beam-spring models in general can be found in Section 2.1.2.

Figure 5.13 shows the comparison of maximum pile bending moments moments computed from pseudostatic analysis and centrifuge data for a p-multiplier of 0.7. A rotational fixity is applied at the pile cap in the numerical model.

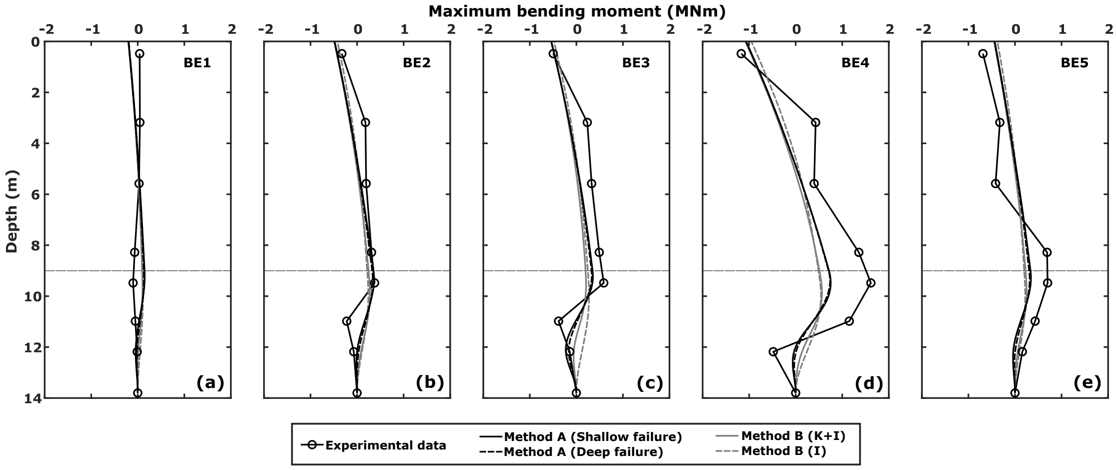

Figure 5.13: Comparison of pile bending moments obtained from centrifuge experiment and numerical study for a pile in pile group with p-multiplier = 0.7

It is clear from Figure 5.13 that the pseudostatic analysis can better predict the shape of the bending moment profile of group piles for all base excitations compared to the single pile analysis, regardless of the p-multiplier. The locations of the sigfinicant bending moments along the pile are also in close agreement between the numerical model and experimental data. In contrast to the single pile tests, the experimental data demonstrates a significant moment at the ground line due to the pile cap. The rotational constraint in the numerical analysis successfully models the pile group cap fixity, and the bending moments are in close agreement. However, the bending moment at the layer interface is still underestimated, which is indicative of the API reaction curves not capturing the pile-soil interection effectively under seismic conditions. The poor representation of kinematic forces evident in Figures 5.10 and 5.11 may also be a contributing factor to the underestimation of the peak bending moment. Similar to the single pile case in Figure 5.12, the influence of kinematic forces on the peak bending moment are negligible. The kinematic loads for the stronger base excitations, namely BE3 to BE5, are likely to have a significant effect on the bending moment profile, which could be the reason for the closer match between the numerical and experimental results for BE1 and BE2 when compared to BE4 and BE5.

In general, Method A predicted the peak bending moments at the interface of layered soils slightly better than Method B. This indicates that soil layering effects can be considered either by equivalent depth approach or just by considering the top layer as overburden on the bottom layer for the case of soil strata with significant stiffness contrast for the fixed-head pile group. Nevertheless, this approach cannot predict the peak bending moments at the interface of layered soils to an acceptable level.

5.4.5 Inertial force from spectral accelerations

To further investigate the suitability of the pseudostatic approach, peak spectral accelerations are used to compute the inertial forces for each base excitation. Spectral acceleration, by definition, is the maximum acceleration that a ground motion will cause in a linear oscillator with a specified natural period and damping ratio. The measured ground accelerations from the centrifuge for each base excitation are used in a time-domain simulation to compute the frequency content of the response. The Newmark-β time marching algorithm (Section 4.1.2) is used to solve the response of a single degree of freedom system for a damping ratio that is to be specified.

Although the geometric calibration space for the API sand and clay models are appropriate for the piles in this study, the loading conditions are not. This means that the reaction curves are not suitable for soils subjected to seismic excitation, especially when considering the kinematic effects. To remedy this, an arbitrarily large damping ratio of 20% is considered when computing the spectral accelerations for deriving the inertial force. This is an attempt to implicitly consider the dissipative properties of the extremely soft clay layer relative to the underlying dense sand layer. Figure 5.14 shows the frequency content for a linear single degree of freedom oscillator with 20% damping driven by the ground acceleration for each base excitation. The peak acceleration for each base excitation from Figure 5.14 is then used to calculate the inertial load of the pseudostatic methodology.

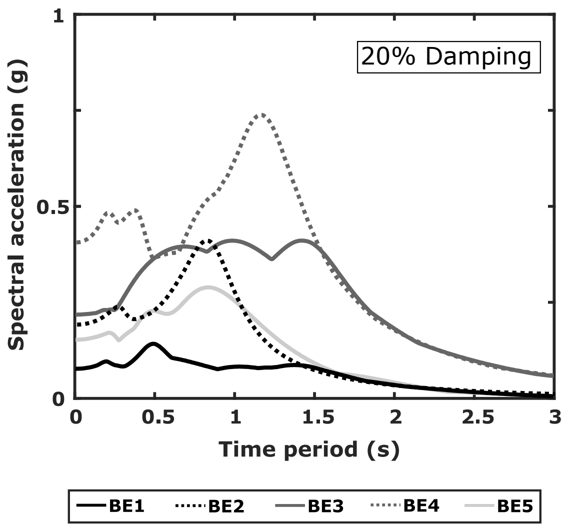

Figure 5.14: acceleration frequency content of the oscillators determined from soil surface accelerations of each base excitation with 20% damping

Figure 5.15 shows the maximum bending moment profiles from centrifuge experiments and numerical models for single piles under kinematic and inertial loading, where the inertial forces are computed from peak spectral accelerations at 20% damping. Only Method A with shallow failure criteria and Method B with both kinematic and inertial loads are considered in this spectral acceleration investigation.

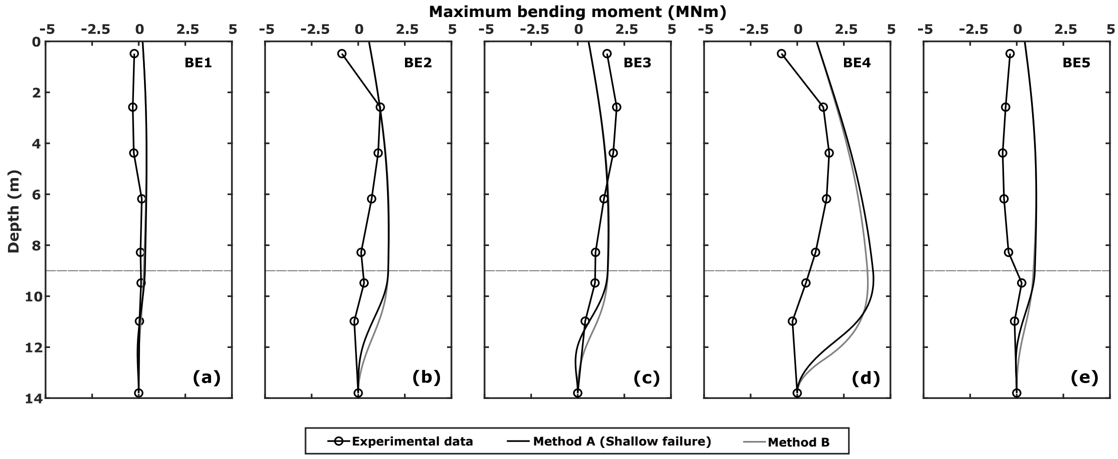

Figure 5.15: Comparison of pile bending moments obtained from centrifuge experiment and numerical analysis for single pile from spectral accelerations with 20% damping (Kinematic + Inertial loads)

Figure 5.15 shows that the pseudostatic model resulted in an improved estimation in the magnitude of peak bending moments, except for BE4. This is again likely due to the in-phase assumption implicit with the pseudostatic method, whereas the experimental data suggests a phase difference between the kinematic and inertial loads that would limit acceleration amplitudes and reduce anticipated bending moments. The estimated location of the peak bending moment is still inadequate.

For group piles, the peak bending moments are compared between the numerical model and the centrifuge experiments for the pile group with p-multipliers of 0.7 and 1 (no group modifications) in Figure 5.16.

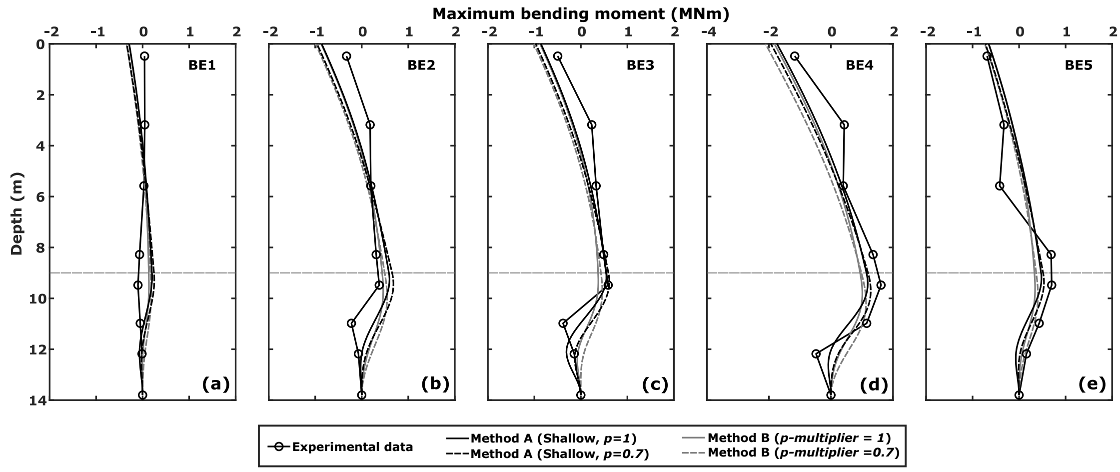

Figure 5.16: Comparison of pile bending moments obtained from centrifuge experiment and numerical analysis for pile group from spectral accelerations with 20% damping (Kinematic + Inertial loads)

Recall that Figure 5.13 demonstrated that considering the peak ground acceleration for computing the pseudostatic inertial force can result in an acceptable peak pile bending response for certain excitations (BE1 to BE3), and the general bending moment profile shape was captured adequately. Figure 5.16 suggests that a spectral acceleration derived with 20% damping can result in an improved estimation for all base excitations, in particular near the soil layer interface. However, it merits mentioning that the inadequate representation of kinematic loads in the pseudostatic model remains unadressed, as the evident improvement in the peak bending moment estimation will be a product of the alternative inertial force computation via spectral accelerations. In other words, the inertial load derived from the spectral accelerations at 20% damping is compensating for the poor kinematic bending moment estimations. Regardless, a clear improvement in the general bending moment profile for the group piles is observed. Additionally, Figure 5.16 indicates that p-multiplier of 0.7 is necessary to improve bending moment estimation for group piles.

5.5 Conclusions

The efficacy of pseudostatic approach for the seismic analysis of pile foundations in layered soils is discussed in this study by comparing the performance of pseudostatic models with centrifuge records. The latter was obtained by the University of Cambridge (Garala, 2020) using centrifuge tests on a single pile and a 1 x 3 row pile group at 60g to evaluate the pile bending moments due to kinematic and inertial loads. The soil profile consists of a soft clay layer underlain by dense sand. A finite element model for pseudostatic analysis was developed that consists of a series of linear-elastic Euler-Bernoulli beam elements and nonlinear p-y spring elements at discrete points taking the form of a beam-spring model. In this study, p-y relationships recommended by the American Petroleum Institute (API, 2014) for the laterally loaded piles (monotonically or cyclically) were used for the clay and sand layer. The pseudostatic model considers both kinematic and inertial loads by considering peak free-field soil displacements and maximum inertial loads at the pile head, respectively. The effect of soil layering on p-y_{el} relationships was accounted for by considering the concept of equivalent depths proposed by Georgiadis (1983) and by considering the top layer as an overburden on the bottom layer. Pile group effects in soil-pile interaction were accounted for by reducing the stiffness and ultimate capacity of the pile group using the concept of p-multipliers. The following are the observations were made:

- The API p-y relationships were not able to capture the kinematic pile bending moments at the interface of the examined layered soil profile for both single and group piles. These p-y curves refer to piles in homogeneous soils subjected to monotonic or cyclic loads, and were not derived for seismic conditions. In this regard, the numerical model critically under-predicted the kinematic pile bending moments, which was observed to exacerbate with increasing base excitation intensity.

- The peak bending moments computed for combined kinematic and inertial loads from pseudostatic analysis using peak ground accelerations at the soil surface may be under-predicted for a free-headed single pile if the kinematic and inertial loads are in-phase. The location of the peak bending moment is represented inadequately in the numerical model, which is likely due to a higher stiffness contrast implicit with the API reaction curve definitions compared to the soil in the centrifuge tests.

- It was observed that the pseudostatic model failed to capture the actual pile bending moments at the interface of layered soils when the inertial force was derived from peak ground acceleration at the soil surface for both single and group piles. However, the general shape of the bending moment profile of the group piles was captured adequately.

- An arbitrarily high damping ratio of 20% was used to derive the inertial force via spectral accelerations due to the soft clay layer. In general, the performance of the pseudostatic model improved as a consequence. For single piles, the magnitude of the peak bending moment was estimated well when the kinematic and inertial loads were in phase, however the calculated depth was insufficient. For group piles, all base excitation response estimations were improved, likely due to the in-phase conditions for all group pile centrifuge tests. However, the poor representation of kinematic loads in the pseudostatic model remains unaddressed.

- There is a negligible difference in the peak bending moment values estimated in the numerical model when using Method A or Method B. However, This is likely only a valid conclusion for soil layers with significant stiffness contrasts.
- Using a p-multiplier of 0.7 for the pile group improves the bending moment estimation for the group piles. The rotational constraint in the numerical model is suitable, and the shape of the bending moment profiles are captured well as a consequence.

Overall, this chapter reviews the efficacy of the API p-y curves when establishing the largest moment experienced during base excitations via the pseudostatic methodology. An attempt was made to correct the issues associated with the calibration space of the reaction curves by modifying the inertial force to encapsulate the dissipative properties using the spectral acceleration approach. The results suggest that, if the base excitation causes in-phase kinematic and inertial conditions, this modification can sufficiently estimate the peak bending moment for both the single and pile groups in layered soils, albeit with a poor representation of the kinematic loads. The location of the peak bending moment for single piles is, however, still poorly captured. These findings may be limited to the specific soil profile and pile geometry considered in this study, and further research is required to validate conclusions.

The soil layering effects can be imposed on the p-y curves by implementing the Georgiadis (1983) modifications or by treating the top layer as an over-burden on bottom layer (for soil profiles similar to the one discussed in this article). Nevertheless, both theories account for the effect of overlying layers on the lower layers but not vice-versa. Relevant studies based on finite element simulations (e.g., Yang and Jeremić (2005)) have demonstrated that layering effects can act in two directions, namely that upper layers can also be affected by the properties of lower layers. This aspect of soil layering effects is not considered in the equivalent depth approach proposed by Georgiadis (1983) or where the top layer is treated as an overburden on the bottom layer. Furthermore, it should be mentioned that the seismic response of pile foundations is governed by lateral motions and axial stresses induced by rocking of the single pile, or group, on piles of a pile group. Lateral motion in only one direction is considered in this analysis, and the more realistic seismic pile behaviour can be captured by modelling both lateral motion and rocking together.

It is of interest to invsetigate alternative p-y curves that are well established in design codes and literature (Byrne et al., 2017; Jeanjean, 2009; Li et al., 2014; Suryasentana & Lehane, 2016), which may be more appropriate for pseudostatic analysis in layered soil deposits. However, these models only consider soil stiffness and do not account for the dynamic response of the soil-structure system. Advanced analysis in the time domain can be performed by incorporating dashpots and hysteretic spring elements to capture the dynamic response of the soil-structure system more appropriately. This is a topic for future research, which could be used to validate the results of the pseudostatic model.

Chapter 6

Conclusions

Each chapter in this thesis focuses on pile models for different types of lateral loading configurations. Specifically, Chapters 3 and 4 investigate the application of one-dimensional beam-spring models to capture the static and dynamic responses of monopiles, respectively. In Chapter 5, the pseudostatic method is examined across a range of pile-soil configurations for seismic loading. Each chapter provides individual conclusions. This chapter serves to summarise the key findings of the thesis and present recommendations for future work.

6.1 Summary

The literature review in Chapter 2 outlined the analysis and design of piles for the various forms of lateral loading. More importantly, this chapter highlighted how traditional methodologies have evolved as a means to keep up with the rapid growth of the offshore wind industry in recent decades. For example, Larger turbines have lead to larger foundations and more dynamically sensitive systems, ultimately leading to a more complex soil-structure interaction. Low L/D monopiles have an increased rigidity which introduces resistance mechanisms traditional methodologies cannot account for. This has necessitated novel approaches to encapsulate additional soil-structure mechanisms from detailed ground investigations. Additionally, because of the increased dynamic sensitivity of modern OWT-monopile systems, the design process necessitates time-domain simulations that enable nonlinear solvers to leverage efficient algorithms to maximise computational spend. Such models should be qualified to facilitate geotechnical phenomena expected when the elastic range of soil is exceeded, such as gapping and ratcheting. Chapter 2 reviewed a variety of hysteresis models which can be used to capture these effects, and the importance of time-domain analysis for capturing dynamic soil-structure interaction was highlighted. The literature review therefore raised the following research questions: (i) Is it possible to inform a multi-spring-beam model utilising only in-situ ground investigation data to streamline the preliminary design process of OWT monopiles? (ii) Can an efficient solver for the dynamic nonlinear response of monopiles under irregular cyclic loading be developed without compromising accuracy? (iii) Can the static nonlinear beam-spring model idealise pile-soil interaction for complex loading configurations?

These questions are answered by building upon the traditional p-y method within each chapter. Chapter 3 details the development and performance of a CPT-based multi-spring model. CPTs are often an early stage of ground investigation in the offshore environment, which would therefore serve as a strong basis for a preliminary design methodology. Given the inherent heterogeneity of offshore soil profiles, the utilisation of CPT data to inform the soil reaction curves, which account for the presence of diameter effects, becomes particularly advantageous. The model is compared with field test reports of numerous open-ended circular steel piles in sand exposed to a monotonic lateral load at the pile head. The results show that the model can capture the response of the pile within $0.01D$ ground line deflections, which is equivalent to 0.25° rotation at the ground line. This is the rotation limit during operation for OWTs defined by the SLS design philosophy. Identifying a suitable correlation between the residual bearing stress and the CPT end resistance improved estimations for larger deflections. However, it has proven difficult to identify a suitable correlation for $q_{b,res}$ and $q_{c,r}$.

The random nature of wind and wave loads necessitate a time-domain approach to modelling the hysteretic behaviour of pile-soil interaction on a cycle-by-cycle basis. Chapter 4 details the development of a dynamic p-y framework that estimates pile deflections due to irregular load histories, where robustness and efficiency are of high priority. This is crucial, as it is common practice to simulate many force time series that are derived from different wind/wave loading configurations as a part of the design process for OWT foundations. This approach not only encapsulates the largest source of energy loss in the system (material damping due to medium to large soil strains), but can also facilitate more advanced geotechnical behaviour such as ratcheting and gap formation. A controlled simulation demonstrated that the Masing and Bouc-Wen hysteresis models exhibit erroneous drifting behaviour due to their dependency on velocity signage, underlining the importance of this qualitative numerical study. It was shown that the Iwan model is the most suitable hysteresis model for dynamic p-y models, as it was the least sensitive to the loading configuration applied and the TMA used. A random wind and wave load history was generated from frequency spectra established from design codes, and applied to an OWT system appended on top of the dynamic p-y model. The Iwan hysteresis and Generalised-α numerical integration algorithm were employed to solve the nonlinear system. It was shown that high frequency modes have a negligible influence on the highly nonlinear response, therefore the Newmark-β TMA can be used. However, the Generalised-α method with $\rho_\infty = 0.6$ is recommended for large Δt values as it is good practice to dissipate the erroneous modal frequencies.

Chapter 5 investigated the pseudostatic approach for general pile design for a variety of different pile-soil configurations exposed to seismic loading. Design codes offer limited guidance for seismic design of pile foundations under such conditions, especially when determining the required moment capacity of a pile due to earthquake excitations. Therefore, the purpose of this study was to examine the effectiveness of the pseudostatic p-y method , a static beam-spring model with idealised seismic loads, when informed using the API soil reaction definitions for layered soils. Single and group piles in two-layer soil deposits were modelled in a 60g geotechnical centrifuged performed at the University of Cambridge, and were used to evaluate the estimated bending moment from the pseudostatic model. It was found that, for dense sand under soft clay, the pseudostatic model was able to estimate the peak bending moment for single and group piles if the kinematic and inertial forces are in-phase, and the inertial force is informed by the peak spectral acceleration. Crucially, the spectral acceleration was determined using a sufficiently high damping ratio, which was deemed appropraite due to the expected dissipative properties of the top loose clay layer. The location of the peak bending moment for single piles was poorly estimated, which may be due to the innappropriate use of monotonically-derived p-y curves or inadequate representation of kinematic forces, or a combination of both. For low-intensity seismic events, the pseudostatic analysis with inertial pile head loading from peak ground acceleration works well. However, for high-intensity earthquakes, using peak spectral acceleration and damping considerations in the pseudostatic model is more accurate for single piles but conservative for pile groups, compared to centrifuge data.

6.2 Future work

In light of the findings and insights from the preceding chapters, several avenues for future work become evident. The following areas warrant further exploration and refinement:

- **Enhanced CPT-based multi-spring model:** The CPT-based multi-spring model can be improved with more consideration for ULS. The p-y relationship contributes the most to lateral resistance, however the current methodology is not suitable for capacity estimation for low L/D monopiles. The underlying assumptions in the distributed m-θ and base springs can also be improved to account for potential gap formation at large displacements.

- **Improved soil reaction curve definition for dynamic p-y model:** A robust and efficient hysteresis MDOF framework has been established, however the API sand model used to describe the backbone function in Chapter 4 is not appropriate for low L/D monopiles. A quantitative study was therefore not sensible. Furthermore, the anticipated load rate under dynamic conditions suggests that p-y functions derived by monotonic calibration procedures may not be appropriate for informing hysteresis models. A p-y curve derived specifically for the expected loading rates (0.1 Hz) and the appropriate monopile dimensions is therefore an area for further investigation.

- **Advanced degrading Iwan model:** It is possible to modify the Iwan hysteresis model to capture hysteresis shapes that resemble common geotechnical behaviour in OWT monopiles. Section 2.2 reviewed cyclic contour diagrams, which are commonly used to estimate the cyclic degradation of offshore substructures based on site investigations and soil sample testing. This includes the accumulated pore pressures and plastic strains from repeated cyclic loading. It is postulated here that the hysteresis parameters that control a hypothetical gapping, ratcheting or pore pressure accumulation model may be informed from cyclic contour diagrams, which is an area for further investigation. However, a suitable backbone curve that encapsulates the diameter effects and load rate needs to be established first.

- **Multi-spring dynamic p-y model:** A natural progression for static multi-spring model derived in Chapter 3 is utilise the framework in a dynamic context. However, the cyclic behaviour of the distributed m-θ and pile base springs is not well understood, and warrants further investigation. Explicitly modelling individual soil reaction mechanisms for low L/D monopiles may be more appropriate for capturing the dynamic nonlinear response under irregular cyclic loading, rather than utilising a hysteretic p-y-only model that captures the diameter effects within its parametrisation space.

- **Alternative p-y curves for the pseudostatic model:** In Chapter 5, the pseudostatic method was examined using API sand and API clay soil elements. As they are well established for piles in design, this chapter reviewed their efficacy in the context modelling the response of seismic excitations. It is worth noting that CPT-based *p*-*y* methods for sand and clay profiles are typically calibrated for piles with dimensions resembling those of the scaled pile tests performed in the geotechnical centrifuge experiments discussed in this study. Future work in this area may involve investigating the application of CPT-based functions, or others, in the context of pseudostatic analysis of single or group piles in layered soils exposed to seismic loading.

- **Cross-comparison between pseudostatic and time-domain earthquake models:** The base excitations used in Chapter 5 can be used to inform a time-domain model similar to the one developed in Chapter 4. This would allow for a direct comparison between the two methodologies, and provide insight into the limitations of the pseudostatic model. The dynamic *p*-*y* model would require modifications to account for the the high-frequency loads expected from seismic events, including moving boundary conditions to emulate the kinematic forces.

References

Abadie, C., Houlsby, G., & Byrne, B. (2019). A method for calibration of the Hyperplastic Accelerated Ratcheting Model (HARM). *Computers and Geotechnics*, *112*, 370–385. https://doi.org/10.1016/j.compgeo.2019.04.017

Abghari, A., & Chai, J. (1995). Modeling of soil-pile-superstructure interaction for bridge foundations. *Performance of Deep Foundations under Seismic Loading*, 45–59.

Adachi, N., Suzuki, Y., & Miura, K. (2004). Correlation between inertial force and subgrade reaction of pile in liquefied soil. *13th World Conference on Earthquake Engineering*, 332.

Alexander, N. (2010). Estimating the nonlinear resonant frequency of a single pile in nonlinear soil. *Journal of Sound and Vibration*, *329*(8), 1137–1153. https://doi.org/10.1016/j.jsv.2009.10.026

Alexander, N., & Bhattacharya, S. (2011). The dynamics of monopile-supported Wind Turbines in nonlinear soil. *8th International Conference on Structural Dynamics*.

Allotey, N., & El Naggar, M. H. (2008). Generalized dynamic Winkler model for nonlinear soil–structure interaction analysis. *Canadian Geotechnical Journal*, *45*(4), 560–573. https://doi.org/10.1139/T07-106

Amar Bouzid, D. J. (2018). Numerical investigation of large-diameter monopiles in sands: Critical review and evaluation of both API and newly proposed p-y curves. *International Journal of Geomechanics*, *18*(11), 04018141. https://doi.org/10.1061/(asce)gm.1943-5622.0001204

Ambrosini, R. D. (2006). Material damping vs. radiation damping in soil–structure interaction analysis. *Computers and Geotechnics*, *33*(2), 86–92. https://doi.org/10.1016/j.compgeo.2006.03.001

Amjadi, A. H., & Johari, A. (2022). Stochastic nonlinear ground response analysis considering existing boreholes locations by the geostatistical method. *Bulletin of Earthquake Engineering*, *20*(5), 2285–2327. https://doi.org/10.1007/s10518-022-01322-1

Andersen, K. (2009). Bearing capacity under cyclic loading — offshore, along the coast, and on land. *Canadian Geotechnical Journal*, *46*(5), 513–535. https://doi.org/10.1139/T09-003

Andersen, K. (2015). Cyclic soil parameters for offshore foundation design. *Frontiers in Offshore Geotechnics III*, *1*, 5–82.

Andersen, K., Puech, A., & Jardine, R. (2013). Cyclic resistant geotechnical design and parameter selection for offshore engineering and other applications. *TC 209 Workshop*.

Andersen, L. (2010). Assessment of lumped-parameter models for rigid footings. *Computers & Structures*, *88*(23-24), 1333–1347. https://doi.org/10.1016/j.compstruc.2008.10.007

Anoyatis, G., & Lemnitzer, A. (2017a). Dynamic pile impedances for laterally–loaded piles using improved Tajimi and Winkler formulations. *Soil Dynamics and Earthquake Engineering*, *92*, 279–297. https://doi.org/10.1016/j.soildyn.2016.09.020

Anoyatis, G., & Lemnitzer, A. (2017b). Kinematic Winkler modulus for laterally-loaded piles. *Soils and Foundations*, *57*(3), 453–471. https://doi.org/10.1016/j.sandf.2017.05.011

Anthes, R. J. (1997). Modified rainflow counting keeping the load sequence. *International Journal of Fatigue*, *19*(7), 529–535. https://doi.org/10.1016/S0142-1123(97)00078-9

API. (2014). *RP 2GEO: Geotechnical and foundation design considerations*.

Arany, L., Bhattacharya, S., Macdonald, J., & Hogan, S. (2017). Design of monopiles for offshore wind turbines in 10 steps. *Soil Dynamics and Earthquake Engineering*, *92*, 126–152. https://doi.org/10.1016/j.soildyn.2016.09.024

Arany, L., Bhattacharya, S., Macdonald, J., & Hogan, S. J. (2015). Simplified critical mudline bending moment spectra of offshore wind turbine support structures: Simplified critical bending moment spectra of offshore wind turbines. *Wind Energy*, *18*(12), 2171–2197. https://doi.org/10.1002/we.1812

Argyris, J. H., & Mlejnek, H.-P. (1991). *Dynamics of structures*. North-Holland ; Distributors for the USA and Canada, Elsevier Science Pub. Co.

Ariannia, S. S. (2017). *Determination of p-y Curves by Direct Use of Cone Penetration Test (CPT) Data*.

Ashford, S. A., & Juirnarongrit, T. (2003). Evaluation of pile diameter effect on initial modulus of subgrade reaction. *Journal of Geotechnical and Geoenvironmental Engineering*, *129*(3), 234–242. https://doi.org/10.1061/(asce)1090-0241(2003)129:3(234)

Ashmawy, A. K., Salgado, R., Guha, S., & Drnevich, V. P. (1995). Soil Damping and Its Use in Dynamic Analyses.

Baber, T. T., & Noori, M. N. (1985). Random Vibration of Degrading, Pinching Systems. *Journal of Engineering Mechanics*, *111*(8), 1010–1026. https://doi.org/10.1061/(ASCE)0733-9399(1985)111:8(1010)

Baber, T. T., & Noori, M. N. (1986). Modeling General Hysteresis Behavior and Random Vibration Application. *Journal of Vibration and Acoustics*, *108*(4), 411–420. https://doi.org/10.1115/1.3269364

Badoni, D., & Makris, N. (1996). Nonlinear response of single piles under lateral inertial and seismic loads. *Soil Dynamics and Earthquake Engineering*, *15*(1), 29–43. https://doi.org/10.1016/0267-7261(95)00027-5

Baldi, G., Bellotti, R., Ghionna, V., Jamiolkowski, M., & Lo Presti, D. (1989). Modulus of sands from CPTs and DMTs. *Proc. 12th international conference on soil mechanics and foundation engineering, Rio de Janeiro, 1989. Vol. 1*, 165–170.

Barnes, G. (2010). *Soil mechanics: Principles and practice [Eurocode compliant]* (3. ed). Palgrave Macmillan.

Basarah, Y. I., Numanoglu, O. A., Hashash, Y. M. A., & Dashti, S. (2019). Impact of Hysteretic Damping on Nonlinear Dynamic Soil-Underground Structure-Structure Interaction Analyses, 208–218. https://doi.org/10.1061/9780784482100.022

Bathe, K. J., & Wilson, E. L. (1976). Numerical methods in finite element analysis.

Bathe, K. J. (2006). *Finite element procedures*. Bathe.

Beck, J. L., & Pei, J. S. (2022). Demonstrating the power of extended Masing models for hysteresis through model equivalencies and numerical investigation. *Nonlinear Dynamics*, *108*(2), 827–856. https://doi.org/10.1007/s11071-022-07237-5

Benz, T. (2007). *Small-strain stiffness of soils and its numerical consequences*.

Bhattacharya, S. (2019). *Design of foundations for offshore wind turbines*. Wiley.

Biot, M. (1937). Bending of an infinite beam on an elastic foundation. *Journal of Applied Mechanics*, *59*, A1–A7.

Bouc, R. (1971). Modèle mathématique d'hystérésis. *Acustica*, (21), 16–25.

Branlard, E. (2010). Generation of time series from a spectrum:Generation of Wind times series from the Kaimal spectrum.

Branlard, E., Shields, M., Anderson, B., Damiani, R., Wendt, F., Jonkman, J., Musial, W., & Foley, B. (2020). Superelement reduction of substructures for sequential load calculations in OpenFAST. *Journal of Physics: Conference Series*, *1452*, 012033. https://doi.org/10.1088/1742-6596/1452/1/012033

Broms, B. B. (1964a). Lateral Resistance of Piles in Cohesive Soils. *Journal of the Soil Mechanics and Foundations Division*, *90*(2), 27–63. https://doi.org/10.1061/JSFEAQ.0000611

Broms, B. B. (1964b). Lateral Resistance of Piles in Cohesionless Soils. *Journal of the Soil Mechanics and Foundations Division*, *90*(3), 123–156. https://doi.org/10.1061/JSFEAQ.0000614

Brown, D. A., Morrison, C., & Reese, L. C. (1988). Lateral load behavior of pile group in sand. *Journal of Geotechnical Engineering*, *114*(11), 1261–1276. https://doi.org/10.1061/(ASCE)0733-9410(1988)114:11(1261)

Brown, D. A., Reese, L. C., & O'Neill, M. W. (1987). Cyclic Lateral Loading of a Large-Scale Pile Group. *Journal of Geotechnical Engineering*, *113*(11), 1326–1343. https://doi.org/10.1061/(ASCE)0733-9410(1987)113:11(1326)

Burd, H. J., Abadie, C. N., Byrne, B. W., Houlsby, G. T., Martin, C. M., McAdam, R. A., Jardine, R. J., Pedro, A. M. G., Potts, D. M., Taborda, D. M. G., Zdravković, L., & Andrade, M. P. (2020a). Application of the PISA design model to monopiles embedded in layered soils. *Géotechnique*, *70*(11), 1067–1082. https://doi.org/10.1680/jgeot.20.PISA.009

Burd, H. J., Byrne, B. W., McAdam, R., Houlsby, G. T., Martin, C. M., Beuckelaers, W. J. A. P., Zdravković, L., Taborda, D. M. G., Potts, D. M., Jardine, R. J., Gavin, K. G., Doherty, J. P., Igoe, D. J. P., Gretlund, J. S., Pacheco, M. A., & Wood, A. (2017). Design aspects for monopile foundations.

Burd, H. J., Taborda, D. M. G., Zdravković, L., Abadie, C. N., Byrne, B. W., Houlsby, G. T., Gavin, K. G., Igoe, D. J. P., Jardine, R. J., Martin, C. M., McAdam, R. A., Pedro, A. M. G., & Potts, D. M. (2020b). PISA design model for monopiles for offshore wind turbines: Application to a marine sand. *Géotechnique*, *70*(11), 1048–1066. https://doi.org/10.1680/jgeot.18.P.277

Butcher, J. (1996). A history of Runge-Kutta methods. *Applied Numerical Mathematics*, *20*(3), 247–260. https://doi.org/10.1016/0168-9274(95)00108-5

Byrne, B. W., & Houlsby, G. T. (2003). Foundations for Offshore Wind Turbines. *Philosophical Transactions: Mathematical, Physical and Engineering Sciences*, *361*(1813), 2909–2930.

Byrne, B. W., Houlsby, G. T., Burd, H. J., Gavin, K., Igoe, D. J. P., Jardine, R. J., Martin, C. M., McAdam, R. A., Potts, D. M., Taborda, D. M. G., & Zdravković, L. (2020a). PISA design model for monopiles for offshore wind turbines: Application to a stiff glacial clay till. *Geotechnique*, *70*(11), 1030–1047. https://doi.org/10.1680/jgeot.18.P.255

Byrne, B. W., McAdam, R., Burd, H. J., Houlsby, G. T., Martin, C. M., Beuckelaers, W. J. A. P., Zdravkovic, L., Taborda, D. M. G., Potts, D. M., Jardine, R. J., Ushev, E., Liu, T., Abadias, D., Gavin, K., Igoe, D., Doherty, P., Gretlund, J., Andrade, M. P., Wood, A. M., … Plummer, M. A. L. (2017). PISA: New Design Methods for Offshore Wind Turbine Monopiles.

Offshore Site Investigation Geotechnics 8th International Conference Proceedings, 142–161. https://doi.org/10.3723/OSIG17.142

Byrne, B. W., McAdam, R. A., Burd, H. J., Houlsby, G. T., Martin, C. M., Zdravković, L., Taborda, D. M. G., Potts, D. M., Jardine, R. J., Sideri, M., Schroeder, F. C., Gavin, K., Doherty, P., Igoe, D. J. P., Wood, A., Kallehave, D., & Gretlund, J. S. (2015). New design methods for large diameter piles under lateral loading for offshore wind applications. *Frontiers in Offshore Geotechnics III*, 705–710. https://doi.org/10.1201/b18442-96

Byrne, B. W., McAdam, R. A., Burd, H. J., Beuckelaers, W. J. A. P., Gavin, K. G., Houlsby, G. T., Igoe, D. J. P., Jardine, R. J., Martin, C. M., Muir Wood, A., Potts, D. M., Skov Gretlund, J., Taborda, D. M. G., & Zdravković, L. (2020b). Monotonic laterally loaded pile testing in a stiff glacial clay till at Cowden. *Géotechnique*, *70*(11), 970–985. https://doi.org/10.1680/jgeot.18.PISA.003

Byrne, T., Gavin, K., Prendergast, L. J., Cachim, P., Doherty, P., & Chenicheri Pulukul, S. (2018). Performance of CPT-based methods to assess monopile driveability in North Sea sands. *Ocean Engineering*, *166*, 76–91. https://doi.org/10.1016/j.oceaneng.2018.08.010

Cao, G., Ding, X., Yin, Z., Zhou, H., & Zhou, P. (2021). A new soil reaction model for large-diameter monopiles in clay. *Computers and Geotechnics*, *137*, 104311. https://doi.org/10.1016/j.compgeo.2021.104311

Carswell, W., Arwade, S. R., DeGroot, D. J., & Myers, A. T. (2016). Natural frequency degradation and permanent accumulated rotation for offshore wind turbine monopiles in clay. *Renewable Energy*, *97*, 319–330. https://doi.org/10.1016/j.renene.2016.05.080

Carswell, W., Johansson, J., Løvholt, F., Arwade, S. R., Madshus, C., DeGroot, D. J., & Myers, A. T. (2015). Foundation damping and the dynamics of offshore wind turbine monopiles. *Renewable Energy*, *80*, 724–736. https://doi.org/10.1016/j.renene.2015.02.058

Castelli, F., Lentini, V., & Maugeri, M. (2010). A Simplified Approach for the Evaluation of Kinematic Pile Bending.

Castelli, F., & Maugeri, M. (2009). Simplified Approach for the Seismic Response of a Pile Foundation. *Journal of Geotechnical and Geoenvironmental Engineering*, *135*(10), 1440–1451. https://doi.org/10.1061/(ASCE)GT.1943-5606.0000107

Castro-Santos, L., & Diaz-Casas, V. (Eds.). (2016). *Floating Offshore Wind Farms* (1st ed. 2016). Springer International Publishing : Imprint: Springer. https://doi.org/10.1007/978-3-319-27972-5

Chang, C. S., & Whitman, R. V. (1988). Drained Permanent Deformation of Sand Due to Cyclic Loading. *Journal of Geotechnical Engineering*, *114*(10), 1164–1180. https://doi.org/10.1061/(ASCE)0733-9410(1988)114:10(1164)

Chen, C. N. (2000). Efficient and reliable solutions of static and dynamic nonlinear structural mechanics problems by an integrated numerical approach using DQFEM and direct time integration with accelerated equilibrium iteration schemes. *Applied Mathematical Modelling*, *24*(8-9), 637–655. https://doi.org/10.1016/S0307-904X(00)00007-X

Chen, C., & Ricles, J. M. (2008). Stability Analysis of Direct Integration Algorithms Applied to Nonlinear Structural Dynamics. *Journal of Engineering Mechanics*, *134*(9), 703–711. https://doi.org/10.1061/(ASCE)0733-9399(2008)134:9(703)

Chopra, A. (2013). *Dynamics of Structures - Theory and applications to earthquake engineering*. John Wiley & Sons, Inc. https://doi.org/10.1002/9781118599792

Chortis, G., Askarinejad, A., Prendergast, L. J., Li, Q., & Gavin, K. (2020). Influence of scour depth and type on p–y curves for monopiles in sand under monotonic lateral loading in a geotechnical centrifuge. *Ocean Engineering*, *197*, 106838. https://doi.org/10.1016/j.oceaneng.2019.106838

Chung, J., & Hulbert, G. M. (1993). A Time Integration Algorithm for Structural Dynamics With Improved Numerical Dissipation: The Generalized-α Method. *Journal of Applied Mechanics*, *60*(2), 371–375. https://doi.org/10.1115/1.2900803

Constantinou, M. C., Adnane, M. A., & Drexel University Department of Civil Engineering. (1987). *Dynamics of soil-base-isolated-structure systems Report 4 : Evaluation of two models for yielding systems*. Dept. of Civil Engineering, Drexel University Philadelphia, Pa.

Corciulo, S. (2015). *Dynamic hydro-mechanical analysis of soil-monopile interaction in Offshore Wind Turbines*.

Cox, W. R., Reese, L. C., & Grubbs, B. R. (1974). Field Testing of Laterally Loaded Piles In Sand. *Offshore Technology Conference*. https://doi.org/10.4043/2079-MS

CSi. (2016). *CSi Analysis Reference Manual for SAP 2000, ETABS, SAFE and CSiBridge*.

Dahlquist, G. G. (1963). A special stability problem for linear multistep methods. *BIT*, *3*(1), 27–43. https://doi.org/10.1007/BF01963532

Damgaard, M., Andersen, J. F. K., Andersen, L. V., & Ibsen, L. B. (2013). Time-Varying Dynamic Properties of Offshore Wind Turbines Evaluated by Modal Testing.

Damgaard, M., Bayat, M., Andersen, L., & Ibsen, L. (2014). Assessment of the dynamic behaviour of saturated soil subjected to cyclic loading from offshore monopile wind turbine foundations. *Computers and Geotechnics*, *61*, 116–126. https://doi.org/10.1016/j.compgeo.2014.05.008

Darvishi-Alamouti, S., Bahaari, M. R., & Moradi, M. (2017). Natural frequency of offshore wind turbines on rigid and flexible monopiles in cohesionless soils with linear stiffness distribution. *Applied Ocean Research*, *68*, 91–102. https://doi.org/10.1016/j.apor.2017.07.009

Desai, C. S., & Zaman, M. (2013). *Advanced Geotechnical Engineering: Soil-Structure Interaction using Computer and Material Models* (1st ed.). CRC Press.
https://doi.org/10.1201/b15578.

Dezi, F., Gara, F., & Roia, D. (2012). Dynamic response of a near-shore pile to lateral impact load. *Soil Dynamics and Earthquake Engineering*, *40*, 34–47. https://doi.org/10.1016/j.soildyn.2012.04.002

Di Laora, R., Mandolini, A., & Mylonakis, G. (2012). Insight on kinematic bending of flexible piles in layered soil. *Soil Dynamics and Earthquake Engineering*, *43*, 309–322. https://doi.org/10.1016/J.SOILDYN.2012.06.020

Di Laora, R., Mylonakis, G., & Mandolini, A. (2013). Pile-head kinematic bending in layered soil. *Earthquake Engineering & Structural Dynamics*, *42*(3), 319–337. https://doi.org/10.1002/EQE.2201

Di Laora, R., & Rovithis, E. (2015). Kinematic Bending of Fixed-Head Piles in Nonhomogeneous Soil. *Journal of Geotechnical and Geoenvironmental Engineering*, *141*(4), 04014126. https://doi.org/10.1061/(ASCE)GT.1943-5606.0001270

DNV. (2021). *DNVGL-ST-0126 - Support structures for wind turbines.* (July). Det Norske Veritas. Oslo, Norway.

Dobry, R., & O'Rourke, M. J. (1983). Discussion of 'Seismic response of end-bearing piles (R. Flores Berrones & R. V. Whitman, Eds.). *Journal of Geotechnical Engineering*, *109*(5), 778–781.

Doherty, P., & Gavin, K. (2011). Laterally loaded monopile design for offshore wind farms. *Proceedings of the Institution of Civil Engineers - Energy*, *165*(1), 7–17. https://doi.org/10.1680/ener.11.00003

Doherty, P., Kirwan, L., Gavin, K., Igoe, D., Tyrrell, S., Ward, D., & O'Kelly, B. (2012). Soil properties at the UCD geotechnical research site at Blessington, 7.

Domaneschi, M., Limongelli, M. P., & Martinelli, L. (2013). Vibration Based Damage Localization Using MEMS on a Suspension Bridge Model. *SMART*

STRUCTURES AND SYSTEMS. https://doi.org/10.12989/sss.2013.12.6.679

Downing, S. D., & Socie, D. F. (1982). Simple rainflow counting algorithms. *International Journal of Fatigue*, *4*(1), 31–40. https://doi.org/10.1016/0142-1123(82)90018-4

Dowrick, D. J. (1977). Earthquake resistant design. A manual for engineers and architects. *Publication of: Wiley (John) and Sons, Limited.*

Dührkop, J., Grabe, J., & Rombach, G. A. (2009). *Zum Einfluss von Aufweitungen und zyklischen Lasten auf das Verformungsverhalten lateral beanspruchter Pfähle im Sand* (Erstausg). Technische Univ. Hamburg-Harburg, Inst. für Geotechnik und Baubetrieb.

Duncan, J. M., & Chang, C.-Y. (1970). Nonlinear Analysis of Stress and Strain in Soils. *Journal of the Soil Mechanics and Foundations Division*, *96*(5), 1629–1653. https://doi.org/10.1061/JSFEAQ.0001458

Dyson, G. J., & Randolph, M. F. (2001). Monotonic Lateral Loading of Piles in Calcareous Sand. *Journal of Geotechnical and Geoenvironmental Engineering*, *127*(4), 346–352. https://doi.org/10.1061/(ASCE)1090-0241(2001)127:4(346)

EC8. (2000). Design Provisions for Earthquake Resistance of Structures, Part 5: Foundations, Retaining Structures and Geotechnical Aspects. *CEN European Committee for Standardization*, *CEN/TC250*.

El Naggar, M. H., & Bentley, K. J. (2000). Dynamic analysis for laterally loaded piles and dynamic p-y curves. *Canadian Geotechnical Journal*, *37*(6), 1166–1183. https://doi.org/10.1139/cgj-37-6-1166

Fan, C. C., & Long, J. H. (2005). Assessment of existing methods for predicting soil response of laterally loaded piles in sand. *Computers and Geotechnics*, *32*(4), 274–289. https://doi.org/10.1016/j.compgeo.2005.02.004

Fan, K., Gazetas, G., Kaynia, A., Kausel, E., & Ahmad, S. (1991). Kinematic seismic response of single piles and pile groups. *Journal of Geotechnical Engineering*, *117*(12), 1860–1879. https://doi.org/10.1061/(ASCE)0733-9410(1991)117:12(1860)

Fayyazi, M. S., Taiebat, M., & Finn, W. L. (2014). Group reduction factors for analysis of laterally loaded pile groups. *Canadian Geotechnical Journal*, *51*(7), 758–769. https://doi.org/10.1139/cgj-2013-0202

Fitzgerald, P. C., Malekjafarian, A., Bhowmik, B., Prendergast, L. J., Cahill, P., Kim, C.-W., Hazra, B., Pakrashi, V., & OBrien, E. J. (2019). Scour Damage Detection and Structural Health Monitoring of a Laboratory-Scaled Bridge Using a Vibration Energy Harvesting Device. *Sensors*, *19*(11), 2572. https://doi.org/10.3390/s19112572

Fu, D., Zhang, Y., Aamodt, K. K., & Yan, Y. (2020). A multi-spring model for monopile analysis in soft clays. *Marine Structures*, *72*, 102768. https://doi.org/10.1016/j.marstruc.2020.102768

Fung, T. C. (2003). Numerical dissipation in time-step integration algorithms for structural dynamic analysis. *Progress in Structural Engineering and Materials*, *5*(3), 167–180. https://doi.org/10.1002/pse.149

Garala, T. K. (2020). *Seismic Response of Pile Foundations in Soft Clays and Layered Soils*. https://doi.org/doi.org/10.17863/CAM.52405

Garala, T. K., & Madabhushi, S. (2020). Influence of phase difference between kinematic and inertial loads on seismic behaviour of pile foundations in layered soils. *https://doi.org/10.1139/cgj-2019-0547*, 1–18. https://doi.org/10.1139/CGJ-2019-0547

Garala, T. K., & Madabhushi, S. (2021). Role of Pile Spacing on Dynamic Behavior of Pile Groups in Layered Soils. *Journal of Geotechnical and Geoenvironmental Engineering*, *147*(3), 04021005. https://doi.org/10.1061/(ASCE)GT.1943-5606.0002483

Garala, T. K., Madabhushi, S., & Di Laora, R. (2020). Experimental investigation of kinematic pile bending in layered soils using dynamic centrifuge modelling. *Géotechnique*, 1–16. https://doi.org/10.1680/jgeot.19.p.185

Gavin, K. G., & Igoe, D. J. P. (2021). A field investigation into the mechanisms of pile ageing in sand. *Géotechnique*, *71*(2), 120–131. https://doi.org/10.1680/jgeot.18.P.235

Gavin, K. G., & Lehane, B. (2007). Base load – displacement response of piles in sand. *Canadian Geotechnical Journal*, *44*(9), 1053–1063. https://doi.org/10.1139/T07-048

Gavin, K. G., & O'Kelly, B. C. (2007). Effect of Friction Fatigue on Pile Capacity in Dense Sand. *Journal of Geotechnical and Geoenvironmental Engineering*, *133*(1), 63–71. https://doi.org/10.1061/(ASCE)1090-0241(2007)133:1(63)

Gavin, K. G., Igoe, D. J. P., & Kirwan, L. (2013). The effect of ageing on the axial capacity of piles in sand. *Proceedings of the Institution of Civil Engineers - Geotechnical Engineering*, *166*(2), 122–130. https://doi.org/10.1680/geng.12.00064

Gazetas, G., & Dobry, R. (1984a). Horizontal response of piles in layered soils. *Journal of Geotechnical Engineering*, *110*(1), 20–40. https://doi.org/10.1061/(ASCE)0733-9410(1984)110:1(20)

Gazetas, G., & Dobry, R. (1984b). Simple Radiation Damping Model for Piles and Footings. *Journal of Engineering Mechanics*, *110*(6), 937–956. https://doi.org/10.1061/(ASCE)0733-9399(1984)110:6(937)

Georgiadis, M. (1983). Development of P-Y Curves for Layered Soils, 536–545.

Gerolymos, N. A., & Gazetas, G. (2005a). Constitutive model For 1D Cyclic Soil Behaviour Applied to Seismic Analysis of Layered Deposits. *Japanese Geotechnical Society*, *45*(3), 137–159.

Gerolymos, N. A., & Gazetas, G. (2005b). Development of Winkler model for static and dynamic response of caisson foundations with soil and interface nonlinearities. *Soil Dynamics and Earthquake Engineering*, *26*(5), 363–376. https://doi.org/10.1016/j.soildyn.2005.12.002

Gerolymos, N. A., & Gazetas, G. (2005c). Phenomenological model applied to inelastic response of soil- pile interaction systems. *Soil and Foundations - Japanese Geotechnical Society*, *45*(4), 119–132. https://doi.org/10.1017/CBO9781107415324.004

Gerolymos, N. A., & Gazetas, G. (2005d). Static and dynamic response of massive caisson foundations with soil and interface nonlinearities - Validation and results. *Soil Dynamics and Earthquake Engineering*, *26*(5), 377–394. https://doi.org/10.1016/j.soildyn.2005.12.001

Gerolymos, N. A., & Gazetas, G. (2005e). Winkler model for lateral response of rigid caisson foundations in linear soil. *Soil Dynamics and Earthquake Engineering*, *26*(5), 347–361. https://doi.org/10.1016/j.soildyn.2005.12.003

Ghosh, B., & Madabhushi, S. P. G. (2002). An efficient tool for measuring shear wave velocity in the centrifuge. *International Conference Physical Modelling in Geotechnics*, 119–124.

Giardina, R. (2017, August 9). *On The Ramberg-Osgood Stress-Strain Model And Large Deformations of Cantilever Beams*.

Giordano, P. F., Prendergast, L. J., & Limongelli, M. P. (2020). A framework for assessing the value of information for health monitoring of scoured bridges. *Journal of Civil Structural Health Monitoring*, *10*(3), 485–496. https://doi.org/10.1007/s13349-020-00398-0

Goudreau, G. L., & Taylor, R. L. (1973). Evaluation of numerical integration methods in elastodynamics. *Computer Methods in Applied Mechanics and Engineering*, *2*(1), 69–97. https://doi.org/10.1016/0045-7825(73)90023-6

Grecu, S., Ibsen, L. B., & Barari, A. (2021). Winkler springs for axial response of suction bucket foundations in cohesionless soil. *Soils and Foundations*, *61*(1), 64–79. https://doi.org/10.1016/j.sandf.2020.10.010

Gupta, B. K., & Basu, D. (2018). Applicability of Timoshenko, Euler–Bernoulli and rigid beam theories in analysis of laterally loaded monopiles and piles. *Géotechnique*, *68*(9), 772–785. https://doi.org/10.1680/jgeot.16.P.244

Hansen, J. (1961). Ultimate resistance of rigid piles against trasnversal forces. *Geoteknisk Institut - Bulletin (Danish Geotechnical Institute - Bulletin)*, *1*(12), 5–9.

Hardin, B. O., & Black, W. L. (1968). Vibration Modulus of Normally Consolidated Clay. *Journal of the Soil Mechanics and Foundations Division*, *94*(2), 353–369. https://doi.org/10.1061/JSFEAQ.0001100

Hardin, B. O., & Drnevich, V. P. (1972a). Shear Modulus and Damping in Soils: Measurement and Parameter Effects. *ASCE J Soil Mech Found Div*, *98*, 603–624. https://doi.org/10.1016/0022-4898(73)90212-7

Hardin, B. O., & Drnevich, V. P. (1972b). Shear Modulus and Damping in Soils: Design Equations and Curves. *Journal of the Soil Mechanics and Foundations Division*, *98*(7), 667–692. https://doi.org/10.1061/jsfeaq.0001760

Hettler, A. (1981). *Verschiebungen starrer und elastischer Gründungskörper in Sand bei monotoner und zyklischer Belastung.*
OCLC: 63236606.

Hilber, H. M., Hughes, T. J. R., & Taylor, R. L. (1977). Improved numerical dissipation for time integration algorithms in structural dynamics. *Earthquake Engineering & Structural Dynamics*, *5*(3), 283–292. https://doi.org/10.1002/eqe.4290050306

Hilber, H. M., & Hughes, T. J. (1978). Collocation, dissipation and [overshoot] for time integration schemes in structural dynamics. *Earthquake Engineering & Structural Dynamics*, *6*(1), 99–117. https://doi.org/10.1002/eqe.4290060111

Houlsby, G. T., Abadie, C. N., Beuckelaers, W. J. A. P., & Byrne, B. W. (2017). A model for nonlinear hysteretic and ratcheting behaviour. *International Journal of Solids and Structures*, *120*, 67–80. https://doi.org/10.1016/j.ijsolstr.2017.04.031

Huang, X.-R., Jézéquel, L., Besset, S., Li, L., & Sauvage, O. (2018). Nonlinear modal synthesis for analyzing structures with a frictional interface using a generalized Masing model. *Journal of Sound and Vibration*, *434*, 166–191. https://doi.org/10.1016/j.jsv.2018.07.027

Hughes, T. J. R. (1983). Analysis of transient algorithms with particular reference to stability behaviour. *Computational Methods for Transient Analysis (A 84-29160 12-64).*

Hughes, T. J. R. (2000). *The finite element method: Linear static and dynamic finite element analysis*. Dover Publications.

Ibsen, L. B., Liingaard, & M. and Nielsen, S. (2005). Bucket Foundation, a status. *Proceedings of the Copenhagen Offshore Wind*, 26–28.

Idriss, I. M., Dobry, R., & Singh, R. D. (1978). Nonlinear Behavior of Soft Clays during Cyclic Loading. *Journal of the Geotechnical Engineering Division*, *104*(12), 1427–1447. https://doi.org/10.1061/AJGEB6.0000727

IEC. (2009). *International Standard IEC 61400-3 Wind Turbines - Part 3: Design requirements for offshore wind turbines* (1.0). International Electrotechnical Commission.

Isenhower, W. M., & Wang, S.-T. (2016). *User's Manual for LPile 2016*.

Ishihara, K. (1997). *Soil behaviour in earthquake geotechnics*. https://doi.org/10.5860/choice.34-5113

Ishihara, T., & Wang, L. (2019). A study of modal damping for offshore wind turbines considering soil properties and foundation types. *Wind Energy*, *22*(12), 1760–1778. https://doi.org/10.1002/we.2401

Iwan, W. D. (1967). On a Class of Models for the Yielding Behavior of Continuous and Composite Systems. *Journal of Applied Mechanics*, *34*(3), 612–617. https://doi.org/10.1115/1.3607751

Jardine, R. J., Chow, F., Overy, R., & Standing, J. (2005). *ICP design methods for driven piles in sands and clays*. Thomas Telford London.

Jeanjean, P., Zhang, Y., Zakeri, A., Anderson, K. H., Gilbert, R., & Senanayake, A. I. M. J. (2011). *A Framework for monotonic p-y curves in clays*.

Jeanjean, P. (2009). Re-assessment of P-Y curves for soft clays from centrifuge testing and finite element modeling. *All Days*, OTC-20158–MS. https://doi.org/10.4043/20158-MS

Jostad, H. P., Grimstad, G., Andersen, K. H., Saue, M., Shin, Y., & You, D. (2014). A FE Procedure for Foundation Design of Offshore Structures – Applied to Study a Potential OWT Monopile Foundation in the Korean Western Sea. *45*.

Kagawa, T., & Kraft, L. M. (1980). Seismic $p \sim y$ Responses of Flexible Piles. *Journal of the Geotechnical Engineering Division*, *106*(8), 899–918. https://doi.org/10.1061/AJGEB6.0001018

Kallehave, D., Thilsted, C. L., & Liingaard, M. A. (2012). Modification of the API P-y Formulation of Initial Stiffness of Sand.

Kallehave, D., Byrne, B. W., LeBlanc Thilsted, C., & Mikkelsen, K. K. (2015). Optimization of monopiles for offshore wind turbines. *Philosophical Transactions of the Royal Society A: Mathematical, Physical and Engineering Sciences*, *373*(2035), 20140100. https://doi.org/10.1098/rsta.2014.0100

Kampitsis, A. E., Sapountzakis, E. J., Giannakos, S. K., & Gerolymos, N. A. (2013). Seismic soil-pile-structure kinematic and inertial interaction-A new beam approach. *Soil Dynamics and Earthquake Engineering*, *55*, 211–224. https://doi.org/10.1016/j.soildyn.2013.09.023

Kassas, K., & Gerolymos, N. A. (2016). Inverse analysis of laterally loaded monopiles subjected to large cyclic loading : Development of a Bouc-Wen type soil reaction model, 7.

Kaynia, A. M. (2019). Seismic considerations in design of offshore wind turbines. *Soil Dynamics and Earthquake Engineering*, *124*, 399–407. https://doi.org/10.1016/j.soildyn.2018.04.038

Kaynia, A. M., & Andersen, K. (2015). Development of nonlinear foundation springs for dynamic analysis of platforms. In V. Meyer (Ed.), *Frontiers in Offshore Geotechnics III* (pp. 1067–1072). CRC Press. https://doi.org/10.1201/b18442-158

Kaynia, A. M., Norén-Cosgriff, K., Andersen, K., & Tuen, K. A. (2015). Nonlinear Foundation Spring and Calibration Using Measured Dynamic Response of Structure. *Volume 1: Offshore Technology; Offshore Geotechnics*, V001T01A024. https://doi.org/10.1115/OMAE2015-41236

Kim, G., Kyung, D., Park, D., Kim, I., & Lee, J. (2016). CPT-based p-y analysis for piles embedded in clays under cyclic loading conditions. *KSCE Journal of Civil Engineering*, *20*(5), 1759–1768. https://doi.org/10.1007/s12205-015-0457-2

Klinkvort, R. T., & Hededal, O. (2013). Lateral response of monopile supporting an offshore wind turbine. *Proceedings of the ICE - Geotechnical Engineering*, *166*, 147–158. https://doi.org/10.1680/geng.12.00033

Kohgo, Y., Nakano, M., & Miyazaki, T. (1993). Theoretical Aspects of Constitutive Modelling For Unsaturated Soils. *Soils and Foundations*, *33*(4), 49–63. https://doi.org/10.3208/sandf1972.33.4_49

Kondner, R., & Zelasko, J. (1963). A hyperbolic stress strain formulation for sands, 289–324.

Konstandakopoulou, F. D., Evangelinos, K. I., Nikolaou, I. E., Papagiannopoulos, G. A., & Pnevmatikos, N. G. (2020). Seismic analysis of offshore platforms subjected to pulse-type ground motions compatible with European Standards. *Soil Dynamics and Earthquake Engineering*, *129*, 105713. https://doi.org/10.1016/j.soildyn.2019.105713

Kontoe, S., Zdravkovic, L., & Potts, D. M. (2008). An assessment of time integration schemes for dynamic geotechnical problems. *Computers and Geotechnics*, *35*(2), 253–264. https://doi.org/10.1016/j.compgeo.2007.05.001

Kottari, A. K., Charalampakis, A. E., & Koumousis, V. K. (2014). A consistent degrading Bouc–Wen model. *Engineering Structures*, *60*, 235–240. https://doi.org/10.1016/j.engstruct.2013.12.025

Kovacic, I., & Brennan, M. J. (2011). Background: On Georg Duffing and the Duffing Equation. In I. Kovacic & M. J. Brennan (Eds.), *The Duffing Equation* (1st ed., pp. 1–23). Wiley. https://doi.org/10.1002/9780470977859.ch1

Krathe, V. L., & Kaynia, A. M. (2016). Implementation of a non-linear foundation model for soil-structure interaction analysis of offshore wind turbines in FAST. *Wind Energy*, 677–689. https://doi.org/10.1002/we.2031

Lai, Y., Wang, L., Zhang, Y., & Hong, Y. (2021). Site-specific soil reaction model for monopiles in soft clay based on laboratory element stress-strain curves. *Ocean Engineering*, *220*, 108437. https://doi.org/10.1016/j.oceaneng.2020.108437

Lam, I. P. (2013). Diameter effects on p-y curves (B. R.B. & E. A., Eds.). *Deep Marine Foundations: A Perspective on the Design and Construction of Deep Marine Foundations*, *Article 16*.

Lam, I. P., & Martin, G. (1986). *Seismic Design of High-way Bridge Foundations*. US Department of Transportation Report No. FHWA/RD-86/102.

Leblanc, C., Byrne, B., & Houlsby, G. (2010a). Response of stiff piles to random two-way lateral loading. *Géotechnique*, *60*(9), 715–721. https://doi.org/10.1680/geot.09.T.011

Leblanc, C., Houlsby, G., & Byrne, B. (2010b). Response of stiff piles in sand to long-term cyclic lateral loading. *Géotechnique*, *60*(2), 79–90. https://doi.org/10.1680/geot.7.00196

Leblanc, C. (2009). Design of Offshore Wind Turbine Support Structures: Selected topics in the field of geotechnical engineering. *... FakultetThe Faculty of Engineering ...*

Lehane, B. M., & Gavin, K. G. (2001). Base Resistance of Jacked Pipe Piles in Sand. *Journal of Geotechnical and Geoenvironmental Engineering*, *127*(6), 473–480. https://doi.org/10.1061/(ASCE)1090-0241(2001)127:6(473)

Lehane, B. M., Li, L., & Bittar, E. J. (2020a). Cone penetration test-based load-transfer formulations for driven piles in sand. *Géotechnique Letters*, *10*(4), 568–574. https://doi.org/10.1680/jgele.20.00096

Lehane, B. M., Liu, Z., Bittar, E., Nadim, F., Lacasse, S., Jardine, R. J., Carotenuto, P., Jeanjean, P., Rattley, M., Gavin, K., & O'Neill, M. W. (2020b). A new 'unified' CPT-based axial pile capacity design method for driven piles in sand. *4th International Symposium on Frontiers in Offshore Geotechnics*, 463–477.

Lehane, B. M., Schneider, A. J., & Xu, X. (2005). The UWA-05 method for prediction of axial capacity of driven piles in sand. *Frontiers in Offshore Geotechnics*, 683–689. https://doi.org/10.1201/noe0415390637.ch76

Lehane, B. M., & Suryasentana, S. (2014). Verification of numerically derived CPT based p-y curves for piles in sand: 3rd International Symposium on Cone Penetration Testing. *3rd International Symposium on Cone Penetration Testing*, *1*, 1013–1020.

Lesny, K., & Hinz, P. (2007). Investigation Of Monopile Behaviour Under Cyclic Lateral Loading.

Lesny, K., Paikowsky, S. G., & Gurbuz, A. (2007). Scale effects in lateral load response of large diameter monopiles. *Contemporary Issues in Deep Foundations (GSP 158)*, 1–10.

Li, W., Igoe, D., & Gavin, K. (2014). Evaluation of CPT-based $P - y$ models for laterally loaded piles in siliceous sand. *Géotechnique Letters*, *4*(2), 110–117. https://doi.org/10.1680/geolett.14.00021

Lin, S.-S., & Liao, J.-C. (1999). Permanent Strains of Piles in Sand due to Cyclic Lateral Loads. *Journal of Geotechnical and Geoenvironmental Engineering*, *125*(9), 798–802. https://doi.org/10.1061/(ASCE)1090-0241(1999)125:9(798)

Little, R., & Briaud, J. (1988). Full Scale Cyclic Lateral Load Tests on Six Single Piles in Sand.

Liu, J., Liu, J., Li, Z., Hou, X., & Dai, G. (2021). Estimating CPT Parameters at Unsampled Locations Based on Kriging Interpolation Method. *Applied Sciences*, *11*(23), 11264. https://doi.org/10.3390/app112311264

Lo Presti, D., Cavallaro, A., M., M., Pallara, O., & F., I. (2000). Modelling of hardening and degradation behavior of clays and sands during cyclic loadings.

Long, J. H., & Vanneste, G. (1994). Effects of Cyclic Lateral Loads on Piles in Sand. *Journal of Geotechnical Engineering*, *120*(1), 225–244. https://doi.org/10.1061/(ASCE)0733-9410(1994)120:1(225)

Lunne, T., Robertson, P. K., & Powell, J. (1997). *Cone Penetration Testing in Geotechnical Practice*. Blackie Academic and Professional.

Lunne, T., & Christoffersen, H. (1983). Interpretation of Cone Penetrometer Data for Offshore Sands. *Offshore Technology Conference*. https://doi.org/10.4043/4464-MS

Luo, L., O'Loughlin, C. D., Bienen, B., Wang, Y., Cassidy, M. J., & Morgan, N. (2020). Effect of the ordering of cyclic loading on the response of suction caissons in sand. *Géotechnique Letters*, *10*(2), 303–310. https://doi.org/10.1680/jgele.19.00031

MacKay, D. (2008). *Sustainable Energy - Without the hot air*.

Madabhushi, S., Haigh, S. K., & Houghton, N. E. (2006). A new automated sand pourer for model preparation at University of Cambridge. *Proc. International Conference on Physical Modelling in Geotechnics*, 217–222.

Makris, N., & Gazetas, G. (1992). Dynamic pile-soil-pile interaction. Part II: Lateral and seismic response. *Earthquake Engineering & Structural Dynamics*, *21*, 145–162. https://doi.org/10.1002/eqe.4290210204

Margason, E., & Halloway, D. M. (1977). Pile bending during earthquakes. *Proceedings of the Sixth World Conference on Earthquake Engineering*, 1690–1696.

Markou, A. A., & Kaynia, A. M. (2018). Nonlinear soil-pile interaction for offshore wind turbines. *Wind Energy*, *21*(7), 558–574. https://doi.org/10.1002/we.2178

Masing, G. (1926). Eigenspannungen und Verfestigung beim Messing [Fundamental stresses and strengthening with brass]. *International Congress of Applied Mechanics, 2d.*

Matasović, N., & Vucetic, M. (1993). Cyclic Characterization of Liquefiable Sands. *Journal of Geotechnical Engineering*, *119*(11), 1805–1822. https://doi.org/10.1061/(ASCE)0733-9410(1993)119:11(1805)

Matlock, H. (1970). Correlation for Design of Laterally Loaded Piles in Soft Clay. *Offshore Technology Conference*. https://doi.org/10.4043/1204-MS

Mayoral, J. M., Pestana, J. M., & Seed, R. B. (2016). Multi-directional cyclic p–y curves for soft clays. *Ocean Engineering*, *115*, 1–18. https://doi.org/10.1016/j.oceaneng.2016.01.033

McAdam, R. A., Byrne, B. W., Houlsby, G. T., Beuckelaers, W. J. A. P., Burd, H. J., Gavin, K. G., Igoe, D. J. P., Jardine, R. J., Martin, C. M., Muir Wood, A., Potts, D. M., Skov Gretlund, J., Taborda, D. M. G., & Zdravković, L. (2020). Monotonic laterally loaded pile testing in a dense marine sand at Dunkirk. *Géotechnique*, *70*(11), 986–998. https://doi.org/10.1680/jgeot.18.PISA.004

Miguel, L. P., Teloli, R. d. O., & da Silva, S. (2020). Some practical regards on the application of the harmonic balance method for hysteresis models. *Mechanical Systems and Signal Processing*, *143*, 106842. https://doi.org/10.1016/j.ymssp.2020.106842

Miner, M. A. (1945). Cumulative Damage in Fatigue. *Journal of Applied Mechanics*, *12*(3), A159–A164. https://doi.org/10.1115/1.4009458

Mizuno, H. (1985). Pile damage during earthquakes in Japan. *ASCE Geotechnical Publication*, (11), 53–78.

Mostafa, Y. E., & Naggar, M. H. E. (2002). Dynamic analysis of laterally loaded pile groups in sand and clay. *Canadian Geotechnical Journal*, *39*(6), 1358–1383. https://doi.org/10.1139/t02-102

Mostaghel, N. (1999). Analytical Description of Pinching, Degrading and Hysteretic Systems. *125*, 216–224.

Murchinson, J. R., & O'Neill, M. W. (1986). Evaluation of p-y relationships in cohesionless soils. *International Journal of Rock Mechanics and Mining Sciences & Geomechanics Abstracts*, *23*(3), 109. https://doi.org/10.1016/0148-9062(86)91228-3

Murphy, G., Igoe, D., Doherty, P., & Gavin, K. (2018). 3D FEM approach for laterally loaded monopile design. *Computers and Geotechnics*, *100*, 76–83. https://doi.org/10.1016/j.compgeo.2018.03.013

Mylonakis, G. (2001a). Elastodynamic Model for Large-Diameter End-Bearing Shafts. *Soils and Foundations*, *41*(3), 31–44. https://doi.org/10.3208/sandf.41.3_31

Mylonakis, G. (2001b). Simplified Model for Seismic Pile Bending at Soil Layer Interfaces. *Soils and Foundations*, *41*(4), 47–58. https://doi.org/10.3208/SANDF.41.4_47

Naggar, M. H. E., & Bentley, K. J. (2000). Dynamic analysis for laterally loaded piles and dynamic p–y curves. *37*, 18.

Newmark, N. (1959). A method of computation for structural dynamics. *Journal of the engineering mechanics division*, *85*(3), 67–94.

Niemunis, A., Wichtmann, T., & Triantafyllidis, Th. (2005). A high-cycle accumulation model for sand. *Computers and Geotechnics*, *32*(4), 245–263. https://doi.org/10.1016/j.compgeo.2005.03.002

Nikolaou, A., Mylonakis, G., & Gazetas, G. (1995). *Kinematic Bending Moments in Seismically Stressed Piles (Report no. NCEER-95-0022)*. University of Buffalo.

Nikolaou, S., Mylonakis, G., Gazetas, G., & Tazoh, T. (2001). Kinematic pile bending during earthquakes: Analysis and field measurements. *Geotechnique*, *51*(5), 425–440. https://doi.org/10.1680/geot.2001.51.5.425

Norén-Cosgriff, K., Jostad, H., & Madshus, C. (2015). Idealized load composition for determination of cyclic undrained degradation of soils. In V. Meyer (Ed.), *Frontiers in Offshore Geotechnics III* (pp. 1097–1102). CRC Press. https://doi.org/10.1201/b18442-163

Novak, M. (1974). Dynamic Stiffness and Damping of Piles. *Canadian Geotechnical Journal*.

Novello, E. (1999). From static to cyclic p-y data in calcareous sediments. In K. Al-Shafei (Ed.), *Engineering for calcareous sediments* (pp. 17–24).

OBrien, E., & Malekjafarian, A. (2016). A mode shape-based damage detection approach using laser measurement from a vehicle crossing a simply supported bridge. *Structural Control and Health Monitoring*, *23*, n/a–n/a. https://doi.org/10.1002/stc.1841

O'Neill, M. W. (2001). Side Resistance In Piles and Drilled Shafts. *Journal of Geotechnical and Geoenvironmental Engineering*, *127*(1), 3–16. https://doi.org/10.1061/(ASCE)1090-0241(2001)127:1(3)

O'Neill, M. W., & Murchison, J. M. (1983). *An evaluation of py relationships in sands. A report to the American Petroleum Institute (GT-DF02-83).* University of Houston. Houston, Texas.

Oztoprak, S., & Bolton, M. D. (2013). Stiffness of sands through a laboratory test database. *Geotechnique*, *63*(1), 54–70. https://doi.org/10.1680/GEOT.10.P.078

Page, A. M., Klinkvort, R. T., Bayton, S., Zhang, Y., & Jostad, H. P. (2021). A procedure for predicting the permanent rotation of monopiles in sand supporting offshore wind turbines. *Marine Structures*, *75*, 102813. https://doi.org/10.1016/j.marstruc.2020.102813

Paik, K., Salgado, R., Lee, J., & Kim, B. (2003). Behavior of Open- and Closed-Ended Piles Driven Into Sands. *Journal of Geotechnical and Geoenvironmental Engineering*, *129*(4), 296–306. https://doi.org/10.1061/(ASCE)1090-0241(2003)129:4(296)

Park. (1988). Ductility evaluation from laboratory analytical testing. *Proceedings of Ninth World Conference in Earthquake Engineering*, *8*.

Pelliciari, M., Briseghella, B., Tondolo, F., Veneziano, L., Nuti, C., Greco, R., Lavorato, D., & Tarantino, A. M. (2020). A degrading Bouc–Wen model for the hysteresis of reinforced concrete structural elements. *Structure and Infrastructure Engineering*, *16*(7), 917–930. https://doi.org/10.1080/15732479.2019.1674893

Pestana, J., Biscontin, G., Nadim, F., & Andersen, K. (2000). Modeling cyclic behavior of lightly overconsolidated clays in simple shear. *Soil Dynamics and Earthquake Engineering*, *19*(7), 501–519. https://doi.org/10.1016/S0267-7261(00)00032-4

Poulos, H. G. (2017). Designing piles for seismic events. *DFI Melbourne*, 1–28.

Poulos, H. G., & Hull, T. (1989). The role of analytical geomechanics in foundation engineering. In F. H. Kulhawy (Ed.), *Foundation Engineering: Current principles and practices* (pp. 1578–1606). ASCE.

Poulos, H. G. (1971). Behavior of Laterally Loaded Piles: I-Single Piles. *Journal of the Soil Mechanics and Foundations Division*, *97*(5), 711–731. https://doi.org/10.1061/JSFEAQ.0001592

Poulos, H. G., & Davis, E. H. (1980). *Pile foundation analysis and design* (Vol. 397). Wiley New York.

Prendergast, L. J., & Gavin, K. (2016). A comparison of initial stiffness formulations for small-strain soil–pile dynamic Winkler modelling. *Soil Dynamics and Earthquake Engineering*, *81*, 27–41. https://doi.org/10.1016/j.soildyn.2015.11.006

Prendergast, L. J., Gavin, K., & Doherty, P. (2015). An investigation into the effect of scour on the natural frequency of an offshore wind turbine. *Ocean Engineering*, *101*, 1–11. https://doi.org/10.1016/j.oceaneng.2015.04.017

Prendergast, L. J., Reale, C., & Gavin, K. (2018). Probabilistic examination of the change in eigenfrequencies of an offshore wind turbine under progressive scour incorporating soil spatial variability. *Marine Structures*, *57*, 87–104. https://doi.org/10.1016/j.marstruc.2017.09.009

Prendergast, L. J., Wu, W., & Gavin, K. (2019). Experimental application of FRF-based model updating approach to estimate soil mass and stiffness mobilised under pile impact tests. *Soil Dynamics and Earthquake Engineering*, *123*, 1–15. https://doi.org/10.1016/j.soildyn.2019.04.027

Prendergast, L. J., Gandina, P., & Gavin, K. (2020). Factors Influencing the Prediction of Pile Driveability Using CPT-Based Approaches. *Energies*, *13*(12), 3128. https://doi.org/10.3390/en13123128

Prendergast, L. J., Hester, D., Gavin, K., & O'Sullivan, J. (2013). An investigation of the changes in the natural frequency of a pile affected by scour. *Journal of Sound and Vibration*, *332*(25), 6685–6702. https://doi.org/10.1016/j.jsv.2013.08.020

Prevost, J. H. (1985). A simple plasticity theory for frictional cohesionless soils. *International Journal of Soil Dynamics and Earthquake Engineering*, *4*(1), 9–17. https://doi.org/10.1016/0261-7277(85)90030-0

Pugasap, K. (2006). *Hysteresis model based prediction of integral abutment bridge behavior*.

Pyke, R. (1979). Nonlinear Soil Models for Irregular Cyclic Loadings. *Journal of the Geotechnical Engineering Division*, *GT6*, 3–8.

Rainey, P. J., & Camp, T. R. (2007). Constrained non-linear waves for offshore wind turbine design. *Journal of Physics: Conference Series*, *75*, 012067. https://doi.org/10.1088/1742-6596/75/1/012067

Randolph, M. F. (1981). The response of flexible piles to lateral loading. *Geotechnique*, *31*(2), 247–259. https://doi.org/10.1680/geot.1981.31.2.247

Randolph, M. F. (2003). *RATZ manual version 4-2: Load transfer analysis of axially loaded piles*. Perth, Australia.

Randolph, M. F., Carter, J. P., & Wroth, C. P. (2009). Driven piles in clay—the effects of installation and subsequent consolidation. *Géotechnique*, *31*(2), 291–295. https://doi.org/10.1680/geot.1981.31.2.291

Randolph, M. F., & Houlsby, G. T. (1984). The limiting pressure on a circular pile loaded laterally in cohesive soil. *Géotechnique*, *34*(4), 613–623. https://doi.org/10.1680/geot.1984.34.4.613

Rascol, E. (2009). *Cyclic properties of sand: Dynamic behaviour for seismic applications*.

Reese, L. C., Cox, W. R., & Koop, F. D. (1974). Analysis of Laterally Loaded Piles in Sand. *All Days*, 95–105. https://doi.org/10.4043/2080-MS

Reese, L. C., Cox, W. R., & Koop, F. D. (1975). Field Testing and Analysis of Laterally Loaded Piles in Stiff Clay. *All Days*, OTC-2312–MS. https://doi.org/10.4043/2312-MS

Reese, L. C., & Van Impe, W. F. (2010). *Single Piles and Pile Groups Under Lateral Loading, 2nd Edition* (2nd ed). CRC Press.
OCLC: 1058399470.

Remmers, J., Reale, C., Pisanò, F., Raymackers, S., & Gavin, K. (2019). Geotechnical installation design of suction buckets in non-cohesive soils: A reliability-based approach. *Ocean Engineering*, *188*, 106242. https://doi.org/10.1016/j.oceaneng.2019.106242

Ren, Z., Verma, A. S., Li, Y., Teuwen, J. J., & Jiang, Z. (2021). Offshore wind turbine operations and maintenance: A state-of-the-art review. *Renewable and Sustainable Energy Reviews*, *144*, 110886. https://doi.org/10.1016/j.rser.2021.110886

Restrepo, D., & Taborda, R. (2018). Multiaxial cyclic plasticity in accordance with 1D hyperbolic models and Masing criteria. *International Journal for Numerical and Analytical Methods in Geomechanics*, *42*(17), 2095–2108. https://doi.org/10.1002/nag.2845

Robertson, P. K., & Cabal, K. (2014). *Soil classification using the cone penetration test* (6th Edition). NRC Research Press Ottawa, Canada.

Rollins, K. M., Lane, J. D., & Gerber, T. M. (2005). Measured and Computed Lateral Response of a Pile Group in Sand. *Journal of Geotechnical and Geoenvironmental Engineering*, *131*(1), 103–114. https://doi.org/10.1061/(asce)1090-0241(2005)131:1(103)

Rollins, K. M., Olsen, R., Egbert, J., Olsen, K., Jensen, D., & Garrett, B. (2003). *Response, Analysis, and Design of Pile Groups Subjected to Static & Dynamic Lateral Loads (Report No. UT-03.03)*. Brigham Young University.

Rollins, K. M., Peterson, K. T., & Weaver, T. J. (1998). Lateral Load Behavior of Full-Scale Pile Group in Clay. *Journal of Geotechnical and Geoenviron-*

mental Engineering, *124*(6), 468–478. https://doi.org/10.1061/(asce)1090-0241(1998)124:6(468)

Ronold, K. O. (1993). Reliability of Marine Clay Foundations in Cyclic Loading. https://doi.org/10.13140/2.1.1506.6405

Rovithis, E., Kirtas, E., & Pitilakis, K. (2009). Experimental p-y loops for estimating seismic soil-pile interaction. *Bulletin of Earthquake Engineering*, *7*(3), 719–736. https://doi.org/10.1007/s10518-009-9116-7

Sanctis, L. de, Maiorano, R. M. S., & Aversa, S. (2010). A method for assessing kinematic bending moments at the pile head. *Earthquake Engineering & Structural Dynamics*, *39*(10), 1133–1154. https://doi.org/10.1002/EQE.996

Schofield, A. N. (1980). Cambridge Geotechnical Centrifuge Operations. *Geotechnique*, *30*(3), 227–268. https://doi.org/10.1680/geot.1980.30.3.227

Seed, H. B., Wong, R. T., Idriss, I. M., & Tokimatsu, K. (1986). Moduli and Damping Factors for Dynamic Analyses of Cohesionless Soils. *Journal of Geotechnical Engineering*, *112*(11), 1016–1032. https://doi.org/10.1061/(ASCE)0733-9410(1986)112:11(1016)

Sengupta, P., & Li, B. (2013). Modified Bouc–Wen model for hysteresis behavior of RC beam–column joints with limited transverse reinforcement. *Engineering Structures*, *46*, 392–406. https://doi.org/10.1016/j.engstruct.2012.08.003

Shadlou, M., & Bhattacharya, S. (2016). Dynamic stiffness of monopiles supporting offshore wind turbine generators. *Soil Dynamics and Earthquake Engineering*, *88*, 15–32. https://doi.org/10.1016/j.soildyn.2016.04.002

Sireteanu, T., Mitu, A.-M., Giuclea, M., Solomon, O., & Stefanov, D. (2014). Analytical method for fitting the ramberg-osgood model to given hysteresis loops. *Proceedings of the Romanian Academy Series A - Mathematics Physics Technical Sciences Information Science*, *15*, 35–42.

Sivaselvan, M. V., & Reinhorn, A. M. (2001). Hysteretic Models for Deteriorating Inelastic Structures. *Journal of Engineering Mechanics*, *127*(11), 1200–1202. https://doi.org/10.1061/(ASCE)0733-9399(2001)127:11(1200)

Snyder, J. L. (2004). *Full-Scale Lateral-Load Tests of a 3x5 Pile Group in Soft Clays and Silts*.

Song, J., & Achmus, M. (2021). *Cyclic overlay model of p-y curves for laterally loaded monopiles in cohesionless soil* (preprint). Material science and structural mechanics. https://doi.org/10.5194/wes-2021-160

Sørensen, S. P. H. (2012). Soil-Structure Interaction for Non-Slender, Large-Diameter Offshore Monopiles: Vol 2.

Sparrevik, P. (2019). Offshore Wind Turbine Foundations State of the Art.

Stewart, H. E. (1986). Permanent Strains from Cyclic Variable-Amplitude Loadings. *Journal of Geotechnical Engineering*, *112*(6), 646–660. https://doi.org/10.1061/(ASCE)0733-9410(1986)112:6(646)

Su, C., Baizan, T., Haiyang, Z., Jianning, W., Xiaojun, L., & Kai, Z. (2020). Experimental investigation of the seismic response of shallow-buried subway station in liquefied soil. *Soil Dynamics and Earthquake Engineering*, *136*, 106153. https://doi.org/10.1016/j.soildyn.2020.106153

Sullivan, W. R., Reese, L. C., & Fenske, C. W. (1980). Unified method for analysis of laterally loaded piles in clay. *Electronique Industrielle (Paris)*, 135–146.

Sun, D., Cui, H., Matsuoka, H., & Sheng, D. (2007). A Three-Dimensional Elastoplastic Model for Unsaturated Compacted Soils with Hydraulic Hysteresis. *Soils and Foundations*, *47*(2), 253–264. https://doi.org/10.3208/sandf.47.253

Sun, D., Matsuoka, H., Cui, H., & Xu, Y. (2003). Three-dimensional elasto-plastic model for unsaturated compacted soils with different initial densities. *International Journal for Numerical and Analytical Methods in Geomechanics*, *27*(12), 1079–1098. https://doi.org/10.1002/nag.313

Suryasentana, S. K., & Lehane, B. M. (2014). Numerical derivation of CPT-based p–y curves for piles in sand. *Géotechnique*, *64*(3), 186–194. https://doi.org/10.1680/geot.13.P.026

Suryasentana, S. K., & Lehane, B. M. (2016). Updated CPT-based p – y formulation for laterally loaded piles in cohesionless soil under static loading. *Géotechnique*, *66*(6), 445–453. https://doi.org/10.1680/jgeot.14.P.156

Swane, I. C., & Poulos, H. G. (1984). Shakedown analysis of a laterally loaded pile tested in stiff clay. (84/2).

Tabesh, A., & Poulos, H. G. (2001). Pseudostatic Approach for Seismic Analysis of Single Piles. *Journal of Geotechnical and Geoenvironmental Engineering*, *127*(9), 757–765. https://doi.org/10.1061/(ASCE)1090-0241(2001)127:9(757)

Taborda, D. M. G., Zdravković, L., Potts, D. M., Burd, H. J., Byrne, B. W., Gavin, K. G., Houlsby, G. T., Jardine, R. J., Liu, T., Martin, C. M., & McAdam, R. A. (2020). Finite-element modelling of laterally loaded piles in a dense marine sand at Dunkirk. *Géotechnique*, *70*(11), 1014–1029. https://doi.org/10.1680/jgeot.18.PISA.006

Taciroglu, E., Rha, C., & Wallace, J. W. (2006). A Robust Macroelement Model for Soil–Pile Interaction under Cyclic Loads. *Journal of Geotechnical and Geoenvironmental Engineering*, *132*(10), 1304–1314. https://doi.org/10.1061/(ASCE)1090-0241(2006)132:10(1304)

Tarp-Johansen, N. J., Andersen, L. V., Christensen, E. D., Mørch, C., Kallesøe, B., & Frandsen, S. (2009). Comparing Sources of Damping of Cross-Wind Motion. *Proceedings of European Offshore Wind 2009 : Conference & Exhibition*, 1–10.

Tedesco, J. W. (1999). *Structural dynamics : Theory and applications* (W. G. McDougal & C. A. Ross, Eds.). Addison Wesley Longman.

Terzaghi, K. (1955). Evalution of Conefficients of Subgrade Reaction. *Géotechnique*, *5*(4), 297–326. https://doi.org/10.1680/geot.1955.5.4.297

Thieken, K., Achmus, M., Lemke, K., & Terceros, M. (2015). Evaluation of p-y Approaches for Large-Diameter Monopiles in Sand. *International Journal of Offshore and Polar Engineering*, *25*(2), 134–144. https://doi.org/10.17736/ijope.2015.cg09

Ting, J. M. (1987). Full-Scale Cyclic Dynamic Lateral Pile Responses. *Journal of Geotechnical Engineering*, *113*(1), 30–45. https://doi.org/10.1061/(ASCE)0733-9410(1987)113:1(30)

Tokimatsu, K., Suzuki, H., & Sato, M. (2005). Effects of inertial and kinematic interaction on seismic behavior of pile with embedded foundation. *Soil Dynamics and Earthquake Engineering*, *25*(7-10), 753–762. https://doi.org/10.1016/j.soildyn.2004.11.018

Tolooiyan, A., & Gavin, K. (2011). Modelling the Cone Penetration Test in sand using Cavity Expansion and Arbitrary Lagrangian Eulerian Finite Element Methods. *Computers and Geotechnics*, *38*(4), 482–490. https://doi.org/10.1016/j.compgeo.2011.02.012

Tott-Buswell, J., Garala, T., Prendergast, L., Madabhushi, S., & Rovithis, E. (2022). Seismic response of piles in layered soils: Performance of pseudo-static Winkler models against centrifuge data. *Soil Dynamics and Earthquake Engineering*, *153*, 107110. https://doi.org/10.1016/j.soildyn.2021.107110

Tsaparli, V., Kontoe, S., Taborda, D. M., & Potts, D. M. (2017). The importance of accurate time-integration in the numerical modelling of P-wave propagation. *Computers and Geotechnics*, *86*, 203–208. https://doi.org/10.1016/j.compgeo.2017.01.017

Ueng, T.-S., & Chen, J.-C. (1992). *Computational procedures for determining parameters in Ramberg-Osgood elastoplastic model based on modulus and damping versus strain* (UCRL-ID-111487). Lawrence Livermore National Lab. (LLNL), Livermore, CA (United States). https://doi.org/10.2172/6496483

Paris Agreement to the United Nations Framework Convention on Climate Change (2015, December 12).

Vaiana, N., Sessa, S., Marmo, F., & Rosati, L. (2019). Nonlinear dynamic analysis of hysteretic mechanical systems by combining a novel rate-independent model and an explicit time integration method. *Nonlinear Dynamics*, *98*(4), 2879–2901. https://doi.org/10.1007/s11071-019-05022-5

Van Impe, W. F., & Wang, S.-T. (2020). The advanced p-y method for analyzing the behaviour of large-diameter monopiles supporting offshore wind turbines (J. McCartney & I. Tomac, Eds.). *E3S Web of Conferences*, *205*, 12008. https://doi.org/10.1051/e3sconf/202020512008

Vesic, A. (1961). Bending of beams resting on isotropic elastic solid. *Journal of Soil Mechanics and Foundation Engineering*, *87*, 35–53.

Viggiani, G., & Atkinson, J. H. (1995). Stiffness of fine-grained soil at very small strains. *Geotechnique*, *45*(2), 249–265. https://doi.org/10.1680/geot.1995.45.2.249

Vucetic, M. (1990). Normalized behavior of clay under irregular cyclic loading. *Canadian Geotechnical Journal*, *27*(1), 29–46. https://doi.org/10.1139/t90-004

Vucetic, M., & Dobry, R. (1988). Degradation of Marine Clays under Cyclic Loading. *Journal of Geotechnical Engineering*, *114*(2), 133–149. https://doi.org/10.1061/(ASCE)0733-9410(1988)114:2(133)

Vucetic, M., & Dobry, R. (1991). Effect of Soil Plasticity on Cyclic Response. *Journal of Geotechnical Engineering*, *117*(1), 89–107. https://doi.org/10.1061/(ASCE)0733-9410(1991)117:1(89)

Wang, H., Lehane, B., Bransby, M., Askarinejad, A., Wang, L., & Hong, Y. (2022a). A simple rotational spring model for laterally loaded rigid piles in sand. *Marine Structures*, *84*, 103225. https://doi.org/10.1016/j.marstruc.2022.103225

Wang, H., Zanten, D., Lange, D., Pisanò, F., Gavin, K., & Askarinejad, A. (2022b, June 7). Centrifuge study on the CPT based p-y models for the monopiles. https://doi.org/10.1201/9781003308829-174

Wang, L., Lai, Y., Hong, Y., & Mašín, D. (2020). A unified lateral soil reaction model for monopiles in soft clay considering various length-to-diameter (L/D) ratios. *Ocean Engineering*, *212*, 107492. https://doi.org/10.1016/j.oceaneng.2020.107492

Wen, Y. (1976). Method for Random Vibration of Hysteretic System. *Journal of the Engineering Mechanics Division*, *102*(2), 249–263.

Whyte, S. A., Burd, H. J., Martin, C. M., & Rattley, M. J. (2020). Formulation and implementation of a practical multi-surface soil plasticity model. *Computers and Geotechnics*, *117*, 103092. https://doi.org/10.1016/j.compgeo.2019.05.007

Williams, S. A., Pelecanos, L., & Darby, A. (2021). Modelling the impact of gapping behaviour in monopile mounted offshore wind turbine dynamics, 5005–5014. https://doi.org/10.7712/120121.8845.18612

Williams, S. A., Pelecanos, L., & Darby, A. P. (2022). A Winkler model of monopile ratcheting under long-term dynamic cyclic loading. *Ocean Engineering*, *266*, 112625. https://doi.org/10.1016/j.oceaneng.2022.112625

Wilson, E. L., Farhoomand, I., & Bathe, K. J. (1972). Nonlinear dynamic analysis of complex structures. *Earthquake Engineering & Structural Dynamics*, *1*(3), 241–252. https://doi.org/10.1002/eqe.4290010305

Wilson, J. F. (2003). *Dynamics of offshore structures* (2nd ed). J. Wiley.

Wind Europe. (2021a). *Offshore wind in Europe: Key trends and statistics 2020*.

Wind Europe. (2021b). *Wind energy in Europe: 2020 Statistics and the outlook for 2021-2025*.

Winkler, E. (1867). *Theory of elasticity and strength*.

Wood, W. L. (1990). *Practical time-stepping schemes*. Clarendon Press ; Oxford University Press.

Wood, W. L., Bossak, M., & Zienkiewicz, O. C. (1980). An alpha modification of Newmark's method. *International Journal for Numerical Methods in Engineering*, *15*(10), 1562–1566. https://doi.org/10.1002/nme.1620151011

Wu, W., Prendergast, L. J., & Gavin, K. (2018). An iterative method to infer distributed mass and stiffness profiles for use in reference dynamic beam-Winkler models of foundation piles from frequency response functions. *Journal of Sound and Vibration*, *431*, 1–19. https://doi.org/10.1016/j.jsv.2018.05.049

Wu, X., Hu, Y., Li, Y., Yang, J., Duan, L., Wang, T., Adcock, T., Jiang, Z., Gao, Z., Lin, Z., Borthwick, A., & Liao, S. (2019). Foundations of offshore wind turbines: A review. *Renewable and Sustainable Energy Reviews*, *104*, 379–393. https://doi.org/10.1016/j.rser.2019.01.012

Yang, Z., & Jeremić, B. (2005). Study of Soil Layering Effects on Lateral Loading Behavior of Piles. *Journal of Geotechnical and Geoenvironmental Engineering*, *131*(6), 762–770. https://doi.org/10.1061/(ASCE)1090-0241(2005)131:6(762)

Yi, F. (2010). Nonlinear cyclic characteristics of soils.

Zdravković, L., Jardine, R. J., Taborda, D. M. G., Abadias, D., Burd, H. J., Byrne, B. W., Gavin, K. G., Houlsby, G. T., Igoe, D. J. P., Liu, T., Martin, C. M., McAdam, R. A., Muir Wood, A., Potts, D. M., Skov Gretlund, J., & Ushev, E. (2020a). Ground characterisation for PISA pile testing and analysis. *Géotechnique*, *70*(11), 945–960. https://doi.org/10.1680/jgeot.18.PISA.001

Zdravković, L., Taborda, D. M. G., Potts, D. M., Abadias, D., Burd, H. J., Byrne, B. W., Gavin, K. G., Houlsby, G. T., Jardine, R. J., Martin, C. M., McAdam, R. A., & Ushev, E. (2020b). Finite-element modelling of laterally loaded piles in a stiff glacial clay till at Cowden. *Géotechnique*, *70*(11), 999–1013. https://doi.org/10.1680/jgeot.18.PISA.005

Zhang, X., Li, B., Yang, Z., Zhu, B., Xu, R., Wang, J., & Gong, X. (2023). Timoshenko beam theory–based analytical solution of laterally loaded large-diameter monopiles. *Computers and Geotechnics*, *161*, 105554. https://doi.org/10.1016/j.compgeo.2023.105554

Zhang, Y., Andersen, K., Jeanjean, P., Mirdamadi, A., Gundersen, A., & Jostad, H. (2017). A Framework for Cyclic p-y Curves in Clay and Application to Pile Design in GoM. *Offshore Site Investigation Geotechnics 8th International Conference Proceedings*, 431–440. https://doi.org/10.3723/osig17.431

Zhang, Y., & Andersen, K. (2017). Scaling of lateral pile p-y response in clay from laboratory stress-strain curves. *Marine Structures*, *53*, 124–135. https://doi.org/10.1016/j.marstruc.2017.02.002

Zhang, Y., & Andersen, K. (2019). Soil reaction curves for monopiles in clay. *Marine Structures*, *65*, 94–113. https://doi.org/10.1016/j.marstruc.2018.12.009

Zhang, Y., Andersen, K., & Jeanjean, P. (2020). Verification of a framework for cyclic p-y curves in clay by hindcast of Sabine River, SOLCYP and centrifuge laterally loaded pile tests. *Applied Ocean Research*, *97*, 102085. https://doi.org/10.1016/j.apor.2020.102085

Zhang, Y., Andersen, K., Klinkvort, R. T., Jostad, H. P., Sivasithamparam, N., Boylan, N. P., & Langford, T. (2016). Monotonic and Cyclic p-y Curves for Clay Based on Soil Performance Observed in Laboratory Element Tests. https://doi.org/10.4043/26942-MS

Ziegler, L., Voormeeren, S., Schafhirt, S., & Muskulus, M. (2015). Sensitivity of Wave Fatigue Loads on Offshore Wind Turbines under Varying Site Conditions. *Energy Procedia*, *80*, 193–200. https://doi.org/10.1016/j.egypro.2015.11.422

Appendix A

Model assembly

This appendix describes the model assembly process, including element description, global matrix population, and boundary conditions. The dynamic multi-degree of freedom model also requires the global mass matrix, which is defined using the same population methodology. All simulations are performed using MATLAB R2019a - R2023a.

A.1 Degrees of freedom and populating elements

The *p*-*y* model consists of elastic beam elements to encapsulate the lateral flexibility of the pile, and nonlinear spring elements to represent the soil-structure interaction. This is illustrated in Figure A.1. Figure A.2 shows the Degrees Of Freedom (DOF) for the beam and spring elements used in this study. The beam element has a rotational and lateral DOF at each end, therefore axial forces are neglected in this type of model. Each end of the beam element is attached to a lateral and spring element shown in Figures A.2b and A.2c, respectively. Each spring type has 2 DOF. Figure A.1 shows that one end of each spring is fixed, which is considered as the boundary condition of the model.

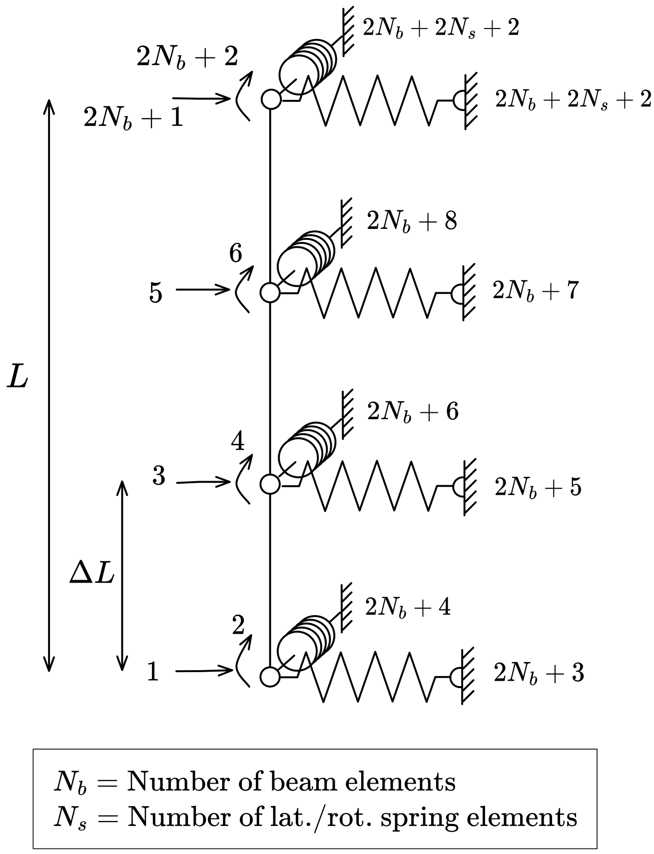

Figure A.1: Modified p-y model DOF configuration

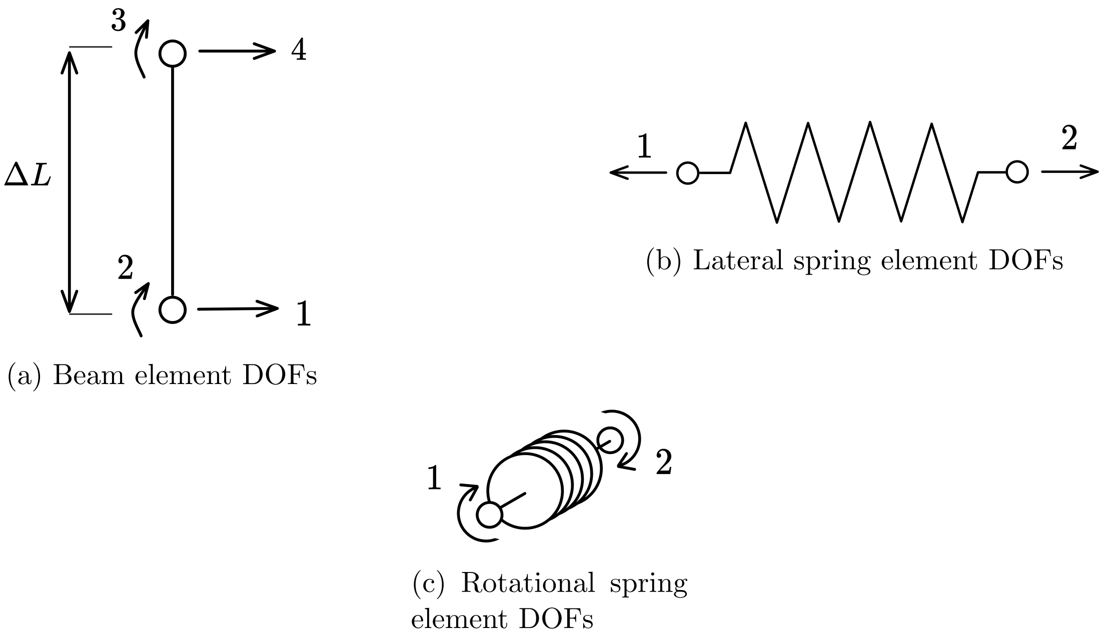

Figure A.2: Element DOFs for beam and spring elements

The elements are connected as shown in Figure A.2 to create the full Winkler model. N_b number of 4 by 4 beam elements are connected end-to-end vertically at ΔL lengths, and spring elements are attached to the shared nodes where appropriate.

The cross-section for all beams that describe the monopile are constant along the depth. The DOFs are numbered sequentially from the bottom of the pile, starting with the lateral DOF at the bottom node, then the rotational DOF at the bottom node, then the lateral DOF at the next node, and so on. The fixed end of the spring subsequently follows after the pile DOFs are defined. the total DOF (T_{DOF}) for the multi-spring is computed as $2N_b + 2N_s + 2$, where N_b is the number of beam elements and N_s is the number of lateral/rotational spring elements. Note that, for the traditional *p*-*y* model (illustrated in Figure 2.2), the rotational spring element is neglected (Figure A.2c), therefore the T_{DOF} reduced to $2N_b + N_s + 1$.

The global stiffness matrix $[K]$ and global mass matrix $[M]$ are assembled by populating a T_{DOF} by T_{DOF} zero matrix with the beam and spring element matrices described in the Appendix A.2. For each node in Figure A.1, the associated DOF indices in the global matrix are populated with the element matrices attached to that specific node. For example, DOF 1 to 4 will include the 4 by 4 beam element matrix; DOF 1 and $2N_b + 3$ will apply the lateral spring stiffness matrix; and DOF 2 and $2N_b + 4$ will apply the lateral spring stiffness matrix. This is done for all beam and spring elements. The boundary conditions are applied by removing associated rows and columns from the global matrix that correspond to the fixed end of the spring elements (i.e. $2N_b + 3$, $2N_b + 4$, ... , $2N_b + 2N_s + 2$ for a model with lateral and rotational springs).

The force vector $\{F\}$ is constructed by populating a T_{DOF} by 1 vector of zeros with the external loads and moments added at the appropriate indices. For the model described in Figure A.1, the external loads and moments are applied at DOFs $2N_b + 1$ and $2N_b + 2$, respectively, which is the position of the ground line relative to the discretised model. Similar to the global matrices, the boundary conditions are applied by removing the associated vector rows in $\{F\}$ that are associated with the fixed ends of the spring. The displacement vector $\{x\}$ can then be solved for using $\{x\} = [K]^{-1}\{F\}$ (for static simulations), where the horizontal displacement and rotation of each node is extracted from $\{x\}$. For dynamic simulations, the global mass matrix $[M]$ is also populated using the same methodology as the stiffness matrix, and $\{x\}$ (including $\{\dot{x}\}$ and $\{\ddot{x}\}$) is solved using the TMA described in Section 4.1.

For the integrated OWT-monopile model described in Chapter 4, the DOFs of the system in Figure A.1 needs to be modified to accommodate additional beam elements that represent the extended monopile above ground level and the appended OWT tower. For N_t additional beam elements, where N_t is the number of beams that describe the structure above the ground line, the updated total DOF is $T_{DOF} = 2N_b + 2N_t + Ns + 1$. Note that the rotational springs are not considered in the dynamic p-y model. The updated formulation for the boundary conditions are therefore $2N_b + 2N_t + 1$, $2N_b + 2N_t + 2$, ... , $2N_b + 2N_t + N_s + 1$. The appended beam elements that encapsulate the OWT tower are tapered, and therefore the beam element matrices are updated to account for this. According to Table 4.4, the beam elements describing the model can have unique lengths (different ΔL values), therefore the beam element matrices should reflect this. The beam stiffness and mass element matrices are described in Section A.2.2.

A.2 Element matrices

The beam and spring element matrices are defined herein.

A.2.1 Spring element matrices

The 2 by 2 spring stiffness matrix is defined using Equation A.1. For each element, the nodes are superimposed with the DOF indices in the global matrix, which depends on the location of the spring (Figure A.1).

$$[K_s] = \begin{bmatrix} -k_s & k_s \\ k_s & -k_s \end{bmatrix} \tag{A.1}$$

where k_s is the lateral/rotational stiffness of the spring, depending on the spring type. Note that k_s is a function of the p-y (or m-θ) relationship, and is defined as $k_s = p\Delta L/y$ (or $k_s = m\Delta L/\theta$). For more details on soil modulus parameters for a typical p-y model, see Table 2.1. For nonlinear simulations, k_s is updated based on the current y or θ value. Details on the nonlinear iteration process can be found in Section B.1. Note that the spring does not have any attributed mass.

A.2.2 Beam element matrices

There are two primary beam theories commonly used in the analysis of beams; the Euler-Bernoulli and Timoshenko beam theory. Euler-Bernoulli is commonly used in structural analysis software and for slender structures, whereas Timoshenko is more accurate for short, thick beams as it can account for shear deformations during bending (Gupta & Basu, 2018). The 4 by 4 beam element matrices for both Euler-Bernoulli and Timoshenko beam theories are detailed in this section.

Euler-Bernoulli beam theory

The stiffness matrix is presented in Equation A.2, and is used in Chapter 5 for the pseudostatic modelling approach.

$$[K_b] = \frac{EI}{L^3}\begin{bmatrix} 12 & 6L & -12 & 6L \\ 6L & 4L^2 & -6L & 2L^2 \\ -12 & -6L & 12 & -6L \\ 6L & 2L^2 & -6L & 4L^2 \end{bmatrix} \tag{A.2}$$

where E and I are the elastic modulus and moment of inertia of the beam element, respectively.

The consistent beam mass matrix is presented in Equation A.3 (Bathe, 2006).

$$[M_b] = [M_{\rho A}] + [M_{\rho I}] \tag{A.3}$$

where

$$[M_{\rho A}] = \frac{\rho AL}{420}\begin{bmatrix} 156 & 22L & 54 & -13L \\ 22L & 4L^2 & 13L & -3L^2 \\ 54 & 13L & 156 & -22L \\ -13L & -3L^2 & -22L & 4L^2 \end{bmatrix}$$

$$[M_{\rho I}] = \frac{\rho I}{30L}\begin{bmatrix} 36 & 3L & -36 & 3L \\ 3L & 4L^2 & -3L & L^2 \\ -36 & -3L & 36 & -3L \\ 3L & L^2 & -3L & 4L^2 \end{bmatrix}$$

A.2.3 Timoshenko beam theory

The stiffness matrix is presented in Equation A.4, and is used in Chapter 3 and Chapter 4 to simulate the stocky behaviour of monopiles. Timoshenko beam theory considers the influence of shear resistance, which is prominent in short, thick beam elements under lateral bending (Gupta & Basu, 2018).

$$[K_b] = C\begin{bmatrix} 12 & 6L & -12 & 6L \\ 6L & (4+\phi)L^2 & -6L & (2-\phi)L^2 \\ -12 & -6L & 12 & -6L \\ 6L & (2-\phi)L^2 & -6L & (4+\phi)L^2 \end{bmatrix} \tag{A.4}$$

where

$$C = \frac{EI}{(1+\phi)L^3}, \qquad \phi = \frac{12}{L^2}\left(\frac{EI}{\kappa GA}\right)$$

The Timoshenko mass matrix is presented in Equation A.5.

$$[M_b] = [M_{\rho A}] + [M_{\rho I}] \tag{A.5}$$

where

$$[M_{\rho A}] = \frac{\rho AL}{210(1+\phi)^2}\begin{bmatrix} a & b & c & -d \\ b & e & d & f \\ c & d & a & -b \\ -d & f & -b & e \end{bmatrix}$$

$$\begin{aligned} a &= (70\phi^2 + 147\phi + 78) & d &= -(35\phi^2 + 63\phi + 26)\frac{L}{4} \\ b &= (35\phi^2 + 77\phi + 44)\frac{L}{4} & e &= (7\phi^2 + 14\phi + 8)\frac{L^2}{4} \\ c &= (35\phi^2 + 63\phi + 27) & f &= -(7\phi^2 + 14\phi + 6)\frac{L^2}{4} \end{aligned}$$

and

$$[M_{\rho I}] = \frac{\rho I}{30(1+\phi)^2 L}$$
$$\begin{bmatrix} 36 & -(15\phi-3) & -36 & -(15\phi-3)L \\ -(15\phi-3) & (10\phi^2+5\phi+4)L62 & (15\phi-3)L & (5\phi^2-5\phi-1)L^2 \\ -36 & (15\phi-3)L & 36 & (15\phi-3)L \\ -(15\phi-3) & (5\phi^2-5\phi-1)L^2 & (15\phi-3)L & (10\phi^2+5\phi+4)L^2 \end{bmatrix}$$

A.2.4 Gradient matrix

To compute the bending moment profile in the pseudostatic model described in Chapter 5, the gradient matrix for Euler-Bernoulli beam theory is required. This can be derived from the shape functions (or interpolation functions) for Euler-Bernoulli beams and are defined in Equation A.6 (Chopra, 2013).

$$[N] = [N_1, N_2, N_3, N_4] \tag{A.6}$$

where

$$N_1 = 1 - \frac{3x^2}{L^2} + \frac{2x^3}{L^3} \qquad N_3 = \frac{3x^2}{L^2} - \frac{2x^3}{L^3}$$
$$N_2 = x - \frac{2x^2}{L} + \frac{x^3}{L^2} \qquad N_4 = -\frac{x^2}{L} + \frac{x^3}{L^2}$$

The bending moment within a beam cross-section is defined as $M = \epsilon\frac{EI}{y_N}$, where y_N is the distance from the neutral axis and ϵ is the strain at point y_N long the cross-section. The maximum moment within the cross-section of the beam occurs at the edge, therefore $y_N = D/2$. The strain is defined as $\epsilon = [B]\{x_b\}$, where $\{x_b\}$ is the displacement vector for a beam element ($\{x_b\} = [x_1, \theta_1, x_2, \theta_2]^T$). $[B]$ is the gradient matrix, and is the second derivative of the shape functions (Bathe, 2006). The gradient matrix is defined in Equation A.7.

$$[B] = y[B_1, B_2, B_3, B_4] \tag{A.7}$$

where

$$B_1 = \frac{12x}{L^3} - \frac{6}{L^2} \qquad B_3 = -\frac{12x}{L^3} + \frac{6}{L^2}$$
$$B_2 = \frac{6x}{L^2} - \frac{4}{L} \qquad B_4 = \frac{6x}{L^2} - \frac{2}{L}$$

The maximum moment M can therefore be determined at any point x along the beam element for a given beam displacement vector $\{x_b\}$.

Appendix B

Programming and validation: Static model

B.1 Nonlinear iterative process for static equilibrium

The nonlinear static simulation is performed by first computing the linear response, where the initial global stiffness matrix $[K^1]$ is populated with spring elements informed with the appropriate initial stiffness k_0. For details on populating the global stiffness matrix, see Section A.1. The initial deflection vector $\{x^1\}$ is then calculated by solving $\{x^1\} = [K^1]^{-1}\{F\}$. $\{x^1\}$ is then used to compute the nodal displacements of the spring elements, which is used to compute the secant stiffness of the lateral spring elements based on current nodal displacements, i.e. $k_s^j = \frac{p(y^{j-1})}{y^{j-1}}\Delta L$, where y is the lateral displacement of the node. For rotational spring elements, $k_s^j = \frac{m(\theta^{j-1})}{\theta^{j-1}}\Delta L$, where θ is the rotational displacement of the node. The secant stiffness values are then used to update the global stiffness matrix $[K^2]$, and the process is repeated until convergence is achieved. The nonlinear static iteration process is detailed in Table B.1, and convergence is calculated by comparing the percentage difference of the ground line displacements between iterations, i.e. $|\delta^{j+1} - \delta^j|/|\delta^j| \leq 10^{-6}$.

Table B.1: Nonlinear static iteration process

Nonlinear iteration for p-y model
1. Let $j = 1$. Compute the initial deflection vector $\{x\}$ using initial stiffness properties by solving $\{x\} = [K]^{-1}\{F\}$ 2. Determine the spring element secant stiffness k_s^j values using nodal deflections from $\{x^j\}$ 3. Update the global stiffness matrix $[K^j]$ by populating with new spring stiffness values 4. Ccalculate the deflection vector $\{x^{j+1}\}$ by solving $\{x^{j+1}\} = [K^j]^{-1}\{F\}$ 5. Check for convergence by comparing the percentage difference of the ground line displacements between iterations, i.e. $\|\delta^{j+1} - \delta^j\|/\|\delta^j\| \leq 10^{-6}$ 6. If convergence is not achieved, advance j and return to step 2

B.2 Nonlinear static model validation

The algorithm presented in Table B.1 is validated by comparing simulation results to the commercially available software LPILE. LPILE is a nonlinear finite element analysis software that is commonly used for the analysis of piles and drilled shafts under lateral loading by also utilising the *p*-*y* methodology (Isenhower & Wang, 2016). Both the LPILE and MATLAB model will utilise the API sand model to compare results. Details on the API sand reaction curves can be found in Section 2.1.2. To simplify the comparative study, only lateral springs are considered in the following analysis. Three piles of varying geometries are considered herein, and are detailed in Table B.2. 100 spring elements are considered for each pile, and the soil properties are detailed in Table B.3. For a better comparison between models, Euler-Bernoulli beam theory is applied to the MATLAB model. The L/D ratio is varied to observe the performance of the model under different geometrical conditions. The MATLAB pile models are illustrated in Figure B.1.

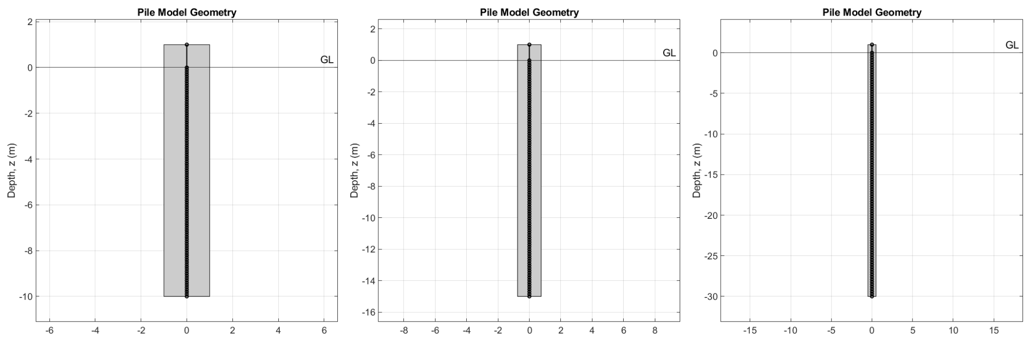

(a) Pile 1 (b) Pile 2 (c) Pile 3

Figure B.1: MATLAB pile model geometries for nonlinear static validation

Table B.2: Pile geometries for nonlinear static validation

Pile	D (m)	L (m)	L/D (-)	t (m)	h (m)	E (GPa)
1	2.0	10	5	0.01	1.0	210
2	1.5	15	10	0.01	1.0	210
3	1.0	30	30	0.01	1.0	210

Table B.3: Soil properties for nonlinear static validation

Parameter	**Value**
Coeff. subgrade reaction, k_{sr}	45 MN/m^3
Eff. unit weight, γ'	19 kN/m^3
Angle of friction, ϕ	40°

The water table is assumed to be below the embedment depth of the monopile. A load eccentricity h is considered by computing the equivalent moment M due to applied lateral load h (i.e. $M = Fh$). The horizontal load is increased until considerable pile mobilisation is observed. The applied load F against head deflections δ are plotted in Figure B.2 for both MATLAB and LPILE simulations. Five arbitrary load cases are considered in the LPILE tests.

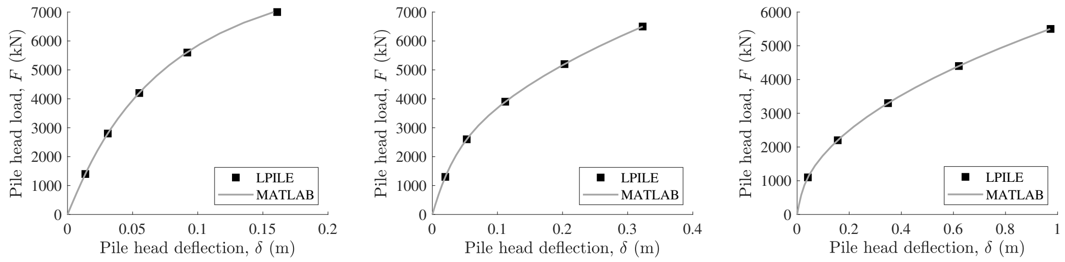

(a) Pile 1 (b) Pile 2 (c) Pile 3

Figure B.2: Pile head displacement comparison between p-y models developed in LPILE and MATLAB

Figure B.2 shows that the MATLAB model is able to replicate the LPILE results with a high level of accuracy, and suggests that the nonlinear iteration process towards static equilibrium is valid, including the implementation of the API sand model. Figure B.3 shows the displacement profile along the depth of the monopile for each model due to the maximum load applied in Figure B.2.

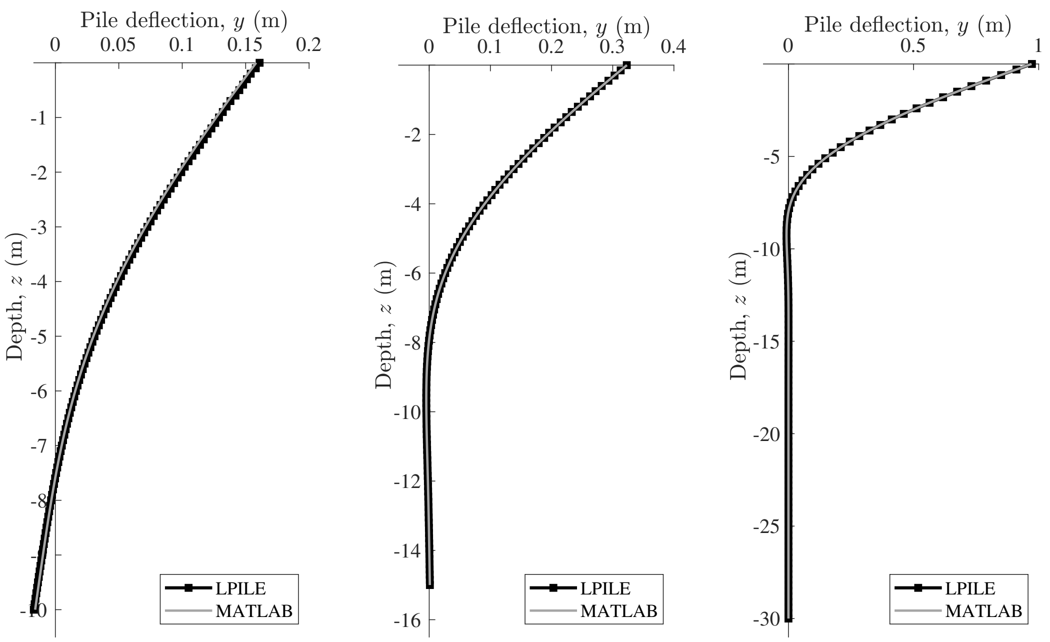

(a) Pile 1 (F = 7000kN) (b) Pile 2 (F = 6500kN) (c) Pile 3 (F = 5500kN)

Figure B.3: Pile deflection profile comparison between p-y models developed in LPILE and MATLAB

Figure B.3 suggests that the global stiffness matrix $[K]$ is correctly assembled and the nonlinear convergence process is valid, as both models are in excellent agreement in estimating the deflection profile of the monopile. It is also shown that the degree of pile rigidity is apparent between the three investigated models. The

Euler-Bernoulli gradient matrices described in Section A.2.4 are used to compute the nodal bending moments along the pile depth, and are plotted in Figure B.4.

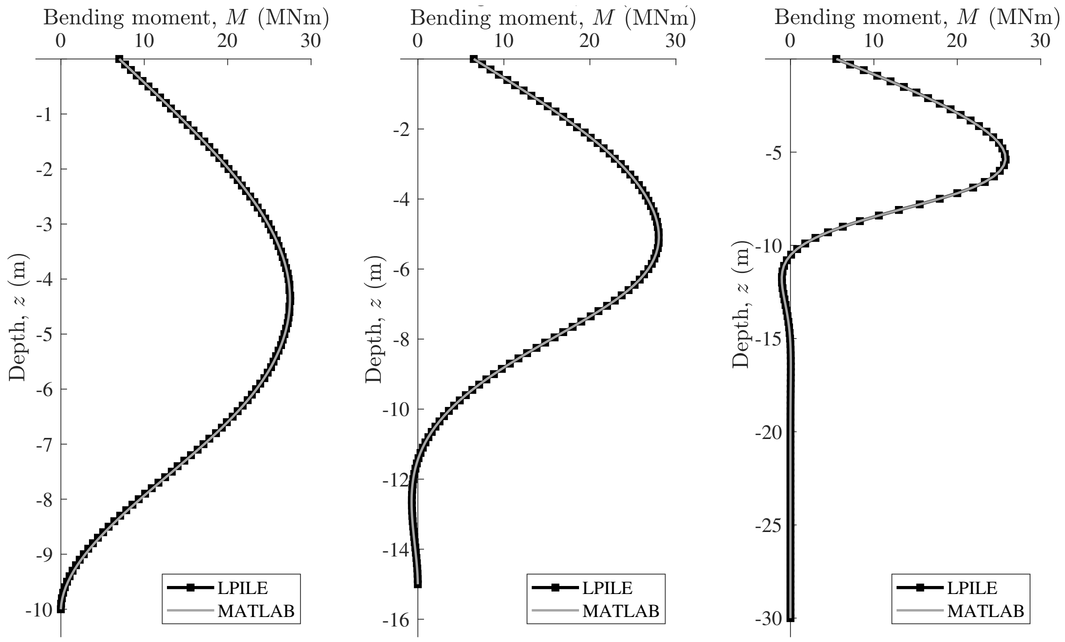

(a) Pile 1 ($F = 7000$kN) (b) Pile 2 ($F = 6500$kN) (c) Pile 3 ($F = 5500$kN)

Figure B.4: Pile bending moment profile comparison between p-y models developed in LPILE and MATLAB

Figure B.4 shows that the MATLAB model is able to replicate the LPILE results with a high level of accuracy, and suggests that the gradient matrices are correctly assembled. The bending moment profiles are also consistent with the applied load, as the bending moment at ground line equates to the moment due to load eccentricity (i.e. $M = Fh$).

In this comparative study, the model's ability represent the nonlinear soil-structure interaction within a traditional lateral spring model (p-y only) has been demonstrated by comparing with the commercially-available software LPILE. Although rotational and base springs were not included in this study, they can be incorporated into the MATLAB model using a similar matrix indexing process employed for the lateral spring elements (as discussed in Appendix A). It is worth noting that options for software validation are limited in facilitating the creation of custom nonlinear reaction curves for numerous nodal points programmatically. However, this study has demonstrated that the framework of the MATLAB model is capable of appropriately accommodating custom reaction curves.

Appendix C

Programming and validation: Dynamic model

C.1 Modal validation

The global stiffness and mass matrices assembled in MATLAB are validated by means of a modal analysis by comparing results against the commercially available software SAP2000 (CSi, 2016). Several simplified monopile models of various L/D ratios are developed using MATLAB and are shown in Figure C.1. The beam-spring models consists of seven nodal points interconnected with beam elements, where all but the top nodes are supported by lateral and rotational spring elements. Both Timoshenko and Euler-Bernoulli beam theory is investigated in this study. The cross-section and material properties are the same for each model, and all pile properties are outlined in Table C.1. The beam element lengths vary depending on the embedment length and node spacing. The matrix assembly process is outlined in previous sections.

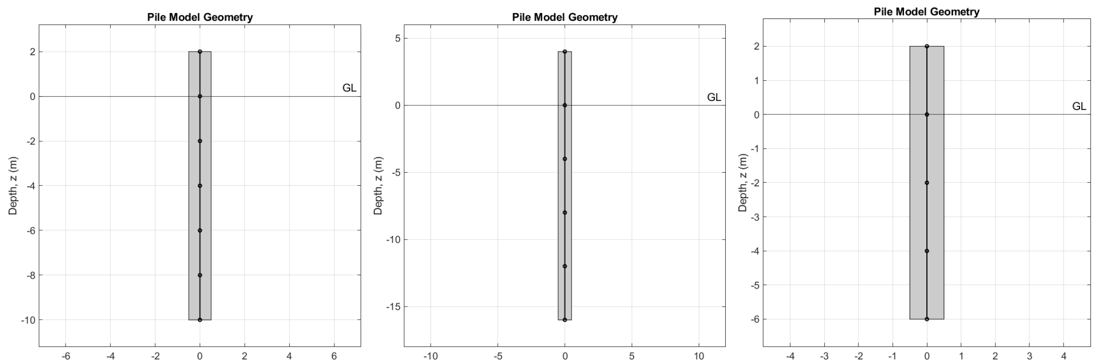

(a) MP1: $L = 10$m, $N_s = 6$ (b) MP2: $L = 16$m, $N_s = 5$ (c) MP3: $L = 6$m, $N_s = 4$

Figure C.1: Simplified monopile model in MATLAB

Table C.1: Section properties for the simplified monopile models

Pile	D	t	L	h	E	G	ρ	N_s
	(m)	(m)	(m)	(m)	(GPa)	(GPa)	(kg/m^3)	(-)
1	1	0.01	10	2	210	80.8	7850	6
2	1	0.01	16	4	210	80.8	7850	5
3	1	0.01	6	2	210	80.8	7850	4

Both lateral and rotational springs are arbitrarily informed using a linearly increasing stiffness function in accordance to depth, i.e. $k_0 = k_{GL} + k_z z$, where k_{GL} is the stiffness at the ground line, and k_z is the rate of stiffness increase with depth z. For the lateral springs, $k_{GL} = 1,000$ kN/m and $k_z = 20,000$ kN/m/m. The rotational springs have stiffness properties of $k_{GL} = 1,000$ kNm/rad and $k_z = 1,000$ kNm/rad/m.

The spring stiffness profile is used to inform the identical spring-beam configuration within SAP2000. The nodes in the SAP2000 model are constrained to only move in the x direction and are free to rotate about the y-axis, matching the boundary conditions of the one-dimensional Winkler model developed in MATLAB. An example SAP2000 model is shown in Figure C.2.

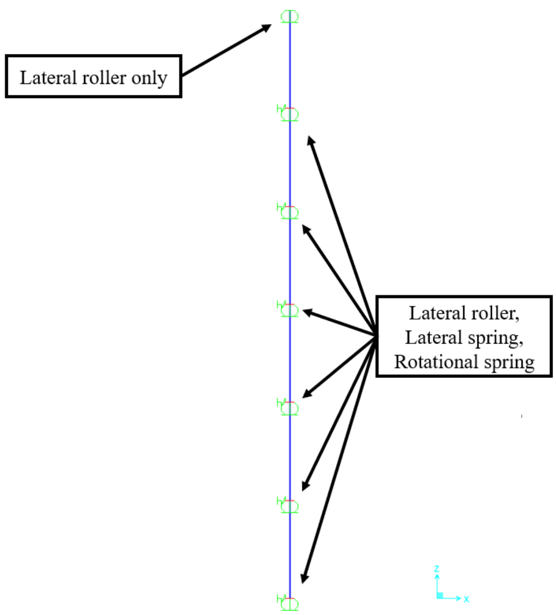

Figure C.2: SAP2000 model of a simplified monopile structure (MP1)

The modal frequencies are computed through an eigenanalysis using the `eig(inv(M)*K)` function in MATLAB. The SAP2000 model is analysed using an eigenvalue solver, which is a standard feature of the software. Table C.2 shows the first five modal frequency computations from both MATLAB and SAP2000 for each pile model. The modal frequencies for both the Euler-Bernoulli (EB) and Timoshenko (TS) beam theories are computed in MATLAB.

Table C.2: First 5 modal frequencies computed using MATLAB and SAP2000 for each pile model

Pile	**Mode number**	**SAP2000 (Hz)**	**MATLAB EB (Hz)**	**% diff. (%)**	**MATLAB TS (Hz)**	**% diff. (%)**
MP1	1	21.073	22.023	**4.5**	21.708	**3.0**
	2	68.818	71.132	**3.4**	70.540	**2.5**
	3	104.991	109.193	**4.0**	107.113	**2.0**
	4	141.419	159.855	**13.0**	153.562	**8.6**
	5	188.611	248.181	**31.6**	228.636	**21.2**
MP2	1	9.386	10.173	**8.4**	10.018	**6.7**
	2	41.164	46.734	**13.5**	46.206	**12.2**
	3	67.882	72.670	**7.1**	72.113	**6.2**
	4	85.230	91.884	**7.8**	90.745	**6.5**
	5	106.936	125.648	**17.5**	122.232	**14.3**
MP3	1	24.253	24.516	**1.1**	24.409	**0.6**
	2	86.476	87.484	**1.2**	87.079	**0.7**
	3	293.820	351.867	**19.8**	321.932	**9.6**
	4	510.432	825.349	**61.7**	649.644	**27.3**
	5	642.203	1419.305	**121.0**	1001.327	**55.9**

For all pile models, it is shown that the percentage error for the first modal frequency estimation is within an acceptable range for both EB and TS beam theories, where TS agrees with SAP2000 better than EB for all cases. Note that, for MP3, TS performs twice as well as EB for all modal frequencies, which is likely due to the shorter pile length where shearing effects are more pronounced. TS theory is capable of capturing the shear deformation effects, whereas it is neglected in EB theory and is more appropriate for slender beams. SAP2000 utilises an alternative beam theory derived in Bathe and Wilson (1976), which can be applied to both short and slender beam elements and therefore appropriately accommodate the stockier pile geometry in MP3 (CSi, 2016).

In general, higher modal frequencies are poorly estimated. This is due to estimations being more sensitive to the discrepancies in the constitutive model's matrix construction. For example, the SAP2000 manual states that the mass matrices are derived using the lumped parameter method, where beam element masses are localised to the nodes and no mass coupling between degrees of freedom are present in the joints (CSi, 2016). In contrast, Section A.2.2 describes consistent mass element matrices for the beams in both EB and TS theory, therefore coupling is assumed. Additional contrasts between the MATLAB model and the underlying stiffness and mass element theory used in the SAP2000 model may also have an impact on the modal frequency computation. Regardless, the results in Table C.2 show that the MATLAB model is capable of estimating the modal frequencies of a simplified monopile structure with a reasonable degree of accuracy, and the stiffness and mass matrices of the model are correctly assembled.

This analysis further highlights the importance of controlled numerical dissipation in time marching algorithms, as discussed in Section 4.1. The Generalised-α method is capable of ensuring that the higher vibration modes are adequately dissipated in the time domain, which have demonstrable inaccuracies in finite element models according to Table C.2.

C.2 Nonlinear iterative process for dynamic equilibrium

The full Generalised-α time marching algorithm, including equilibrium iterations, are described in Table C.3. The derivation of the Generalised-α integration scheme and the hybrid Newton Raphson iteration scheme are available in Section 4.1. It should be noted that the pseudocode in Table C.3 is written in a way that an estimate solution for a nonlinear SDOF and MDOF system can be achieved. Steps where the pseudocode is dependent on the type of system are highlighted accordingly. Parameters are defined in Chapter 4.

Table C.3: Pseudocode describing Generalised-α algorithm with a hybrid Newton-Raphson equilibrium iteration scheme for nonlinear dynamic system (both SDOF and MDOF)

1.0 Initial calculations:

1.1 Choose x_0, $\dot{x}_0$, Δt and ρ_∞

1.2 †Determine initial spring state $f_s(x_0)$ and K_T^*

1.3 ††Initial acceleration $\ddot{x}_0 = \dfrac{F_0 - c\dot{x}_0 - f_s(0)}{m}$

1.4 Compute α_m, α_f, β, γ, and $a_{1,2,3}$ terms...

$$\alpha_m = \frac{2\rho_\infty - 1}{\rho_\infty + 1}, \quad \alpha_f = \frac{\rho_\infty}{\rho_\infty + 1}$$
$$\beta = \frac{1}{4}(1 - \alpha_m + \alpha_f)^2, \quad \gamma = \frac{1}{2} - \alpha_m + \alpha_f$$

$$a_1 = (1-\alpha_m)m\left(\frac{1}{\beta\Delta t^2}\right) + (1-\alpha_f)c\left(\frac{\gamma}{\beta\Delta t}\right)$$
$$a_2 = (1-\alpha_m)m\left(\frac{1}{\beta\Delta t}\right) - (1-\alpha_f)c\left(1-\frac{\gamma}{\beta}\right) - \alpha_f c$$
$$a_3 = (1-\alpha_m)m\left(\frac{1}{2\beta} - 1\right) - (1-\alpha_f)c\Delta t\left(1-\frac{\gamma}{2\beta}\right) - \alpha_m m$$

2.0 Calculations for each time step, $\mathbf{i = 1, 2, 3, ...}$

2.1 †Initialise $j = 1$, $x_{i+1}^{(j)} = x_i$, $f_s(x_{i+1})^{(j)} = f_s(x_i)$

2.2 $\hat{F}_{i+1} = (1-\alpha_f)F_{i+1} + \alpha_f F_i + a_1 x_i + a_2\dot{x}_i + a_3\ddot{x}_i$

2.3 $\hat{K}_T = K_T + a_1$

3.0 For each iteration, $\mathbf{j = 1, 2, 3, ...}$

3.1 $^{\dagger}\hat{f}_s(x_{i+1})^{(j)} = (1-\alpha_f)f_s(x_{i+1}^{(j)}) + \alpha_f f_s(x_i) + a_1 x_{i+1}$

3.2 $\Delta\hat{R}^{(j)} = \hat{F}_{i+1} - \hat{f}_s(x_{i+1})^{(j)}$

3.3 Check for convergence $||\hat{R}^{(j)}|| \leq 10^{-6}$. If condition is not met, implement step 3.3 to 3.8. Otherwise, go to 4.0.

3.4 ††If $j \geq 100$, unsuccessful convergence from Modified Newton Raphson method. Therefore, switch to Original Newton Raphson iteration scheme by update $\hat{K}_T$ for $x_{i+1}^{(j)}$ and go to step 3.5

3.5 $^{\dagger\dagger}\Delta x^{(j)} = \Delta\hat{R}^{(j)}/\hat{K}_T$

3.6 $x_{i+1}^{(j+1)} = x_{i+1}^{(j)} + \Delta x^{(j)}$

3.7 $^{\dagger}\dot{x}_{i+1}^{(j+1)} = \dfrac{\gamma}{\beta\Delta t}(x_{i+1}^{(j+1)} - x_i) + \left(1 - \dfrac{\gamma}{\beta}\right)\dot{x}_i + \Delta t\left(1 - \dfrac{\gamma}{2\beta}\right)\ddot{x}_i$

3.8 $^{\dagger\,\dagger\dagger}$Determine nodal restoring forces from spring states, $f_s(x_{i+1}^{(j+1)})$ and update K_T. For MDOF systems, $f_s(x_{i+1}^{(j+1)}) = f_s(x_{i+1}^{(j)}) + K_T(x_{i+1}^{(j+1)} - x_i)$

3.9 Advance j by $j+1$ and repeat steps 3.1 to 3.8; denote final value of $x_{i+1}^{(j+1)}$ as x_{i+1}

4.0 Calculate velocity and acceleration at $\mathbf{t = t_{i+1}}$

4.1 $\dot{x}_{i+1} = \dfrac{\gamma}{\beta\Delta t}(x_{i+1} - x_i) + \left(1 - \dfrac{\gamma}{\beta}\right)\dot{x}_i + \Delta t\left(1 - \dfrac{\gamma}{2\beta}\right)\ddot{x}_i$

4.2 $\ddot{x}_{i+1} = \dfrac{1}{\beta\Delta t^2}(x_{i+1} - x_i) - \dfrac{1}{\beta\Delta t}\dot{x}_i - \left(\dfrac{1}{2\beta} - 1\right)$

5.0 Repeat for next time step...

5.1 Advance i by $i+1$ and implement steps 2.0 to 4.2 for the next time step

† Step is dependent on hysteresis model. $f_s(x_{i+1})$ can also be a function of velocity, therefore $\dot{x}_{i+1}$ is calculated within j iterations. See Section 4.2 for details.

†† Step varies depending on type of model. Modify accordingly for MDOF systems to accommodate matrix operations.

Step 3.4 exists due to the hysteretic restoring forces exhibiting reversals at maximum displacements. The modified Newton Raphson iteration scheme fails to converge due to a large change in stiffness when the time step starts before the reversal point and ends after the reversal point. Therefore, convergence failure is arbitrarily identified as many iteration counts (i.e. $j > 100$). The original

Newton Raphson iteration scheme is then implemented by updating the stiffness value/global stiffness matrix, which is then used to compute the displacement increment based on post-reversal stiffness properties.

C.3 Dynamic equilibrium validation

The algorithm described in Table C.3 is validated by evaluating the internal forces at each time step and ensuring that the sum is equal to the applied external force at that node. The validation is performed for three MDOF pile models, each with lateral spring elements informed using different hysteresis methods; Masing, Iwan and Bouc-Wen. The purpose of the following analyses is to confirm the underlying physics of the numerical model are adequately captured. For this reason, the parameters describing the soil and the pile geometry are arbitrarily selected for convenient analysis. A quantitative study is not necessary. The monopile and simulation properties are summarised in Table C.4. A sinusoidal load profile is applied at the top of the monopile and the amplitude is arbitrarily large to encourage hysteretic behaviour.

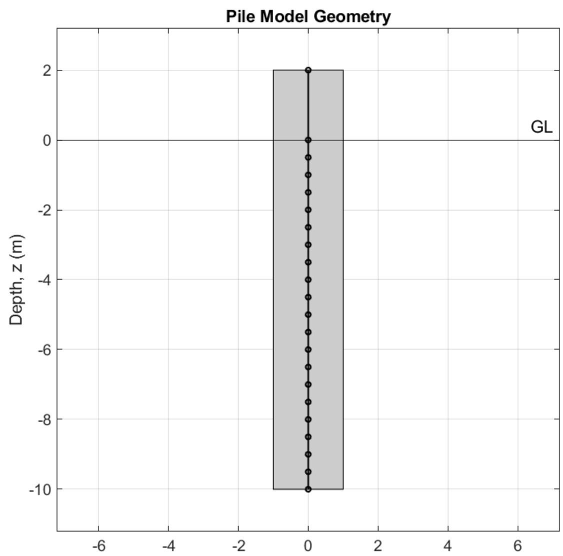

Figure C.3: Simplified monopile model for dynamic equilibrium validation

Table C.4: Simulation parameters for dynamic equilibrium validation

Property	**Value**	**Unit**
Diameter, D	2.5	m
Embedment Length, L	10	m
Slenderness ratio, L/D	4	-
Eccentricity, h	2	m
Wall thickness, t	0.01	m
Young's modulus, E	210	GPa
Shear modulus, G	80.8	GPa
Density, ρ	7850	kg/m^3
Damping ratio, ζ	0.02	-
Load type	sine	-
Load amplitude, $F(t)$	5	MN
Load frequency, f_{ext}	1	Hz
Number of springs	20	-
Sim. duration	10	s
Time step, Δt	0.01	s
ρ_∞	0	-

Twenty lateral springs are used to model the lateral soil resistance. The backbone function for the Masing and Iwan restoring force models are informed using the API sand methodology described in Section 2.1.2. The Bouc-Wen model defined in accordance to Section 4.2.4 such that it is comparable with the Masing and Iwan model. The number of bilinear springs in the Iwan model is set to $N = 20$. The soil profile used in this analysis is the same as the static model validation in Section B.2, therefore the soil properties are summarised in Table . It is important to note that, although the API sand methodology is for static p-y models only, this investigation is only concerned with evaluating the internal forces of the constitutive model and ensuring equilibrium. The API sand model is only used as a convenient method to parametrise the hysteresis models.

The Generalised-α algorithm solves for equilibrium within the time stepped interval using α coefficients applied to each forcing term (see Section 4.2.1). Therefore, to validate the algorithm described in Table C.3, the internal and external forces must be computed at each time step with the α coefficients applied. The internal and external forces are computed using the following equations:

$$F_{i+1} = (1 - \alpha_f)F_{i+1} + \alpha_f F_i \tag{C.1}$$

$$F_{I,i+1} = (1 - \alpha_m) m\ddot{x}_{i+1} + \alpha_m m\ddot{x}_i \tag{C.2}$$

$$F_{D,i+1} = (1 - \alpha_f) c\dot{x}_{i+1} + \alpha_f c\dot{x}_i \tag{C.3}$$

$$F_{K,i+1} = (1 - \alpha_f) f_s(x_{i+1}) + \alpha_f f_s(x_i) \tag{C.4}$$

where F_{i+1}, $F_{I,i+1}$, $F_{D,i+1}$ and $F_{K,i+1}$ are the external force, inertial force, damping force and spring force at $t = t_{i+1}$, respectively. The algorithm is validated by ensuring that the external force is equal to the sum of the inertial, damping and spring forces at each time step. This can be done by observing the nodal forces during the simulation at different depths along the pile. The forces for each spring model at various depths are shown in Figures C.4, C.5 and C.6 for the Masing, Iwan and Bouc-Wen models, respectively. Only the first 4 seconds of the simulation are shown for clarity.

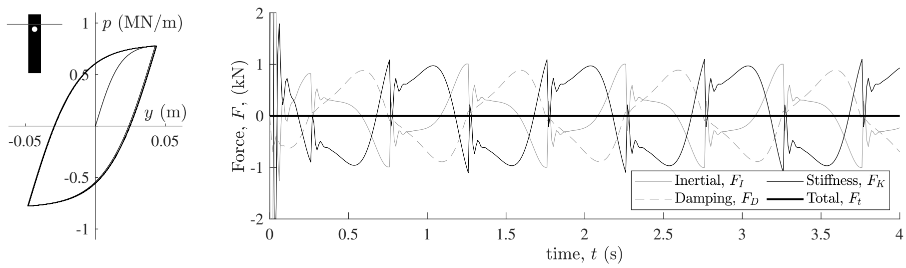

(a) Depth = 1 m

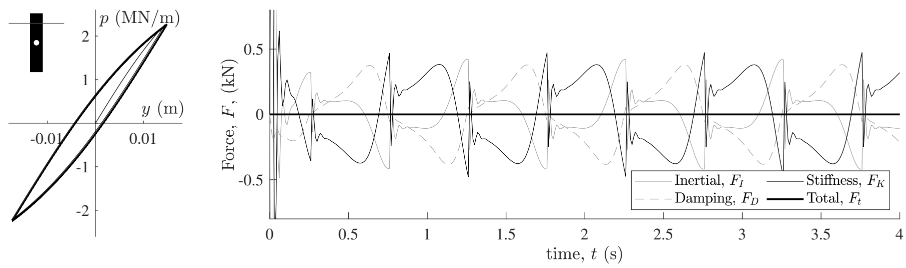

(b) Depth = 4 m

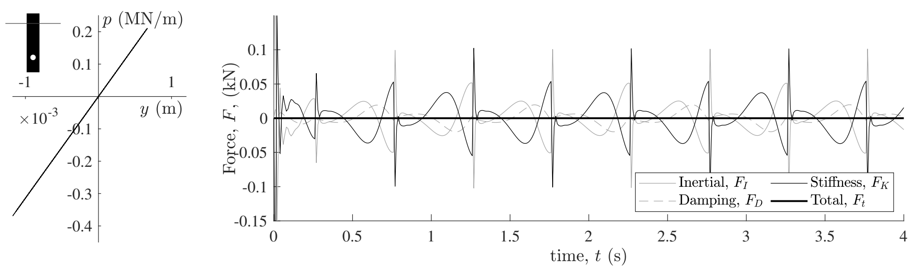

(c) Depth = 7 m

Figure C.4: Internal nodal forces for the Masing model at various spring depths

Figure C.4 shows that the internal force sum to 0 at each point in time. Note that the external force is not evident at these depths as there is no external force applied at these nodes. It is also important to note that F_K includes the lateral stiffness of the beam as well as soil pressure p. Each node demonstrates a transient period during the first time steps of the simulation due to the fast initial loading rate of the sine function. This is quickly dissipated due to the presence of viscous damping ($\zeta = 0.02$), the generalised alpha algorithm ($\rho_\infty = 0$), and the material damping effects of the hysteretic springs. The algorithm still facilitates equilibrium during the transient oscillations. The performance of the MDOF Iwan hysteresis model is shown in Figure C.5.

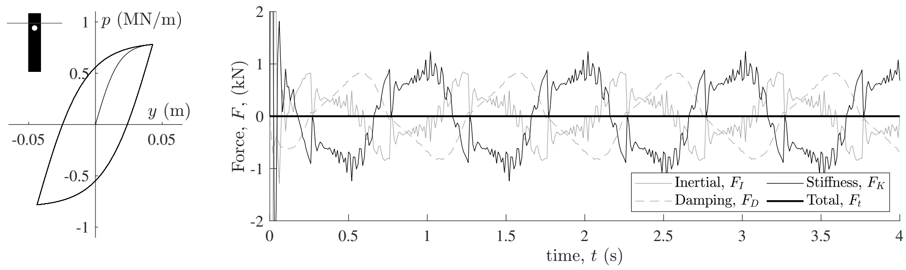

(a) Depth = 1m

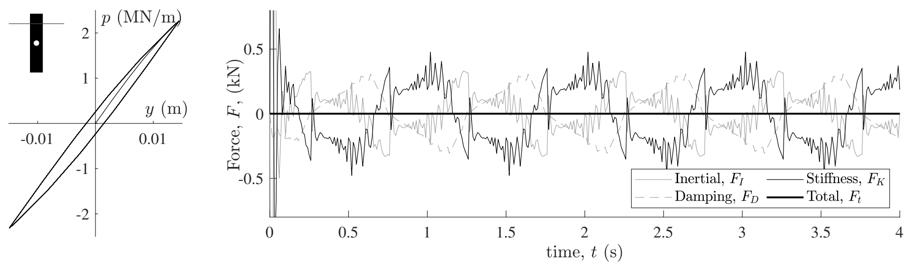

(b) Depth = 4m

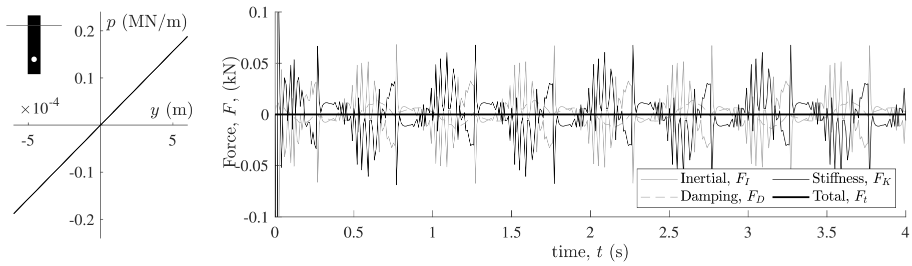

(c) Depth = 7m

Figure C.5: Internal nodal forces for the Iwan model at various spring depths

The internal forces in Figure C.5 exhibit a high frequency oscillation that is not apparent in the Masing model. This is due to the piece-wise linear nature of the Iwan model and the yielding of the bilinear springs continually redistributing forces as the springs mobilise. The Masing hysteresis does not exhibit this behaviour due to it's continuous formulation. Regardless, the equilibrium iteration algorithm is still capable of balancing the internal and external forces at each time step.

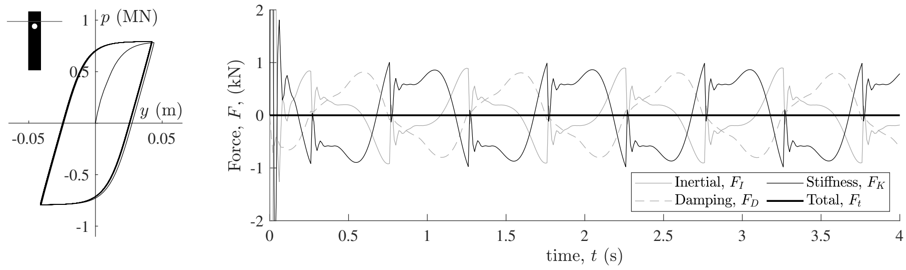

(a) Depth = 1m

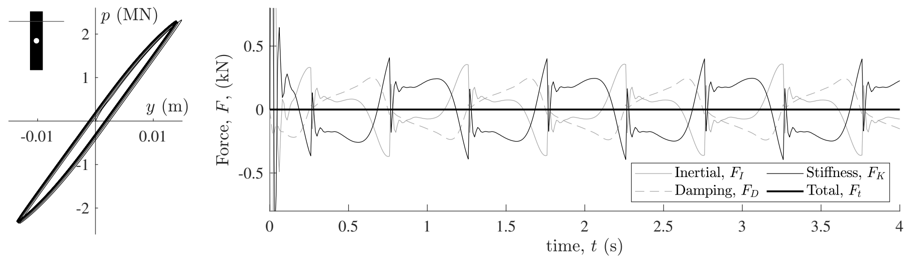

(b) Depth = 4m

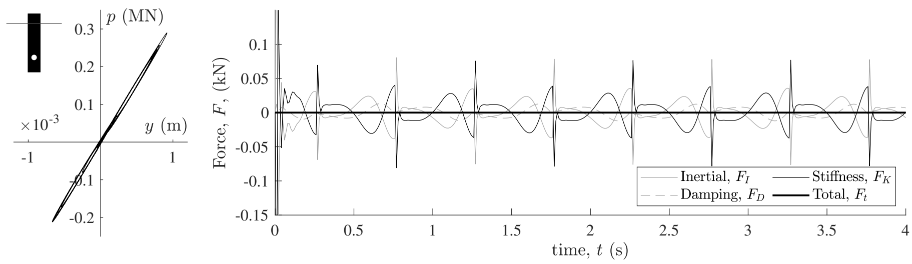

(c) Depth = 7m

Figure C.6: Internal nodal forces for the Bouc-Wen model at various spring depths

Similar to the Masing model, Figure C.6 demonstrates that the Bouc-Wen model does not exhibit high frequency oscillations due to its continuous form. The equilibrium iteration algorithm is still capable of balancing the internal and external forces at each time step, despite the drift.

Summary

This analysis demonstrated the efficacy of the nonlinear dynamic equilibrium iteration scheme by evaluating the nodal internal forces of a MDOF pile model informed using three different hysteresis models. The model was validated by demonstrating that, when a sinusoidal lateral load is applied to the top of the monopile model, the inertial, damping and stiffness forces were balanced at each time step.

C.4 Dynamic pushover test

The dynamic p-y model is validated against LPILE by applying a force history at the pile head that resembles a monotonic lateral push-over load, which is shown in Figure C.7. The model monopiles are informed with identical properties to those used in Appendix B. The pile properties are summarised in Table C.5, and the soil properties can be found in Table B.3.

Table C.5: Pile properties for dynamic pushover validation

Pile	D (m)	L (m)	L/D (-)	t (m)	h (m)	E (GPa)	F (kN)
1	2.0	10	5	0.01	1.0	210	7000
2	1.5	15	10	0.01	1.0	210	6500
3	1.0	30	30	0.01	1.0	210	5500

The monotonic loading function is modelled by taking the first quarter period of a sine function and maintaining the amplitude for the remainder of the simulation. The loading function is shown in Figure C.7, where $F(t)$ is slowly increased to maximum load such that inertial effects are minimal. Increasing the loading for five seconds and then holding for an additional five seconds was deemed appropriate. The simulation is run with $\Delta t = 0.01$ s and $\rho_\infty = 0$ for 10 seconds to observe monotonic behaviour. The maximum load applied for piles 1, 2, and 3 are 7000 kN, 6500 kN and 5500 kN, respectively. The pile head displacements over time for the dynamic p-y model are compared to the head deflections estimated from LPILE, and the results are shown in Figure C.8.

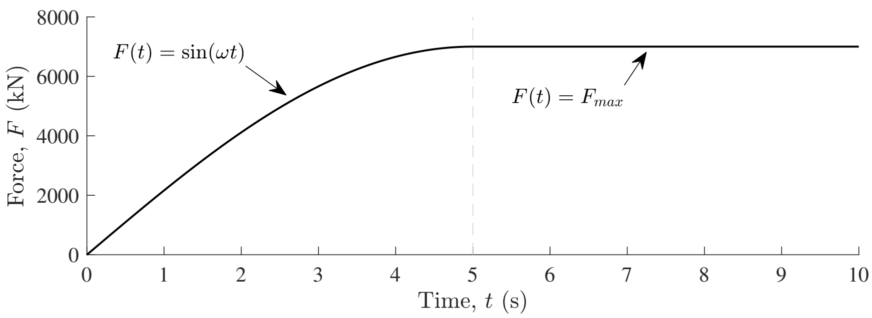

Figure C.7: Loading function for the dynamic pushover test

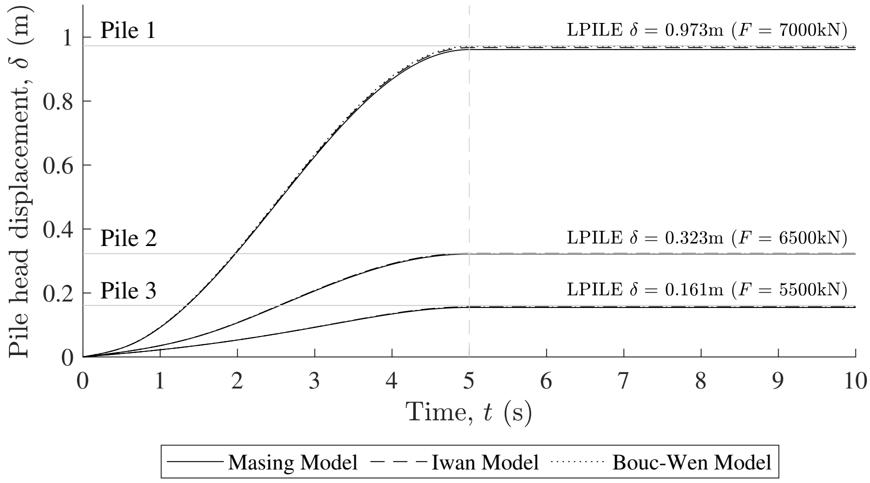

Figure C.8: Pile head displacement during 10 second pushover test for each pile and hysteresis model

Figure C.8 show that the dynamic model is capable of replicating the LPILE results for all piles and hysteresis models. The load rate is slow enough to limit inertial effects, and the head displacement is maintained for the last 5 seconds of the simulation.

All three hysteresis models are capable of replicating the LPILE results. The Masing and Iwan models are explicitly informed by the API sand function, therefore the performance of the models are expected. The Bouc-Wen differential equation that describes the hysteretic behaviour is parametrised to resemble the API sand function, and the results show that the model is capable of replicating the LPILE results. The Bouc-Wen model's response to increasing load is the same as both the Masing and Iwan model. This verifies that, when $\beta = \gamma = 0.5$ and $n = 2$, the exact solution of the Bouc-Wen, at least when on the initial loading curve, is a hyperbolic tangent and therefore identical to Equation 2.3.

Appendix D

Amplification matrices

The amplification matrix $[A]$ encapsulates a time marching algorithm for a SDOF system in matrix form, such that $[A]$ is a linear transformation of the state vector from $t = t_i$ to $t = t_i + \Delta t$. The amplification matrix is used to determine the stability of a system, and is therefore a useful tool for evaluating the performance of a time marching algorithm. The kinematics at $t = t_{i+1}$ can be determined using the following relationship:

$$\begin{Bmatrix} x_{i+1} \\ \dot{x}_{i+1} \\ \ddot{x}_{i+1} \end{Bmatrix} = [A] \begin{Bmatrix} x_i \\ \dot{x}_i \\ \ddot{x}_i \end{Bmatrix} \tag{D.1}$$

where

$$[A] = \begin{bmatrix} a_{11} & a_{12} & a_{13} \\ a_{21} & a_{22} & a_{23} \\ a_{31} & a_{32} & a_{33} \end{bmatrix} \tag{D.2}$$

The following sections will detail the amplification matrices for the Generalised-α and the Wilson-θ methods. Note that the Generalised-α algorithm is an extension to the Newmark-β algorithm, and therefore the amplification matrix for the Newmark-β method is a special case of the Generalised-α amplification matrix.

D.1 Generalised-α amplification matrix

If $\Omega = \omega\Delta t$, where ω is the circular frequency of the system, then the amplification matrix for the Generalised-α method is given using the Equations D.5 to D.9. Note that the Newmark-β amplification matrix is obtained if $\alpha_m = 0$ and $\alpha_f = 0$.

$$a_{11} = \frac{(1-\alpha_m) + 2(1-\alpha_f)\zeta\Omega\gamma - \alpha_f\beta\Omega^2}{(1-\alpha_m) + 2(1-\alpha_f)\zeta\Omega\gamma + (1-\alpha_f)\Omega^2\beta} \tag{D.3}$$

$$a_{12} = \frac{[(1-\alpha_m) + 2(1-\alpha_f)\zeta\Omega(\gamma-\beta) - 2\alpha_f\zeta\Omega\beta]\,\Delta t}{(1-\alpha_m) + 2(1-\alpha_f)\zeta\Omega\gamma + (1-\alpha_f)\Omega^2\beta} \tag{D.4}$$

$$a_{13} = \frac{[(1-\alpha_m-2\beta) + 2(1-\alpha_f)\zeta\Omega\gamma(1-2\beta) - 4(1-\alpha_f)\zeta\Omega\beta(1-\gamma)]\,\frac{\Delta t^2}{2}}{(1-\alpha_m) + 2(1-\alpha_f)\zeta\Omega\gamma + (1-\alpha_f)\Omega^2\beta} \tag{D.5}$$

$$a_{21} = \frac{-\Omega^2\gamma}{[(1-\alpha_m) + 2(1-\alpha_f)\zeta\Omega\gamma + (1-\alpha_f)\Omega^2\beta]\,\Delta t} \tag{D.6}$$

$$a_{22} = \frac{(1-\alpha_m) + (1+\alpha_f)(\beta-\gamma)\Omega^2 - 2\alpha_f\gamma\zeta\Omega}{(1-\alpha_m) + 2(1-\alpha_f)\zeta\Omega\gamma + (1-\alpha_f)\Omega^2\beta} \tag{D.7}$$

$$a_{23} = \frac{\left[(1-\gamma-\alpha_m) + (1-\alpha_f)\Omega^2(\beta-\frac{\gamma}{2})\right]\Delta t}{(1-\alpha_m) + 2(1-\alpha_f)\zeta\Omega\gamma + (1-\alpha_f)\Omega^2\beta} \tag{D.8}$$

$$a_{31} = \frac{-\Omega^2}{[(1-\alpha_m) + 2(1-\alpha_f)\zeta\Omega\gamma + (1-\alpha_f)\Omega^2\beta]\,\Delta t^2} \tag{D.9}$$

$$a_{32} = \frac{-2\zeta\Omega - (1-\alpha_f)\Omega^2}{[(1-\alpha_m) + 2(1-\alpha_f)\zeta\Omega\gamma + (1-\alpha_f)\Omega^2\beta]\,\Delta t} \tag{D.10}$$

$$a_{33} = \frac{-\alpha_m - (1-\alpha_f)(\frac{1}{2}-\beta)\Omega^2 - 2(1-\alpha_f)\zeta\Omega(1-\gamma)}{(1-\alpha_m) + 2(1-\alpha_f)\zeta\Omega\gamma + (1-\alpha_f)\Omega^2\beta} \tag{D.11}$$

D.2 Wilson-θ amplification matrix

The amplification matrix entries for the Wilson-θ method is given using the Equations D.12 to D.20.

$$\lambda = \left(\frac{\theta}{\omega^2\Delta t^2} + \frac{\zeta\theta^2}{\omega\Delta t} + \frac{\theta^3}{6}\right)^{-1} \quad \text{and} \quad \kappa = \frac{\zeta\lambda}{\omega\Delta t}$$

$$a_{11} = -\frac{\lambda}{\Delta t^2} \tag{D.12}$$

$$a_{12} = -\frac{\lambda\theta + 2\kappa}{\Delta t} \tag{D.13}$$

$$a_{13} = 1 - \frac{\lambda\theta^2}{3} - \frac{1}{\theta} - \kappa\theta \tag{D.14}$$

$$a_{21} = -\frac{\lambda}{2\Delta t} \tag{D.15}$$

$$a_{22} = 1 - \frac{\beta\theta}{2} - \kappa \tag{D.16}$$

$$a_{23} = 1 - \frac{1}{2\theta} - \frac{\lambda\theta^2}{6} - \frac{\kappa\theta}{2}\Delta t \tag{D.17}$$

$$a_{31} = 1 - \frac{\lambda}{6} \tag{D.18}$$

$$a_{32} = 1 - \frac{\beta\theta}{6} - \frac{\kappa}{3}\Delta t \tag{D.19}$$

$$a_{33} = \frac{1}{2} - \frac{1}{6\theta} - \frac{\lambda\theta^2}{18} - \frac{\kappa\theta}{6}\Delta t^2 \tag{D.20}$$